Optical Tamm States for novel optical and quantum optical devices

By

MATTHEW J PARKER

Department of Physics
UNIVERSITY OF BRISTOL

A dissertation submitted to the University of Bristol in accordance with the requirements of the degree of DOCTOR OF PHILOSOPHY in the Faculty of Science.

Beware of the man who works hard to learn something, learns it, and finds himself no wiser than before. He is full of murderous resentment of people who have come by ignorance without having come by it through such a hard way.

KURT VONNEGUT, CAT'S CRADLE

A physicist had a horseshoe hanging on the door of his laboratory. His colleagues were surprised and asked whether he, a man of science, believed that it would bring luck to his experiments. He answered: "No, I don't believe in superstitions. But I'm told that it works even if you don't believe in it."

I. BERNARD COHEN

I hear the cottonwoods whisperin' above
Tammy, Tammy, . . .

AUTHOR'S DECLARATION

I declare that the work in this dissertation was carried out in accordance with the requirements of the University's Regulations and Code of Practice for Research Degree Programmes and that it has not been submitted for any other academic award. Except where indicated by specific reference in the text, the work is the candidate's own work. Work done in collaboration with, or with the assistance of, others, is indicated as such. Any views expressed in the dissertation are those of the author.

SIGNED: ..... DATE: .....

ABSTRACT

The growth in demand for bright, efficient and solid state single-photon sources (SPSs) over the last decades has occurred concurrently with the appearance of quantum information applications that employ the quantized nature of photons. This has led to the development of innovative and complex photonic structures that seek to maximize the quality (Q) factor and coupling rate between a single-emitter (such as quantum dots) and a collectible mode. In this thesis I propose that optical Tamm states, an analogue to the electronic Tamm surface states that occur where a periodic material is terminated at an interface, are a potential alternative to these structures for SPSs and other optical devices. Tamm plasmons (TPs), which occur at the interface of a Bragg mirror and metal layer, has the further attraction that confinement can be added by changing the dimensions of the metal layer.

In this thesis I will demonstrate the first measured interaction of quantum dots (QDs) within a confined TP (CTP) at 1.3 μm. A simulation study is used to explore their mode behaviour as a function of various parameters, such as metal layer thickness and shape, and the tolerance to emitter position within the mode. New physical phenomena and insights into the effect on collection efficiency are demonstrated, as is a general method for optimizing efficiency of low Q photonic structures, such as confined TPs and low Q micropillars, for SPSs. Finally, these structures are fabricated and characterized. The photoluminescence collected through the top of the device is shown to increase by at least an order of magnitude compared to when the metal layer is absent, showing QD coupling to the mode. This effect is successfully utilized to make CTP photodetectors. These results demonstrate that CTPs are suitable modes for making scalable SPSs.

ACKNOWLEDGEMENTS

I have been extremely privileged to have been member of the QD group at the University of Bristol the past four years. It is of course an already great university in a wonderful city, but it is the generous and supportive people of the QD group that have been responsible for the most illuminating discussions and exciting physics during my time here. John, Petros, Andrew, Dara, Tunmise, Tom, Joe, Sam and Will have all given helpful assistance and input - they certainly made it a very interesting place to work - with particular thanks directed to Ben and Janna for many restorative tea breaks and fanciful discussions.

I would like to thank Martin Lopez-Garcia and Lifeng Chen for their help with the Fourier imaging spectroscope, Sebastian Knauer for his early assistance with Lumerical FDTD, our growers, Ed Clarke and Ken Kennedy, at the University of Sheffield, and to Jayanta Sarma for our many interesting and fruitful discussions on surface modes. Shout outs must also go to my collaborators at the University of Essex, Ben Cemlyn, Ian Henning and Mike Adams for their work on the photodetector devices.

Special thanks must go to my supervisors. Dr Edmund Harbord has unceasingly offered his help, insight and academic support throughout my time at Bristol (and had the unenviable task of proofreading my thesis); and Prof. Ruth Oulton, for her expertise, patience and guidance, and for kicking me out of a rut.

Finally, I would like to thank my parents Stephen and Jane for their constant love and support.

TABLE OF CONTENTS

Page

List of Figures **xvii**

1 Introduction **1**

1.1 Single-photon sources 1

1.1.1 Quantum dots 4

1.2 Photonic structures 6

1.2.1 Semiconductor cavities 6

1.2.2 Surface modes 8

1.3 Thesis overview 10

2 Optical waves at surfaces and layered media **11**

2.1 Maxwell's equations 12

2.2 Light at a single interface 14

2.2.1 Role of β and ϵ_{eff} 16

2.3 Surface Plasmon Polaritons 17

2.3.1 Solving the wave equation for a SPP 18

2.3.2 Characteristics of SPPs 20

2.3.3 Purcell enhancement and surface plasmon-coupled emission 22

2.4 Light in layered media 23

2.4.1 The transfer matrix method (TMM) 23

2.4.2 Photonic Crystals 27

2.5 Summary 32

3 Optical Tamm states **35**

3.1 Surface states at photonic crystal interfaces 36

3.1.1 Bloch surface waves 36

3.1.2 Impedance matching 38

3.1.3 Reflection from a DBR 39

3.1.4 Characteristics of BSWs 40

3.2 Tamm states . . . 42
3.2.1 DBR heterostructures . . . 42
3.2.2 Tamm plasmons . . . 43
3.2.3 Characteristics of TPs . . . 46
3.2.4 Confined Tamm plasmons . . . 49
3.2.5 Other Tamm states . . . 51
3.3 Naming conventions . . . 52
3.4 Summary . . . 52

4 Methods **55**
4.1 Fourier image spectroscopy (FIS) . . . 55
4.1.1 Fourier microscope . . . 55
4.1.2 Experimental setup . . . 56
4.1.3 Characterizing the Fourier image output . . . 59
4.2 Simulation methods . . . 62
4.2.1 Transfer Matrix Method . . . 62
4.2.2 Finite-difference time-domain simulations . . . 65
4.3 Summary . . . 67

5 Simulations **69**
5.1 TMM results . . . 70
5.1.1 Designing 1.3 μm TPs . . . 70
5.1.2 Designing 1.3 μm TPs at low temperature . . . 76
5.2 FDTD results of CTPs . . . 78
5.2.1 Effect of disc diameter . . . 78
5.2.2 Effect of spatial displacement of the source . . . 86
5.3 FDTD results of micropillar . . . 89
5.3.1 Optimizing β factor . . . 89
5.3.2 Designing micropillars at 1.3 μm . . . 96
5.4 Summary . . . 97

6 Experimental results **101**
6.1 The Sample . . . 101
6.2 Reflectivity measurements . . . 103
6.3 PL measurements . . . 105
6.3.1 Varying metal thickness . . . 105
6.3.2 Varying disc diameter . . . 107
6.4 Photodetector CTPs . . . 108
6.5 Summary . . . 113

7 Conclusion **115**

A Dispersion relation of SPPs **119**

A.1 Separation of variables 119

A.2 Disperion relation of SPP 119

A.3 Matching condition for a surface state 120

B Simulation Methods and Figures **123**

B.1 TMM code 123

B.2 Materials 129

B.3 Transmission boxes 131

B.4 Additional figures for chapter 5 133

Bibliography **137**

List of Publications

M. Parker, E. Harbord, A. Young, P. Androvitsaneas, J. Rarity, and R. Oulton, "Tamm plasmons for efficient interaction of telecom wavelength photons and quantum dots," *IET Optoelectronics*, vol. 12 no. 1, pp. 11-14, 2017

Submitted for Initial Review

M. Adams, B. Cemlyn, I. Henning, **M. Parker**, E. Harbord, and R. Oulton, "A model for confined Tamm plasmon devices," Submitted to: *JOSA B*, 2018

In Progress

M. Parker, E. Harbord, L. Chen, E. Clarke, K. Kennedy, J. Rarity, and R. Oulton, "Tamm plasmon emitters at telecoms wavelength,"

E. Harbord, B. Cemlyn, **M. Parker**, E. Clarke, I. Henning, M. Adams, and R. Oulton, "Confined Tamm plasmons Coupled to Quantum Dots in a photoconductive detector for spectroscopy and polarimetry of a chip,"

A. Young, **M. Parker**, D. McCutcheon, E. Harbord, A. C. Dada, P. Androvitsaneas, S. Knauer, J. Rarity, and R. Oulton,"A blueprint for a bright (1 MHz) source of photon cluster states based on a quantum dot in a high beta factor microcavity"

List of Abbreviations

AFM	atomic force microscopy
AlAs	aluminium arsenide
Au	gold
BC	boundary conditions
BFP	back focal plane
BSW	Bloch surface wave
CP	circular polarization
CTP	confined Tamm plasmon
CZT	chirp[ed] z-transform
DBR	distributed Bragg reflector
DWELL	[quantum-]dot-in-a-well
FDTD	finite-difference time-domain
FIS	Fourier image spectroscope
FWHM	full width at half maximum
GaAs	gallium arsenide
HBT	Hanbury-Brown and Twiss
IC	interface conditions
InGaAs	indium gallium arsenide
LDOS	local density of states
MBE	molecular beam epitaxy
MFD	mode field diameter
NA	numerical aperture
ND	neutral density
NMP	negative magnetic permeability
NP	negative permittivity
OTS	optical Tamm state
PhC	photonic crystal
PL	photoluminescence
Q	quality [factor]
QD	quantum dot

RT	room temperature
SIL	solid immersion lens
SPDC	spontaneous parametric down-conversion
SPS	single-photon source
SPCE	surface plasmon-coupled emission
SPP	surface plasmon polariton
TE	transverse electric
TIR	total internal reflection
TM	transverse magnetic
TMM	transfer matrix method
TP	Tamm plasmon
TPCE	Tamm plasmon-coupled emission

List of Figures

Figure **Page**

1.1 Graph of photon distribution with a mean photon number of one (a) for a coherent state and (b) Fock state. (c) Diagram of a Hanbury-Brown and Twiss interferometer; the signal is split by a beamsplitter into two channels leading to single photon detectors. The arrival times in each channel are recorded by the counter. (d) Predicted $g^2(\tau)$ for a coherent source (red line) and anti-bunched source (a QD with zero detuning and 1 ns lifetime) 2

1.2 Attenuation in silica fibers (black line) and theoretical limits given by Rayleigh scattering (blue dashed line) and IR absorption from molecular vibrations (red dashed line). 3

1.3 Schematic diagram of different semiconductor heterostructures (a) bulk material (3D), (b) quantum wells (2D) and (c) quantum dots (0D). The lighter blue shows the host (higher bandgap) semiconductor. Underneath are shown their density of states as a function of energy; the bulk material has a continuity of states (proportional to $E^{1/2}$) while the others become increasing discretized with confinement. 4

1.4 Bandstructure of an GaAs/InAs QD (of the type used in this thesis) showing above band (i.e. non-resonant) pumping and emission. The first three energy levels in the QD are labeled s, p and d by analogy with the corresponding atomic orbitals. 5

1.5 (a) SEM image of a micropillar. (b) Diagram of a QD containing micropillar showing the main photon decay channels. (c) Fit of measured Q/Q_0 (black dashed line), calculated $F_p/(F_p + \frac{\gamma}{\gamma_{hom}})$ (red line) and ζ (green line) as a function of micropillar diameter. The maximum efficiency of around 70% occurs for an intermediate diameter between 2 μm and 3 μm. 9

2.1 Definition of TE and TM configuration (these are also known as s- and p-polarization). The blue arrows show the direction of the electric field components. 13

2.2 Diagram of reflection and transmission of a TM plane wave in the x-z plane, at the interface between two dielectric media. 15

2.3 Diagram of SPP mode at a dielectric-metal interface. The amplitude of the field decays evanescently in both directions perpendicular to the interface. 17

2.4 Dispersion relation of SPPs between a Drude metal (i.e. with negligible collision damping) and air (black) and silica (grey) interface. Real values of β are shown as the solid lines and the light lines ($\omega = c\kappa$) as dashed lines. The frequency has been normalized to the metal's plasma frequency ω_p. There also exist real solutions of β *within* the light cone, for $\omega > \omega_p$, which is the transparency regime of the metal. As the name implies, here the metal allows propagating waves and there is no confinement. Between these two regimes β only has imaginary values, so there is no mode propagating in the direction along the boundary, whether as a SPP ($< \omega_p$) or as a radiating mode ($> \omega_p$). 20

2.5 (a) Prism coupling to SPPs using the Kretschmann configuration. (b) The SPP dispersion (solid line) at the interface between the metal and low ϵ material; excited SPPs (red line) have propagation constants above the light line of the prism material and can therefore emit radiative modes. 21

2.6 Diagram of a single layer structure 23

2.7 Diagram of a multiple-layer structure 25

2.8 Diagram of periodic layered structure 27

2.9 Dispersion diagram showing the bandstructure for a DBR with n_a = 3, n_b = 1, a = 75 nm, b = 150 nm for TE and TM polarization. The blue regions show the allowed wavelengths and the red regions the forbidden stopbands, which form the photonic bandgap. The black dashed lines are the light lines in air. Note that in the TM case there are wavevectors where the forbidden bands shrink to zero, which occur at the Brewster angle for the two materials of the DBR; since TM polarized light at this angle is not reflected at the interfaces there is no interference effect to form the stopband. . 30

2.10 Reflectivity spectra for an 18x pair $\lambda/4$ DBR with a photonic stopband centered on 1300 nm (n_1 = 3.5, n_2 = 2.9), showing the first band edge and photonic stopband as a function of wavelength and ($n_1 a/\lambda$). Calculated using the transfer matrix method. . . 31

2.11 Reflectivity spectra for 1300 nm centered DBR using the same parameters as figure (2.10). As the number of pairs increases the reflectivity over the range of the stopband approaches unity and the frequency of Fabry-Pérot resonances, the fringes seen at wavelength above and below the stopband, increases. Calculated using the transfer matrix method. 32

3.1 Diagram of a semi-infinite DBR. 37

3.2 (a) The reflection spectrum of a DBR at normal incidence (case A). **Inset**: diagram of different terminations of the DBR surface, from ending on a complete unit cell (A), with $\frac{d_1}{2}$ (B), on the n_2 material (C) and with $\frac{d_2}{2}$ (D). (b); The reflection phase shift as a function of wavelength for various terminations of the DBR (A-D). Light is incident normal to the DBR from an n = 1 layer. 41

3.3 (a) The reflection spectra of the two DBRs; PhC1 (red) has n_1 = 3, n_2 = 1.5, d_1 = 100 nm, d_2 = 100 nm and PhC2 (blue) has n_1 = 3.5, n_2 = 1.5, d_1 = 84 nm, d_2 = 80 nm. Both have 8 pairs. The termination for PhC1 ends with n_2 and $\frac{d_2}{2}$, and for PhC2 with n_1 and $\frac{d_1}{2}$, which are analogous to cases (D) and (B) in figure (3.2) respectively. (b) Reflection phase shift for PhC1 and PhC2. The black dashed line is their sum. (c) Power reflectivity spectra of the combined structure. The dip in reflection shows where an optical Tamm state (OTS) occurs at 944.5 nm, where the sum of the DBR phase shifts equals zero. 44

3.4 Refractive index and electric field cross-section for the DBR-DBR structure described in figure (3.3) at 944.5 nm. Calculated using TMM. 45

3.5 (a) Diagram of a Tamm plasmon structure. (b) Calculated reflectivity spectra at normal incidence for a 17.5x pair GaAs/AlAs DBR, GaAs spacer (s = 75 nm) and with (red line) and without (blue line) m = 25 nm gold layer. Black lines show the first minima of the DBR stopband (the stopband does not have unity reflectivity, as it did in previous figures, as actual materials with non-zero absorption have been modelled; see section (4.2.1.2)). The TP mode can be seen as a dip in reflectivity within the stopband. Calculated using TMM. 46

3.6 Calculated reflectivity for the DBR and TP structures described in figure (3.5) as a function of incidence angle (θ) and for TE polarization. The dispersion of the TP is parabolic. Calculated using TMM. 47

3.7 (a) Diagram of a confined Tamm plasmon structure. (b) FDTD simulation (see section 5.2) of a CTP structure consisting of 17.5x pair GaAs/AlAs DBR, d = 2.6 μm, s = 75 nm and m = 25 nm (gold), showing the absolute electric field intensity at the fundamental resonance of the CTP (λ = 1300 nm). A cross-section of the field through the center of the structure (x = 0) is shown by the red line. Like the cross-section of the TMM (1D) results, the field peaks within the spacer layer and extends mostly into the DBR region. 50

3.8 Measured emission dispersion for CTP consisting of 30x pair AlAs/AlGaAs DBR and 40 nm silver layer, for (a) d = 20 μm and (b) d = 5μm. At large diameters the dispersion is parabolic, like that of the planar TP. As the field becomes increasingly confined these modes become discrete. 51

4.1 (a) Any arbitrary propagating field (i.e. assuming no effervescent fields) can be decomposed into a superposition of plane waves with different amplitudes and propagation angles. (b) Diagram of the focusing of a plane wave by a lens onto the BFP. Every wave with the same angle is focused by the objective to the same position of the BFP. This can be extended to the 2D case where $\vec{\kappa}(\theta,\phi)$. 56

4.2 Fourier microscope setup; the first objective with focal length f_1 collects light with the same wavevector onto the same point at the BFP, which produces an image of the optical Fourier transform. The second lens, with a focus length of f_2 and located a distance S_1 away from this lens, produces a magnified image at S_2. 57
4.3 Diagram of the FIS showing the optical setup for (a) critical illumination and (b) Kohler illumination. In both, a 50% beam splitter is placed between L2 and the objective. L3 is located $f_{obj} + f_{L3}$ from the objective lens. On the camera path is a tube lens (not shown), positioned at its focal length's distance from the Fourier image plane and from a CCD camera, so a magnification of the real image of the sample is obtained at the camera. 58
4.4 Diagram of the collected image at the BFP for a mirror sample. The two different rays with angle θ_1 and θ_2 are collected a distance Y_1 and Y_2 from the optical axis. 60
4.5 Diagram of the zeroth and first order diffraction from a periodic grating. 61
4.6 Diagram of the collected emission for a grating sample. The ray incident at angle θ_{NA} has a zeroth order response ($\theta_{m=0} = \theta_{NA}$) that hits the BFP at the edge Y_{max}, and a first order response that hits the BFP at Y_{y2}. Conversely, a ray incident at θ_{y2} (i.e. its zeroth order would hit at Y_{y2}) will have a first order diffraction at Y_{max}. 62
4.7 Reflectivity spectra of a Λ = 1000 nm grating as a function of x position for an NA = 0.75 objective. Reflectance profiles for single wavelengths (λ = 1100 nm, 1300 nm, 1500 nm) are shown by the black, red and blue lines respectively. The onset of diffraction, corresponding to the Bragg angle, is shown by the black arrows (this corresponds to Y_B in figure (4.6)). These can be used to calibrate the grating for different wavelengths. 63
4.8 (a) Plot of $\theta(x)$ calibration using the measured onset of diffraction at different wavelengths (b) Plot of reflectance as a function of angle for a Λ = 1000 nm grating. The solid line shows the calculated angle for onset of diffraction ($arcsin(1 - \frac{\lambda}{\Lambda})$), and the dashed line where the same order re-enters the objective ($arcsin(NA - \frac{\lambda}{\Lambda})$). 63
4.9 Diagram of a Yee cell. (i, j, k) are the unit vectors in the x, y and z directions respectively. 66
4.10 The leapfrog method: at each step of Δt the electric or magnetic fields are calculated using the values of the other field at previous time steps. 67

5.1 Reflectivity spectrum for an ideal (λ/4) 18x DBR with n_1 = 3.5 and n_2 = 2.9 (black line), and for a GaAs/AlAs (95/110 nm) 18x DBR with material dispersion (red line), centered at 1300 nm. The phase shift for the ideal structure is shown when the terminating (spacer) layer is the higher (blue) or lower (green) of the two materials. 70
5.2 Reflectivity of TP structure (red line), bare DBR only (blue line) and gold layer only (gold line) for a 17.5x GaAs/AlAs DBR, 75 nm GaAs spacer and 25 nm gold layer. The former is the same as shown previously in figure (3.5(b)). (b) Reflection phase shift for the bare DBR and gold layer along with their sum (red dashed line). The TP mode, seen as the dip in reflectivity, occurs at the $\phi_{DBR} + \phi_M$ =0 condition 71

5.3 Cross-section of the refractive index and electric field for a DBR-metal (black and red lines) and DBR-air structure (blue line) at normal incidence. Note that the latter case does not form a surface state (BSW) at the interface but propagates into the dielectric; at normal incidence there is no TIR and the dielectric behaves like any normal $\epsilon > 0$ material. The dashed lines in the TP case show the position of the first four TP antinodes, where our InAs/GaAs QD layers are deposited. 72

5.4 Reflectivity of TP containing 25 nm gold layer and GaAs/AlAs DBRwith 8 (black line), 18 (blue line) and 50 (red line) number of pairs (spacer layer is included and kept fixed). 73

5.5 Sum of the ϕ_{DBR} and ϕ_M for a 17.5x GaAs/AlAs DBR + 75 nm GaAs spacer and 25 nm gold layer respectively, as a function of angle ($\kappa = n(\omega/c)sin(\theta)$) and wavelength. The white regions, showing where this sum ≈ 0, correspond to the dispersion of the TP mode seen as the dip in the reflectivity plot on the right. Black dashed lines correspond to the edges of the DBR stopband. 74

5.6 (a) Variation of TP resonance as function of spacer thickness (metal layer is fixed at 25 nm). The dashed lines show the phase shift sum (same scale as y axis, in units of π) of the DBR and metal for s = 75 nm and 25 nm, showing where the $\phi_{DBR} + \phi_M = 0$ condition occurs. (b) Variation of TP resonance as function of metal thickness (spacer layer fixed at 75 nm). Blue line shows the reflectivity of the bare DBR (m = 0). **Inset**: reflection phase shift of 5, 25 and 55 nm gold layer. 75

5.7 (a) and (b) Calculated shift in TP resonance as a function of metal and spacer layer thickness respectively (with the other remaining constant at 75 nm and 25 nm respectively). (c) and (d) Variation of Q-factor as function of metal and spacer layer respectively. 76

5.8 Room temperature (blue) and low temperature (red) TP designs at 273 and 15 K (solid and dashed lines respectively). Inset; bare DBR (17.5x GaAs/AlAs, λ = 1300 nm, s = 75 nm) showing the 30 nm blueshift between room and liquid helium temperature. . 77

5.9 (a) TMM reflectivity of bare DBR (disc diameter d = 0). Dashed black lines show the first Bragg modes. **Inset**: Refractive index (black line) and electric field cross-section at λ = 1300 nm (red line) and = 1375 nm (green line). (b) normalized energy spectrum taken from a CZT of the electric field recorded within the spacer layer as a function of wavelength. 79

5.10 Normalized energy spectrum for different disc diameters, showing the energy stored by the different frequency components of the electric field in the spacer layer for the duration of the CTP; resonances appear as peaks at frequencies where that component of the field has a longer lifetime within the CTP. (a) For the smallest discs there is a clear fundamental mode that shifts from λ = 1.296 μm (for d = 2.6 μm) to higher energies as the disc diameter is reduced and the mode becomes more confined. (b) At higher diameters (e.g. d = 8.0 μm, brown line) higher order modes can be seen, though the fundamental mode is (slightly) redshifted compared to the 2.6 μm disc shown for comparison. **Inset**: Q-factors calculated at the fundamental resonances using Gaussian fits to the energy spectra peaks (some examples are shown as dotted lines), as a function of disc diameter. The dashed red line is a guide to the eye. 80

5.11 Plot of the internal collection efficiency $\zeta = \beta\eta[1-\alpha])$ (red line; see (B.3)), Purcell enhancement (blue line) and normalized energy spectra (black line; scaled to right axis) for a d = 2.6 μm CTP. All three indicate a fundamental resonance occurring at 1.296 μm (black dashed line). 81

5.12 (a) Normalized energy spectrum for a d = 2.6 μm disc. The CTP is excited by a CP Gaussian source above the disc as described in (5.2.1.1). **Inset** is a zoom-in showing the energy spectrum on the higher energy side of the fundamental peak. (b) Profiles of the absolute electric field under the disc at the center of the spacer layer ($y = 0$, $z = \frac{s}{2}$) at the wavelengths corresponding to the black, blue and green dashed lines in (a). Gold lines show the location of the disc edge. (c) Distribution of the absolute electric field of the CTP at the frequencies marked in (a). These are identified as corresponding to the fundamental (black line) and the first and second order (blue and green line) transverse modes for a cylindrically-symmetric system, i.e. 00, 10 and 20, respectively. For comparison, spatial profiles of these modes calculated in MATLAB using the standard formula are shown to the right. 83

5.13 (a) Normalized spectrum and Purcell enhancement for a d = 5.0 μm disc. Red dashed lines are Gaussian fits to the peaks and black dotted lines indicate the resonant wavelengths of these fitted modes. (b) Plot of the internal collection efficiency, $\zeta = \beta\eta[1-\alpha]$. 84

5.14 Shift of the fundamental modes of the CTP as a function of disc diameter (m = 25 nm, s = 75 nm). Red circles are the resonances identified for intermediate disc diameters between 3 μm and 8 μm, where multimode behaviour makes identifying individual modes difficult, by the energy spectrum, Purcell factor and collection efficiency. The dashed line is a guide to the eye. 85

5.15 Plot of the collection efficiency ($\zeta = \beta\eta[1-\alpha]$) as a function of disc diameter. (b) plot of $\beta\eta$ and (c) (1 - α) as a function of disc diameter. The black dashed lines are an exponential and asymptotic fit respectively to these points, and the red dashed line is their product. 86

5.16 (a) Diagram of dipole position under the microdisc. (b) Farfield emission profile through the top of the structure as a function of source y position for a 2.6 μm CTP. The profiles are shown for a fixed ϕ angle orientated along the electric dipole moment and at the mode's fundamental resonance (λ = 1296 nm). The dashed line shows the Gaussian fit for the y = 0 emission. (c) Farfield collection efficiency as a function of numerical aperture. Collection is shown as the percentage of power integrated over all ϕ for a cone with solid angle of 2θ, i.e. the collection by a lens with $NA = sin(\theta)$, over power collected by a lens with NA = 1. (d) Purcell factor as a function of source displacement. Black line shows a linear fit to the data and gold line shows the position of the disc edge. Inset includes additional Purcell factors (red squares) for sources approaching the edge of the disc. 88

5.17 (a) FDTD simulation showing the absolute electric field intensity at the fundamental resonance (λ = 910 nm) of a 5x top and 18.5x bottom DBR, (λ/n) cavity micropillar. The source is a CP Gaussian positioned above the pillar. White lines mark the pillar structure. (b) Cross-section of the refractive index and electric field through the center of the structure (x = 0) 90

5.18 (a) Normalized spectrum (red line) for the d = 2.0 μm 5x top and 18.5x bottom GaAs/AlAs pillar. The blue line shows the losses through the side channels of the pillar (γ) normalized by the dipole power. (b) Purcell enhancement of the micropillar. 91

5.19 (a) Optimization of diameter for a micropillar consisting of a 5x top and 18.5x bottom DBR and (λ/n) GaAs cavity (λ = 900 nm). The oscillations in collection efficiency occur with the period of the effective wavelength in the cavity layer. (b) Optimization of the β (solid squares) and η factors (hollow circles) as a function of different numbers of top and bottom DBR pairs for a d = 1.55 μm pillar. (c) Optimization of the total internal efficiency ($\zeta = \beta\eta$). 92

5.20 Comparison between a 7x (35.5x) d = 1.55 μm free-standing pillar (blue line) and GaAs substrate pillar (orange line); (a) Purcell factor. (b) Normalized spectrum. (c) $\beta = \Gamma/(\Gamma+\gamma)$. (d) The % of photons collected within an NA = 0.4 objective as a function of detuning from the cavity, calculated using the farfield emission through the top of the pillar. 94

5.21 The farfield collection through the top of a free-standing 7x (35.5) pillar for different frequencies, shown as a percentage of power collected within a cone with solid angle (= 2θ), i.e. the collection by a lens with NA = $sin(\theta)$, normalized by the power collected by an NA = 1. The red (a) and green (c) lines correspond to the wavelengths marked by dashed lines in figure (5.20(d)). The black lines correspond to an NA of 0.4 and 0.75. (b) and (d) show the farfield projection of these modes through the top surface of the pillar; the fundamental mode at λ = 908 nm (b) shows a Gaussian spatial profile. . . . 95

5.22 Gaussian fitted to the cross-section of the electric field strength through the top of the pillar at the fundamental mode. The Gaussian gives an MFD of 1.28 ± 0.07 μm. The red line shows the cross-section calculated for a fiber mode (HP780 fiber) with an MFD = 5 μm. Its magnitude is scaled so that the overlap between them illustrates the transmission between pillar and fiber when directly butt-coupled (z = 0), calculated using the Marcuse approximation, based on their respective MFDs. **Inset**: Pillar to fiber transmission as a function of thickness of a new optical layer, z, in which the pillar mode can expand. 96

5.23 Shift in fundamental mode resonance (red line) and β factor (black line) as a function of pillar diameter. As in figure (5.19(a)), the latter oscillate with a period of the effective wavelength. Pillar consists of 7x (35.5x) top (bottom) GaAs/AlAs DBR and 403 nm cavity. 98

5.24 Optimization of the β (squares), η (hollow circles; both (a)), and ζ (b) factor as a function of different numbers of top and bottom DBR pairs for a d = 2.25 μm pillar. . 98

5.25 (a) Normalized spectrum (red line) and side losses (blue line) for the d = 2.25 μm, 7x (30.5x) DBR pillar. (b) Purcell enhancement. (c). Collection % within an NA = 0.4 objective. 99

5.26 TMM calculations showing the transmission for a (97/114) nm GaAs/AlAs DBR and 407 nm cavity micropillar at room temperature (black line) and cold temperature (red line). Both have had their resonances shifted by $\frac{1}{1.01}$ to account for the blueshift of pillar confinement. The blue line shows the resonance (via plotting the Purcell enhancement) of the same specification 7x (30.5x) micropillar in FDTD using the standard material refractive indices; it aligns well with the shift-corrected TMM and would be resonant at 1.3 μm if a similar 30 nm blueshift occurs when cooled. 100

6.1 Characterization of the QDs. (a) AFM measurement of uncapped QDs grown using the method described. (b) Room temperature PL of the sample before metal deposition (i.e. bare DBR only) with an above-resonance laser source. The emission peak occurs at 1312 nm (FWHM = 40 nm). Measurements were performed by Dr Ed Clarke, University of Sheffield. 102

6.2 Normal incidence reflectivity measurement for the bare DBR (green line) and d = 20 μm CTP (orange line). For comparison blue and red lines show the reflectivity calculated by TMM for the DBR and m = 23.1 nm TP respectively (the metal thickness is characterized by AFM). 103

6.3 (a) Angle-resolved reflectivity measurements showing the dispersion relation for a bare DBR and d = 20 μm CTP. (b) Reflectivity profiles through the latter taken at 0°, 15° and 30° (blue lines) compares the shift in the position of the TP resonance with those predicted by the TMM. (c) Position of reflectivity dip as a function of metal thickness (black squares). The blue line shows the calculated shift in the TP resonance using TMM (figure 5.7(a)). 104

6.4 (a) Room temperature non-resonant (635 nm) photoluminescence spectra of the QDs without (black line) and with a m = 23 nm (d = 20 μm) metal layer (blue line). Note that in the latter case this increase occurs despite pumping through the metal layer decreasing the excitation power at the QD layer by an estimated 88% (b) PL counts plotted as a function of lasing power to demonstrate that the TP-enhanced dot emission has not been saturated. The highest excitation power from the laser is 0.80 mW, which is reduced by adding ND filters with increasing optical density. (c) Angle-resolved reflectivity and PL measurement (both taken with 40x objective) of the d = 20 μm CTP. The dispersion of PL enhancement has the same relation at higher angles as the relation for the TP mode, demonstrating this is the cause of the increased QD emission. (d) Q-factors of PL peaks as a function of metal thickness. Blue line shows the calculated Q-factor using TMM (figure 5.7(d)). 106

6.5 (a) Normalized PL spectra of QDs in a CTP for varying disc diameters (m = 23 nm), with the QD sideband (measured from the bare DBR) subtracted and Gaussian fits (dashed lines) added. (b) PL resonance as a function of disc diameter. The red dashed line is a guide to the eye. **Inset**: Real image of the microdiscs taken with the 40x objective (Kohler illumination). (c) PL Q-factors as a function of disc diameter. The red and blue dashed lines are fitted exponentials to the measured and FDTD results respectively. 109

6.6 Angle-resolved PL (100x objective) for different disc diameters. As confinement is increased by reducing the diameter, there is a transition from a continuous and parabolic dispersion, seen in the planar TPs, to discrete mode at the TP fundamental resonance. 110

6.7 (a) Schematic diagram of the CTP photodetector. Light is incidence from above the metal layer. A layer of InAs/GaAs QDs in an InGaAs well act as the absorption medium, reducing the resistance between the two metal contacts.(b) Diagram of the experimental setup; OSA - optical spectrum analyser. The sample is excited by a lens-ended fiber attached to an x-y stage and aligned to the center of the disc (this occurs when the reflected power measured by the OSA is at its minimum). 111

6.8 (a) SEM image of a d = 13 μm device, and its photodetector response when pumped on (black line) and off (green and red) the disc by a non-resonant (650 nm) laser as a function of wavelength. (b) Photodetector response for different disc diameters. 112

6.9 (a) Real image (40x objective) of a 3 μm × 8 μm rectangular device. (b) Photodetector responses when the pumping laser is linearly polarized parallel to the long (H) and short (V) axis of the CTP (black and red lines respectively). 113

A.1 Diagram showing the virtual interfaces as dotted lines within a uniform layer of a multilayer structure. The wave gains a phase Φ propagating between them. 121

B.1 Real component of refractive index of Gold (Au). The inset shows a plot of the imaginary component. 129

B.2 Real component of refractive index of gallium arsenide (GaAs). The inset shows a plot of the imaginary component. 130

B.3 Real component of refractive index of aluminium arsenide (AlAs). 131

B.4 (a) Transmission box (red lines) and (b) refractive index profile for a d = 2.6 μm 17.5x DBR CTP. 132

B.5 (a) Transmission box (red lines) and (b) refractive index profile for a d = 2.0 μm, 7x (30.5x) top (bottom) DBR micropillar. 132

B.6 (a) Normalized spectrum for the DBR only structure (17.5x GaAs/AlAs DBR + spacer layer). (b) Vertical profiles showing the electric field intensity at the wavelength in the center of the DBR's stopband (λ = 1300 nm, red square) and first Bragg mode (λ = 1377 nm, green square). The simulation is excited by a Gaussian source from above the structure, as described in (5.2.1.1). 133

B.7 (a) Normalized spectrum and Purcell enhancement for a d = 3.575 μm disc. The dashed red lines are Gaussians fitted to the spectrum but whose resonances are taken from the resonance in the Purcell enhancement, marked by the dashed lines, though we are unsure of this interpretation. (b) Plot of the internal collection efficiency, ζ. 134

B.8 Projections showing the electric field intensity in the farfield collected (for λ = 1.296 μm) through the top of (a) d = 2.6 μm CTP and (c) DBR. Electric field profiles through these at ϕ angles parallel and perpendicular to the electric dipole moment are shown by the blue and orange lines respectively in (b) and (d). The dashed lines show Gaussian fits to these distributions. Note that the intensity scale of the DBR is one fifth that of the CTP structure. 135
B.9 Normalized spectrum for a d = 2.25 μm pillar with 5 (30.5) and 7 (30.5) top (bottom) DBR pairs. The arrows display their respective Q-factors for the fundamental (1.3 μm) mode. 136

CHAPTER 1

INTRODUCTION

Since the first developments of quantum mechanics at the beginning of the last century it has become clear that the laws of nature at the smallest scale are very different to the clockwork and continuous world of our experiences. Properties of superposition and entanglement have no counterpart in the classical world. The latter, where entangled quantum objects maintain correlations even when separated by non-local distances, lead to particularly counterintuitive results [1].

However, it is only much more recently that devices have been proposed that use the peculiar quantum nature of light to achieve a useful outcome. Proposed applications include quantum computation [2], below shot-noise measurement [3], and secure communication using quantum key distribution [4]. Realizing these have led to advancements in the manipulation, detection and theory of light, but one necessary component all share are deterministic single-photon sources [5, 6].

1.1 Single-photon sources

In an ideal case, a single-photon source (SPS) deterministically emits one and only one photon when triggered externally. This probability distribution is shown in figure (1.1(b)) and is called a Fock (or number) state. It is clear such a state is non-classical since such a probability distribution requires the quantization of the photon field into a discrete number state. A thermal or coherent source, such as a laser, will produce a distribution around a mean photon number (1.1(a)) but will never produce a single number state with a probability of unity. Attenuating the source increases the probability of a zero and one photon number state occurring but does not fundamentally change the type of distribution.

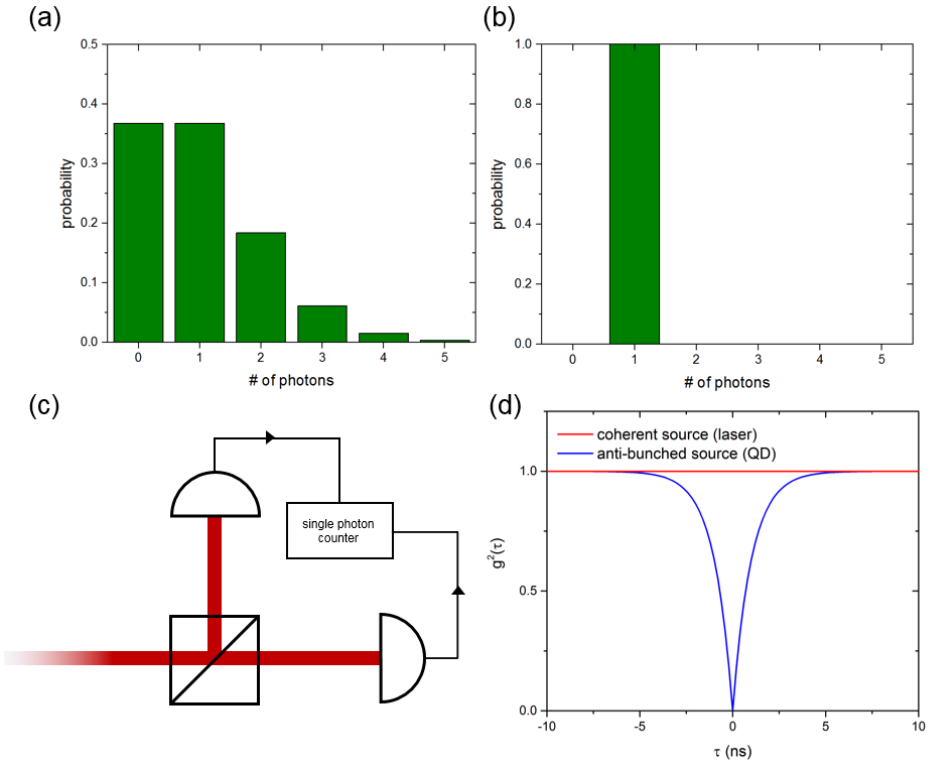

Figure 1.1: Graph of photon distribution with a mean photon number of one (a) for a coherent state and (b) Fock state. (c) Diagram of a Hanbury-Brown and Twiss interferometer; the signal is split by a beamsplitter into two channels leading to single photon detectors. The arrival times in each channel are recorded by the counter. (d) Predicted $g^2(\tau)$ for a coherent source (red line) and anti-bunched source (a QD with zero detuning and 1 ns lifetime)

A single photon Fock state therefore requires non-classical mechanisms to produce. Such methods could be via (a) non-linear processes such as spontaneous parametric down-conversion (SPDC) or (b) an isolated single emitter. In SPDC a laser source is targeted at a nonlinear material (i.e. a material with high second order susceptibility), which splits single photons into a photon pair with the combined energy of the original photon. This has the benefit of producing photons in an entangled pair, so the detection of a photon in one channel guarantees the presence of a single photon Fock state in the other. However, the conversion efficiency for every incoming photon is very low ($\sim 10^{-6}$) making it difficult to use these as bright or deterministic source.

A single emitter is a two-level system containing a higher energy (excited) and lower energy (ground) electron level. Example single emitters include single molecules [7], trapped ions [8], color defects in diamond [9], and semiconductor quantum dots (QDs) [10]. The system in an excited state will emit a photon when an electron spontaneously decays to the ground state. A second photon cannot be emitted until the system returns to an excited state again, meaning subsequent photons are separated by some time delay. This property is called anti-bunching and

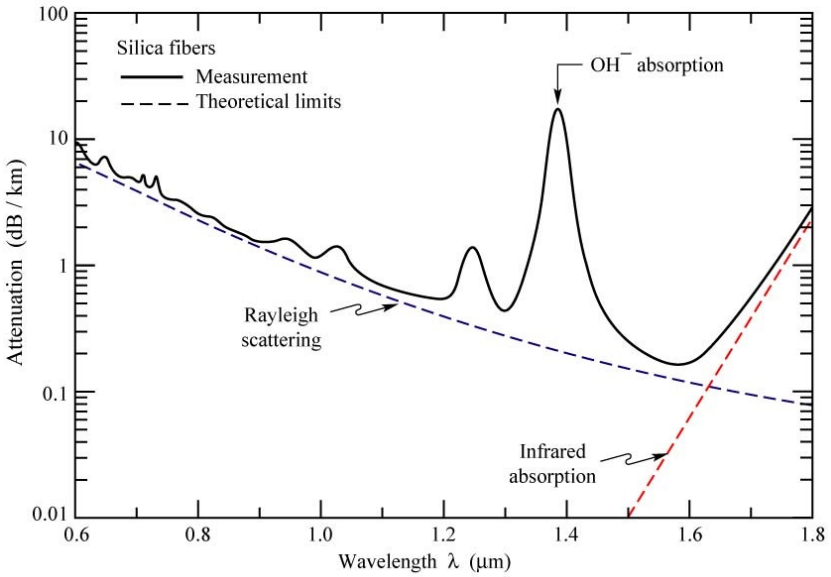

Figure 1.2: Attenuation in silica fibers (black line) and theoretical limits given by Rayleigh scattering (blue dashed line) and IR absorption from molecular vibrations (red dashed line). Figure from [11].

is characterized experimentally using a Hanbury-Brown and Twiss (HBT) correlation interferometer, shown in figure (1.1(c)).

Incoming light is split by a beamsplitter and into one of two detection channels, which records the photon arrival times. The second order autocorrelation ($g^2(\tau)$) gives the probability given a photon detection at time t in the one channel of another detection occurring within $t+\tau$ in the other. At $\tau = 0$ this gives the probability of detecting a correlated photon pair. For coherent light sources (such as a laser), which have photon distributions given by Poissonian statistics, the detections are uncorrelated and results in $g^2(0) = 1$. For a perfectly anti-bunched Fock ($n = 1$) state $g^2(0) = 0$ (figure 1.1(d)). Having $g^2(0) < \frac{1}{2}$ is confirmation of anti-bunching, which is only possible in a non-classical light source.

There are additional characteristics an ideal SPS might be required to have, depending on the intended application. Having a high repetition rate ('brightness') between triggers is necessary if many single photons are needed in succession. For example, a rate that is too low will limit the bandwidth for quantum communications. Indistinguishable pairs are necessary for proposed quantum information protocols that rely on two-photon interference [12]. For the same reason the source should be close to deterministic so that a single photon is emitted (and not a zero-photon state) on demand with each trigger with a high confidence. Lastly, it is important to tune the emission wavelength for the application. In communication devices wavelengths are chosen where the attenuation in silica fibers are lowest (figure 1.2). These are 1.3 μm (the O-band) and 1.55 μm (the C-band). A SPS for quantum communications would want to match these wavelengths since

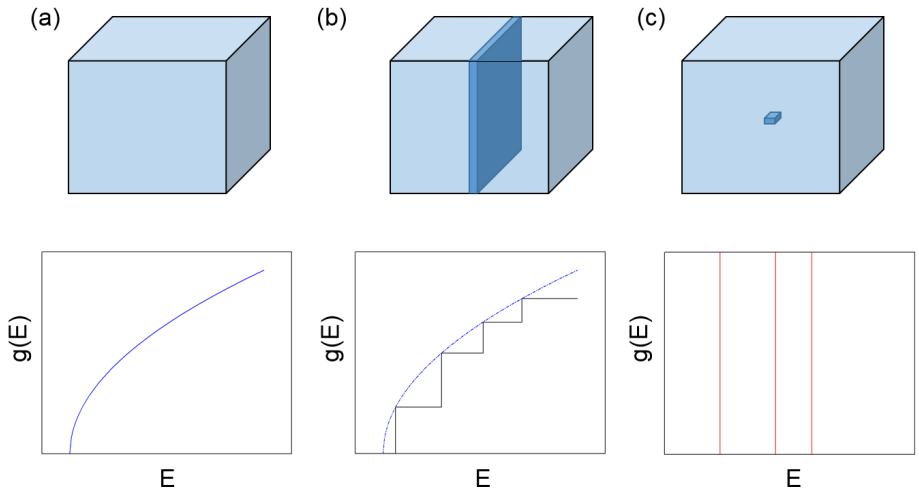

Figure 1.3: Schematic diagram of different semiconductor heterostructures (a) bulk material (3D), (b) quantum wells (2D) and (c) quantum dots (0D). The lighter blue shows the host (higher bandgap) semiconductor. Underneath are shown their density of states as a function of energy; the bulk material has a continuity of states (proportional to $E^{1/2}$) while the others become increasing discretized with confinement.

it could rely on well-developed commercial fibers, while a lower attenuation rate would mean a lower density of quantum repeaters.

1.1.1 Quantum dots

A QD is a type of heterostructure consisting of two semiconductors with an offset in the bandgaps that separate the energies of the conduction and valence band. When a photon is absorbed an electron is excited into the conduction band and a paired hole is created in the valence band. When bound these form an exciton. Embedding the lower bandgap materials in the higher bandgap material creates an energy barrier that spatially confines the exciton wavefunction. This results in discretized energy levels in the direction of the confinement. Semiconductor heterostructures with different levels of confinement are shown in figure (1.3). In a QD the lower bandgap material is only a few tens of nanometers in all directions and the exciton is confined in all dimensions. In this limit the QDs have discrete, atom-like energy levels. It is for this reason QDs are sometimes referred to as 'artificial atoms'. Like atoms, these energy levels correspond to a series of optical transitions; excitons excite and recombine to produce photons at well-defined energies (figure 1.4). The excitation can be done optically or electrically.

It is this confinement that makes QDs suitable as single emitters. They are bright, have high quantum yields and have narrow linewidths of a few μeV (at low temperatures) comparable with the fixed linewidths of atoms and molecules [10, 13]. QDs can be fabricated using a variety of techniques; in epitaxial grown QDs an initial layer of high bandgap semiconductor (e.g. GaAs) is

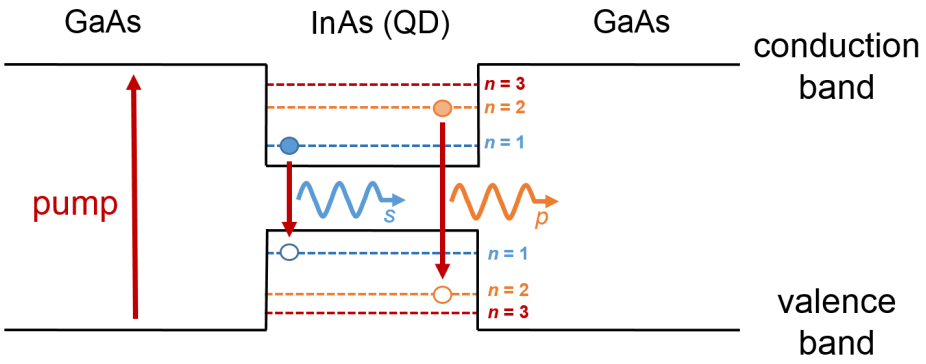

Figure 1.4: Bandstructure of an GaAs/InAs QD (of the type used in this thesis) showing above band (i.e. non-resonant) pumping and emission. The first three energy levels in the QD are labeled s, p and d by analogy with the corresponding atomic orbitals.

grown, onto which is deposited the lower bandgap semiconductor (e.g. InAs). Dots spontaneously form in the low bandgap semiconductor due to the strain induced by the lattice mismatch between the two materials [14]. The bandgap difference of the two semiconductors (and so the emission wavelength) can be controlled by altering the alloying mix and growth temperature of the semiconductor. QDs can be grown to emit at telecom wavelengths [15, 16]. By adding dopants to the semiconductor or applying an electric field it is possible to address the electron spin of an exciton with the polarization of the emitted photon. Both spin and polarization states can be a basis for a qubit, meaning QDs can act as a platform to transfer between them in quantum information applications [17, 18].

QDs are solid-state devices which means they are scalable and can be integrated into other semiconductor structures that enhance light emission and collection, such as optical micropillars. However, solid-state devices also suffer from linewidth broadening caused by interaction with the vibrational modes in the semiconductor crystal lattice, called phonons. At high temperatures this broadening is the dominant source of exciton dephasing and can be enough for its optical transitions to overlap and lose the indistinguishability desired of a single-photon source [10]. Therefore, for SPS use, QDs are operated at cryogenic temperature to minimize this interaction.

Additionally, the simplest method of optical excitation, and the one employed in this thesis, is to pump with photons non-resonant to the optical transitions and instead above the QDs conduction band. Excitons are created with a continuum of energies in the surrounding semiconductor, a fraction of which will fall into an excited state of the QD and relax to the lowest (s) energy level. The benefit of above-resonance excitation is that the pumping source can be easily spectrally separated from the emission but produces photons with lower indistinguishability since a) it increases the likelihood of charge carriers being captured by defects in the surround bulk material close to the dot, which causes linewidth broadening, and b) the relaxation from the

higher to first excited state in the dot occurs non-radiatively via phonon interactions. Though these are fast compared to the exciton recombination lifetime it introduces a random timing jitter with each emission, further reducing the photon indistinguishability.

However, the biggest limitation of QDs for SPSs is brightness, or rather (since QDs have relatively fast spontaneous emission rates) low collection efficiencies from which the generated photon can be captured. Single-emitters mostly have emission that can be approximated as isotropic which makes capturing more than a small percentage of their total emission difficult. In reality, epitaxially grown QDs are rarely symmetrical but are elongated along their growth direction resulting in a permanent dipole moment along this axis, and the highest photon emission rates in directions orthogonal to this (i.e. parallel to the growth plane) [19]. As QDs are grown in high refractive index semiconductor the critical angle with the surrounding air is very low and so much of this light cannot be collected due to total internal reflection. In bulk, efficiencies of only 1% might be expected using a typical collection aperture [20]. A common solution is instead to place the QD into a photonic structure that enhances emission into a single, highly-collectable mode while limiting all other emission channels.

1.2 Photonic structures

In an ideal SPS all the photons from the emitter will emit exclusively into a single mode with a well-defined energy, direction, polarization etc., and where this single mode has characteristics that allow it to be efficiently collected. Controlling emission from fluorophores such as QDs is an active area of research in general as it has wide applications beyond single-photon sources; fluorescence sensing, lasing and LEDs all require channelling light from an emitter to where it is needed as losslessly as possible. With free space optics being limited by the diffraction limit, interest has switched to manipulating light at the quantum scale. Yet this is made difficult at a fundamental level by the disparity in scale between optical modes (of the order of the wavelength of light) and single-emitters (of the order of the wavelength of an electron wavefunction) [20].

Two of the most common structures are semiconductor microcavities/micropillars and plasmonics. Others include ring-resonators [21], photonic nanowires [22], or metallic nanorings [23]. What is in common is that these structures in some way confine the electromagnetic field into volumes smaller than can be achieved with classical lens optics. This raises the local density of states (LDOS), which results in stronger light-matter interactions with an emitter and more efficient coupling.

1.2.1 Semiconductor cavities

The obvious method of raising the LDOS is to confine light in a highly reflective cavity, for example by placing two parallel mirrors around a single layer of certain thickness, L, and refractive index, n, to form an optical resonator. These form modes at wavelengths which satisfy the resonance

conditions $\lambda_m = \frac{nL}{m}$. The dissipation from a cavity is represented by the quality factor (Q-factor), which is the ratio of the energy stored in the cavity against the rate of energy loss.

$$Q = \frac{\omega_c}{\kappa} = \frac{\omega_c}{\delta\omega} \tag{1.1}$$

where ω_c is the angular frequency of the cavity mode and $\kappa(= \tau^{-1})$ the rate photons emit from the cavity, which also gives the resonance linewidth ($\delta\omega$). Hence, in a high Q cavity a stronger interaction might be expected since the lifetime of a photon in the cavity is many times longer than that of an emitter. These mirrors are usually made of dielectric materials as they have much lower intrinsic losses compared to metallic materials. These instead rely on total internal reflection (TIR) or periodically alternating structures, called distributed Bragg reflectors (DBRs). These create a highly-reflective stopband that forbids propagation by certain frequencies, analogous to the forbidden energy bands of electrons in crystal lattices (section 2.4.2), to confine the light. Q-factors of 10^5 have been achieved using the same GaAs/AlAs semiconductor DBRs in this thesis [24]. Micropillars are made by vertically etching a planar cavity consisting of two DBRs around a (λ/n) cavity layer. The cavity is single-sided, e.g. by having fewer pairs in the DBR on one side, so light is preferentially emitted in one direction out of the cavity. By confining in three dimensions (lateral confinement at the semiconductor-air interface is due to TIR), the modes are blueshifted relative to the resonant modes of the planar cavity and increase their spectral separation.

The fraction of photons emitted into the desired single cavity mode over all other modes is characterized by what is called the β factor

$$\beta = \frac{\Gamma}{\Gamma + \gamma} \tag{1.2}$$

Where Γ and γ are the coupling rate into the cavity and non-cavity modes respectively [25]. Possible emission channels include the fundamental mode, higher-order modes and leaky modes.

The spontaneous emission rate of a QD into the cavity mode is enhanced relative to the rate of a bulk emitter by the Purcell factor F_p, which is the ratio between the total emission rate in the cavity and in an homogenous medium $= \frac{\Gamma+\gamma}{\gamma_{hom}}$. This is proportional to the ratio of the cavity Q-factor to its effective mode volume. Since Purcell enhancement selectively enhances emission into on resonant modes the higher order modes can be neglected. If the diameter is sufficiently small the cavity modes are separate enough for an interaction with a QD to be effectively single-moded [20]. In an ideal cavity β is related to the Purcell factor [26] by

$$\beta = \frac{F_p}{F_p + \frac{\gamma}{\gamma_{hom}}} \tag{1.3}$$

Leaky and lossy modes include scattering from the etched sidewalls, intrinsic losses of the materials, and side losses when the light is incident below the TIR critical angle. Of these,

sidewall roughness is the dominant mechanism, especially as the diameter is reduced [27]. The total quantum efficiency is [28]

$$\zeta = \left(\frac{F_p}{F_p + \frac{\gamma}{\gamma_{hom}}} \right) \frac{Q}{Q_0} \tag{1.4}$$

where Q/Q_0, the ratio of the micropillar and planar cavity qualities (which can be understood as the fraction of photons in the cavity mode that are then emitted into the desired external mode). Reducing the diameter results in smaller mode volumes and so higher Purcell factor, but also reduces Q/Q_0 (due to increased sidewall losses), so to maximize ζ a compromise pillar diameter must be found [29]. This is shown in figure (1.5(c)). Lastly, there is the external collection efficiency of the emitted mode. One reason micropillars are preferred to other high Q systems is because the fundamental mode that the light emits into has a farfield emission pattern that closely approximates a Gaussian, so it can be efficiently out-coupled into optical fibers [30].

The ability of micropillars to be optimized for extremely high Q-factors (and relatively low mode volumes) make them well-suited to achieving strong, near-deterministic light-matter interactions. However, this does not always translate into an effective device. These high Purcell enhancements are only achieved when the QD is spectrally resonant with the cavity mode, but for a high Q pillar containing a distribution of QD emitters the chances that such an alignment occurs is reduced, since the linewidth is narrow relative to the separation between the QD emission lines. Achieving a good coupling is often a stochastic process; producing and characterizing many devices until a good overlap occurs. Secondly, this enhancement does not distinguish between the fundamental and leaky modes. Though there is a high probability of interaction with the emitter in a high Q/high lifetime micropillar, which raises Γ, the emission rate into unwanted modes, γ, will also increase if the photon spends longer in the cavity, putting a limit of the total efficiency. A more scalable and efficient device may therefore be one with a lower cavity lifetime but well-defined output mode, for example, a low Q-factor micropillar [31].

1.2.2 Surface modes

Surface modes are electromagnetic modes confined at the interface between two different materials. The field decays evanescently in both directions normal to the interface so high field intensities can be achieved. This is typically done using surface plasmon polaritons (SPPs), which occur at the interface of a dielectric and metal layer at frequencies when the metal has a negative real part of its electric permittivity. Plasmonics are rarely considered for single QDs due to having very low Q-factors.

However, modes that occur at the surface of 1D photonic crystals called Tamm states, by analogy with the electronic states that appear at the surface of semiconductor crystal lattices [32], can occur in dielectric materials and offer a low loss alternative to SPPs. When 3D confinement

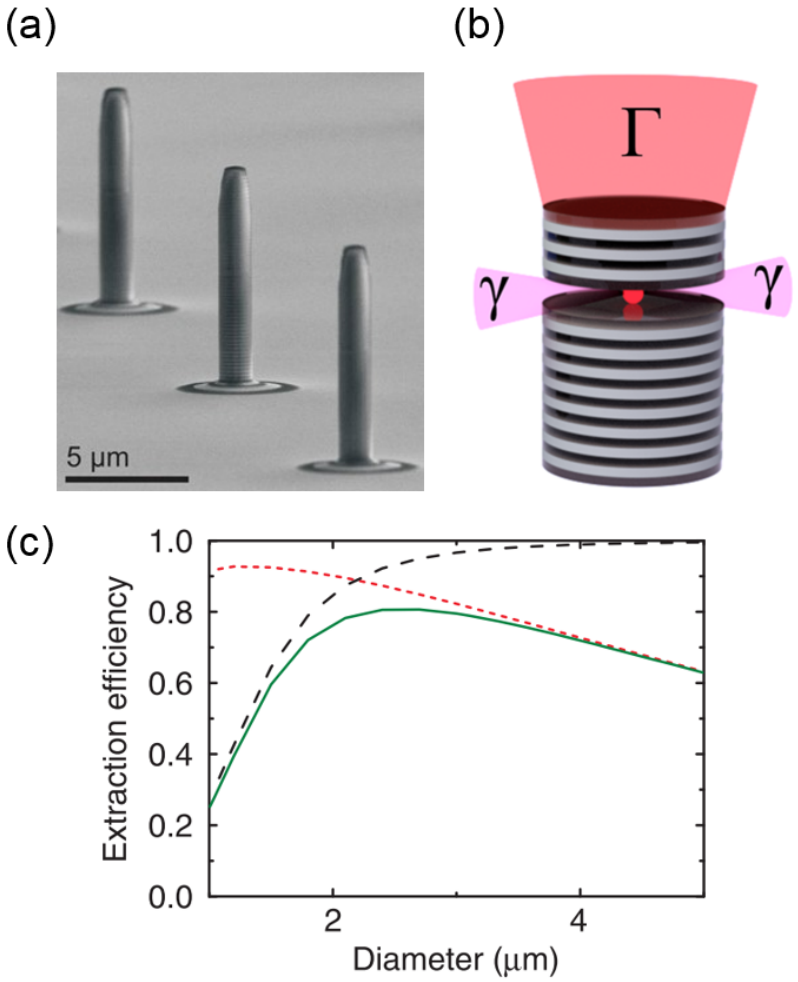

Figure 1.5: (a) SEM image of a micropillar. (b) Diagram of a QD containing micropillar showing the main photon decay channels. (c) Fit of measured Q/Q_0 (black dashed line), calculated $F_p/(F_p+\frac{\gamma}{\gamma_{hom}})$ (red line) and ζ (green line) as a function of micropillar diameter. The maximum efficiency of around 70% occurs for an intermediate diameter between 2 μm and 3 μm. (b) is reproduced from [31] and (c) from [29].

is introduced these present an alternative platform to micropillars for QD-based single-photon sources. These will be covered in much greater detail in the subsequent chapters.

1.3 Thesis overview

In this thesis, I will study the interaction of QDs with a range of low Q photonic structures, particularly a class of surface modes known as confined Tamm plasmons (CTPs). These modes exist at the interface between a DBR and a metal layer. Simulations are performed to find the dependence of resonance and emission properties for several parameters. We also experimentally characterize TPs designed to be resonant at 1.3 μm as a step to demonstrating TPs as a component of optical and quantum optical devices.

In chapter 2 I will describe in more detail the physics of electromagnetic modes at surfaces, starting from Maxwell's equations and ending with the SPP. We also consider the case of light propagating through parallel layered structures. We derive the transfer matrix method (TMM) for calculating the field solutions in layered structures. Lastly, we describe the result of periodic layered structures. Chapter 3 continues by describing the result when a periodic structure is terminated by an interface. The Tamm states that appear are shown to result from the solutions derived in chapter 2. In particular their different characteristics to SPPs result from the solutions to Maxwell's equations when in periodically repeating media. Lastly, I describe CTPs where the TP mode is confined by limiting the dimensions of a capping metal layer.

In chapter 4, I describe the Fourier image spectrometer (FIS) used in later chapters. This allows angularly-resolved experiments by measuring in the spatial Fourier transform (i.e. in the κ domain) of its optical response. The principles of Fourier imaging are introduced, and a description of the experimental set-up and method are given. These are demonstrated with a calibration measurement of a linear grating. We also describe the simulation techniques used, such as the finite-difference time-domain (FDTD) method. In Chapter 5 simulations are perform of CTPs and low Q micropillars using the TMM and FDTD respectively. Structures resonant at 1.3 μm and the effect of varying structure parameters are shown. I show how the design of CTPs and low Q-factor micropillars can be improved to optimize a high β factor. The spectral and transverse resonances of the modes of CTPs 'cavities' as confinement is increased are shown, as is the effect on emission for a resonant QD.

Finally, chapter 6 presents experimental results of CTPs resonant at 1.3 μm. QD-coupling is demonstrated by the enhancement in the measured photoluminescence (PL) and confinement of the CTP is shown as the disc diameter is reduced. These structures are shown to produce a simple photodetecting device operating at telecoms wavelength. Polarization sensitivity is also demonstrated by shaping the metal layer. These results demonstrate that CTPs can be a viable mechanism for realizing new optical and quantum optical devices.

CHAPTER 2

OPTICAL WAVES AT SURFACES AND LAYERED MEDIA

The study of light confined at interfaces has a history much older than the specific case of the Tamm state; the first mathematical description of surface waves goes back to the beginnings of the twentieth century [33, 34] as does the first experimental observation of plasmonic effects [35]. In this chapter, we treat the problem of electromagnetic waves in two cases. Despite their application to quantum optics, both result from purely classical solutions to Maxwell's equations.

First, at the interface between two media using the example of the surface plasmon polariton (SPP), a propagating mode bound at the interface between a dielectric and metal layer. An understanding of the physics involved in the formation and characteristics of SPPs will be useful, not only in comparing the features between them and Tamm plasmons later, but also understanding how the conditions for bound surface modes arise.

Second, the case of propagation in layered media: layered media play an important role in many applications of optics, such as Fabry-Pérot etalons and anti-reflection coatings in lenses, and can be readily fabricated, such as through molecular beam epitaxy (MBE). There are several methods for analyzing this problem; we will describe one of these, the transfer matrix method. Last, we consider the special case of periodic media such as the distributed Bragg reflector (DBR). The addition of periodicity adds new physical effects and borrows many of the concepts of electrons propagating in periodic crystal lattices. This work culminates in the next chapter in the case of the Tamm plasmon, a surface mode at the interface of a DBR and a metal.

2.1 Maxwell's equations

Understanding the optical response of any structure starts with Maxwell's equations, which describe the relation between the four macroscopic electromagnetic fields; $\vec{D}$, the displacement field; $\vec{E}$, the electric field; $\vec{H}$, the magnetic field; and $\vec{B}$, the magnetic induction or magnetic flux density.

(2.1a) $$\vec{\nabla} \cdot \vec{D} = \rho$$

(2.1b) $$\vec{\nabla} \cdot \vec{B} = 0$$

(2.1c) $$\vec{\nabla} \times \vec{E} = -\frac{\partial \vec{B}}{\partial t}$$

(2.1d) $$\vec{\nabla} \times \vec{H} = \vec{J} + \frac{\partial \vec{D}}{\partial t}$$

where ρ and $\vec{J}$ are the electric charge density and total current density respectively. These fields are further linked by the constitutive equations

(2.2a) $$\vec{D} = \epsilon_0 \vec{E} + \vec{P} = \epsilon_0 (\vec{E} + \chi \vec{E})$$

(2.2b) $$\vec{B} = \mu_0 \vec{H} + \vec{M}$$

where $\vec{P}$ and $\vec{M}$ are the polarization and magnetization field, induced by the presence of electric and magnetic fields respectively and dependent on the specific media. χ is the electric susceptibility (the ratio of the material's electric polarization to the applied electric field), ϵ_0[1] is the electric permittivity of vacuum and μ_0[2] is the magnetic permeability of vacuum. These can be further simplified using the relative permittivity (ϵ) and permeability (μ).

(2.3a) $$\vec{D} = \epsilon_0 \epsilon \vec{E}$$

(2.3b) $$\vec{B} = \mu_0 \mu \vec{H}$$

where $\epsilon = 1 + \chi$ and, since we only consider non-magnetic materials ($\mu = 1$), relates to the refractive index by $\epsilon = n^2$. We also only consider materials which have no external charges ($\rho = 0$)

[1] $\epsilon_0 \approx 8.854 \times 10^{-12}$ Fm^{-1}
[2] $\mu_0 \approx 1.257 \times 10^{-6}$ Hm^{-1}

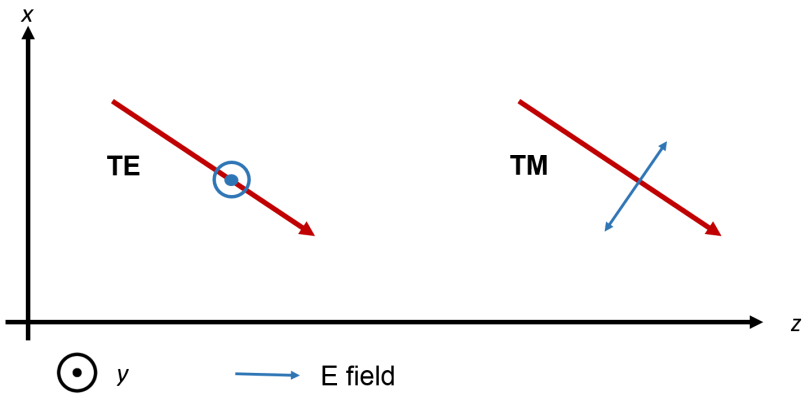

Figure 2.1: Definition of TE and TM configuration (these are also known as s- and p-polarization). The blue arrows show the direction of the electric field components.

and currents ($\vec{J} = 0$), and which have no spatial dependence of ϵ (the material is homogeneous). Using equations (2.1) and (2.3) we can form a wave equation for either field component F (= E, H).

$$\nabla^2 \vec{F} - \epsilon_0 \epsilon \mu_0 \frac{\partial^2 \vec{F}}{\partial t^2} = 0 \tag{2.4}$$

Assuming the field has a harmonic time dependence so $\vec{\tilde{F}}(\vec{r},t) = \vec{F}(\vec{r})e^{i\omega t}$ and substituting into 2.4, we get the *Helmholtz equation*.

$$\nabla^2 \vec{F} + \kappa_0^2 \epsilon \vec{F} = 0 \tag{2.5}$$

where κ_0 is the light wavevector in vacuum ($= \omega\sqrt{\epsilon_0 \mu_0}$). The solution to (2.5) is $F(\vec{r}) = Ae^{-i\vec{\kappa}\cdot\vec{r}}$. This is the monochromatic plane wave that, for any particular instant t, defines a plane $\vec{\kappa}\cdot\vec{r}$ of constant phase ($\omega t - \vec{\kappa}\cdot\vec{r}$) and which is perpendicular to the direction of propagation. This results in two sets of coupled equations and each can be treated independent of the other. Transverse Electric (TE) and Transverse Magnetic (TM) describe modes where the F_y field component is transverse to the x-z plane i.e. (TE) consists of orthogonal field components E_y, H_x and H_z, and (TM) of orthogonal field components H_y, E_x and E_z. This geometry is shown in figure (2.1).

Let's consider a TF plane wave propagating in the in the x-z plane. There cannot be a field variation in the plane perpendicular to the direction of propagation, so $\partial_y \equiv 0$ ($\nabla^2 \rightarrow \partial_x^2 + \partial_z^2$). We also separate the variables $\vec{F}(x,z) = \vec{F}(z)e^{i\beta_p x}$, where β_p is the in-plane component of the wavevector in the x direction[3] and is called the *propagation constant* (A.1).

$$\frac{d^2F(z)}{dz^2} + (\kappa_0^2\epsilon - \beta_p^2)F(z) = \frac{d^2F}{dz^2} + \kappa^2 F = 0 \tag{2.6}$$

where $\kappa^2 = \kappa_z^2 = (\kappa_0^2\epsilon - \beta_p^2)$.

[3]Note β_p is different from the β factor describing the ratio of photon emission into a cavity (1.2).

2.2 Light at a single interface

Across an interface between different media there are abrupt changes of ϵ and μ and it is no longer correct to assume that the fields are always continuous, which is required for the differential form of Maxwell's equations given above. However, by integrating both sides of these equations and using divergence theorem and Stokes' theorem it is possible to derive continuity relations for fields at an interface between different media [36]. Since we have assumed only cases with no charge or current density these become

(2.7a) $$E_{1t} = E_{2t}$$

(2.7b) $$H_{1t} = H_{2t}$$

(2.7c) $$D_{1n} = D_{2n}$$

(2.7d) $$B_{1n} = B_{2n}$$

where D_n and B_n are the components of the displacement field and magnetic induction normal to the interface, and E_t and H_t are the electric and magnetic field tangential to it. These must be continuous at the interface. It also follows from the second of these that the wavevector tangential to the boundary must also be continuous across the interface ($\beta_1 = \beta_2$).

In figure (2.2) a TM plane wave with amplitude E_1 and wavevector $|\vec{\kappa}_1| = n_1 \frac{\omega}{c}$ is incident on an interface between n_1 and n_2 and with angle to the normal axis θ_1. In most cases the wave will split into a reflected (E_r) and transmitted (E_t) component. Since β is constant the resulting waves must satisfy

(2.8) $$\kappa_1 sin(\theta_1) = \kappa_r sin(\theta_r) = \kappa_t sin(\theta_2)$$

This results in the well-known law of reflection ($\theta_1 = \theta_r$) and Snell's law of refraction ($n_1 sin(\theta_1) = n_2 sin(\theta_2)$). The interface conditions (ICs) also allow the calculation of the reflection and transmission coefficients. The electric field at $z < 0$ is given by the solution to (2.6)

(2.9) $$E_y = (E_1 e^{-i\kappa_{1z} z} + E_r e^{i\kappa_{1z} z}) e^{i\beta x}$$

and H_x can be derived (from 2.1) using $\vec{H} = -\frac{i}{\omega\mu}\vec{\nabla} \times \vec{E}$

(2.10) $$H_x = \frac{i}{\omega\mu_1}\frac{\partial E_y}{\partial z} = \frac{1}{\omega\mu_1}(\kappa_{1z} E_1 e^{-i\kappa_{1z} z} - \kappa_{1z} E_r e^{i\kappa_{1z} z}) e^{i\beta x}$$

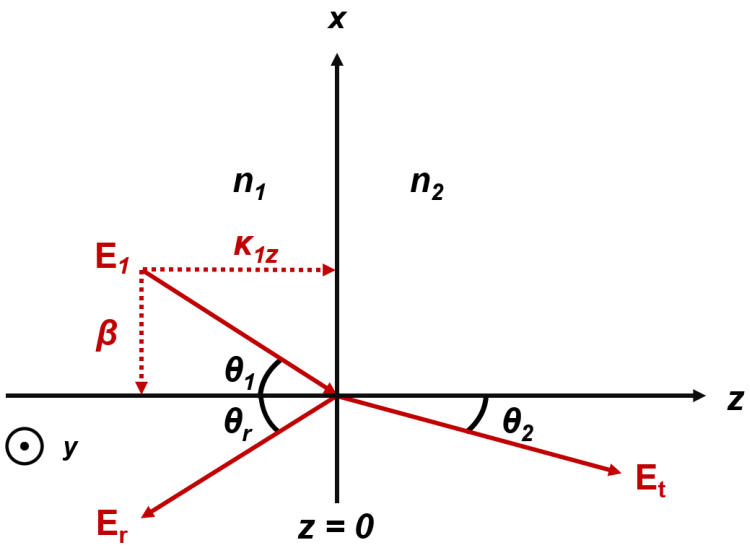

Figure 2.2: Diagram of reflection and transmission of a TM plane wave in the x-z plane, at the interface between two dielectric media.

Continuity of E_y and H_x at the interface $z = 0$ (and assuming $\mu_1 = \mu_2$), results in two coupled equations

(2.11a) $$E_1 + E_r = E_t$$

(2.11b) $$n_1(E_1 - E_r)cos(\theta_1) = n_2 E_t cos(\theta_2)$$

from which we can easily produce the reflection and transmission coefficients

(2.12a) $$r_{TE} = \left(\frac{E_r}{E_1}\right) = \frac{n_1 cos(\theta_1) - n_2 cos(\theta_2)}{n_1 cos(\theta_1) + n_2 cos(\theta_2)} = \frac{\kappa_{1z} - \kappa_{2z}}{\kappa_{1z} + \kappa_{2z}}$$

(2.12b) $$t_{TE} = \left(\frac{E_t}{E_1}\right) = \frac{2n_1 cos(\theta_1)}{n_1 cos(\theta_1) + n_2 cos(\theta_2)} = \frac{2\kappa_{1z}}{\kappa_{1z} + \kappa_{2z}}$$

A similar treatment for TM polarized light produces

(2.13a) $$r_{TM} = \frac{n_1 cos(\theta_2) - n_2 cos(\theta_1)}{n_1 cos(\theta_2) + n_2 cos(\theta_1)} = \frac{n_1^2 \kappa_{2z} - n_2^2 \kappa_{1z}}{n_1^2 \kappa_{2z} + n_2^2 \kappa_{1z}}$$

(2.13b) $$t_{TM} = \frac{2n_1 cos(\theta_1)}{n_1 cos(\theta_2) + n_2 cos(\theta_1)} = \frac{2n_1^2 \kappa_{1z}}{n_1^2 \kappa_{2z} + n_2^2 \kappa_{1z}}$$

(2.12) and (2.13) are known as the Fresnel equations and are suitable even at the interface of materials with complex permittivities, such as metals. It should be noted that these coefficients relate the *amplitudes* of the fields across an interface, and that this is not the same as the energy the field carries. This is given by the Poynting vector

$$\vec{S} = \vec{E} \times \vec{H} \tag{2.14}$$

The power reflection and transmission coefficients are calculated by comparing the ratios of the time-averaged Poynting vectors normal to the surface, $\langle \vec{S} \rangle = \frac{1}{2}\Re\{\vec{E} \times \frac{\kappa}{\omega\mu}\vec{E}^*\} = \frac{\kappa}{2\omega\mu}|\vec{E}|^2$

$$R_s = \left| \frac{\langle \vec{S}_r \cdot \hat{z} \rangle}{\langle \vec{S}_1 \cdot \hat{z} \rangle} \right| = \left| \frac{E_r}{E_1} \right|^2 = |r_s|^2 \tag{2.15a}$$

$$T_s = \left| \frac{\langle \vec{S}_t \cdot \hat{z} \rangle}{\langle \vec{S}_1 \cdot \hat{z} \rangle} \right| = \frac{\kappa_2}{\kappa_1} \left| \frac{E_t}{E_1} \right|^2 = \frac{\kappa_2}{\kappa_1} |t_s|^2 \tag{2.15b}$$

The appearance of the additional factor for the transmission coefficient arises from the need to normalize the transmitted power between two different materials. This is unnecessary in the case of reflection since the ingoing and reflected wave occur in the same layer.

2.2.1 Role of β and ϵ_{eff}

It is apparent that since $\kappa_z = (\kappa_0^2 \epsilon - \beta^2)^{\frac{1}{2}}$ the optical response at an interface between different media is not only dependent on the different values of ϵ but also on the initial choice of the plane wave momentum parallel to the boundary, β, and how it effects the sign inside the square root. In figure (2.2) we can consider three outcomes depending on the value of β:

- $\beta^2 < \kappa_0^2 \epsilon_2$

This results in κ_{2z} that is purely real and propagating solutions exist in region ϵ_2. There is transmission from region ϵ_1 to ϵ_2

- $\beta^2 = \kappa_0^2 \epsilon_2$

There is no transmission since $\kappa_{2z} = 0$. Solving this equality for $\beta = \kappa_1 sin(\theta_1)$ we derive the condition for total internal reflection (TIR).

- $\beta^2 > \kappa_0^2 \epsilon_2$

This results in κ_{2z} that is imaginary. The wave in region ϵ_2 decays exponentially but energy is not transmitted. Note that it is not claimed the fields do not penetrate the second region - only that the real Poynting vector normal to the interface is zero. One way of considering the role of β

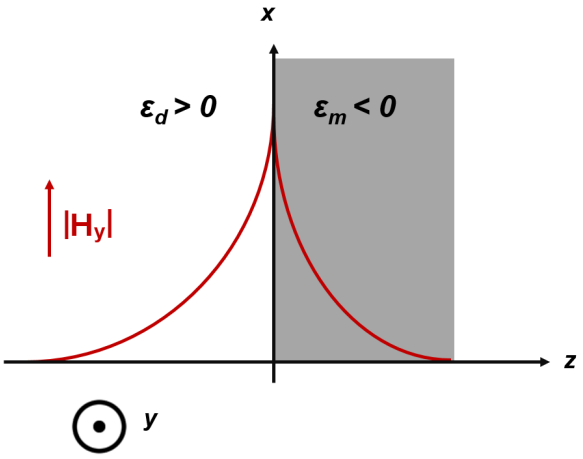

Figure 2.3: Diagram of SPP mode at a dielectric-metal interface. The amplitude of the field decays evanescently in both directions perpendicular to the interface.

is that it creates a new, 'effective' electric permeability ϵ_{eff} with respect to propagation into the material. Defining $\epsilon_{eff} = \epsilon_2 - \frac{\beta}{\kappa_0^2}$, equation (2.6) can be written

$$\frac{d^2F}{dz^2} + (\kappa_0^2\epsilon_2 - \beta^2)F = \frac{d^2F}{dz^2} + \kappa_0^2\epsilon_{eff}F = 0 \tag{2.16}$$

In this way, by setting a sufficiently large β, it is possible to have negative ϵ_{eff} that result in decaying solutions (which otherwise require having a negative permittivity material) in purely dielectric medium.

2.3 Surface Plasmon Polaritons

SPPs are confined, electromagnetic waves that propagate along the interface between a metal and a dielectric [37]. The mode decays evanescently away from the interface in both directions, in the metal layer due to its negative electric permittivity and in the dielectric layer due to TIR.

The simplest SPP mode is one that propagates along a single interface between a dielectric (ϵ_1) and metal (ϵ_2) layer (figure 2.3). In the case of a plane wave propagating in the $x-z$ plane there are two sets of equation corresponding to TE and TM polarization which can be written (where $F = E, H$) as a general wave equation (2.6)

$$\frac{d^2F}{dz^2} + \kappa_z^2 F = 0 \tag{2.17}$$

In addition to satisfying the wave equation, these solutions must also meet the boundary conditions (BCs) and ICs that result from being bound at an interface and which ensure they

are physically realistic. In the case of our single interface SPP the BCs require there must be a decaying term, so the field becomes zero as $|z| \to \infty$. The ICs require that the electric and magnetic field components tangential to the interface must be continuous.

2.3.1 Solving the wave equation for a SPP

2.3.1.1 TE polarization

First, we consider TE polarization. The solutions for (2.6) gives us the general form of E_y:

$$E_y = [A_1 e^{-i\kappa_z z} + A_2 e^{i\kappa_z z}]e^{i\beta x} \tag{2.18}$$

Using Maxwell's equations (2.1) to find the magnetic field components H_x and H_z:

$$\vec{\nabla} \times \vec{E} = -i\omega\mu_0 \vec{H} = \begin{vmatrix} \hat{u}_x & \hat{u}_y & \hat{u}_z \\ \partial_x & \cancel{\partial_y} & \partial_z \\ \cancel{E_x} & E_y & \cancel{E_z} \end{vmatrix}. \tag{2.19}$$

$$H_z = \frac{-i}{\omega\mu_0}\left(\frac{\partial E_y}{\partial x}\right) = \frac{-\beta}{\omega\mu_0} E_y \tag{2.20}$$

$$H_x = \frac{i}{\omega\mu_0}\left(\frac{\partial E_y}{\partial z}\right) \tag{2.21}$$

Applying the BCs results in (2.18) taking the form:

$$E_y = \begin{cases} A_1 e^{-i\kappa_{1z} z} e^{i\beta x}, & z < 0 \\ A_2 e^{i\kappa_{2z} z} e^{i\beta x}, & z > 0 \end{cases} \tag{2.22}$$

$$H_x = \frac{i}{\omega\mu_0}\left(\frac{\partial E_y}{\partial z}\right) = \begin{cases} \frac{-\kappa_{1z}}{\omega\mu_0} A_1 e^{-i\kappa_{1z} z} e^{i\beta x}, & z < 0 \\ \frac{\kappa_{2z}}{\omega\mu_0} A_2 e^{i\kappa_{2z} z} e^{i\beta x}, & z > 0 \end{cases} \tag{2.23}$$

A bound mode must have positive imaginary parts of κ_1 and κ_2, which follows from the BCs. Solving the continuity equations $E_{y1} = E_{y2}$ and $H_{x1} = H_{x2}$ that exist at the interface ($z = 0$) leads to the conditions $A_1 = A_2$ and $A_1(\kappa_{1z} + \kappa_{2z}) = 0$, which only has trivial solution $A_1 = A_2 = 0$.

Having values for κ that did satisfy the IC (e.g. having $\kappa_1 > 0$ and $\kappa_2 < 0$) would then violate the boundary conditions for a confined mode. Therefore, *there exists no SPPs for TE polarization*. Note that the actual condition is $(\frac{\kappa_{1z}}{\mu_1} + \frac{\kappa_{2z}}{\mu_2}) = 0$ and we have only assumed all materials have a positive magnetic permeability. It is possible for an interface between a positive and negative magnetic permeability (NMP) material to support bound TE surface modes [38].

2.3.1.2 TM polarization

$$H_y = [A_1 e^{-i\kappa_{1z} z} + A_2 e^{i\kappa_{2z} z}] e^{i\beta x} = \begin{cases} A_1 e^{-i\kappa_{1z} z} e^{i\beta x}, & z < 0 \\ A_2 e^{i\kappa_{2z} z} e^{i\beta x}, & z > 0 \end{cases} \tag{2.24}$$

$$E_x = \frac{-i}{\omega\epsilon_0\epsilon}\left(\frac{\partial H_y}{\partial z}\right) = \begin{cases} \frac{-\kappa_{1z}}{\omega\epsilon_0\epsilon_1} A_1 e^{-i\kappa_{1z} z} e^{i\beta x}, & z < 0 \\ \frac{\kappa_{2z}}{\omega\epsilon_0\epsilon_2} A_2 e^{i\kappa_{2z} z} e^{i\beta x}, & z > 0 \end{cases} \tag{2.25}$$

Solving the continuity equations $H_{y1} = H_{y2}$ and $E_{x1} = E_{x2}$ gives the conditions $A_1 = A_2$ and

$$A_1\left(\frac{\kappa_{1z}}{\epsilon_1} + \frac{\kappa_{2z}}{\epsilon_2}\right) = 0 \tag{2.26}$$

Ignoring the trivial solution, the value inside the brackets can only equal zero if there is a change in sign between the real parts of ϵ_1 and ϵ_2. The only way for the bound mode to have positive values of κ_1 and κ_2 while also satisfying (2.26) is when ϵ_1 and ϵ_2 have opposite signs.

This could be considered intuitively as requiring a SPP to have a decaying field into both the positive and negative z directions. This is achieved by TIR in the dielectric (where the permittivity is seen as effectively negative) and the metal (where it is). But this by definition necessitates a change in sign of the gradient of the field in the z direction (figure 2.3) and these derivatives must also match across the interface; these derivatives give the complementary electric or magnetic field component tangential to the interface (i.e. the component parallel to β) - and the IC require these fields also be continuous. If we were to consider an electron in a potential well, we might instead talk of matching the wavefunction ψ and $\frac{\partial\psi}{\partial z}$. Such an electron state might not be possible under usual circumstances - but for EM waves we are matching $\frac{1}{\mu}\frac{\partial E}{\partial z}$ and $\frac{1}{\epsilon}\frac{\partial H}{\partial z}$. This can be satisfied if μ (for TE) or ϵ (for TM) also reverse sign across the interface to compensate.

The Drude model of metal permittivity considers the metal as a plasma of free electrons that dominate the optical response [37]. Light incident on the metal excite the free electrons so that they oscillate coherently and in resonance with the excitation source:

$$\epsilon_m(\omega) = 1 - \frac{\omega_p^2}{\omega^2 + i\omega\gamma} \tag{2.27}$$

where ω_p is the metal plasma frequency and γ is the damping rate, representing the carrier collision frequency. The condition (2.26) is therefore satisfied between a metal and a dielectric for frequencies below the plasma frequency, due to the metal's negative permittivity. Note that though a decaying solution is produced for light propagating into the dielectric ($\epsilon_{eff} < 0$) due to $\beta > \kappa_0^2\epsilon_1$, the sign of ϵ_1 is still that of a dielectric.

Using equation (2.26) and the relation $\kappa_j^2 = \kappa_0^2\epsilon_j - \beta^2$ we can derive the dispersion relation for an SPP at the interface (A.2):

$$\beta = \kappa_0\sqrt{\frac{\epsilon_d\epsilon_m}{\epsilon_d + \epsilon_m}} \tag{2.28}$$

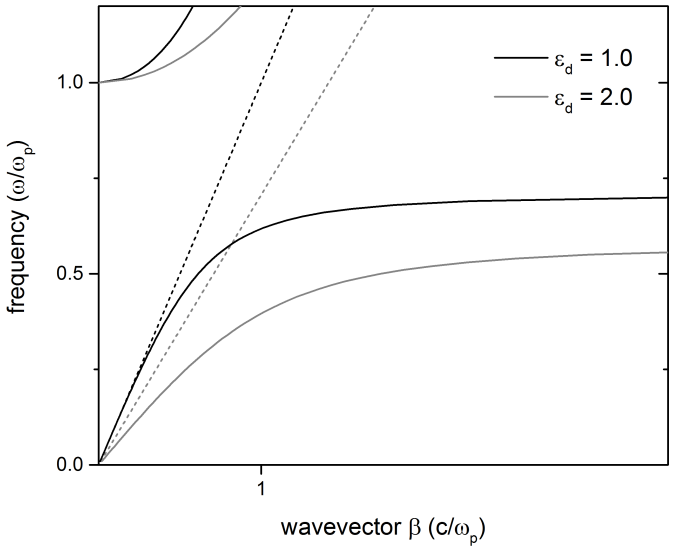

Figure 2.4: Dispersion relation of SPPs between a Drude metal (i.e. with negligible collision damping) and air (black) and silica (grey) interface. Real values of β are shown as the solid lines and the light lines ($\omega = c\kappa$) as dashed lines. The frequency has been normalized to the metal's plasma frequency ω_p. There also exist real solutions of β *within* the light cone, for $\omega > \omega_p$, which is the transparency regime of the metal. As the name implies, here the metal allows propagating waves and there is no confinement. Between these two regimes β only has imaginary values, so there is no mode propagating in the direction along the boundary, whether as a SPP ($< \omega_p$) or as a radiating mode ($> \omega_p$).

2.3.2 Characteristics of SPPs

The dispersion relation of a SPP is demonstrated in figure (2.4) at an interface between a metal, modelled by the real Drude equation (2.27), and an air ($\epsilon_d = 1.0$) and silica ($\epsilon_d = 2.0$) dielectric. The real solutions below the metal plasma frequency (ω_p) have dispersion curves to the right of their respective air and silica light lines; at these frequencies that values of ϵ_m cause the square root in equation (2.28) to be greater than one and β to always have a value greater than κ_0 in the dielectric. This is due to the condition for TIR; for a surface wave the tangential component of the wavevector must exceed that of the wavevector propagating in the positive permittivity material to produce a decaying mode.

This difference in momentum between a radiating mode (modes within the light cone $|\kappa| = \frac{n\omega}{c}$) and the SPP can be associated with the binding energy of the SPP. It is what makes it bound; it is not possible for a SPP to emit into a radiating mode since it cannot both satisfy (2.28) and have a non-imaginary wavevector into the dielectric [39]. Unless this extra momentum is added there is no emission or 'leaking'.

Being outside the light cone similarly prevents SPP excitation by propagating light unless

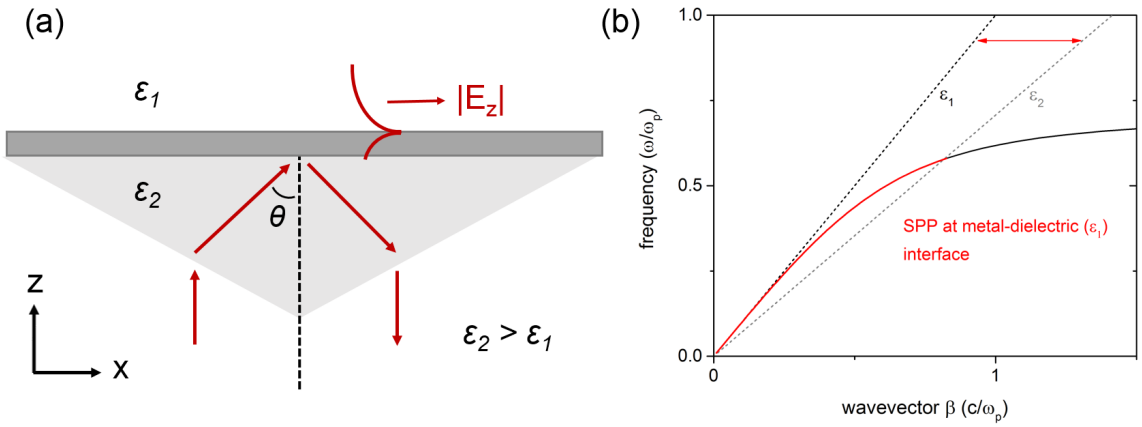

Figure 2.5: (a) Prism coupling to SPPs using the Kretschmann configuration. (b) The SPP dispersion (solid line) at the interface between the metal and low ϵ material; excited SPPs (red line) have propagation constants above the light line of the prism material and can therefore emit radiative modes.

special matching methods are used. One method is to excite through a prism of higher dielectric material on the other side of the metal layer, at an incidence greater than the critical angle. The prism decreases the effective wavelength of the light, so that it is able to couple to the non-radiative SPP at the adjacent interface between the metal and a dielectric with a lower refractive index. The in-plane wavevector at the first interface $\beta = \kappa_2 sin(\theta)$ is sufficient to excite SPPs with β values between the light lines of the low and high refractive index materials. The most common configuration, the Kretschmann configuration [40], is shown in figure (2.5).

The second is to pattern the metal surface with a periodic grating [35, 41]. Light scatters off a grating with grating period Λ with a dispersion relation of

$$\beta = \kappa sin(\theta) \pm mG \tag{2.29}$$

where θ is the angle of incidence of light with wavevector κ_0, G is the reciprocal lattice vector of the grating with modulus $|\vec{G}| = \frac{2\pi}{\Lambda}$, and m is an integer (called the order of the scattering). In other words, the incident light gains momentum in multiples of G in the direction of the grating periodicity, allowing it to couple to a higher momentum SPP mode. In addition to excitation with incident light the grating is also used for the reverse; to outcouple a SPP into a radiating mode. Compared to the prism-coupling method it has less attenuation (since the light does not need to tunnel through the metal film) and allows transmission-based measurements (the former method typically only looks for dips in the reflection intensities). The match to a grating period requires a particular angle for each of the various wavelengths so it can be used to spectrally filter the plasmon-coupled emission [39]. This angle is also sensitive to the refractive index of the incident medium, so can be used as a sensor [42].

2.3.3 Purcell enhancement and surface plasmon-coupled emission

So far these plasmonic structures have been considered as passive devices that are excited by an incident mode and result in a bound SPP. Because the field decays rapidly normal to the interface the field is confined to volumes below the diffraction limit, which produce strong field intensities beyond that achievable with classical optics [43]. This field enhancement alters the emission properties of a fluorophore located in the near-field of the SPP, such as its spontaneous emission rate (Purcell factor) and emission direction.

The enhancement (or inhibition) an optical environment has on emission rate is quantified by the Purcell factor [44]

$$F_p = \frac{3}{4\pi^2}\left(\frac{\lambda}{n}\right)^3\left(\frac{Q}{V}\right) \tag{2.30}$$

where Q is the mode quality factor and V the effective mode volume. The Q-factor is the ratio of the resonance frequency with the linewidth at full-width half-maximum (FWHM), and so is proportional to the lifetime of the emitter photon "in" the plasmon. Q and V respectively describe a mode's spectral and spatial energy density [37].

In the Kretschmann configuration shown in figure (2.5) the SPP is no longer totally bound; since the SPP lies within the prism's light cone it can emit radiative modes (into the higher dielectric material). If the ϵ_1 material is replaced with a fluorophore containing layer these will be excited by the evanescently decaying fields of the SPP close to the metal-ϵ_1 interface. Conversely, an excited fluorophore within the near-field can couple to and excite a SPP, which then produces a radiative mode (via the prism) at the fluorophore's emission frequency. This reverse process is called surface plasmon-coupled emission (SPCE). Like surface plasmons, all SPCE is TM polarized. The emission angle of SPCE is given by $\beta = \kappa_2 sin(\theta_{SP})$ (the same equation for SPP resonance) so there is a strong dependence between emission angle and wavelength. As wavelength decreases, the angle θ_{SP} increases. Therefore, SPCE has an intrinsic spectral filtering with emission occurring over a narrow angular distribution. This effect is independent of the orientation of the emitter, so by mediating with a surface plasmon it is possible to convert isotropic emission into directional emission for efficient collection. It is possible to improve collection efficiencies from around 1% to 50% with SPCE [45].

It is these two characteristics, of enhancing emission rate (via Purcell enhancement) and controlling emission direction (via SPCE), that make plasmonics of such interest for optical devices, even accounting for the performance limit caused by resistive losses [46]. Later in the thesis it will be demonstrated that Tamm plasmon structures are able to recreate both these effects.

2.4 Light in layered media

Having considered the case of light at a single interface between materials with different electric permittivities it is now possible to consider layered structures where the continuity conditions are linked across multiple interfaces between layers of homogeneous and isotropic material. The permittivity through the structure can be described by a piecewise constant function. It is also assumed that the interfaces are optically flat and that the incident light is a plane wave.

Waves propagating through layered media is a common occurrence in many areas of physics and several different methods have been developed to solve this problem such as the scattering matrix method or using recursive functions [47]. The transfer matrix method (TMM) is a relatively simple technique that can be used to calculate the reflection, transmission and absorption coefficients of a structure consisting of a series of layers with different thicknesses and refractive indices [48, 49].

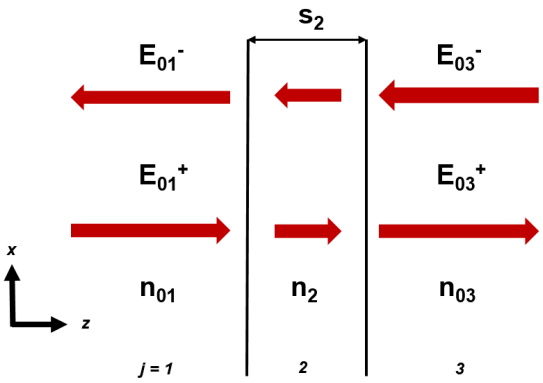

Figure 2.6: Diagram of a single layer structure

2.4.1 The transfer matrix method (TMM)

Let us consider the simplest such structure, consisting of one layer with thickness s_2 and complex refractive index n_2, positioned between two semi-infinite media with refractive index n_{01} and n_{03} (the ambient and substrate materials), and shown in figure (2.6). As Maxwell's equations are linear, the electric field at any point can be described as the sum of the forward and backward propagating component.

$$E_j(z) = E_j^+(z) + E_j^-(z) \tag{2.31}$$

First, let us only consider how the electric field changes as it propagates through the single layer of thickness s_2. Each component will experience a change in phase (Φ) that will be equal in

magnitude but with opposite signs as they have opposite wavevectors.

$$E_2(z) = E_2^+(z+s_2)e^{-i\Phi} + E_2^-(z+s_2)e^{i\Phi} \tag{2.32}$$

which can be written as a 2x2 matrix, called the **propagation matrix** (or layer matrix)

$$\vec{E}_2(z) = L_2\vec{E}_2(z+s_2) = \begin{bmatrix} e^{-i\Phi} & 0 \\ 0 & e^{i\Phi} \end{bmatrix} \vec{E}_2(z+s_2) \tag{2.33}$$

where $\vec{E}$ is a column vector of the amplitudes of the forward and backward travelling wave

$$\vec{E} = \begin{bmatrix} E^+ \\ E^- \end{bmatrix} \tag{2.34}$$

and

$$\Phi = n_2\frac{\omega}{c}s_2 = \kappa_2 s_2 \tag{2.35}$$

where s_2 gives the layer's thickness and $n_2(\omega/c)$ the spatial frequency (assuming normal incidence). The propagation matrix calculates the change in phase and amplitude after propagating through the layer, though if n_2 is purely real then there will be no absorption and it only describe a phase change.

Next, the effect of the interface is accounted for. Consider a single interface between two layers 1 and 2, and that has light incident on both sides. The reflection coefficient r_{ij} is the ratio of the reflected amplitude going from layer i to j to the incident amplitude, and t_{ij} the same for the transmitted amplitude. These are related by

$$E_1^- = r_{12}E_1^+ + t_{21}E_2^- \tag{2.36a}$$

$$E_2^+ = t_{12}E_1^+ + r_{21}E_2^- \tag{2.36b}$$

Using the additional constraints that $r_{12} = -r_{21}$ and that $t_{12}t_{21} - r_{12}r_{21} = 1$ we can derive a pair of equations that link the amplitudes of the foward and backward propagating wave in terms of these ratios:

$$E_1^+ = \frac{1}{t_{12}}\left(E_2^+ + r_{12}E_2^-\right) \tag{2.37a}$$

$$E_1^- = \frac{1}{t_{12}}\left(r_{12}E_2^+ + E_2^-\right) \tag{2.37b}$$

which can also be written as a 2x2 **interface matrix**

$$\vec{E}_1 = I_{1,2}\vec{E}_2 = \left(\frac{1}{t_{12}}\right)\begin{bmatrix} 1 & r_{12} \\ r_{12} & 1 \end{bmatrix}\vec{E}_2 \tag{2.38}$$

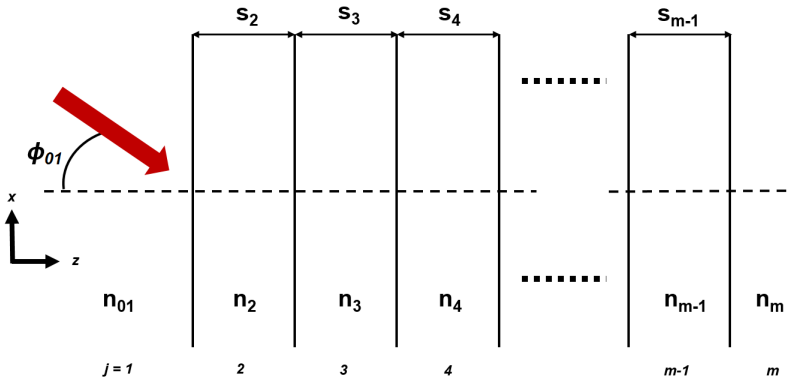

Figure 2.7: Diagram of a multiple-layer structure

The transfer matrix of a multilayer structure is a product of these two types of matrices; the propagation matrix and interface matrix. So in the case considered in figure (2.6) the propagation through *the whole structure* can be described as the product of the correct sequence of interface and propagation matrices, starting with the last interface and working backwards from the direction of propagation. The result is a single 2x2 matrix, T, the transfer matrix of the structure.

$$\vec{E}_{01} = I_{1,2}L_2I_{2,3}\vec{E}_{03} = T\vec{E}_{03} \tag{2.39}$$

The structure can be extended to include multiple layers of thicknesses $s_{j=2}, s_3 \ldots s_{m-1}$ and refractive indices $n_2, n_3 \ldots n_{m-1}$, as shown in figure (6.2). A transfer matrix for the whole structure can be constructed, one that links the forward and backward amplitudes for the fields on either side, by calculating the individual propagation and interface matrices and multiplying them together in the reverse order:

$$\vec{E}_{01} = T\vec{E}_m = \left(\prod_{j=2}^{m-1} I_{(j-1),j}L_j\right) I_{(m-1),m}\vec{E}_m \tag{2.40}$$

where L_j is the propagation matrix through layer j

$$L_j = \begin{bmatrix} e^{-i\Phi_j} & 0 \\ 0 & e^{i\Phi_j} \end{bmatrix} \tag{2.41}$$

and $I_{j,j+1}$ is the interface matrix connecting the field amplitudes across the interface between layer j and $j+1$

$$I_{j,j+1} = \left(\frac{1}{t_j}\right)\begin{bmatrix} 1 & r_j \\ r_j & 1 \end{bmatrix} \tag{2.42}$$

where $\Phi_j = \kappa_{jz}s_j = n_j(\omega/c)q_j s_j$ is the phase thickness of layer j perpendicular to the interface, q_j is the cosine of angle ϕ_j in layer j, and r_j and t_j are the complex Fresnel coefficient of reflection

and transmission at the interface between layer j and $j+1$. For TE waves these are (2.12)

$$r_j = \frac{n_j q_j - n_{j+1} q_{j+1}}{n_j q_j + n_{j+1} q_{j+1}} \tag{2.43a}$$

$$t_j = \frac{2 n_j q_j}{n_j q_j + n_{j+1} q_{j+1}} \tag{2.43b}$$

and for TM waves

$$r_j = \frac{n_{j+1} q_j - n_j q_{j+1}}{n_{j+1} q_j + n_j q_{j+1}} \tag{2.44a}$$

$$t_j = \frac{2 n_j q_j}{n_{j+1} q_j + n_j q_{j+1}} \tag{2.44b}$$

Once a transfer matrix has been calculated for the whole structure it can be used to find its reflection and transmission coefficients. Consider the case of light entering from one side of a structure, with an incoming amplitude defined as 1 and reflection and transmission amplitudes r and t.

$$\begin{bmatrix} 1 \\ r \end{bmatrix} = T \begin{bmatrix} t \\ 0 \end{bmatrix} = \begin{bmatrix} T_{11} & T_{12} \\ T_{21} & T_{22} \end{bmatrix} \begin{bmatrix} t \\ 0 \end{bmatrix} \tag{2.45}$$

$$r = \frac{T_{21}}{T_{11}} \tag{2.46}$$

$$t = \frac{1}{T_{11}} \tag{2.47}$$

Therefore, the elements in the transfer matrix can be used to express the amplitude reflection and transmission coefficients for the total system. The power coefficients are calculated using equation (2.15)

$$R = \left| \frac{T_{21}}{T_{11}} \right|^2 \tag{2.48}$$

$$T = \frac{n_m q_m}{n_{01} q_{01}} \left| \frac{1}{T_{11}} \right|^2 \tag{2.49}$$

2.4.2 Photonic Crystals

Photonic crystals are structures with regular periodic variations in refractive index that affect the propagation of photons in a way analogous to how the periodic potential in a semiconductor crystal lattice affects the motion of electrons. Just as electrons in crystalline atomic lattices encounter bands of energy values they are forbidden from having, so too are photons in photonic crystals forbidden from having certain frequencies (energies), called a photonic bandgap. Because these frequencies cannot propagate through the structure, this is manifested as a spectral window where reflectivity is close to unity (called the stopband).

Though the term photonic crystal was first used in 1987 [50] the earliest photonic crystals, consisting of stacked, alternating layers of two dielectric materials with different refractive indices, have been around for much longer [51]. These are called distributed Bragg reflectors (DBRs) and have a one-dimensional bandgap that forbids frequencies propagating normal to the layer periodicity. An example structure is shown in figure (2.8) consisting of layers with thickness a and b and refractive index n_a and n_b.

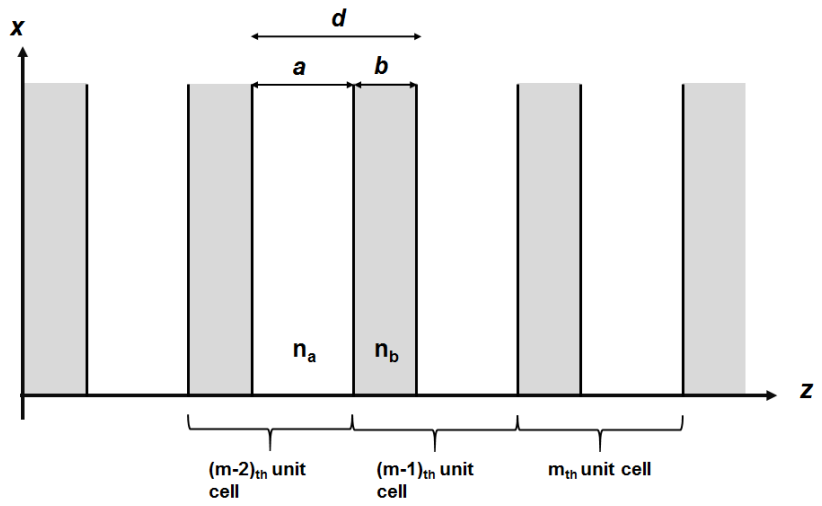

Figure 2.8: Diagram of periodic layered structure

The DBR stopband can be intuitively understood as an interference effect. At each interface there is a partial reflection that imparts a phase change on the reflected component. If the optical thickness of the layers are a quarter-wavelength ($= \lambda/4n$) these components interfere constructively in the reflected direction. However, to understand how the DBR can form surface states it is necessary to understand more precisely the propagation of electromagnetic waves in these media. Fortunately, this theory has much in common with the quantum theory of electrons in solids [52].

The motion of electrons in a solid is given by the Schrödinger equation

$$\left[\vec{\nabla}^2 + (E - V(\vec{r}))\right]\psi(\vec{r}) = 0 \tag{2.50}$$

while the propagation of photons (assuming source-free, harmonic time dependence, etc.) is given by the wave equation (2.5)

$$\nabla^2\vec{F} + \kappa_0^2\epsilon\vec{F} = 0 \tag{2.51}$$

These are both eigenvalue equations for E and κ_0^2 respectively, and both share the same linear form (the curl term can be intuitively considered to correspond to the 'kinetic energy' and ϵ to the 'potential'; photons in higher ϵ material will have a lower potential [52]). Further defining of our geometry (here considering the TE mode) led to (2.6)

$$\frac{d^2E(z)}{dz^2} + \kappa(z)^2E(z) = 0 \tag{2.52}$$

where $\kappa^2 = (\kappa_0^2\epsilon(z) - \beta^2)$. Like $V(z)$ in a one-dimensional periodic crystal lattice, the permittivities in a DBR also have a periodic function

$$\epsilon(z) = \epsilon(z + d) \tag{2.53}$$

where $d = a + b$. Equation (2.52) therefore now takes the form of a set of differential equations whose solutions (in one dimension) were first found by Floquet's theorem and, while studying electrons in crystals, more generally by Felix Bloch in 1928, known as Bloch (or Bloch-Floquet) theorem. This states that the solutions must be of the form

$$E(z) = E_K(z)e^{iKz} \tag{2.54}$$

where $E_K(z)$ is a periodic function with period d and K is the Bloch wavevector. These are known as Bloch waves and form the basis of possible eigenmodes [53]. It should be briefly noted that K is not unique; it can be shown that the periodic component $E_K(z) = E_{K+nG}(z)e^{inGz}$, where $G = \frac{2\pi}{d}$ is the reciprocal lattice vector and n is an integer number. Just as the Bloch wave is spatially invariant with period d it is also invariant in the reciprocal space with a period G. However, because these have the same solutions it is only necessary to find the eigenmode for each particular K value in the first cell of the reciprocal lattice ($n = 1$) and this region, called the first Brillouin zone, contains a complete set of all the possible eigensolutions.

The exponential in equation (2.54) describes a plane wave envelope when K is a real number, which is a requirement to describe modes in the bulk of the DBR. Complex values of K, which describe exponentially growing or decaying modes, cannot satisfy the BCs for an infinite DBR

since the field will not decay as $|z| \to \infty$. It will be shown later that these correspond to the forbidden stopbands of the DBR. However, it will be demonstrated in chapter 3 that these are also key to the formation of Tamm states.

For now, it is useful to introduce a translation operator T for one unit cell. Using the TMM (section 2.4.1) a translation matrix that links the field amplitudes of the forward and backward propagating waves at equivalent points across a single unit cell of the form

$$\vec{E}(z) = T\vec{E}(z+d) = I_{a,b}L_bI_{b,a}L_a\vec{E}(z+d) \tag{2.55}$$

which has matrix elements (using equations (2.12), (2.41) and (2.42))

$$T_{11} = e^{-i\phi_a}\left(cos(\phi_b) - \frac{i}{2}\left[\frac{\kappa_{b,z}}{\kappa_{a,z}} + \frac{\kappa_{a,z}}{\kappa_{b,z}}\right]sin(\phi_b)\right) \tag{2.56a}$$

$$T_{12} = e^{i\phi_a}\left(-\frac{i}{2}\left[\frac{\kappa_{b,z}}{\kappa_{a,z}} - \frac{\kappa_{a,z}}{\kappa_{b,z}}\right]sin(\phi_b)\right) \tag{2.56b}$$

$$T_{21} = e^{-i\phi_a}\left(\frac{i}{2}\left[\frac{\kappa_{b,z}}{\kappa_{a,z}} - \frac{\kappa_{a,z}}{\kappa_{b,z}}\right]sin(\phi_b)\right) \tag{2.56c}$$

$$T_{22} = e^{i\phi_a}\left(cos(\phi_b) + \frac{i}{2}\left[\frac{\kappa_{b,z}}{\kappa_{a,z}} + \frac{\kappa_{a,z}}{\kappa_{b,z}b}\right]sin(\phi_b)\right) \tag{2.56d}$$

where $\phi_a = \kappa_{a,z}a$ and $\phi_b = \kappa_{b,z}b$. Firstly, it follows that the translation operator commutes with the operator on E in equation (2.52), since it leaves ϵ unchanged and so they share common eigenfunctions. It also follows from (2.54) that the same operation can be represented

$$E(z+d) = E_K(z+d)e^{iKz}e^{iKd} = E(z)e^{iKd} \tag{2.57}$$

since $E_K(z)$ is periodic. Comparing (2.55) with the above, it's clear that the Bloch wave must satisfy the eigenvalue problem [54]

$$T\vec{E} = e^{-iKd}\vec{E} \tag{2.58}$$

where e^{-iKd} are the eigenvalues of the translation matrix T. Using the fact T is unimodular ($T_{11}T_{22} - T_{12}T_{21} = 1$) these are shown to be

$$e^{-iKd} = \frac{1}{2}(T_{11} + T_{22}) \pm \sqrt{\frac{1}{4}(T_{11} + T_{22})^2 - 1} \tag{2.59}$$

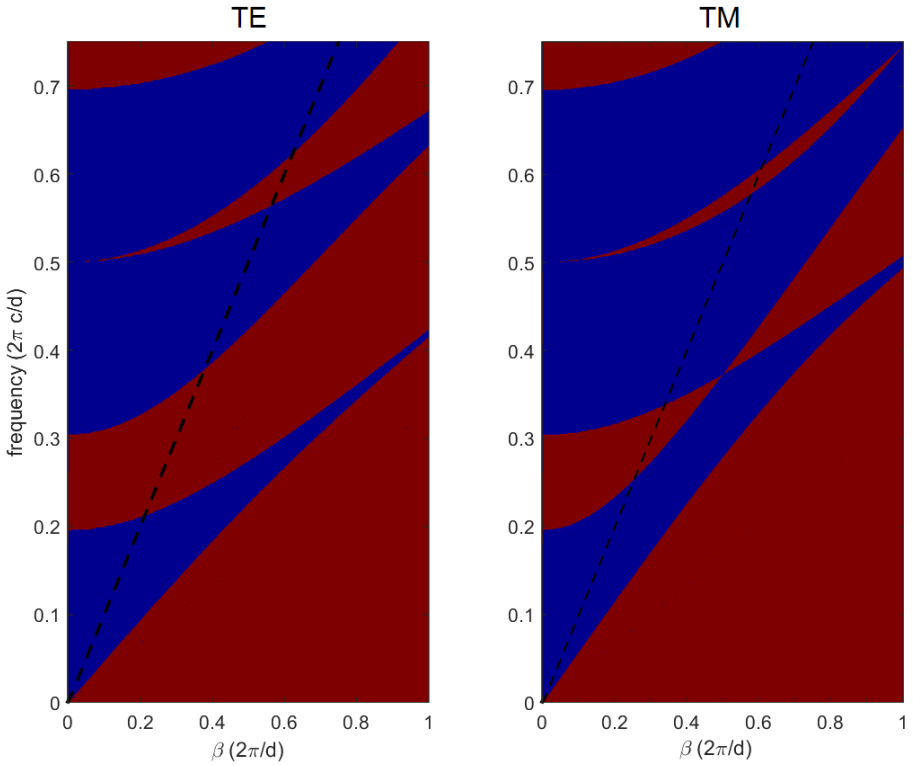

Figure 2.9: Dispersion diagram showing the bandstructure for a DBR with n_a = 3, n_b = 1, a = 75 nm, b = 150 nm for TE and TM polarization. The blue regions show the allowed wavelengths and the red regions the forbidden stopbands, which form the photonic bandgap. The black dashed lines are the light lines in air. Note that in the TM case there are wavevectors where the forbidden bands shrink to zero, which occur at the Brewster angle for the two materials of the DBR; since TM polarized light at this angle is not reflected at the interfaces there is no interference effect to form the stopband.

This gives the dispersion relation for the Bloch wave

$$\cos(Kd) = \frac{T_{11} + T_{22}}{2} \tag{2.60}$$

When $\frac{1}{2}|T_{11} + T_{22}| < 1$ this results in K with real values. These correspond to propagating modes, and the eigenvalues $\omega(K)$ form a continuous function, or bulk band, in the DBR. When this inequality is not the case K has a complex value. The Bloch wave is evanescent and does not transmit energy through the structure. These complex value wavevectors are the cause of the DBR's stopbands. An example of this dispersion is shown in figure (2.9) for a DBR centered at 900 nm, with n_a = 3, n_b = 1.5, a = 75 nm, b = 100 nm. The blue and red regions show the allowed wavelengths (the bulk bands) and forbidden wavelengths (the stopbands) respectively.

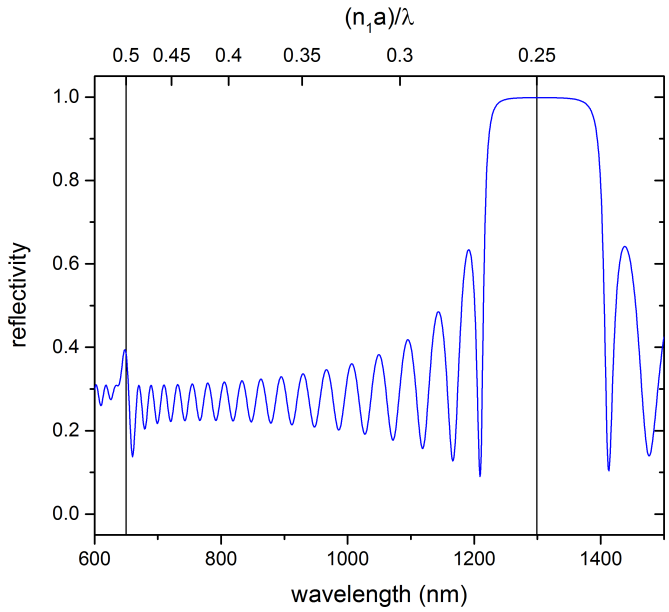

Figure 2.10: Reflectivity spectra for an 18x pair $\lambda/4$ DBR with a photonic stopband centered on 1300 nm (n_1 = 3.5, n_2 = 2.9), showing the first band edge and photonic stopband as a function of wavelength and ($n_1 a/\lambda$). Calculated using the transfer matrix method.

The corresponding eigenvectors for (2.59) are

$$\vec{u}_0 = \begin{bmatrix} v_0 \\ w_0 \end{bmatrix} E_K(z) = \begin{bmatrix} T_{12} \\ e^{-iKd} - T_{11} \end{bmatrix} E_K(z) \tag{2.61}$$

An example DBR for telecoms wavelength is shown in figures (2.10) and (2.11) consisting of 18x pairs of n_a = 3.5, n_b = 2.9, a = 95 nm and b = 110 nm. Both show the reflection power coefficients at normal incidence to the DBR. The photonic stopband is the window of high reflectivity between 1230 and 1380 nm. When at normal incidence ($\beta = 0$ and $\kappa_{i,z} = n_i(\omega/c)$) the values from (2.56) give a dispersion relation

$$cos(Kd) = cos(\kappa_a a)cos(\kappa_b b) - \frac{1}{2}\left(\frac{n_b}{n_a} + \frac{n_a}{n_b}\right) sin(\kappa_a a) sin(\kappa_b b) \tag{2.62}$$

The center of the first bulk band occurs when $\kappa_a a = \kappa_b b = \pi$, which equates to $n_a a = n_b b = \lambda/2$, and results in $K(= \frac{2\pi}{d} m)$ with no imaginary component. Conversely, when $\kappa_a a = \kappa_b b = \frac{\pi}{2}$ ($n_a a = n_b b = \lambda/4$) the dispersion is

$$cos(Kd) = -\frac{1}{2}\left(\frac{n_b}{n_a} + \frac{n_a}{n_b}\right) \tag{2.63}$$

This results in K with the maximum value of its imaginary component, corresponding to the most rapid field decay within the DBR. Therefore, the center of the first DBR stopband occurs (at

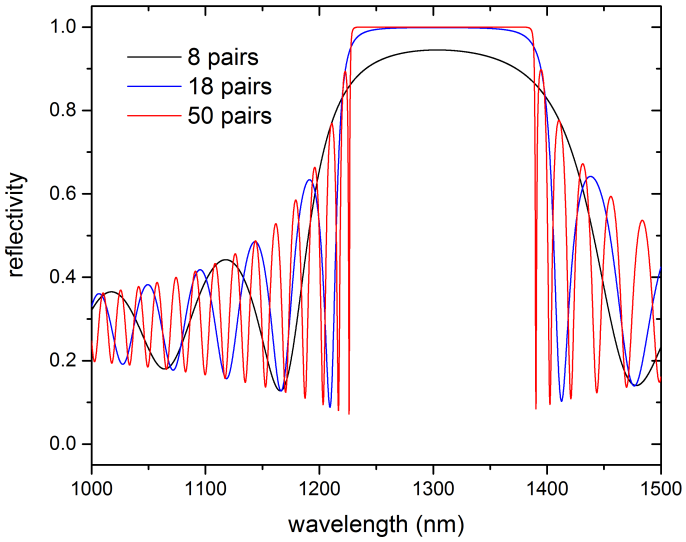

Figure 2.11: Reflectivity spectra for 1300 nm centered DBR using the same parameters as figure (2.10). As the number of pairs increases the reflectivity over the range of the stopband approaches unity and the frequency of Fabry-Pérot resonances, the fringes seen at wavelength above and below the stopband, increases. Calculated using the transfer matrix method.

normal incidence) when the quarter-wavelength condition is satisfied (figure 2.10). At non-normal incidence the optical length of the layers (and periodicity of the DBR) changes, so the stopband shifts to higher energies, as seen in figure (2.9).

The reflectivity at the center of the stopband can be shown to follow the equation [55]

$$R \approx 1 - \left(\frac{n_a}{n_b}\right)^{2N} \tag{2.64}$$

where N is the number of DBR pairs. Hence, even a very small number of pairs can achieve close to unity reflectivity. There are also a series of characteristic fringes outside the stopband edges that are the result of Fabry-Pérot resonance, which increase in density as the number of pairs increase, as seen in figure (2.11) for 8 (black line), 18 (blue) and 50 (red) DBR pairs.

2.5 Summary

In this chapter we have considered the propagation of electromagnetic plane waves through structures consisting of single, and then multiple, interfaces separated by layers of homogenous and isotropic media. Bound surface modes, the SPP, have been shown to exist at the interface between a dielectric and materials with negative permittivities, such as metals below the plasma

frequency, and that this condition follows from the need to meet both the continuity conditions at the interface and the BCs that the field must evanescently decay.

It should be noted though that occurrences of decaying waves appeared in purely dielectric materials; in the case of total internal reflection, when the tangential component of the wavevector is greater than the modulus on the radiating wavevector; second, when the structure is periodic it can result in Bloch waves with imaginary wavevectors, resulting in forbidden bands where no modes propagated. In the last case such solutions to Bloch's theorem were ignored as physically unacceptable; since they do not decay as $|z| \to \infty$ they result in fields with infinite energy when it is assumed the DBR continues infinitely. In the next chapter we consider the case of a semi-infinite DBR ending with a boundary, where this assumption is no longer true.

CHAPTER 3

Optical Tamm states

In 1933, Igor Tamm predicted that electronic states could exist within the forbidden energy bands of crystals when the periodicity of the crystal is terminated by a surface [32]. These became known as (electronic) Tamm States. The same mechanism was later used to posit the existence of *optical* states in the photonic stopband at the surface of photonic crystals. For these similarities these modes are named optical Tamm States. This opened the possibility of structures with plasmonic-like surface waves that can be used to enhance or direct emission but containing only dielectric materials, without the intrinsic lossiness of metal.

In this chapter I will describe the theory of Tamm states[1] at the interface of 1D photonic crystals (i.e. DBRs) with different cases of media, starting with dielectric material. We will make use of the concepts that appeared in the previous chapter; the appearance of solutions with imaginary wavevectors in DBRs (Bloch waves) or via total internal reflection at high β_p wavevectors, which allow the BCs of an interface mode to be satisfied. This allows the substitution of purely dielectric materials, with *effective* negative permittivity (NP) and negative magnetic permeability (NMP), in place of the metal layers used in the case of the SPP. Secondly, we consider the modes at the interface of a DBR and metal layer (the Tamm plasmon), how it differs to conventional SPPs, and the opportunities it offers for fully three-dimensional confinement compared to other Tamm states.

[1] From now I will describe these as Tamm states, with their optical nature being implicit.

3.1 Surface states at photonic crystal interfaces

3.1.1 Bloch surface waves

Surface electromagnetic waves (i.e. SPPs) were previously shown to exist along the boundary between two media where the permittivity switched sign, such as between a dielectric ($\epsilon_d > 0$) and metal ($\epsilon_m < 0$) [37]. SPPs are confined by the metal due to its negative permittivity and by the dielectric due to TIR. Hence, the dispersion curve of the plasmon has a tangential wavevector that is always larger than the radiating wavevector in the dielectric medium ($\kappa = n\frac{\omega}{c}$). This condition, which arose from meeting the boundary (BC) and interface conditions (IC) of a surface state, is why SPPs cannot usually couple into radiating waves or be directly excited, and certain measures like prism or grating-coupling must be used.

Photons propagating in photonic crystal stopbands were also shown to produce imaginary wavevectors. These structures have periodically alternating dielectric materials with different permittivities. Fields in these crystals are solutions of Bloch's theory and have eigenmodes (Bloch waves) that are products of a periodic amplitude function and an exponential with a Bloch wavevector K. The simplest example, the one-dimensional DBR stack, was shown to have dispersion relation given by equation (2.60)

$$cos(K\Lambda) = \frac{T_{11} + T_{22}}{2} \tag{3.1}$$

where Λ is the period of the DBR and T_{11} and T_{22} are the diagonal elements of the transfer matrix across one unit cell, which are functions of ω and β_p. When $\frac{1}{2}|T_{11} + T_{22}| < 1$, K is real and the eigenmodes are plane wave solutions, i.e. they propagate through the DBR, and are called bulk bands. When K has complex values then the eigenmodes are exponentially decaying or increasing, which are forbidden and result in the DBR's stopband. This assumed that the DBR continued infinitely. Solutions with complex K were forbidden since these would violate the BCs that the wave must decay to zero as $|z| \to \infty$.

In reality, DBRs are not infinite but will be bounded by a surface. In this case K can take complex values (specifically, solutions that are exponentially damped), and solutions with eigenvalues in what previously would have been in the forbidden energy band become realizable [54]. Consider the case of a semi-infinite DBR that terminates with some dielectric, homogenous material shown in figure (3.1). The refractive indices profile is given by

$$n(z) = \begin{cases} n_0 & z \leq 0 \\ n_a & m\Lambda < z \leq m\Lambda + a \\ n_b & m\Lambda + a \leq z \leq (m+1)\Lambda \end{cases} \tag{3.2}$$

For a TE mode, the electric field in the dielectric region of figure (3.1) is given by the wave equation (2.6) and in the DBR by a Bloch wave (2.54).

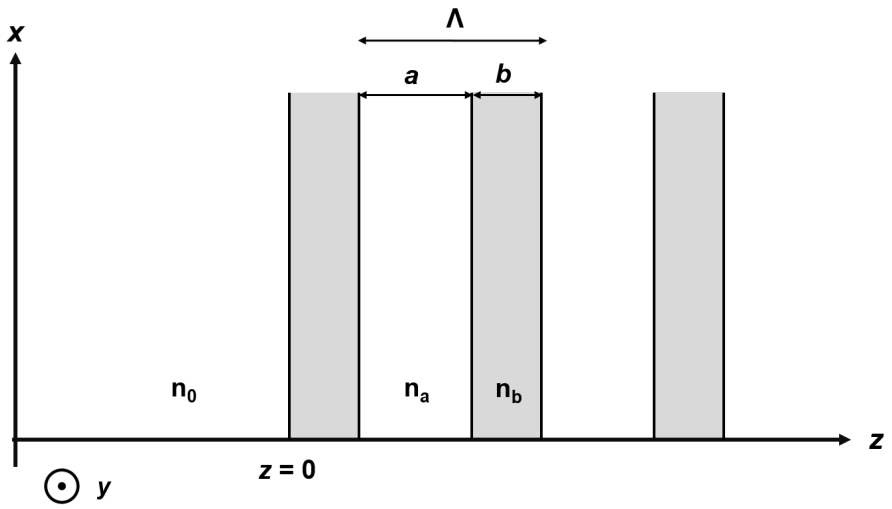

Figure 3.1: Diagram of a semi-infinite DBR.

$$E(z) = \begin{cases} Ae^{-i\kappa_z z} + Be^{i\kappa_z z} & z \leq 0 \\ E_K(z)e^{iKz} & z \geq 0 \end{cases} \tag{3.3}$$

where $\kappa_z^2 = (n_i^2(\omega/c)^2 - \beta_p^2)$ and E_K is a periodic function whose eigenfunctions (v_0 and w_0) are given by equation (2.61). The BCs for a surface state require decaying solutions, so $B = 0$ in the $z < 0$ (dielectric) region. Within the forbidden band of the DBR the Bloch wavevector will have complex values $K = m\frac{\pi}{\Lambda} + iK''$. This will produce a decaying envelope into the DBR with distance (in this instance in the positive z direction, i.e $e^{-K''z}$).

Secondly, there are the continuity conditions of the in-plane components of the electric and magnetic field (section 2.2). Matching the electric and magnetic fields across the interface results in two coupled equations

$$A = v_0 + w_0 \tag{3.4}$$

and

$$-i\kappa_0 A = -i\kappa_a(v_0 - w_0) \tag{3.5}$$

This produces a dispersion relation

$$\kappa_0 = -\kappa_a \frac{e^{-iK\Lambda} - T_{11} - T_{12}}{e^{-iK\Lambda} - T_{11} + T_{12}} \tag{3.6}$$

where values for T_{11} and T_{22} are given by equation (2.56) and $e^{-iK\Lambda}$ by equation (2.59). The conditions from equation (3.6) follow from matching an evanescent wave in the dielectric material

and a Bloch wave with an exponentially decaying envelope. In other words, it describes modes that transmit no power in either direction away from the interface (i.e. a surface mode). This occurence is very similar to the appearance of localized electronic surface states, or Tamm states, at the surface of crystalline solids. Optical analogues of these were proposed by Kossel in 1966 [56] and experimentally demonstrated for DBRs in 1978 [57] but are more commonly called Bloch surface waves (BSWs), particularly when the interface is between a photonic crystal and a homogenous dielectric [58][2].

The decay in the DBR follows from having an imaginary Bloch wavevector, which follows from being within the photonic stopband. In the dielectric material a decaying solution is imposed from the BCs but the physical cause is that the tangential wavevector in the positive ϵ and μ material produced when equation (3.6) is satisfied is greater than the light line ($\beta_p^2 > \kappa_0^2 \epsilon$). Hence, as with surface plasmons, the condition for total internal reflection is produced. Because BSWs have dispersions outside the light line they also, like SPPs, require coupling techniques such as prisms [59] or gratings [60] to excite.

Unlike SPPs however, they occur for both TE and TM polarization. For a TM-polarized SPPs the electric permittivity is required to change sign across the interface to match the tangential magnetic (H_y) and electric ($E_x = \frac{1}{\epsilon}\frac{\partial H_y}{\partial z}$) field components (since the BCs require the derivates must also switch signs in the positive and negative z regions). For TE-polarized light magnetic permeability must switch signs. The oscillating solution, within a decaying envelope, of Bloch waves have the effect that the derivative may be positive at isolated points within a unit cell of the DBR, while still decaying on the order of multiple periods (i.e. the envelope function has a negative derivative) [61]. Hence, it is possible to meet both the BC and matching (interface) conditions for a surface state without requiring a change in sign of permittivity or magnetic permeability across the interface. In this sense a DBR can perform the role of an effective NP or NMP material [38, 62]. Hence BSWs can be both TM and TE polarized. The particular eigenfrequency of a BSW occurs when these isolated points at the interface of the DBR match the decaying evanescent wave. It should be noted that the materials in the stopband frequencies of the DBR are still all purely dielectric ($\epsilon, \mu > 0$); the decay results purely from the coherent effects of scattering and interference from its periodic structure.

3.1.2 Impedance matching

The eigenfrequency of the BSW is described by equation (3.6), which matches the two decaying fields in the DBR and dielectric for when the DBR terminates with a full unit cell. The frequency can be altered by terminating the DBR with a fraction of a unit cell, which changes the field and its derivative occurring at the position of the interface that must be matched. This has the benefit of not only giving some control of the BSW wavelength (within the range of the stopband) but by positioning it close to the stopband center the quality of the mode is improved [63]. This adds

[2]For now, I will refer to these as BSWs. More details on the naming conventions can be found in section (3.3)

an extra factor for calculating the eigenfrequency of the BSW. Fortunately, there is a simpler technique to find these, and which can be used for a variety of structures at DBR interfaces; impedance matching.

The surface impedance ζ is the ratio of the tangential electric and magnetic field ($\zeta = E_t/H_t$). A full description of impedance is beyond the scope of this thesis; what is important is that the existence of a surface state is related to the impedances by a simple equation [64–66]

$$\zeta_L + \zeta_R = 0 \tag{3.7}$$

where ζ_L and ζ_R are the surface impedances of the left ($z < 0$) and right (z > 0) regions respectively. In this way the problem of matching the fields can be split into matching two impedances, even if each semi-infinite region contains complex multilayered structures.

Within the stopband only evanescent Bloch waves exist, so (assuming lossless material) their impedances are purely imaginary. In homogenous material the ratio E_t/H_t generally have a fixed value but in Bloch waves the surface impedance varies periodically from $\pm i\infty$ within each unit cell (the zero or infinite impedances occur at the nodes of the electric or magnetic field within the Bloch wave's amplitude function) [61]. During TIR the impedance in a positive permittivity and permeability material is also purely imaginary. Hence, there is always some frequency within the stopband where a Bloch wave will match to this and produce a BSW. The value of ζ_R occurring at the surface depends on the choice of termination of the unit cell, so the frequency of the BSW can be swept from one edge of the stopband to the other; as more material is added or removed to the final layer the frequency is lowered or raised respectively, which can be intuitively understood when it is recalled (section 2.4.2) that adding high permittivity material is analogous to lowing the potential energy [58, 67]. Because the choice and thickness of the final layer is so important, it is called the **spacer** layer.

3.1.3 Reflection from a DBR

These impedances can be written in terms of the (amplitude) reflection coefficients r_L and r_R

$$\zeta_L = \frac{1+r_L}{1-r_l}\zeta_0 \tag{3.8a}$$

$$\zeta_R = \frac{1+r_R}{1-r_R}\zeta_0 \tag{3.8b}$$

where ζ_0 is the impedance of vacuum ($= \sqrt{\frac{\varepsilon_0}{\mu_0}}$). The condition described in equation (3.7) becomes

$$r_L r_R = 1 \tag{3.9}$$

or, if the coefficients are expressed in complex form $r_j = |r_j|e^{i\phi_j}$ where ϕ_j is the reflection phase shift, then as $\phi_L + \phi_R = 2\pi m$, where $m = 0, 1, 2, \ldots$ Given a sufficient number of DBR layers, an analytical expression for the reflection coefficient can be derived from the transfer matrix method [48]

$$r_{n_a > n_b} = -e^{i\left(\pi \frac{n_a}{n_a - n_b} \frac{(\omega - \omega_0)}{\omega}\right)} \tag{3.10a}$$

$$r_{n_b > n_a} = e^{i\left(\pi \frac{n_b}{n_b - n_a} \frac{(\omega - \omega_0)}{\omega}\right)} \tag{3.10b}$$

where n_a is the refractive index of the spacer layer and ω_0 is the frequency of the stopband center. As before, the choice of termination of the final DBR pair causes ϕ_R to shift, which is shown for an 8x ($\lambda/4$) pair DBR (n_1 = 3, n_2 = 1.5, d_1 = 75 nm, d_2 = 150 nm) in figure (3.2). When the DBR terminates with a full layer, as in cases (A) and (C) in the figure (black and green lines) the reflection phase shift within the stopband varies between $-\pi$ to π. Reversing the order of the layers result in a π phase change between them, though in both cases the sign of the phase shift switches around the Bragg frequency ω_0 at 900 nm due to the change in sign of $(\omega - \omega_0)$.

However, the phase shift can be varied if the spacer layer deviates from the ($\lambda/4$) condition due to the changes in the electric field distribution that occur at the surface; in cases where the DBR terminates with exactly a half-thickness spacer layer the reflection phase shift at the stopband edges are either zero or $|\pi|$, with the spacer being the higher or lower of the two refractive indices determing which edge this occurs at. In cases (B) and (D) the reflection phase changes from π to zero and from zero to $-\pi$ respectively (red and blue lines). It can be seen that the, for example, zero phase shift condition occurs at the top edge in (B) and at the bottom edge in (D), since the shift in the electric field distibution between these two frequencies is exactly one DBR period [68], the same as the shift in position of the surface between these two cases.

3.1.4 Characteristics of BSWs

Initially BSWs were considered an unwanted phenomenon to be overcome; the aim being for the photonic crystals to be as reflective as possible and the resonance of BSWs (when coupled to radiating modes) an unwanted pathway for loss in photonic crystal stopbands [58]. However, since the 1990s there has been great interest in using BSWs as a less lossy, dielectric alternatives to surface plasmons, particularly for sensing applications [69–78]. Surface states (by definition) decay evanescently in both directions normal to an interface these modes result in strong vertical field confinement and therefore strong light-matter interactions. However, because of the high absorption losses of metals, SPP-based sensors suffer from very low quality factors, which limits the sensitivity of the device. Metals such as silver, gold and aluminium are used because they have negative real parts of their permittivities and relatively small imaginary parts (their extinction coefficient), meaning sharper resonances, yet these are prone to tarnishing (e.g. silver) or have

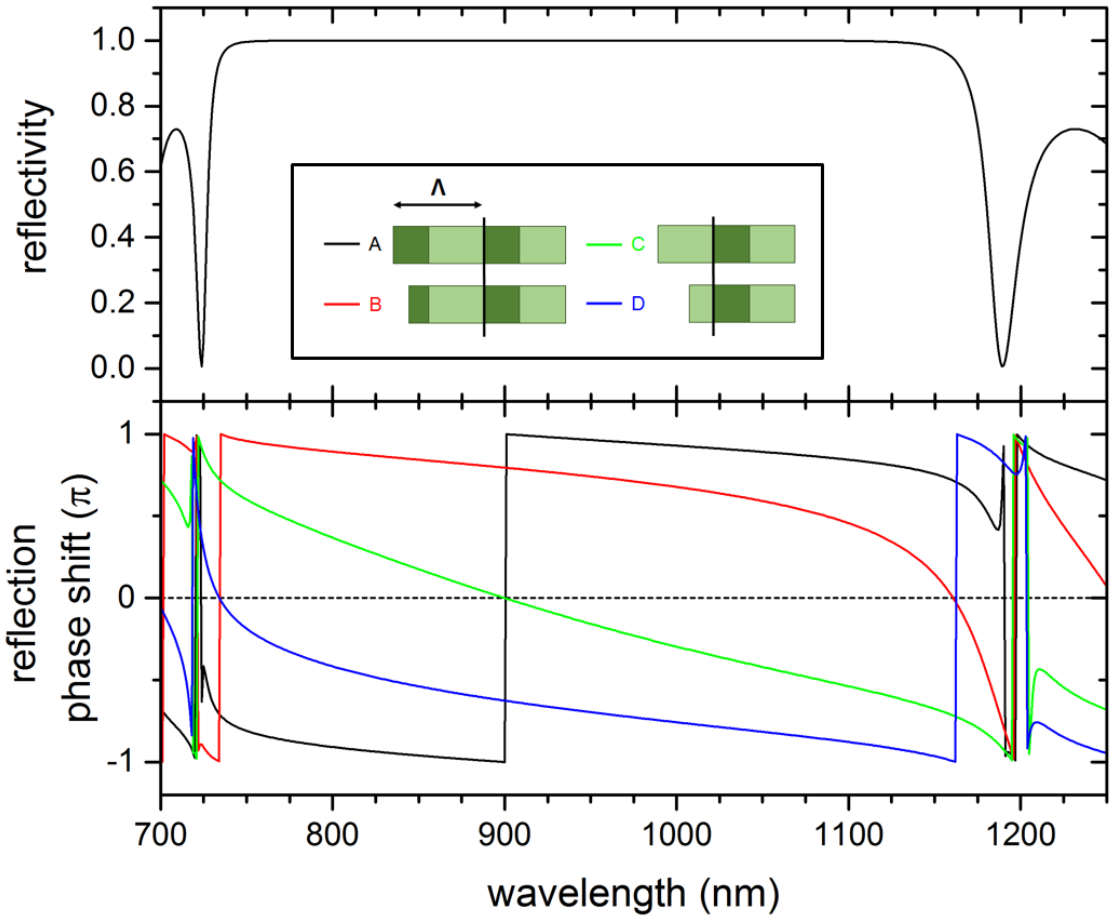

Figure 3.2: (a) The reflection spectrum of a DBR at normal incidence (case A). **Inset**: diagram of different terminations of the DBR surface, from ending on a complete unit cell (A), with $\frac{d_1}{2}$ (B), on the n_2 material (C) and with $\frac{d_2}{2}$ (D). (b); The reflection phase shift as a function of wavelength for various terminations of the DBR (A-D). Light is incident normal to the DBR from an $n = 1$ layer.

permittivities that have optimal values only above certain wavelengths (e.g. gold has interband transitions that make it too lossy for wavelengths below 600 nm).

Robertson et al. first demonstrated BSWs at the surface of a DBR (using a Kretschmann configuration) and their potential as a replacement for metal films in sensors [59, 69]. In contrast to metals, which combine negative real permittivity and (relatively) low imaginary permittivity only within a fixed spectral range, a photonic crystal stopband can be tuned to virtually any wavelength by the choice of refractive index and layer thickness of the DBR, from blue light to THz regimes [79]. The BSW dispersion, which occurs within this stopband, can be tuned to the desired wavelength accordingly. Unlike SPPs, they can be excited with both TM and TE polarizations. BSWs are highly sensitive to changes at the terminating surface layer so make effective sensors for characterizing thin films [70]. For example, adding a layer containing a target substance onto

the surface of the DBR changes the surface impedance of the whole structure, so the wavelength and emission angle of the BSW resonance will shift from its position relative to without the deposited material. The shift in the resonance dip (e.g. under reflectivity measurements) can be used to analyse the substance. This can also be used to measure changes in the index of the dielectric medium. In a direct comparison between SPP and BSW-based biochips [71] the latter was shown to outperform the former (commercial) sensors, and that the limiting factor is the interfacial roughness of the DBR.

Because BSWs contain only dielectric material their possible field enhancement is not limited but high metal losses, which leads to higher possible quality factors and narrower resonances (as seen in reflectivity or emission measurements). The field intensities can be an order of magnitude greater than for a metal surfaces [72]. Additionally, in contrast to SPPs the position of the maximum field confinement does not occur precisely at the metal-dielectric interface but extends into the top DBR layer, which reduces losses from surface roughness. This combination of field confinement with lower losses make them suitable for increasing emission from fluorophores positioned in this field, similar to SPCE (section 2.3.3). As before, the benefit of this light-matter coupling is twofold; (a) there is the enhancement of the emitter's spontaneous emission rate (Purcell effect) and (b) there is a directional enhancement imposed by the angular resonances of the BSW, which allow emission to be collected more effectively [73, 74]. This can in cases be further enhanced by adding a diffraction grating positioned close to the localized field [60, 75]. Other applications that require strong light-matter interactions, such as Raman scattering, also benefit [80].

3.2 Tamm states

3.2.1 DBR heterostructures

In the above states were considered at the interface between a DBR and dielectric with $\epsilon > 0$ and $\mu > 0$. It is also possible to excite surface modes at the interface between a DBR and a NP or NMP material. An obvious example is to replace the dielectric with another, different DBR. If their photonic stopbands overlap then surface states exist consisting of two decaying Bloch waves (the exact frequency can be found by matching the impedances of the two half-structures) [64, 68, 81]. From the impedance matching equation, we derived the equation for a state at an interface (3.9)[3]

$$r_{PhC1} r_{PhC2} = 1 \tag{3.11}$$

which occurs when

$$\phi_{PhC1} + \phi_{PhC2} = 0 \tag{3.12}$$

[3] see also appendix (A.3)

when r_{PhC1} and ϕ_{PhC1} are the reflection coefficient and phase shift of the left-hand DBR for light incident from the right (and vice versa for PhC2). If both DBRs terminated with layers of the same type (e.g. both lower refractive index material) it can be seen from figure (3.2) that this condition is impossible to satisfy and no state can form. If DBRs with sequence (B) and (D) are brought together to form an interface, it is possible to satisfy $\phi_{PhC1} + \phi_{PhC2} = 0$ within the bandgap of both DBRs and a surface state is formed. This is shown in figure (3.3) for λ = 944.5 nm. The electric field cross-section (figure 3.4) confirms this is a surface state.

However, since there is no confinement by TIR in the NP (or effective NP) material there is also no longer any minimum tangential wavevector that must be satisfied and no requirement to be excited outside the light line. Hence, we now have surface waves that can have continuous, parabolic dispersion curves for any value of the propagation constant. This even extends to standing waves ($\beta_p = 0$) [81]. Since these are no longer limited by the light line, and in analogy with electronic Tamm states, these are called optical Tamm states (OTSs). Unlike SPPs or BSWs, they do not require a prism or diffraction grating to be excited. They can be both TE and TM polarized.

3.2.2 Tamm plasmons

Another surface state can be excited at the interface of a DBR and a metal below its plasma frequency [82–84]. Though similar to the SPP in one respect - the confinement in the metal layer is due to its negative permittivity - they are confined into the DBR by its photonic stopband (as opposed to by TIR in the SPP). Hence, they are more like the DBR-DBR heterostructures in that they have parabolic dispersion curves that are within the light line. These modes were experimentally demonstrated soon after [85, 86] and are called Tamm plasmons polaritons, or Tamm plasmons (TPs). Because the dispersion curves are within the light line they can be directly excited by light incident on the air side, with no need for prism-coupling or gratings.

Since the DBR can also act as a NMP material TPs can be excited in TE and TM polarization (note that the layer adjacent to the metal, the spacer, is still $\epsilon > 0$ and $\mu > 0$; it is only effectively negative in the stopband with respect to light propagating normal to the DBR periodicity. This combination allows the matching conditions at the interface to be met simultaneously with the decaying solutions required of a surface modes). Returning to (3.9), the condition for a Tamm plasmon becomes

$$r_M r_{PhC} = 1 \tag{3.13}$$

where r_{PhC} is the amplitude reflection coefficient of light incident on the DBR surface, which is given by equation (3.10), and $r_M = (n_a - n_M)/(n_a + n_M)$ is the amplitude reflection coefficient of the metal. Using the Drude equation (2.27), in cases below the metal plasma frequency (i.e. $\omega_p^2 \gg \omega^2$) when $n_M \approx i\frac{\omega_p}{\omega}$ [84]

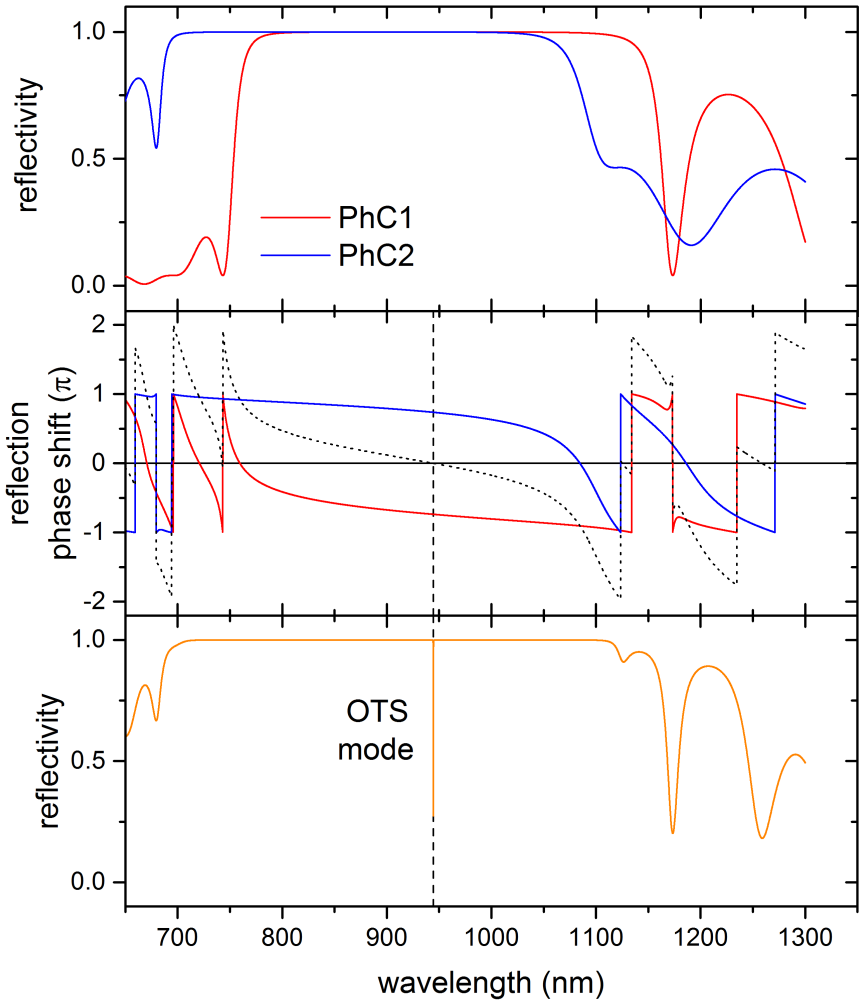

Figure 3.3: (a) The reflection spectra of the two DBRs; PhC1 (red) has n_1 = 3, n_2 = 1.5, d_1 = 100 nm, d_2 = 100 nm and PhC2 (blue) has n_1 = 3.5, n_2 = 1.5, d_1 = 84 nm, d_2 = 80 nm. Both have 8 pairs. The termination for PhC1 ends with n_2 and $\frac{d_2}{2}$, and for PhC2 with n_1 and $\frac{d_1}{2}$, which are analogous to cases (D) and (B) in figure (3.2) respectively. (b) Reflection phase shift for PhC1 and PhC2. The black dashed line is their sum. (c) Power reflectivity spectra of the combined structure. The dip in reflection shows where an optical Tamm state (OTS) occurs at 944.5 nm, where the sum of the DBR phase shifts equals zero.

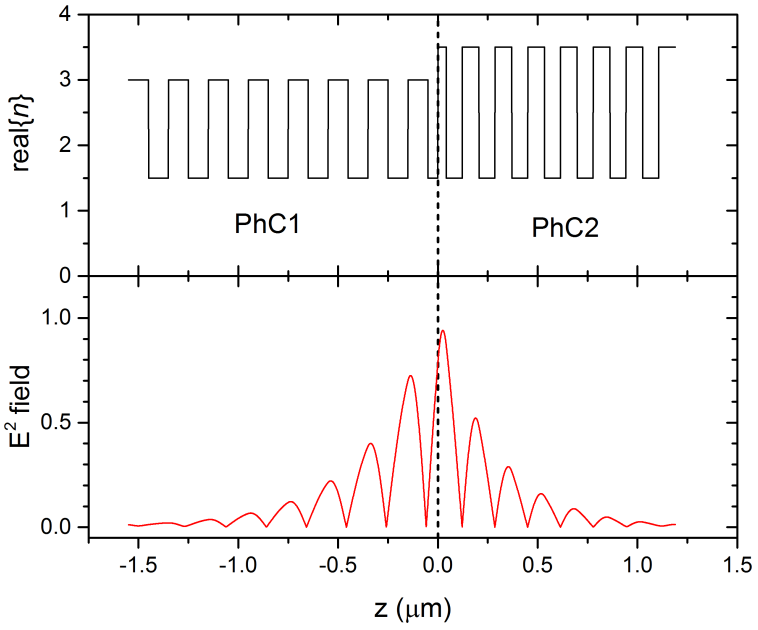

Figure 3.4: Refractive index and electric field cross-section for the DBR-DBR structure described in figure (3.3) at 944.5 nm. Calculated using TMM.

$$r_M \approx -1 - \frac{2in_a\omega}{\omega_p} \approx -e^{\frac{2in_a\omega}{\omega_p}} = e^{[i(\pi+\frac{2n_a\omega}{\omega_p}]} \tag{3.14}$$

So r_M and r_{PhC} both have near unity reflectivity (due to their negative permittivity and stopband respectively) but reflection of the metallic layer always causes a negative phase change, so $r_M = -1$. To satisfy (3.13) it is necessary to compensate by having $r_{PhC} = -1$, which is achieved when the spacer is the higher refractive index of the two DBR materials [84]. This can be restated in terms of the reflection phase; the metal reflection phase shift is around $-\pi$ and $-\pi/2$ and so the DBR's must be positive, similar to case (B) from figure (3.2). Conversely, for frequencies only slightly above the bulk plasma frequency then $r_M = +1$ and the reflectivity phase shift is close to zero, which can be achieved close to the stopband center when the spacer is of the lower refractive index material [87]. Varying the thickness of the spacer layer changes the reflection phase of the DBR, and so the frequency of the TP can be carefully controlled [86]. Changing the metal layer thickness can also be used to tune the TP resonance, though the change in phase shift, and hence wavelength, is comparatively smaller. Together, this allows great control of the mode wavelength and quality [88, 89].

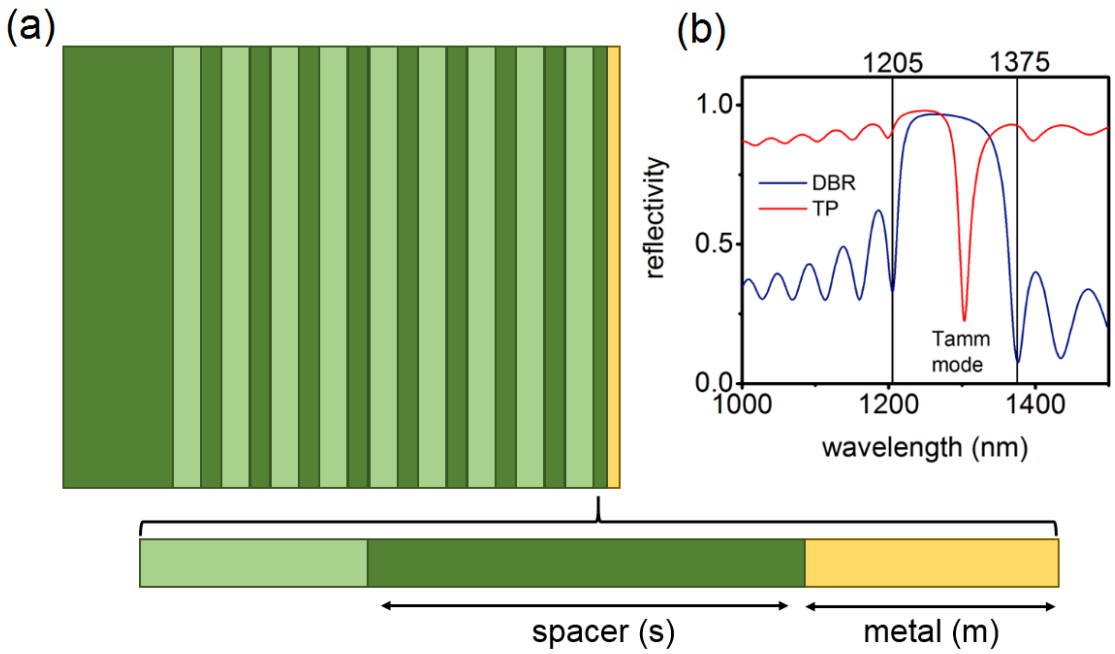

Figure 3.5: (a) Diagram of a Tamm plasmon structure. (b) Calculated reflectivity spectra at normal incidence for a 17.5x pair GaAs/AlAs DBR, GaAs spacer (s = 75 nm) and with (red line) and without (blue line) m = 25 nm gold layer. Black lines show the first minima of the DBR stopband (the stopband does not have unity reflectivity, as it did in previous figures, as actual materials with non-zero absorption have been modelled; see section (4.2.1.2)). The TP mode can be seen as a dip in reflectivity within the stopband. Calculated using TMM.

3.2.2.1 Are Tamm plasmons 'plasmons'?

If the defining features of SPPs are they are bound modes (have dispersions outside the light line) that propagate along the interface, then it is debatable how TPs fit this, since they are neither bound nor necessarily even propagating. However, the confinement in the metal region is due to its plasmonic response (which make it a NP material). A useful depiction is that Tamm states are a type of cavity mode [38, 84] and that TPs exhibit characteristics of both cavity and plasmons. The negative phase change that follows reflection from a metal layer, or from a DBR with reverse-ordering of its layers, allows the meeting of a cavity resonance condition without the need of a distinct cavity layer (see appendix (A.3)). These modes are therefore more localized than a typical microcavity, and even more so in the case of the TP because of the sharp decay into the metal layer [86].

3.2.3 Characteristics of TPs

An example TP structure is shown in figure (3.5(a)) and the calculated reflectivity at normal incidence ($\beta_p = 0$) for a 17.5x pair GaAs/AlAs (d_1 = 95 nm, d_2 = 110 nm) DBR, a 75 nm GaAs

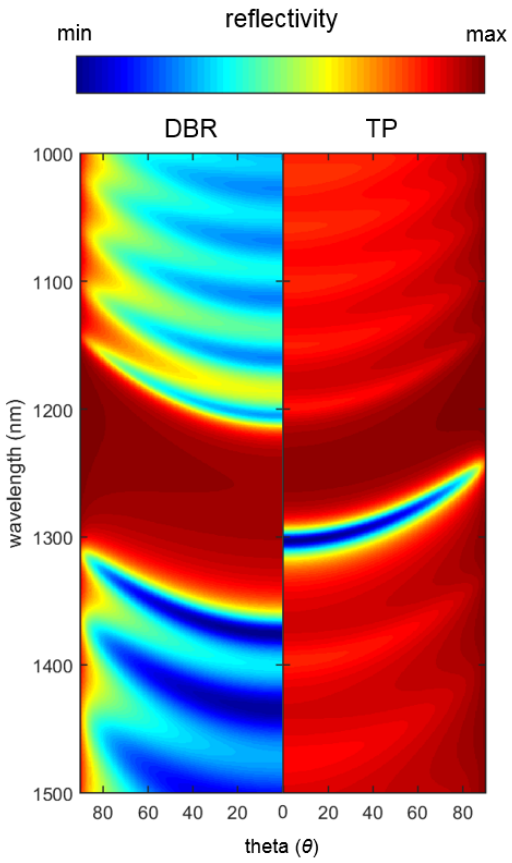

Figure 3.6: Calculated reflectivity for the DBR and TP structures described in figure (3.5) as a function of incidence angle (θ) and for TE polarization. The dispersion of the TP is parabolic. Calculated using TMM.

spacer layer and 25 nm gold layer is shown in figure (3.5(b)). When the metal is removed a photonic stopband is clearly visible between 1205 nm and 1375 nm. When the gold film is added (red line) the TP can be seen by the appearance of a dip in the reflectivity spectrum centered at λ = 1300 nm, where the light now couples into the Tamm mode. The cross-section of the electric field intensity profiles through these structures at λ = 1300 nm is shown in figure (5.3). Without the metal layer the field decays exponentially into the DBR stopband (though it does not form a BSW since at normal incidence, $\beta_p = 0$, it is within the light line and forms a radiative mode into the air region). With the metal layer, the TP is seen as the enhanced electric field that is most intense *below* the semiconductor-metal interface, i.e. within the spacer layer, and decaying evanescently in either direction. This contrasts with the SPP, where the field peaks exactly at the interface. Because the TP extends into the DBR region they have larger mode volumes yet this is offset by the greater reduction in optical loss and heating that occur in SPPs, which decrease the quality factor and largely prevent their use in optoelectronics [90]. Typical Q-factors using silver films are of an order of 10^3 [91] (with gold slightly lower), though specialized structures

have achieved Q-factors as high as 5000 [92]. The dispersion relation for the same example structures when the propagation constant ($\beta_p = \kappa sin(\theta)$) is varied are shown in figure (3.6) (for TE polarization). The resonance of the TP mode (seen as the dip in reflectivity) has the expected parabolic shape. Kaliteevski et al. [84] calculated the TP effective mass as $m^* = 1.7 \times 10^{-5} m_e$, where m_e is the electron rest mass. The energy for TE and TM modes are degenerate for $\beta_p = 0$ but split for high in-plane wavevectors since at non-zero incidence the optical path length (and hence reflection phase change) of the DBR differs for TE and TM polarization (reflection from the metal is largely unchanged).

As with the other surface states, the appeal of TPs lies in their ability to confine electromagnetic fields and enhance the light-matter interaction strength. In contrast to typical planar cavities the TP mode itself fulfils the role of the cavity layer [93]. This not only allows devices that are compact and easier to fabricate but allows the optical properties to be controlled by shaping of the metal layer without intentionally introducing defects into the active layer. This is particularly important for single-photon sources as it is necessary to achieve a high degree of control in the emission properties to maximize collection, but modifying the cavity produces lossy non-radiative modes, while etching through the cavity (such as in micropillars) introduces charge noise to the quantum dots [94]. In the case of the TP, first only the metal layer is treated, eliminating any need to etch the active layer. Secondly, by shifting the position of maximum field coupling away from the interface it reduces the loss mechanisms the occur due to defects at the metal interface. In some cases [95], the lifetime of QDs coupled to the TP even increase compared to that of the bulk DBR (i.e. they have inhibition of their spontaneous emission rate) if positioned in a node of the 'cavity', as well as when spectrally detuned. Though non-radiative processes remain the limiting factor, the measurement of high inhibition, as well as enhancement, of emission rates show that QDs retain very high quantum efficiencies despite the presence of a metal interface.

These properties are also attractive for making lasers, since the TP can replace the cavity layer and allow control of emission direction via the metal layer [91, 96]. TPs have been proposed for enhancing non-linear effects, such as Raman scattering [97] and third-harmonic generation [98], and for use in sensors [99–101], optical absorbers [102] and switches [103]. It has been shown that depositing a metal layer onto a DBR containing an exciton layer can result in strong coupling between a TP and an exciton-polariton [104–108]. This is seen by the appearance of two characteristic anticrossing modes corresponding to the higher and lower energy polariton branches. In addition to lower losses and easier excitation setup compared to typical plasmonics, the lower polariton mode is confined under the metal layer and this can be used to realize exciton-polariton circuits by patterning the metal layer into channels [105, 106]. The metal layer can jointly function as the top contact for electrical tuning [107]. Though this describes only a specific type of hybrid-TP mode, it is the potential to change a TP's properties by limiting the metal layer that is a key attraction to this kind of structure.

3.2.3.1 Tamm plasmon-coupled emission

An emitter positioned within the electric field of the TP will display Tamm plasmon-coupled emission (TPCE), experiencing an enhanced emission rate and sharper angular distribution of emission direction compared to the unaltered isotropic emission [109–111]. This phenomena occurs close to the interface of other surface mode, for example when between homogeneous dielectric (i.e. without the DBR) and metal layer this is called SPCE (section 2.3.3). Unlike SPPs, the maximum electric field is located below the metal-dielectric interface, which allows a higher quality mode. However, it also means to get the best coupling excitation and collection is done through the metal layer. Additionally, the coupled emission from SPP and BSW type surface states all occur at greater angles to the optical axis, since it is a condition of their formation that they be above the critical angle of the adjacent dielectric (a coupling device such as a prism is needed to turn these into radiative modes). This makes the emission difficult to collect without high numerical aperture (NA) objectives. In contrast, TPCE allows excitation and emission to occur within the light line, even with $\beta_p = 0$, and without the use of a prism or grating coupler. The incident light can be S or P polarized, and directly from the air-side of the sample. TPCE angle is highly sensitive to wavelength, allowing sorting for sensing and imaging applications [110]. In terms of a SPS, this can be used to improve the brightness and collection efficiency.

3.2.4 Confined Tamm plasmons

Unlike the SPP and BSW, Tamm states can be excited within the light cone, allowing a range of experimental configurations and easier measurements. Yet compared to other Tamm states, such as DBR-DBR heterostructures, it seems strange why we should consider TPs at all; re-introducing metallic components results in loss through absorption, which lowers the quality and broadens the resonance peak. Also, while DBRs can be tuned to practically any wavelength, metals like gold and silver have a fixed operating wavelength that is not suitable for blue- or white- light applications (though this is less of a problem at telecoms wavelength).

The main attraction of TPs is that they do not need to be limited to planar structures; TP modes can be confined by limiting the spatial dimensions of the metal layer [95, 96, 112–117]. Without the metallic layer a surface mode cannot be excited within the DBR (unless coupling methods are used above the critical angle), so under normal excitation only a TP occurs, limited to the lateral extent of the metal layer. Vertical confinement remains due to the metal's negative permittivity and the DBR's stopband. In this way fully 3D confinement can be realized using simple metal patterning techniques, such as photolithography or e-beam writing, on top of the DBR. These are called confined Tamm plasmons (CTPs). A diagram of a CTP using a metal microdisc with diameter d is shown in figure (3.7(a)). Compared to micropillar cavities, CTPs are easier to fabricate and avoid etching through micrometer thick multilayers (including the active layer). 2D SPP and BSW devices have been developed but these have too short propagation lengths (because of metal absorption) or otherwise lack the favourable dispersion properties of

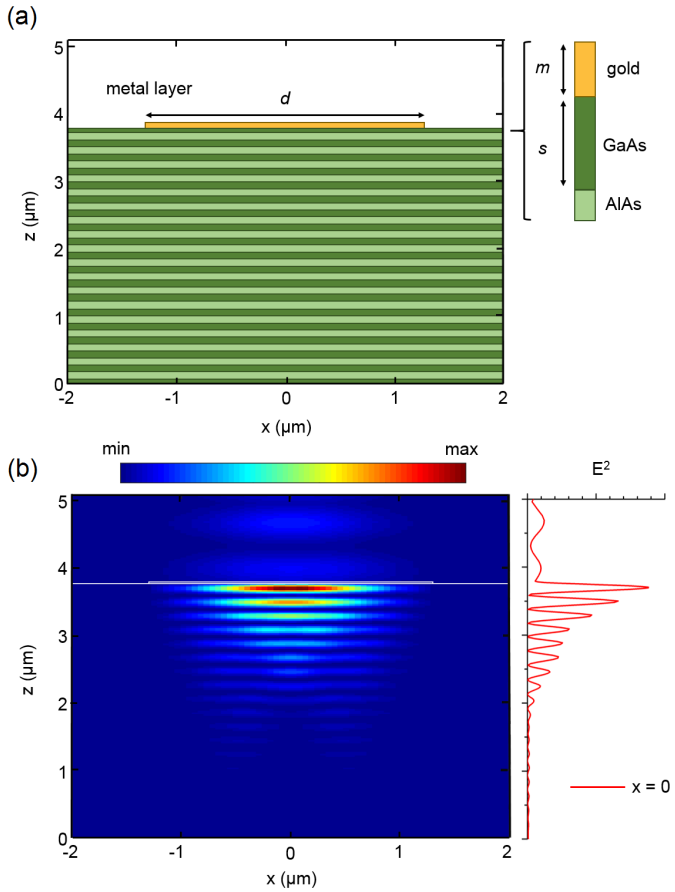

Figure 3.7: (a) Diagram of a confined Tamm plasmon structure. (b) FDTD simulation (see section 5.2) of a CTP structure consisting of 17.5x pair GaAs/AlAs DBR, d = 2.6 μm, s = 75 nm and m = 25 nm (gold), showing the absolute electric field intensity at the fundamental resonance of the CTP (λ = 1300 nm). A cross-section of the field through the center of the structure (x = 0) is shown by the red line. Like the cross-section of the TMM (1D) results, the field peaks within the spacer layer and extends mostly into the DBR region.

Tamm states [118]. Confined modes at the surface of 3D photonic crystals have been demonstrated [119] but these crystals are fragile, and difficult to design and fabricate.

CTPs were first experimentally demonstrated in 2011 [95]. For microdisc structures the mode energies are found to be well-described by those used for micropillar cavities. The electric field profile under the disc is made from a basis consisting of the product of cylindrically symmetrical modes and a radial wavevector [96]. As the disc diameter is reduced and confinement increases these become increasingly blueshifted and discretized (with increasing spectral separation between modes). This is shown in figure (3.8). This 3D confinement extends to using asymmetrical metal structures to create birefringent modes; for example, [112] used metal micro-rectangles to split the CTP resonance along two orthogonal modes along the two axes of the structure. In this way, polarization control can be added.

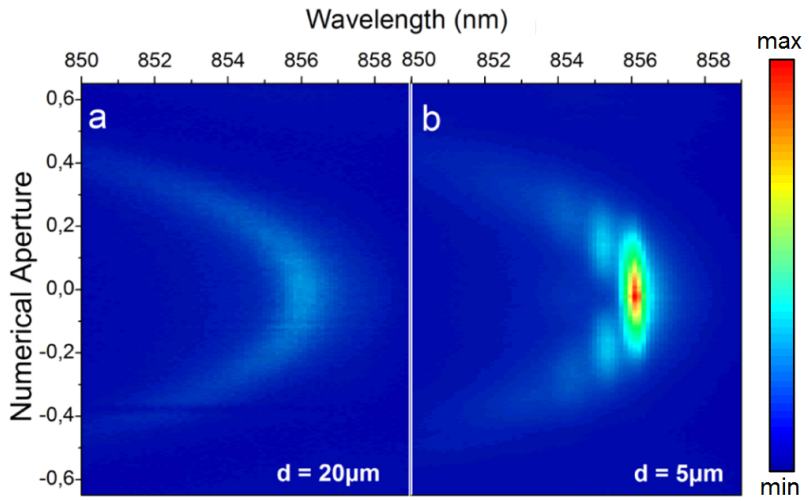

Figure 3.8: Measured emission dispersion for CTP consisting of 30x pair AlAs/AlGaAs DBR and 40 nm silver layer, for (a) d = 20 μm and (b) d = 5 μm. At large diameters the dispersion is parabolic, like that of the planar TP. As the field becomes increasingly confined these modes become discrete. Figure from [96]

The quality factor is controlled by the metal thickness and diameter. Decreasing the diameter results in a smaller mode volume and hence larger Purcell enhancement ($F_p \propto Q/V$), but this is limited by decreases in Q-factor due to metal absorption and scattering from the disc edge. QDs spectrally detuned from CTP mode in contrast experience a strong emission inhibition [95]. This combination of Purcell enhancement and strong inhibition allow potentially very high β factors (the coupling factor into the mode, described in section (1.2.1); not the propagation constant β_p). This lowers the lasing threshold, in addition to any control of the lasing direction and polarization [96, 113]. High β factors also make CTPs attractive as potential single-photon sources [114, 115], with a theoretical collection efficiency of 60% predicted for optimum structures.

3.2.5 Other Tamm states

There exist a range of modes in planar structures that exploit TP interactions; for example, with cavity polaritons [108] or in M-DBR-M waveguides [120]. Tamm plasmons have been produced where the metal has been replaced as the NP material with an excitonic dye-doped layer [121], left-handed metamaterial [122] or graphene [123, 124].

Though we have considered DBRs consisting of two kinds of dielectric material it is possible to encounter DBRs that contain other materials that also support Tamm surface states, for example, alternating pairs of metal and dielectric layers. Provided the separation between adjacent layers if sufficient to prevent SPP coupling (i.e. greater than an effective wavelength), metal-dielectric DBRs form Tamm states that follow those of previous described Tamm states [125]. When this is not the case these behave as metamaterials with modes with markedly different dispersion

relations and field distributions at their interface. In contrast to the parabolic dispersion curves of TPs, these have hyperbolic dispersion curves, lie outside the light line and resemble those of SPPs [126–128]. What is important is that these all differ to some degree from the Tamm plasmons described so far but are often similarly named ([128], for example, distinguishes between 'Bragg TPs' and 'metallo-dielectric TPs'). More detail on the different naming conventions for types of optical Tamm state is found in section (3.3).

3.3 Naming conventions

Research of Tamm plasmons is still relatively recent and are not covered by many standard textbooks [129], so there is some ambiguity in the terms different authors use. Electronic Tamm states are surface states that form when the translational symmetry of a periodic crystal lattice is broken, and which must have frequencies in the forbidden (to bulk waves) energy regions. Explicitly optical states in photonic crystals were suggested by Kossel [56] in 1966, and the earliest theoretical [54] and experimental work [57] on these states that occurred in the West largely settled on the term Bloch surface wave (BSW). In a physical sense this is an accurate description, since the Tamm state is after all a Bloch wave solution (one with a complex wavevector) which would otherwise be forbidden *except* at a surface.

Later research done independently by Russian authors on optical states in DBR heterostructures and DBR-metal structures use Tamm state or derivatives (e.g. Tamm plasmon), while BSW remains largely (but not exclusively) used for DBR-dielectric structures. Though there are important differences between these (for example, BSWs cannot be excited within the light cone due to the need for TIR in the dielectric layer), both result from finding solutions that match the fields in the capping medium with decaying Bloch waves that occur only at the surface of, and in the stopband energies of, photonic crystals. These physical differences follow only from the choice of capping medium. This is the convention I have tried to follow through the thesis: BSW for DBR-dielectric structures and TP for DBR-metal structures. I have used Tamm state as the most general term for the entire class of modes, to emphasize their equivalence with the electronic Tamm states. They are still all arguably types of Tamm state or types of Bloch surface wave (according to the preference of the reader).

3.4 Summary

In this chapter we have considered the appearance and properties of surface states on 1D photonic crystals (DBRs). When the DBR is no longer infinite but capped by a surface then Bloch waves with imaginary Bloch wavevectors, i.e. within the photonic stopband, are no longer forbidden provided they correspond to exponentially decaying solutions. Beyond the light line surface states exist called Bloch surface waves (BSWs) that are confined by the stopband and TIR into the homogenous material. Since the in-plane component of the BSW wavevector is greater than that

of a radiative mode, they cannot be directly excited. It was shown how these can be TE and TM polarized, and how changing the spacer layer can be used to shift the resonance position. These have been proposed as lossless alternatives to SPP surface states, particularly for sensing.

Next, we considered DBRs capped with an NP (or effective NP material) so that confined states occurs with the light line. In analogy with electronic Tamm states in periodic crystal lattices, these are called Tamm states. The impedance matching method was explored and how Tamm states act like a cavity mode. Last we focused on a type of Tamm state, the Tamm plasmon, where a metal layer is used as the NP material. The attraction of this choice of material is the ability to control, confine and direct the TP mode and subsequent fluorophore emission by shaping and patterning of the metal layer.

CHAPTER 4

METHODS

In this chapter I will describe the main experimental techniques used to characterize the TPs and CTPs. Particular attention is given to Fourier microscopy, where the spatial optical Fourier transform is measured, a setup which allows angle resolved spectroscopy of the sample's optical response. I will also describe briefly the methodology of the simulations used, particularly the finite-difference time-domain used for the 3D simulations of the CTPs.

4.1 Fourier image spectroscopy (FIS)

4.1.1 Fourier microscope

Optical spectroscopy is a widely used technique to characterize photonic structures. With simple planar structures this might be limited to recording the reflection and transmission at normal incidence, for example to find the photonic bandgap of a DBR. Alternatively, to measure the DBR's dispersion relation will require angle resolved spectroscopy. One way to obtain this is to perform the measurement on the spatial Fourier transform of the sample image, which contains information of the wavevector, and hence angular, distribution of its response.

Any electric field can be represented as a superposition of plane waves with different amplitudes and propagating directions. Each plane wave (by definition) has a wavefront of constant phase perpendicular to a chosen axis (z) and described by a field $\vec{E}(x,y)$. Consider the case shown in (4.1(a)). When a plane wave passes through a lens with angle to the optical axis θ it will be focused to a point a distance from the lens along the optical axis, f, the focal length of the lens. The plane at f is called the back focal plane (BFP). Assuming the wave is monochromatic, every ray from the sample with the same spatial frequency $\kappa(\theta)$ will be focused by the lens at the same

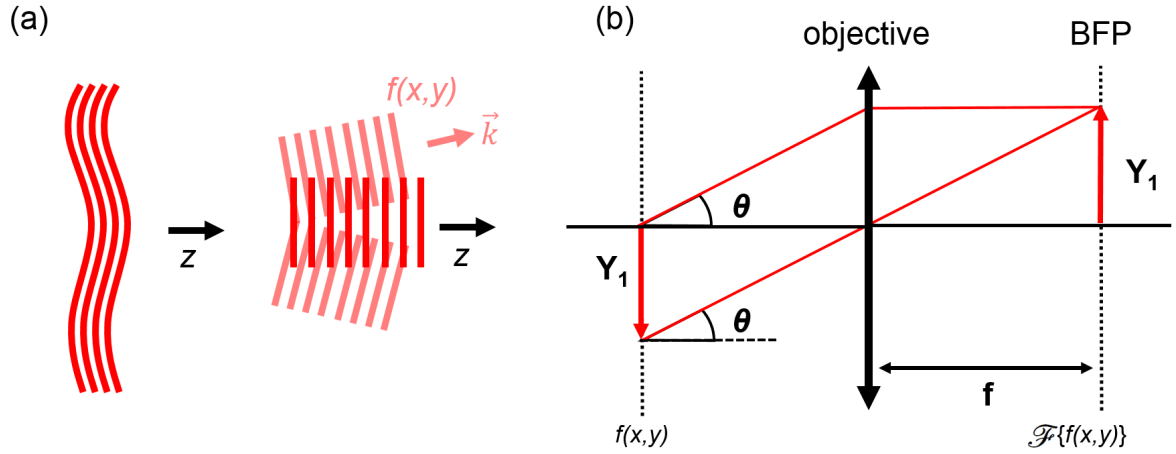

Figure 4.1: (a) Any arbitrary propagating field (i.e. assuming no effervescent fields) can be decomposed into a superposition of plane waves with different amplitudes and propagation angles. (b) Diagram of the focusing of a plane wave by a lens onto the BFP. Every wave with the same angle is focused by the objective to the same position of the BFP. This can be extended to the 2D case where $\vec{\kappa}(\theta,\phi)$.

point on the BFP, irrespective of their distance from the optical axis (figure 4.1(b)).

The entire propagating wavefront (the interference from all the individual plane waves) passing through a lens will produce an intensity pattern. Each point in turn can be tied back to a unique plane wave incident on the lens and characterized by a wavevector and amplitude. At the BFP this intensity is proportional to the spatial Fourier transform of the wavefront [129]

$$I(x,y) \propto |\hat{\vec{E}}(\kappa_x,\kappa_y)|^2 = |\mathcal{F}\{\vec{E}(x,y)\}|^2 \tag{4.1}$$

Hence, at the BFP an image is produced of the spatial Fourier transform of the object at the lens's focus. Though this can be measured directly, it is usually necessary to magnify this image with a second lens, as shown in the setup in figure (4.2), called a Fourier Microscope. Using the thin lens approximation the magnification is $M = \frac{Y_2}{Y_1} = \frac{f_2}{f_2 - S_1}$. Given that $Y_1 = f_1 tan(\theta)$ then the size of the magnified image of the optical Fourier transform is

$$Y_2 = \frac{f_1 f_2}{f_2 - S_1} tan(\theta) \tag{4.2}$$

4.1.2 Experimental setup

The Fourier microscope used is described in [130] and is based on earlier setups designed for visible wavelengths [131, 132]. The setup was built by the authors of the former paper and is not my own work.

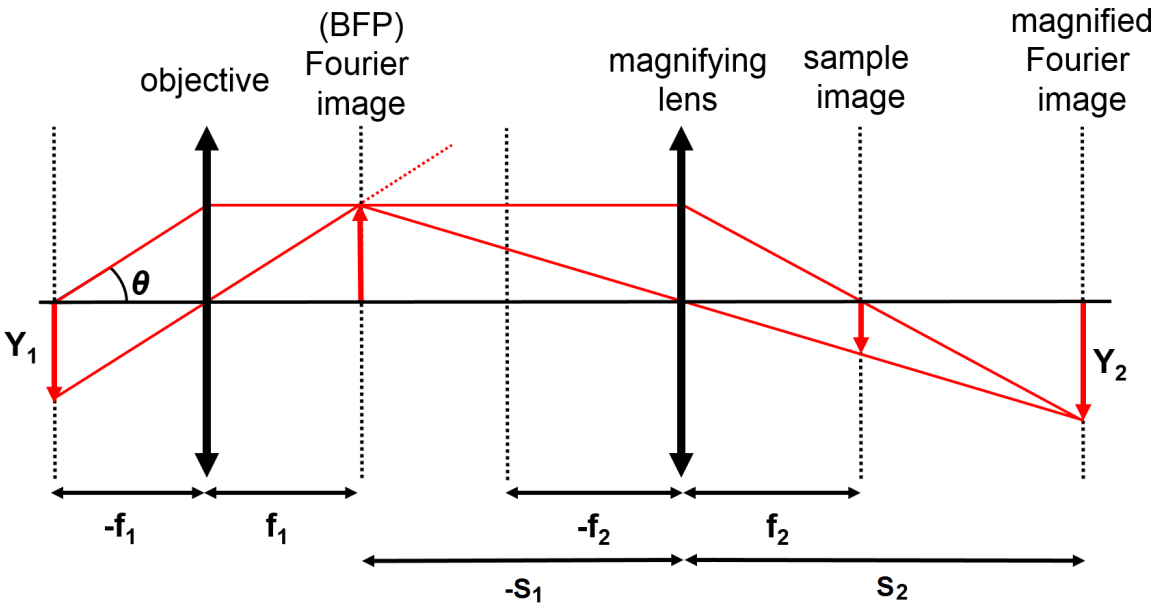

Figure 4.2: Fourier microscope setup; the first objective with focal length f_1 collects light with the same wavevector onto the same point at the BFP, which produces an image of the optical Fourier transform. The second lens, with a focus length of f_2 and located a distance S_1 away from this lens, produces a magnified image at S_2.

4.1.2.1 Illumination and Excitation

The excitation source can be switched between an unpolarized white light[1] for reflectivity measurements or a 635 nm laser[2] for photoluminescence (PL) by means of a kinematic mounted mirror. The laser source is above the bandgap for the QDs used. The experiments are almost all performed without lens L2 (which is held in a quick release magnetic mount) in what is called 'critical illumination'. The beam is collimated at the objective lens and so is focussed onto the sample over the full range of angles $0 < \theta < \theta_{NA}$ that the objective's NA allows (figure 4.3(a)). When L2 is added the beam is focussed at the objective's BFP and is collimated at the sample i.e. is always normal to the surface (figure 4.3(b)). This is called 'Kohler illumination' and is used largely when imaging the sample on the camera (since this maximizes the area of the sample being illuminated). In either case, the arrangement after the objective for the collection of the real or Fourier image is unchanged.

4.1.2.2 Collection

This collection consists of two achromatic lenses (L3 and L4). L3, located its focal length from the BFP of the objective, produces a real image of the sample at the image plane (also its focal

[1] WLSE100 300-2500 nm, Bentham Instruments
[2] HLS635, Thorlabs, 2.5 mW

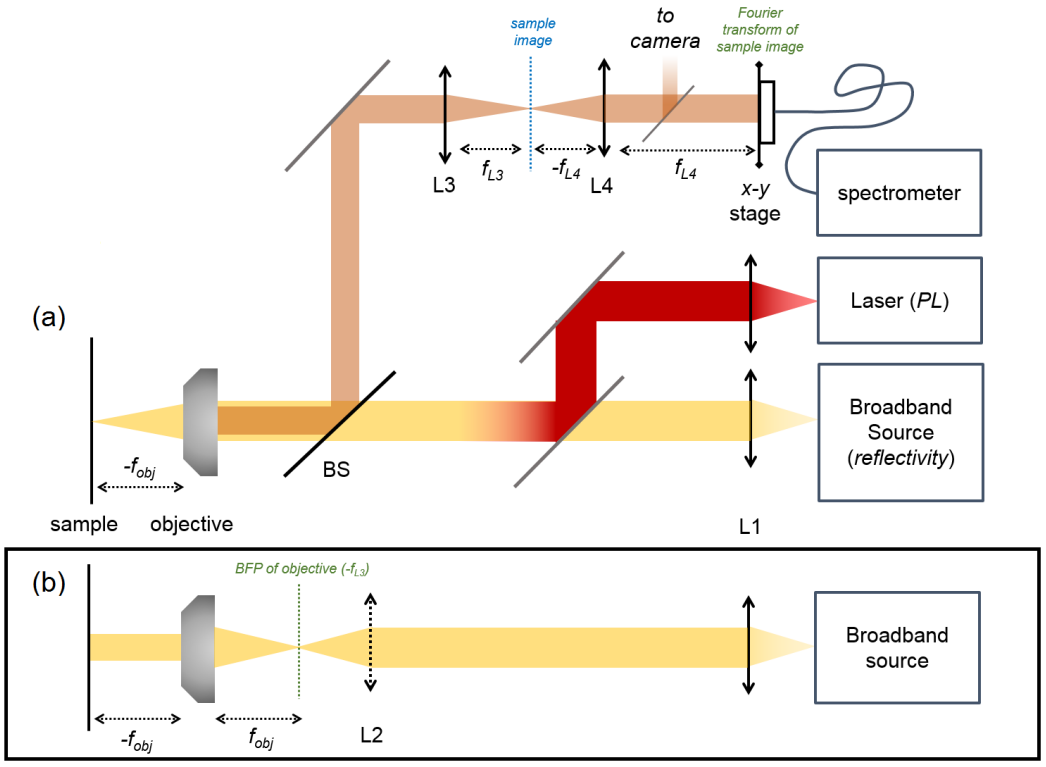

Figure 4.3: Diagram of the FIS showing the optical setup for (a) critical illumination and (b) Kohler illumination. In both, a 50% beam splitter is placed between L2 and the objective. L3 is located $f_{obj} + f_{L3}$ from the objective lens. On the camera path is a tube lens (not shown), positioned at its focal length's distance from the Fourier image plane and from a CCD camera, so a magnification of the real image of the sample is obtained at the camera.

length away in the opposite direction) shown by the blue dashed line in figure (4.3(a)), which is converted back into a Fourier image by L4.

Note that this arrangement is not identical to that seen in figure (4.2). The lenses L3 and L4 replicates the pattern at $-f_{L3}$ at $+f_{L4}$ (though it is not a strict requirement, in this setup $f_{L3} = f_{L4}$, which is called a $4f$ system). In this case the image being relayed is that of the BFP of the objective lens; L3 produces a transformed (i.e. real) image at $+f_{L3} = -f_{L4}$ and L4 then produces a Fourier image at $+f_{L4}$ (the BFP of L4), where the detector is positioned. Hence, at the detection plane an intensity pattern is formed which is the spatial Fourier transform of the sample.

To take spectra of the reflectivity or emission an optical multimode fiber is mounted at the detection plane on a motorized x-y stage[3] and connected to an 900-1700 nm InGaAs based spectrometer[4]. The motorized stage is programmed to raster scan across the BFP automatically

[3] Z812, Thorlabs
[4] NIRQuest512, Ocean Optics

and collect a spectrum at each position in the plane (normally along a fixed y axis). Since each point in the BFP (x,y) collects all waves leaving the sample with the same angle (θ,ϕ), the full scan allows us to examine the angular response of the reflection/PL. This arrangement is described as a Fourier image spectroscope (FIS). By converting these positions first to angle and then to κ-space, it is possible to directly measure the dispersion relation of the Tamm plasmon (the calibration from x position to angle is described in the next section). For PL the laser line is eliminated by placing an 850 nm longpass filter[5] between L4 and the detection plane. In theory, polarization resolution can also be added by adding a half-wave plate and linear polarizer.

The highest incidence ray that is collected by the objective is given by its NA (= $nsin(\theta_{NA})$). A higher NA will give a greater range of angles at the Fourier plane, but this also means the spatial separation between different angles will be reduced. This can be compensated for with a sufficiently high grating density of the spectrometer. Other limitations to the setup are the collection fiber into the spectrometer and the step size of the stepper motor. The fiber integrates all the light within a solid angle given by its core diameter. The minimum distance between adjacent steps that can be usefully resolved is when the overlap between the solid angles at each step position is less than half, so for the 200 μm diameter core fiber used in our measurements the step size is set to 100 μm (this is equivalent to $\delta\theta = 1.2°$). Reducing the diameter creates a better angular resolution but also reduces the counts collected, increasing the ratio of noise to signal.

Lastly, a kinematic mounted mirror can be inserted between L4 and the detection plane. This path contains another lens (L5) its focal distance away from L4's BFP (i.e. a distance $f_{L4} + f_{L5}$ from L4), which recreates (at $+f_{L5}$) the magnified real image that occurs at the sample image plane, where it is captured by a Thorlabs CCD camera. The overall response of this setup is now that of a traditional imaging microscope.

4.1.3 Characterizing the Fourier image output

The Fourier microscope setup can be used to perform emission (e.g. PL) and reflectance measurements (it can also be used for transmission, though none were taken for this thesis). The simplest case to consider is that of an isotropic point source. Since such a source emits over all wavevectors equally, the optical Fourier transform seen at the BFP is a homogeneous intensity. However, there is a limit of angles a lens will collect, so the actual image will be a circle with radius, Y_{max}, given by the maximum angle collected by the objective θ_{NA}.

$$Y_{max} = f_1 tan(\theta_{NA}) \tag{4.3}$$

When measuring reflectivity it is necessary to also consider the angular distribution of the excitation source. Suppose a monochromatic and collimated beam is incident upon the objective

[5] FGL850M, Thorlabs

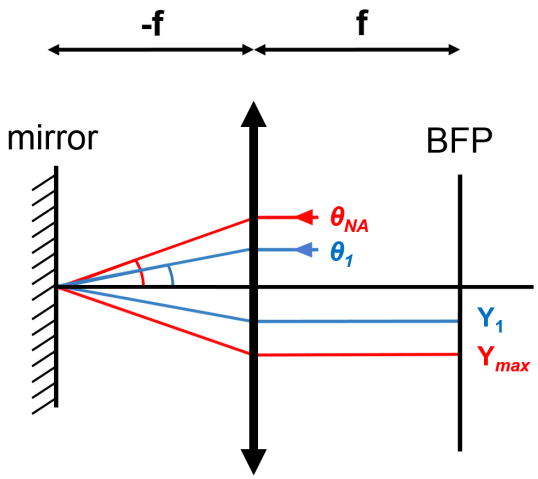

Figure 4.4: Diagram of the collected image at the BFP for a mirror sample. The two different rays with angle θ_1 and θ_2 are collected a distance Y_1 and Y_2 from the optical axis.

lens, so the beam is focussed onto the sample with all incident angles between $0 < \theta < \theta_{NA}$ occurring i.e. critical illumination (figure 4.4). If the sample is a perfect mirror then the incident beams are reflected with an identical output angle, with each angle hitting the BFP at a given radius from the optical axis. The Fourier image is again a homogenous circle with a maximum radius given by the NA. The limiting factor in both cases is the NA of the objective, so as high an NA should be used.

Now suppose the mirror is replaced with a linear grating, with structuration along the y axis and grating period Λ (figure 4.5). Gratings, which have a well-known angular response, are used to calibrate the angular response of the system since the relation of Y and θ is not always linear and depends on the setup used. Light scatters from a grating according to the relation

$$\vec{\kappa}_{||out} - \vec{\kappa}_{||in} = \kappa_0(sin(\theta_m) - sin(\theta_i)) = m\vec{G} \tag{4.4}$$

where $\kappa_{||}$ is the components of the wavevector parallel to the grating surface, $\vec{G}$ is the grating's reciprocal lattice vector ($|\vec{G}| = \frac{2\pi}{\Lambda}$) and m is an integer that specifies the order of the diffraction. The case where $\theta_m = \theta_i$, i.e. normal reflection, corresponds to $m = 0$ and is called the zeroth-order response. An optical Fourier transform consisting only of this is the same as the mirror - an uniform intensity distribution (4.6(a)). The appearance of higher grating orders occur for incident angles greater than θ_{Bragg}, which is defined as the limit that produces a grazing angle ($\theta_m = 90°$). This can be found using equation (4.4) (for the first diffraction order):

$$\theta_{Bragg} = arcsin\left(1 - m\frac{\lambda|\vec{G}|}{2\pi}\right) = arcsin(1 - \frac{\lambda}{\Lambda}) \tag{4.5}$$

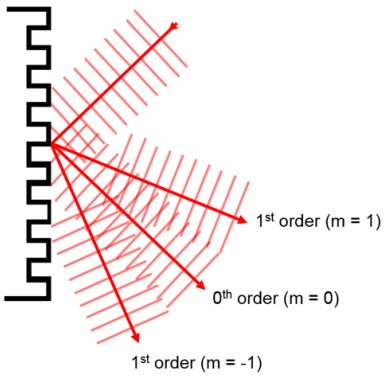

Figure 4.5: Diagram of the zeroth and first order diffraction from a periodic grating.

If the angle satisfies the first diffraction condition ($\theta_i > \theta_{Bragg}$) the reflected intensity will consist of the zeroth and first order response. However, it is easy to imagine cases where Λ is so small that $\theta_{m=1} > \theta_{NA}$ and is not collected by the objective. The intensity is still distributed between a zeroth response (which occurs for all incident angles between $0° < \theta_i < \theta_{NA}$), and an uncollected first order response, so there will be a drop in intensity measured at the BFP. To collect the higher orders it is necessary for $\theta_m < \theta_{NA}$. For a first order diffraction to be collected in the limit $\theta_m = \theta_{NA}$ requires an input angle

$$\theta_{y2} = arcsin\left(\frac{NA}{n_a} - \frac{\lambda}{\Lambda}\right) \tag{4.6}$$

where n_a is the refractive index between the objective and the grating (in this case, air). The first order diffraction from a ray with this input angle will hit the BFP at Y_{max}. Conversely, the first diffraction order for an incoming ray at θ_{NA} has a $\theta_{m=1} = \theta_{y2}$, which will be the first diffracted ray to re-enter the objective (since no higher incident angles are possible for that objective). These are shown by the blue solid and dashed lines respectively in figure (4.6(b)).

This is shown experimentally in figure (4.7), which shows the reflection spectra for a range of x positions of a Λ = 1000 nm grating. Two dark bands of low reflectivity appear that correspond to the first diffraction order. The internal edge shows the onset of diffraction where $\theta_i = \theta_{Bragg}$, which corresponds to Y_B in figure (4.6). As this produces a diffracted ray with grazing angle greater than the NA of the objective there is a drop in intensity by about 50%, since only the zeroth orders are collected. The external edge shows where the first diffraction order re-enters the objective, which is limited by the maximum input angle $\theta_i = \theta_{NA}$. This corresponds to Y_{y2} in (4.6).

By taking the x-positions for the onset of diffraction at different wavelengths, a set of angles can be constructed (since the grating period and NA of the objective are known) and fitted to

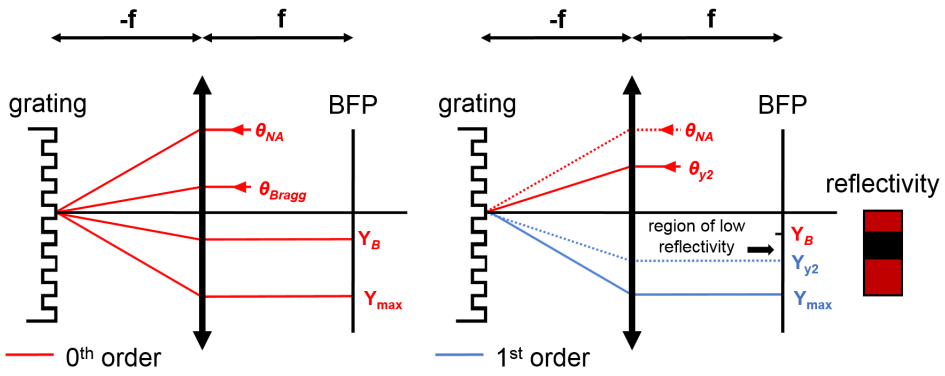

Figure 4.6: Diagram of the collected emission for a grating sample. The ray incident at angle θ_{NA} has a zeroth order response ($\theta_{m=0} = \theta_{NA}$) that hits the BFP at the edge Y_{max}, and a first order response that hits the BFP at Y_{y2}. Conversely, a ray incident at θ_{y2} (i.e. its zeroth order would hit at Y_{y2}) will have a first order diffraction at Y_{max}.

make a calibration function for x position in the Fourier plane. This is shown by the horizontal lines in (4.7), which show the reflectivity profile at fixed wavelengths. Figure (4.8(a)) shows the angular calibration by taking the x position where the first diffraction order occurs at different wavelengths, calculating the corresponding Bragg angle, and fitting to a third-order polynomial function. The reflectance as a function of wavelength and angle after calibration has been applied is shown in figure (4.8(b)). A very good agreement can be seen between the measured bands and the theoretical angular dispersion showing onset (solid line) and re-entry (dashed line) of the first diffraction order.

4.2 Simulation methods

4.2.1 Transfer Matrix Method

TMM is used to calculate the propagation of electromagnetic fields through planar multilayer structures. The method creates a series of 2x2 matrices for each layer and interface and multiplies them in sequence to produce a final transmission matrix that describes the reflection and transmission coefficients for the whole structure. This is described in section (2.4.1). It is assumed that each layer is isotropic and homogenous, and that the interfaces are all parallel and optically flat.

An additional feature not described in (2.4.1) is calculating the electric field profile through the structure. This allows the position of the nodes and antinodes to be seen. To do this, two sub-structures are defined around a single layer $j = k$. The total transfer matrix can be written

(4.7) $$T = T'_k L_k T''_k$$

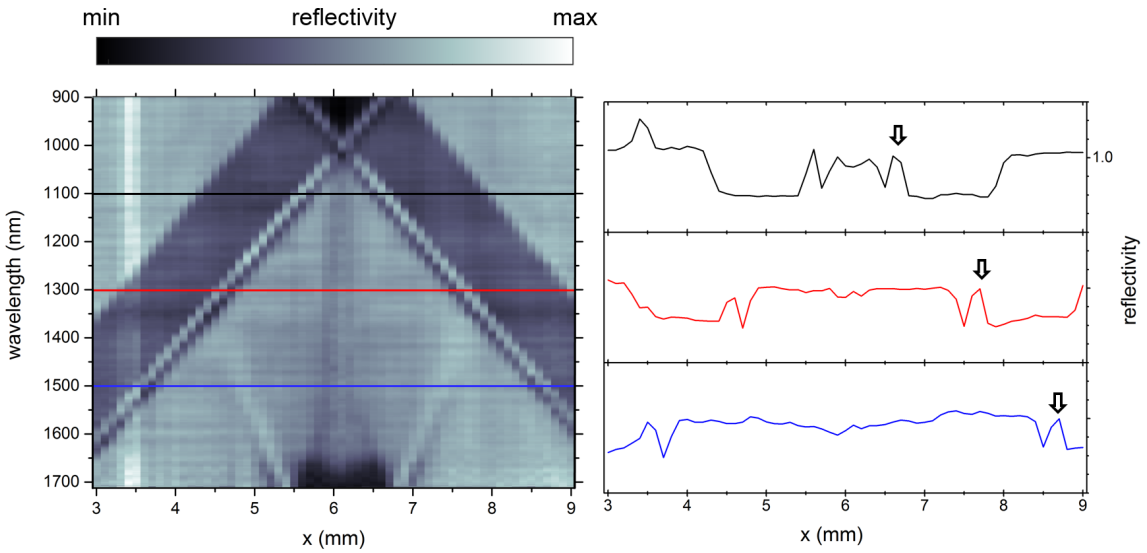

Figure 4.7: Reflectivity spectra of a Λ = 1000 nm grating as a function of x position for an NA = 0.75 objective. Reflectance profiles for single wavelengths (λ = 1100 nm, 1300 nm, 1500 nm) are shown by the black, red and blue lines respectively. The onset of diffraction, corresponding to the Bragg angle, is shown by the black arrows (this corresponds to Y_B in figure (4.6)). These can be used to calibrate the grating for different wavelengths.

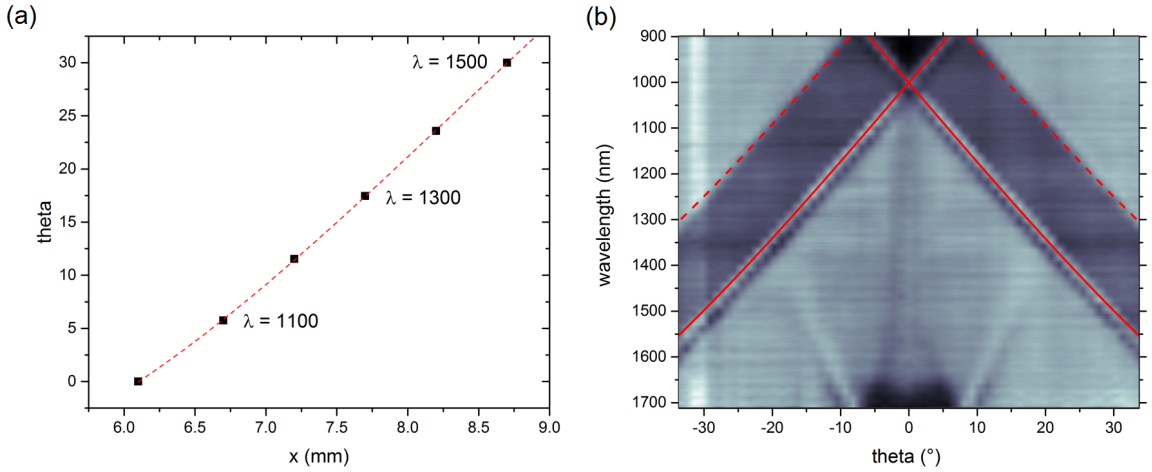

Figure 4.8: (a) Plot of $\theta(x)$ calibration using the measured onset of diffraction at different wavelengths (b) Plot of reflectance as a function of angle for a Λ = 1000 nm grating. The solid line shows the calculated angle for onset of diffraction ($arcsin(1-\frac{\lambda}{\Lambda})$), and the dashed line where the same order re-enters the objective ($arcsin(NA-\frac{\lambda}{\Lambda})$).

where T' and T'' are the 'partial' transfer matrices from layers 1 to $(k-1)$ and layers $k+1$ to m respectively

$$\vec{E}_0 = T'_k \vec{E}_k = \left(\prod_{j=2}^{k-1} I_{(j-1),j} L_j \right) I_{(k-1),k} \vec{E}_k \tag{4.8a}$$

$$\vec{E}_k = T''_k \vec{E}_m = \left(\prod_{j=k+1}^{m-1} I_{(j-1),j} L_j \right) I_{(m-1),m} \vec{E}_m \tag{4.8b}$$

Using these matrices an internal transfer coefficient (t_k^+), linking the forward incident plane wave at the interface $[(k-1),k]$, can be derived [133]. A similar coefficient is derived for a reverse propagating wave (t_k^-) for $[k,(k+1)]$. The electric field (in layer k) can then be calculated

$$E_k(z) = \begin{bmatrix} t_k^+ e^{i\xi_k z} \\ t_j^- e^{-i\xi_k z} \end{bmatrix} E_0^+ \tag{4.9}$$

where $\xi_k = n_k(\omega/c)q_k$ is the wavevector normal to the interface. This can be written out in terms of the partial transfer matrix elements

$$E_k(z) = \frac{T''_{k11} \cdot e^{-i\zeta_k(s_k - z)} + T''_{k21} \cdot e^{i\zeta_k(s_k - z)}}{T'_{k11} T''_{k11} \cdot e^{-i\zeta_k s_k} + T'_{k12} T''_{k21} \cdot e^{i\zeta_k s_k}} E_0^+ \tag{4.10}$$

This equation is sequentially applied to each layer (starting with $k = 2$) to describe an electric field profile through the whole structure from layers $k = 2$ to $k = m - 1$.

4.2.1.1 TMM code

I prepared a TMM code to calculate the reflection and transmission coefficients, reflection phase and internal electric field in a programme language suited for matrix solving (MATLAB, 2015a). This code is included in an appendix (B.1).

4.2.1.2 Materials

Values of the refractive indices of the materials modelled are taken from the existing literature and then an interpolation is fitted to these experimental points to make dispersion functions that cover the sampling density of wavelengths used in the TMM (B.1). These are plotted in an appendix (B.2). Our basic TP structure consists of a gallium arsenide (GaAs)/ aluminium arsenide (AlAs) DBR, a GaAs spacer with thickness s nm and a capping gold layer with thickness m nm. Though silver is a commonly used metal for plasmonics, and has a sharper plasmonic resonance than gold, gold is chosen due to its greater resistance to tarnishing.

Refractive index values of gold are taken from [134] and AlAs from [135]. For GaAs, no sole source of experimental data covered the full wavelength range used. Values for wavelengths higher than 0.83 μm are taken from [136] and for lower wavelength from [137]. The former does not include the imaginary component (the extinction coefficient, κ) so these are found by extending the values from the lower wavelength data with a fitted regression. These compared favourably to the predicted values from a single oscillator model [138]. The intrinsic losses for AlAs (also [138]) are extremely small over the wavelengths being studied ($\kappa < 0.01$) and so are neglected. These values are taken at room temperature.

4.2.2 Finite-difference time-domain simulations

To simulate fully 3D structures where lateral confinement is included (such as a CTP) it is necessary to use the finite-difference time-domain (FDTD) method [139]. FDTD is a widely used numerical method for solving Maxwell's equations which, when written in terms of their orthogonal field components, produce six coupled partial differential equations relating the electric ($\vec{E}$) and magnetic ($\vec{H}$) fields (2.1); one each for E_x, E_y, E_z and H_x, H_y, H_z

(4.11a) $$\frac{\partial E_x}{\partial t} = \frac{1}{\epsilon_0}\left(\frac{\partial H_z}{\partial y} - \frac{\partial H_y}{\partial z} - J_x\right)$$

(4.11b) $$\frac{\partial E_y}{\partial t} = \frac{1}{\epsilon_0}\left(\frac{\partial H_x}{\partial z} - \frac{\partial H_z}{\partial x} - J_y\right)$$

(4.11c) $$\frac{\partial E_z}{\partial t} = \frac{1}{\epsilon_0}\left(\frac{\partial H_y}{\partial x} - \frac{\partial H_x}{\partial y} - J_z\right)$$

(4.11d) $$-\frac{\partial H_x}{\partial t} = \frac{1}{\mu_0}\left(\frac{\partial E_z}{\partial y} - \frac{\partial E_y}{\partial z}\right)$$

(4.11e) $$-\frac{\partial H_y}{\partial t} = \frac{1}{\mu_0}\left(\frac{\partial E_x}{\partial z} - \frac{\partial E_z}{\partial x}\right)$$

(4.11f) $$-\frac{\partial H_z}{\partial t} = \frac{1}{\mu_0}\left(\frac{\partial E_y}{\partial x} - \frac{\partial E_x}{\partial y}\right)$$

In FDTD these are discretized using a central-difference approximation for both the space and time derivatives. The simulation region is discretized into a Cartesian mesh of cells (called Yee cells) [140]. Each component is solved at a different edge or face within the Yee cell (figure 4.9); for example, the top face (containing H_z in figure (4.9)) has at its edges electric fields $E_x(i, j, k+1)$, $E_x(i, j+1, k+1)$ and $E_y(i, j, k+1)$, $E_y(i+1, j, k+1)$. The curl of the electric field gives the time

derivative of the magnetic field normal to that face. Applying the central difference approximation to equation (4.11f), written out in full, becomes

$$-\left(\frac{H_z^{t+\frac{1}{2}\Delta t}(i+\frac{1}{2},j+\frac{1}{2},k+1)-H_z^{t-\frac{1}{2}\Delta t}(i+\frac{1}{2},j+\frac{1}{2},k+1)}{\Delta t}\right)= \tag{4.12}$$
$$\frac{1}{\mu_0}\left(\frac{E_y^t(i+1,j+\frac{1}{2},k+1)-E_y^t(i,j+\frac{1}{2},k+1)}{\Delta x}-\frac{E_x^t(i+\frac{1}{2},j+1,k+1)-E_x^t(i+\frac{1}{2},j,k+1)}{\Delta y}\right)$$

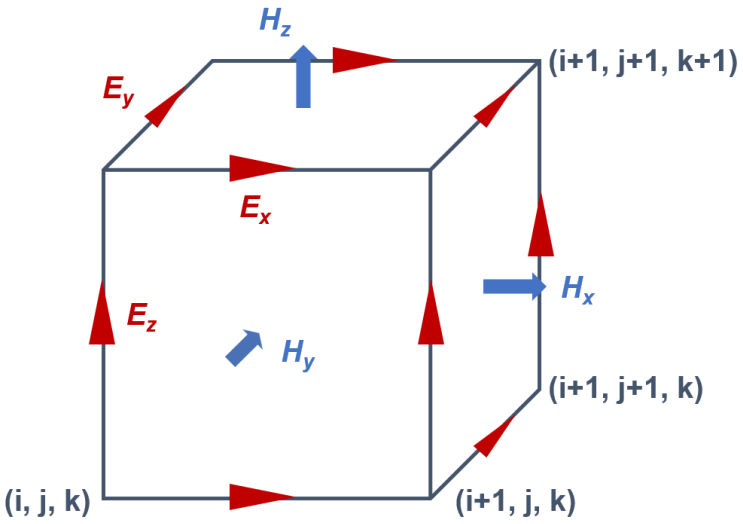

Figure 4.9: Diagram of a Yee cell. (i,j,k) are the unit vectors in the x, y and z directions respectively.

In the Yee cell each E component is in contact with four H components and each H component with four E components. Such equations are successively solved using the leapfrog method (figure 4.10); at each half-time step the electric or magnetic fields are calculated for that instant in time using the previous values of the alternate field at the previous half-time step. This is then repeated for the complementary field using these new values. To ensure numerical stability the size of the time step is limited so the field cannot propagate more than the one cell size during Δt. If $c_{max}(= c/n_{min})$ is the maximum light velocity in the simulation region then [139]

$$\sqrt{(\Delta x)^2+(\Delta y)^2+(\Delta z)^2} \geq c_{max}\Delta t \tag{4.13}$$

so the computational time (in 3D) for FDTD varies as $1/(\Delta x^4)$. The simulation domains are terminated using perfectly matched layers (PMLs) [141] which are impedance matched to the material at the simulation domain boundaries. This will in theory produce no reflection at its interface and hence absorb the energy of any outgoing waves at the simulation boundary (though

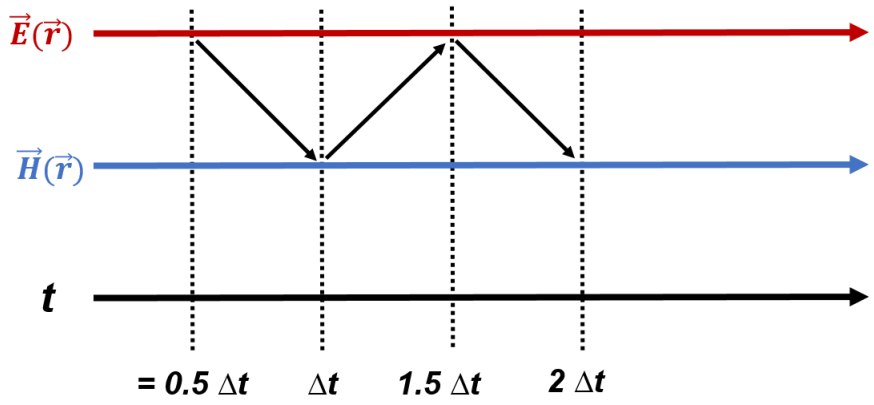

Figure 4.10: The leapfrog method: at each step of Δt the electric or magnetic fields are calculated using the values of the other field at previous time steps.

since FDTD produces a discretized approximation of Maxwell's equations, these are no longer continuous solutions and some small reflection remains).

For these simulations a commercial FDTD solver is used [142]. A feature that distinguishes Lumerical FDTD solver is its conformal meshing technique; in a standard FDTD implementation the permittivity is constant within a single cell (this being the smallest resolution of structure that can be represented by the mesh) so if a cell contains an interface the permittivity that takes up the greater volume of the cell is chosen (this is called 'staircasing'). Lumerical uses conformal meshing to account for subcell changes in permittivity [143], which in turn allows for a coarser mesh. As computing time is inversely proportional to grid size raised to the fourth power, even a small change can significantly reduce this.

4.3 Summary

In this chapter I have presented an experimental configuration for performing angular resolved spectrometry for reflectance and PL measurements and the method for calibration. Compared to other angle-resolved measurement techniques the sample and illumination stages are fixed in relation to each other, so the spot size (and hence intensity) remains constant. It also allows interchanging between white light and laser source so the same point on the sample can be both imaged and measured in reflectance and PL. Polarization resolution can also be added. I also described the methodology of the transfer matrix and FDTD simulation method, and how the computational time for FDTD can be reduced without compromising its results.

CHAPTER 5

SIMULATIONS

Previous work on photonic structures for bright SPSs focused on high Q-factor structures that create a high Purcell enhancement, which increases the coupling rate between the light and the single photon emitter (e.g. a QD). Using low Q devices therefore seems counterintuitive, yet the benefit for a SPS is twofold; first, it is more difficult to produce the precise spectral coupling between a single QD (within a broad distribution of such emitters) and a single cavity mode with a narrow linewidth than with a broader one. This reduces the device yield and makes high scalability difficult. Secondly, leaky modes (e.g. from fabrication imperfections) put a lower limit on the device efficiency as the emission rate into these channels increase in proportion with the cavity lifetime [31].

In contrast, using a structure with a low Q and short cavity lifetimes it is possible to realize high coupling rates to a preferred output mode (preferably one well-defined and with an efficient external collection, e.g. for coupling into a fiber) and low rates into leaky modes. These high β factor (1.2) structures include CTPs which have Q-factors of the order of 10-100s. Before the fabrication of samples, I performed computer simulations of TP, CTP and micropillar structures. First, TMM is used to calculate the passive response in one dimensional structures. Next a commercial FDTD solver [142] is used to simulate various low Q structures coupling to a QD, to find how these can be optimized for single photon generation.

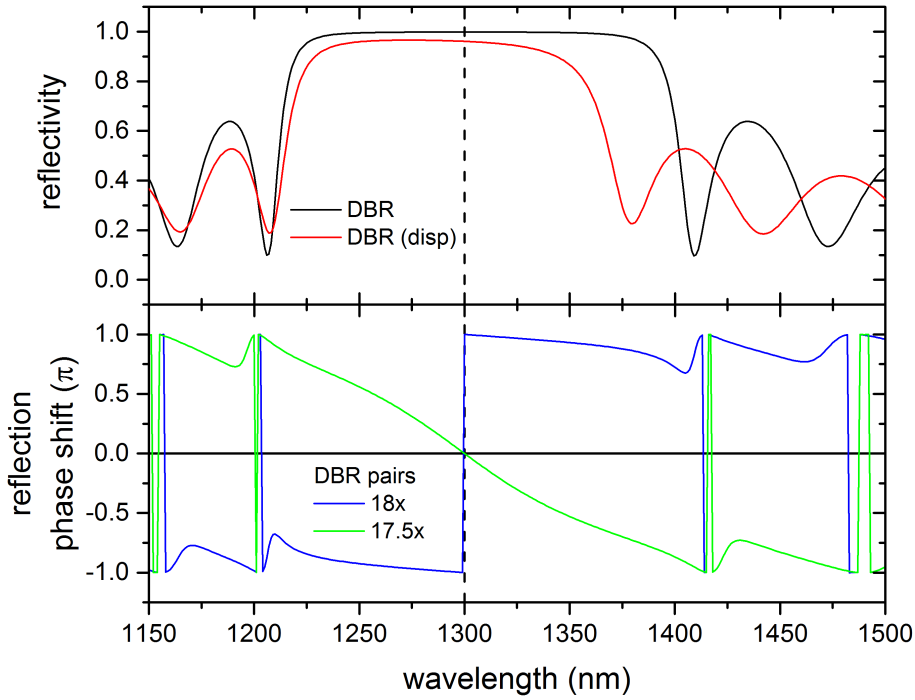

Figure 5.1: Reflectivity spectrum for an ideal ($\lambda/4$) 18x DBR with n_1 = 3.5 and n_2 = 2.9 (black line), and for a GaAs/AlAs (95/110 nm) 18x DBR with material dispersion (red line), centered at 1300 nm. The phase shift for the ideal structure is shown when the terminating (spacer) layer is the higher (blue) or lower (green) of the two materials.

5.1 TMM results

5.1.1 Designing 1.3 μm TPs

To start, a DBR is modelled that has a photonic stopband centered at λ = 1.3 μm. The reflectivity of an ideal $\lambda/4$ 18x pair DBR (with fixed n_1 = 3.5 and n_2 = 2.9) is shown by the black line in figure (5.1), below which is shown the reflectivity phase shift when terminating with a n_1 (blue line) and n_2 (green line) spacer layer. The red line reflectivity is that of a GaAs/AlAs DBR with the material dispersion function taken into account; this causes a blueshift of the low energy stopband edge, which now occurs over the wavelengths between 1205 nm and 1375 nm. The intrinsic losses of GaAs reduce the maximum reflectivity in the stopband; nevertheless, the reflectivity is still over 96%.

The TP resonance condition was shown to be (3.13)

$$r_{DBR} r_M = |r_{DBR}||r_M| e^{i(\phi_{DBR}+\phi_M)} = 1 \tag{5.1}$$

so a TP occurs where $|\phi_{DBR}| = -|\phi_M|$. This condition can be tuned to occur at 1.3 μm via the thickness of the metal (ϕ_M) or spacer layer (ϕ_{DBR}). Though the former is important, in the

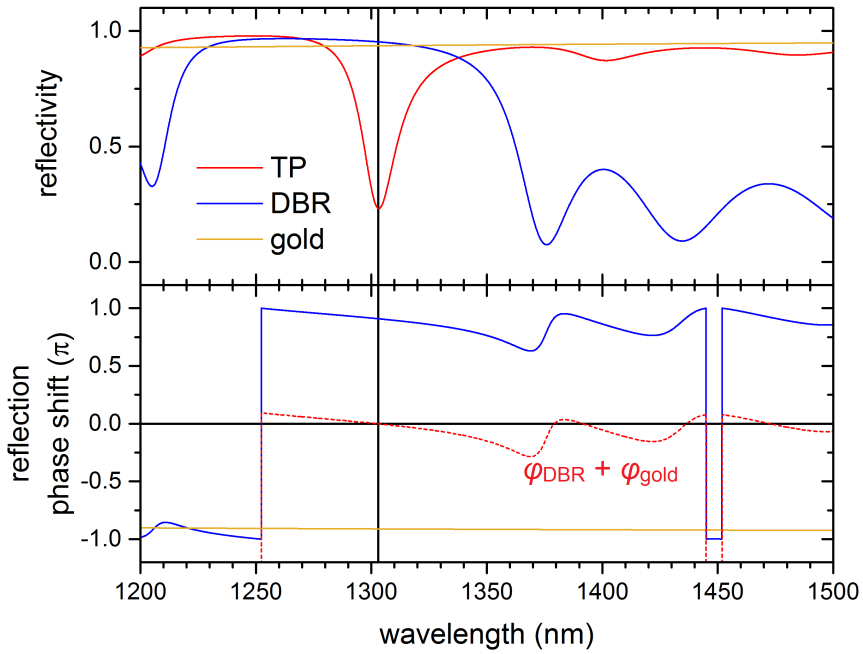

Figure 5.2: Reflectivity of TP structure (red line), bare DBR only (blue line) and gold layer only (gold line) for a 17.5x GaAs/AlAs DBR, 75 nm GaAs spacer and 25 nm gold layer. The former is the same as shown previously in figure (3.5(b)). (b) Reflection phase shift for the bare DBR and gold layer along with their sum (red dashed line). The TP mode, seen as the dip in reflectivity, occurs at the $\phi_{DBR} + \phi_M$ =0 condition

initial design phase it is sensible to tune the spacer layer as (a) its phase shift sensitivity is much greater and can cover a greater range of the wavelengths within the stopband, and (b) the thickness of the metal layer is constrained by additional requirements, since if it is too thin ($|r_M| \ll 1$) a TP will not form, or too thick and any emission will be absorbed. I found that a 75 nm GaAs spacer layer and 25 nm gold layer produces a TP resonance at λ = 1303 nm, which is shown by the reflectivity dip (red line) in figure (5.2). The modulus and phase shift of reflectivity for the bare DBR (17.5x DBR plus 75 nm spacer) and metal layer are also shown as the blue and gold lines respectively. The TP resonance occurs when their sum (red dashed line) satisfies the resonance condition. Since the metal phase is always around $-\pi$ the phase shift of the DBR must be positive, which occurs near the center of the photonic stopband when the spacer material is the higher of the two refractive index materials.

The refractive index structure and electric field cross section when excited at λ = 1303 nm is shown in figure (5.3) for the TP and bare DBR. The TP has its maximum field intensity within the spacer layer, 70 nm from the GaAs - Au interface. In SPPs, where the maximum intensity occurs directly at the metal-dielectric interface, the emitter must be located close to the interface and this results in significant losses due to coupling into surface defects that inevitably result

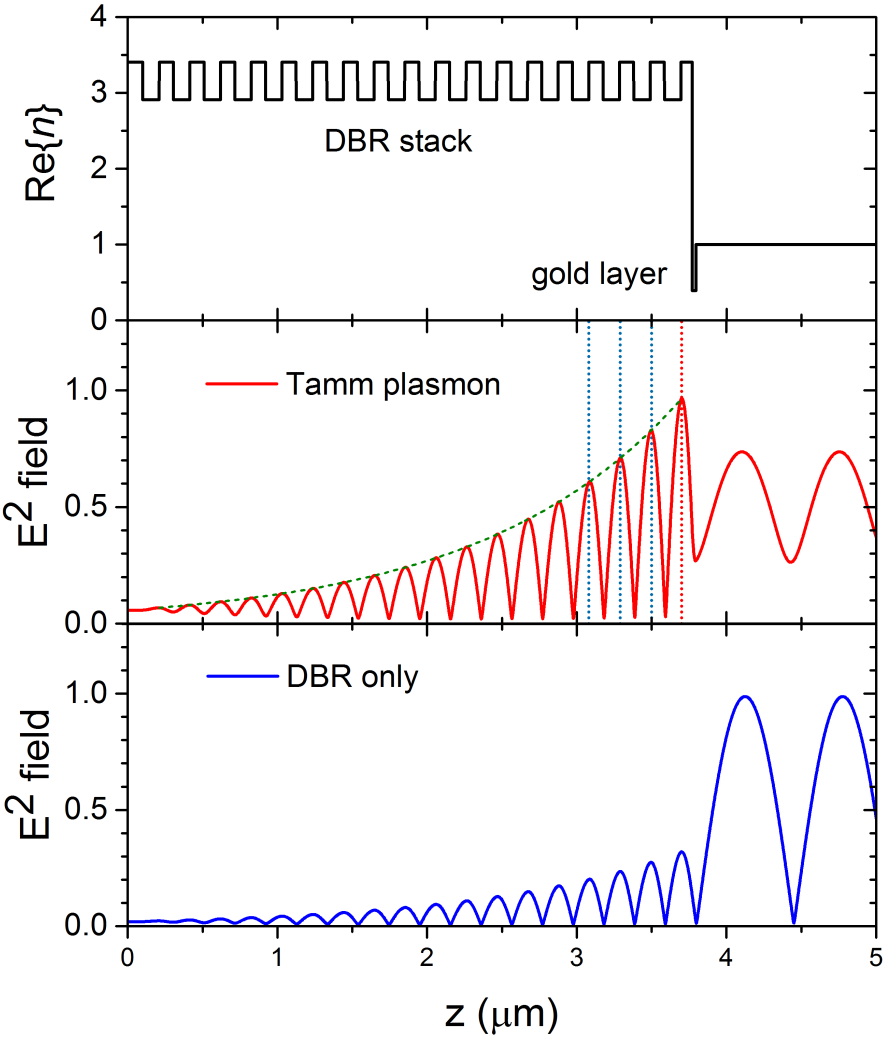

Figure 5.3: Cross-section of the refractive index and electric field for a DBR-metal (black and red lines) and DBR-air structure (blue line) at normal incidence. Note that the latter case does not form a surface state (BSW) at the interface but propagates into the dielectric; at normal incidence there is no TIR and the dielectric behaves like any normal $\epsilon > 0$ material. The dashed lines in the TP case show the position of the first four TP antinodes, where our InAs/GaAs QD layers are deposited.

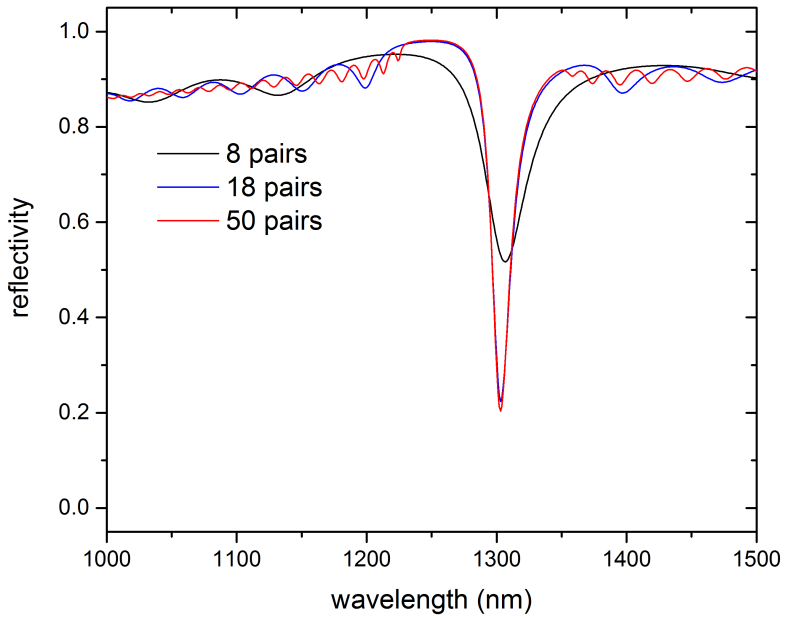

Figure 5.4: Reflectivity of TP containing 25 nm gold layer and GaAs/AlAs DBRwith 8 (black line), 18 (blue line) and 50 (red line) number of pairs (spacer layer is included and kept fixed).

from the etching and fabrication at an interface between two media. Though there still exists a metal-dielectric interface in TPs (and an interface in Tamm states in general), that the dielectric is part of a photonic crystal means the ICs (i.e. the spatial derivatives of the electric field match) can be met and the field still be continuous across the interface, while the turning point of the field (and position of maximum field intensity) occurs *within* the spacer layer. This means that QDs positioned here maximimze their light-matter interaction without the loss channels associated close to an etched surface. Even in the case of the TP, where there is still absorptive loss in the metal layer, this results in a substantial improvement in mode quality over the SPP.

It should also be noted that, being a Bloch wave, the field has a generally decaying envelope into the DBR but that oscillates within this, and there are several other antinodes located in GaAs layers and separated by a DBR period. These are potential sites for QD layers if a higher density is required (e.g. for lasing or photodetection devices). An exponential function e^{-zL} fitted to the decay (green dashed line) gives a propagation length of $L = 0.75\ \mu\text{m}^{-1}$. The field decays by half within the first five pairs. Once the field has disappeared almost completely increasing the number of DBR pairs N has little effect on the reflectivity; provided it is sufficient for the magnitude of reflection $|r_{DBR}|$ to be near unity the TP will form. Nor does this effect the position of the resonance since adding more pairs to what is a periodic system does not shift the DBR's reflection phase. This is shown with the 18 pair (blue line) and 50 pair (red line) structures in

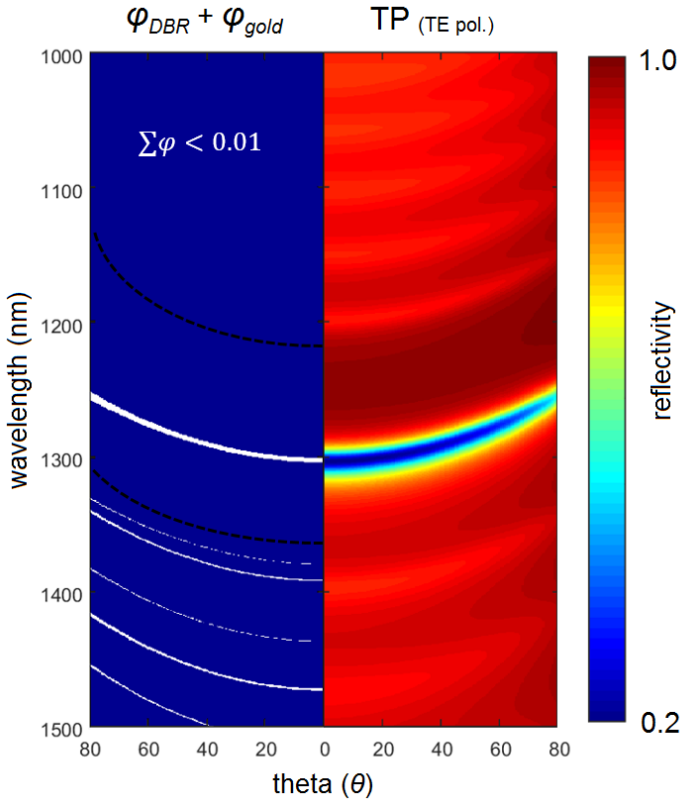

Figure 5.5: Sum of the ϕ_{DBR} and ϕ_M for a 17.5x GaAs/AlAs DBR + 75 nm GaAs spacer and 25 nm gold layer respectively, as a function of angle ($\kappa = n(\omega/c)sin(\theta)$) and wavelength. The white regions, showing where this sum ≈ 0, correspond to the dispersion of the TP mode seen as the dip in the reflectivity plot on the right. Black dashed lines correspond to the edges of the DBR stopband.

figure (5.4). Because GaAs and AlAs have a small refractive index difference, a relatively high number of pairs are needed compared to other dielectric DBR systems.

At non-normal angles of incidence, the TP is expected to show the parabolic dispersion curve previously reported. This is shown by the position of the reflectivity dip in figure (3.6) for TE polarization. A similar plot is compared with the summed reflection phase shift of the metal and DBR parts of the structure as a function of wavevector and frequency in figure (5.5).

5.1.1.1 Varying metal and spacer layer thickness

As described in section (3.2.2), the resonance and Q-factor of the TP depends on the metal and spacer layer thicknesses. To find modes resonant at telecoms wavelength I initially varied the spacer layer thickness. An example of this shift for our GaAs/AlAs structures with a fixed gold layer thickness (m = 25 nm) and GaAs spacer is shown in figure (5.6(a)). As the spacer layer is reduced the TP resonance shifts to higher energies, consistent with the 'potential' energy of the

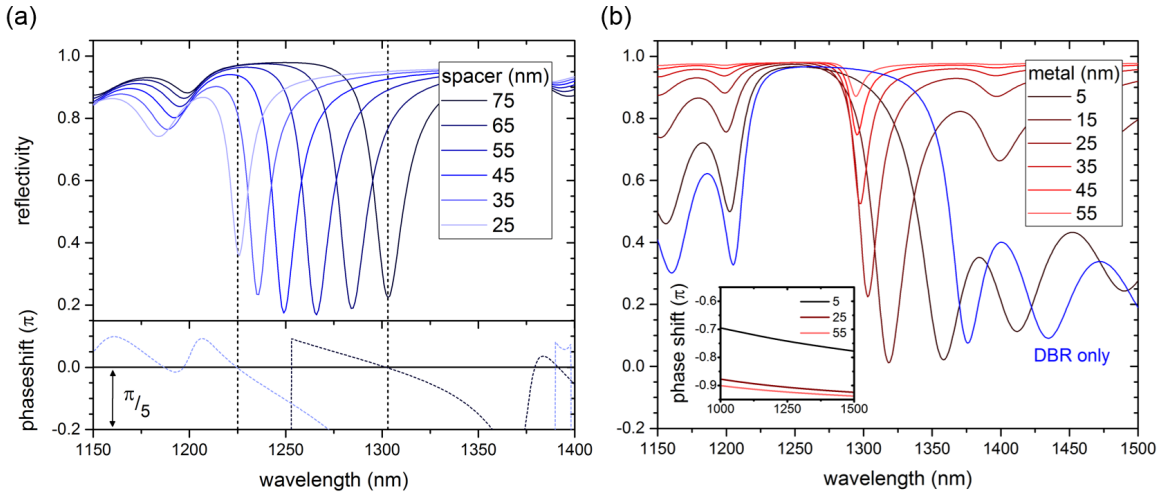

Figure 5.6: (a) Variation of TP resonance as function of spacer thickness (metal layer is fixed at 25 nm). The dashed lines show the phase shift sum (same scale as y axis, in units of π) of the DBR and metal for s = 75 nm and 25 nm, showing where the $\phi_{DBR} + \phi_M = 0$ condition occurs. (b) Variation of TP resonance as function of metal thickness (spacer layer fixed at 75 nm). Blue line shows the reflectivity of the bare DBR (m = 0). **Inset**: reflection phase shift of 5, 25 and 55 nm gold layer.

mode being raised as material is removed. In terms of the reflection phase, reducing the spacer causes it to transition from something resembling case (A) in figure (3.2), to (B) and to (C); given the metal phaseshift is largely constant across the stopband the occurence of the TP resonance condition follows to lower wavelengths.

A similar change can be affected by varying the gold layer thickness, which is an important once the DBR has been fabricated and the spacer layer thickness fixed (5.6(b)). As the metal thickness is increased the TP energy increases. Beyond a certain thickness the reflection phase experiences little shift (5.6 (b; inset)) and the change in the resonance position is smaller. However, a thicker metal layer does increase the amount of light absorbed or reflected when excited through the top, which reduces the magnitude of the reflectivity dip. It is also noted that the metal phase shift always remains negative, so for a high-index spacer any resonance will only occur within the upper half of the stopband (where ϕ_{DBR} is positive). Conversely if the metal layer is too thin its magnitude of reflection is too low to act as an effective mirror and light will not be confined regardless of the reflection phase. This contrasts with the spacer, where the magnitude is a function of the number of DBR pairs and only the reflection phase is sensitive to the spacer layer thickness.

Plots of the TP resonance and Q-factors as both spacer and metal layer thickness are independently varied are shown in figure (5.7) for a 17.5x GaAl/AlAs DBR (the spacer layer is considered separate) at normal incidence from m = 5 nm to 60 nm (s = 75 nm), and for s = 40 nm to 100 nm (m = 25 nm). Our final design produced a TP with $Q \approx 70$. The Q-factor of the spacer varying

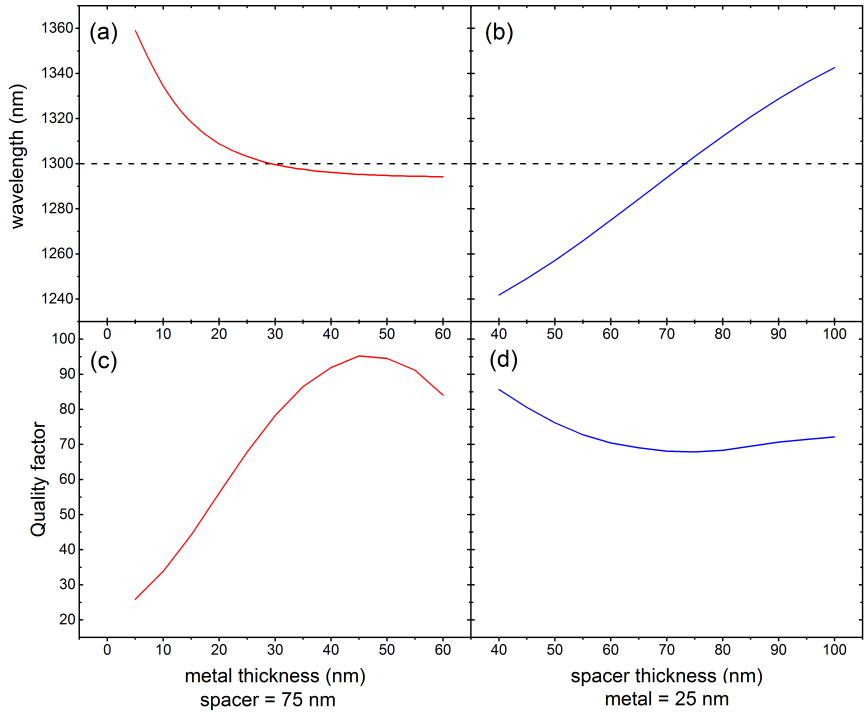

Figure 5.7: (a) and (b) Calculated shift in TP resonance as a function of metal and spacer layer thickness respectively (with the other remaining constant at 75 nm and 25 nm respectively). (c) and (d) Variation of Q-factor as function of metal and spacer layer respectively.

structure is relatively constant while if the gold layer is varied (5.7(c)) it drops when the metal becomes too thick (from absorption) or too thin. It should be noted that, with the DBR fixed, the strength of the confinement is affected by the metal layer thickness but also the spectral position of the TP within the DBR stopband, so in the thin case this decrease is partly because there is a minimum thickness needed to effectively form a TP, and partly because its resonant wavelength shifts so much that it hits the upper edge of the stopband. Simulations where the spacer layer is varied to compensate for any wavelength shift caused by different metal thicknesses show TPs can form with metal layers as thin as 5 nm, though there remains a steady decrease of the Q-factor as the metal layer becomes thinner independent of its position relative to the stopband edge.

5.1.2 Designing 1.3 μm TPs at low temperature

The designs described in section (5.1.1) are suitable for producing proof-of-principle devices containing high densities of QD layers and that can be operated at room temperature (RT). Though these may be suitable for lasing or photodetection applications, for single QD emission the TPs must operate at low temperatures to eliminate phonon decoherence and non-radiative

processes. The increase in the bandgap energies at lower temperatures produces a blueshift in the QD emission that is accounted for by growing dots that emit (at RT) at lower energies. A common fitting relationship for the temperature dependence of the bandgap energy is the Varshni formula, which is linear at high temperatures and asymptotic at lower temperatures [144]. The resonance of the TP also blueshifts due to changes in the material permittivity though at a much lower rate. The thermal dependence of the refractive indices of GaAs and AlAs are taken from [145, 146] and applied to the values described in appendix (B.2). This produces a blueshift of 30 nm (figure 5.8 (inset)). The effect of any thermal expansion of the layers changing the geometry of the DBR is small compared to the temperature-dependent changes in permittivity [147].

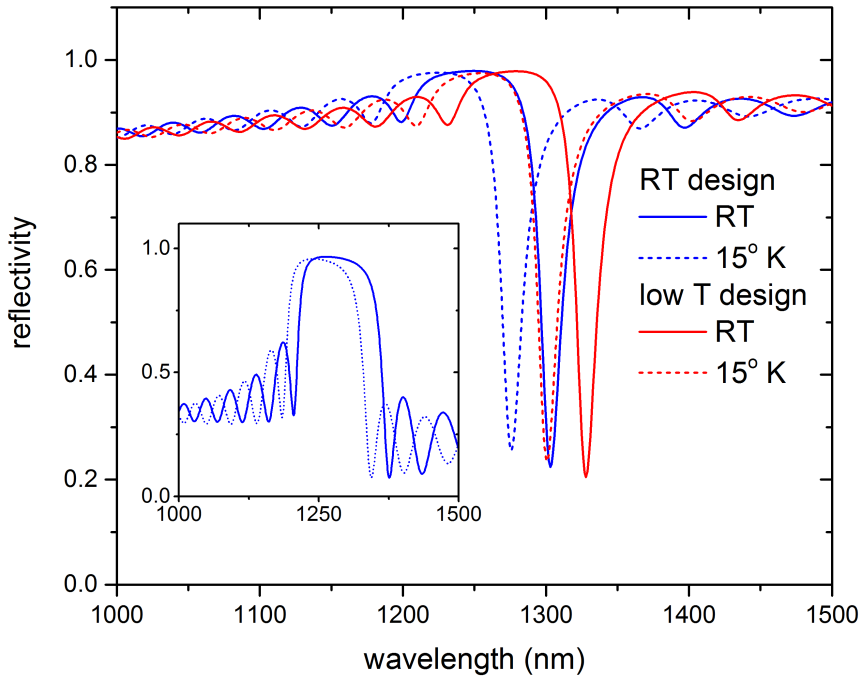

Figure 5.8: Room temperature (blue) and low temperature (red) TP designs at 273 and 15 K (solid and dashed lines respectively). Inset; bare DBR (17.5x GaAs/AlAs, λ = 1300 nm, s = 75 nm) showing the 30 nm blueshift between room and liquid helium temperature.

The effect of temperature on the permittivity of gold can be found via the temperature-dependent Drude equation [148], which accounts for the variation of the plasma frequency ω_p and the electron damping rate, γ. This model is only effective for gold for wavelengths longer than 550 nm, due to the onset of interband transitions. The largest change occurs for the damping rate, which increases the extinction coefficient with increasing temperature. This is important for applications that use surface or localized plasmons, which can become very hot during excitation [149] but is less relevant for devices operating at low temperatures and in the single photon regime (where the aim is precisely to reduce the amount of absorption in the metal). If this

were to have an effect, I predict it would be as a decrease in the quality factor as metals with decreased imaginary parts of their permittivity are effectively thinner at cold temperature (5.7(c)). In contrast, the change in the real part of the permittivity with temperature is small (< 3%).

Structures are designed by first altering the DBR pair thicknesses to produce a stopband at λ = 1330 nm at RT, and then by reduced the spacer layer thickness to tune the TP resonance (figure 5.8). At cold temperature these reproduced the expected blueshift of 30 nm, so the TP dip now occurs at 1300 nm.

5.2 FDTD results of CTPs

I next simulated fully confined Tamm plasmons where 3D confinement is included (section 3.2.4). Our structures consist of a $\lambda/4$ 17.5x pair GaAs/AlAs DBR, 75 nm GaAs spacer layer and 25 nm gold disc. Simulations with variable disc diameter, d, are run to explore the effect of increasing confinement on the mode as the diameter is reduced.

5.2.1 Effect of disc diameter

To find the resonant frequencies of the CTP the structures are first excited by a broadband (1100 nm to 1400 nm)[1] TE dipole source positioned in the middle of the spacer layer ('the cavity'), under the center of the microdisc. Several time-domain monitors are placed within the cavity. These record the electric and magnetic field components as a function of time from the start of recording until the end of the simulation. A 200 fs start time is set for the monitors to remove transients from the initial pulse. Because these are low Q structures the field fully decays (i.e. the energy in the simulation region reaches 10^{-5} of its initial value) within the set running time.

These are analyzed in the frequency-domain by performing a chirp z-transform (CZT) on these recorded fields, which produces a discrete Fourier transform of the time-domain data. Because frequencies further detuned from the resonant modes have shorter lifetimes than those on resonance, the resonant modes will have decayed less over the later duration of the simulation, and the energy stored by fields in the spacer layer (plotted as a function of frequency) will show peaks. This result is called the *energy spectrum* of the cavity. The absolute magnitude of these peaks vary with the source and monitor setup so, though plotted in normalized units, are only used to identify the position and quality of the resonances [150]. An example of such a spectrum is shown in figure (5.9(b)) for the bare DBR; two energy peaks occur which correspond to the first Bragg modes at the edge of the DBR stopband (seen as the reflectivity minima in the TMM for comparison). Unlike the frequencies at the center of the stopband, that decay exponentially into the DBR (inset; red line), these have a large field centered in the DBR (green line). Profiles of the electric field in the bare DBR structure for frequencies on and off the first Bragg mode are shown in figure (B.6). In terms on the energy spectrum, modes at the stopband edge have very low group

[1] pulse length = 7.2 fs, pulse offset = 20.6 fs

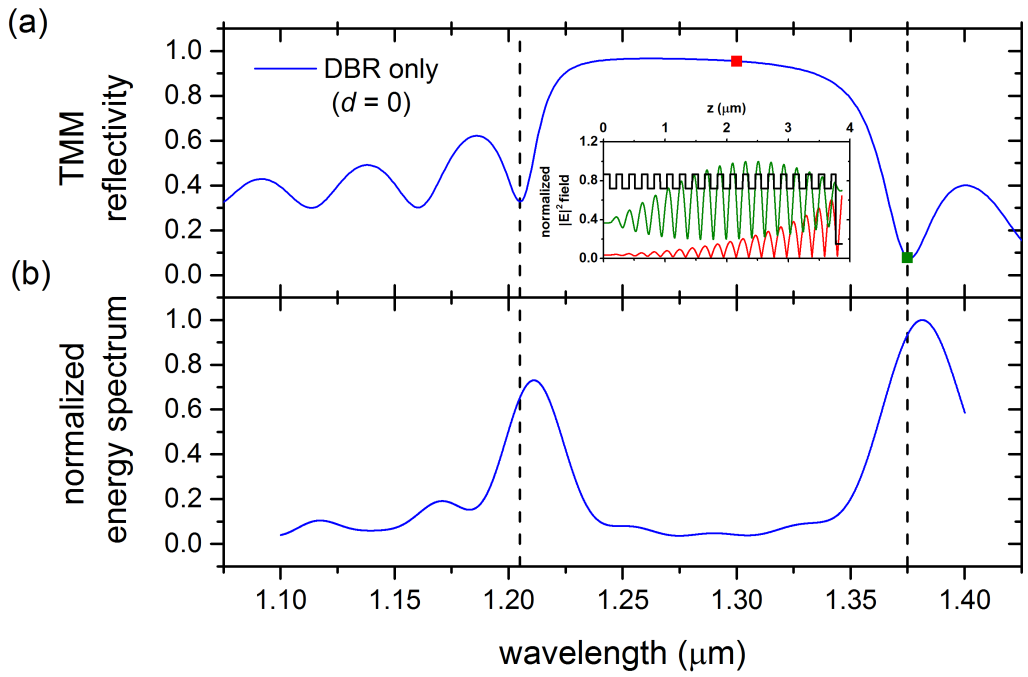

Figure 5.9: (a) TMM reflectivity of bare DBR (disc diameter d = 0). Dashed black lines show the first Bragg modes. **Inset**: Refractive index (black line) and electric field cross-section at λ = 1300 nm (red line) and = 1375 nm (green line). (b) normalized energy spectrum taken from a CZT of the electric field recorded within the spacer layer as a function of wavelength.

velocities and decay slower. Therefore, the energy stored by the fields in the spacer layer (where the time-domain monitors are positioned) over the duration of the simulation is higher at these frequencies, producing the observed peaks.

Quality factors are calculated by isolating the energy spectrum peak identified as the fundamental mode and dividing the peak's resonance by its FWHM (see equation 1.1). I also analyze the emission rate enhancement, the Purcell factor; this is calculated by the ratio of the total power emitted by the dipole versus the emitted power if the dipole were simulated in an homogeneous medium, γ_{hom}[2]. Since power emission is proportional to emission rate this ratio gives the Purcell factor, which is itself proportional to the enhancement of the photonic environment's local density of states. To measure the collection efficiency, β, a power transmission box is placed around the structure. This is further described in appendix (B.3).

Figure (5.10(a)) shows the spectrum of the CTP across a range of small ($< 2.6\mu m$) disc diameters. The fundamental resonances of the CTP are distinct and blueshift to higher energies as the confinement increases, the effect becoming stronger at the smallest diameters. Figure (5.14) shows a plot of these resonances taken from the spectrum data (black squares) as a function

[2]because of the method Lumerical uses to calculate the emitted power, this only works if the bulk material that the dipole is in is lossless

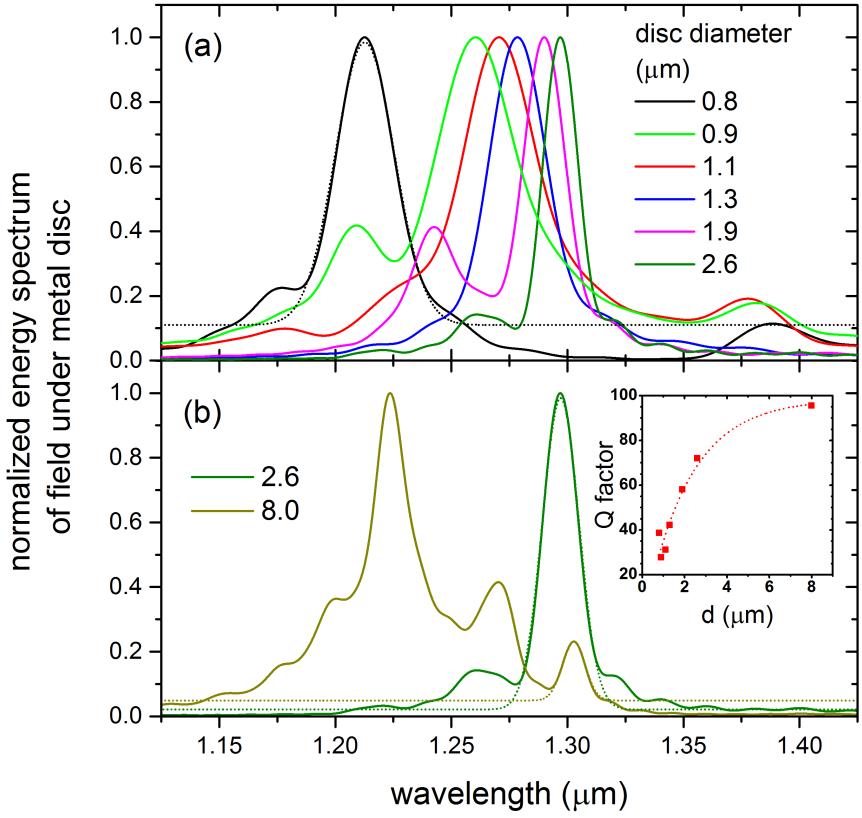

Figure 5.10: Normalized energy spectrum for different disc diameters, showing the energy stored by the different frequency components of the electric field in the spacer layer for the duration of the CTP; resonances appear as peaks at frequencies where that component of the field has a longer lifetime within the CTP. (a) For the smallest discs there is a clear fundamental mode that shifts from λ = 1.296 μm (for d = 2.6 μm) to higher energies as the disc diameter is reduced and the mode becomes more confined. (b) At higher diameters (e.g. d = 8.0 μm, brown line) higher order modes can be seen, though the fundamental mode is (slightly) redshifted compared to the 2.6 μm disc shown for comparison. **Inset**: Q-factors calculated at the fundamental resonances using Gaussian fits to the energy spectra peaks (some examples are shown as dotted lines), as a function of disc diameter. The dashed red line is a guide to the eye.

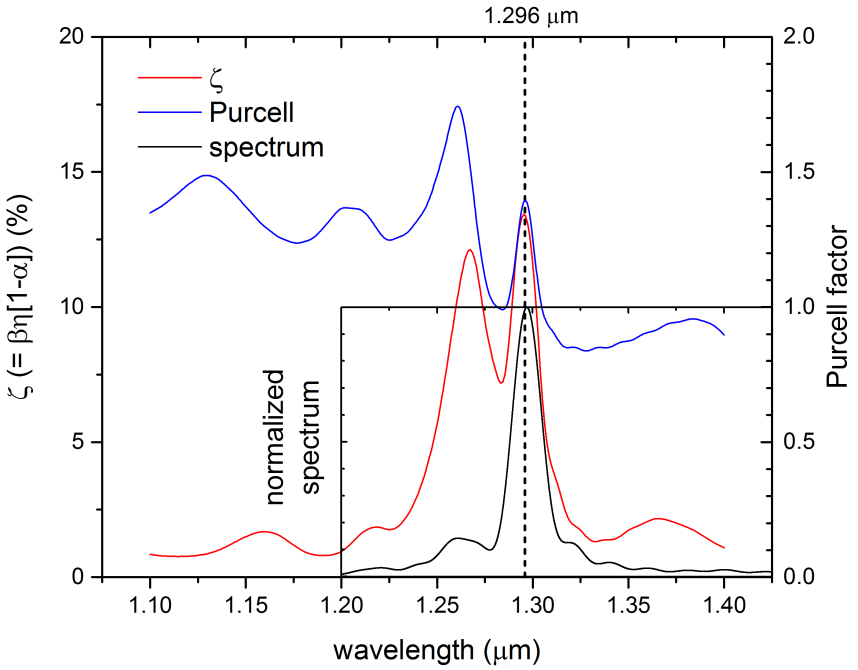

Figure 5.11: Plot of the internal collection efficiency $\zeta = \beta\eta[1-\alpha])$ (red line; see (B.3)), Purcell enhancement (blue line) and normalized energy spectra (black line; scaled to right axis) for a d = 2.6 μm CTP. All three indicate a fundamental resonance occurring at 1.296 μm (black dashed line).

of disc diameter. There is also good alignment between these resonances and the peaks in the Purcell enhancement (blue line in figure 5.11). For larger disc diameters higher order modes begins to appear; this is shown most clearly in figure (5.10(b)) for a d = 8.0 μm disc (a d = 2.6 μm is shown for comparison). Three resonances can be seen; the fundamental resonance at λ = 1303 nm and two higher order peaks at 1270 and 1223 nm. The resonance at λ = 1303 nm is the same wavelength as that produced in the purely 1D (i.e. non-confined) case by the TMM.

Q-factors ($= \lambda/\delta\lambda$) at the fundamental resonances are calculated to Gaussian functions fitted to the plotted energy spectra, examples of which are shown by the dotted lines. These are plotted as an inset in figure (5.10(b)). As the diameter becomes smaller the Q-factor decreases due to increased emission into the side channels and increased scattering at the disc edge. The standard errors of these fits produce uncertainties in Q that are very small ($\pm\delta Q < 1$); however, this does not account for any uncertainty identifying the parts of the spectrum peak that comprise the fundamental mode to which the functions are subsequently fitted. For this reason figure (5.10) does not show Q-factors for intermediate diameters discs between 3 μm and 8 μm, where overlapping of the modes makes identifying the fundamental difficult (section 5.2.1.2); in contrast the spectra plotted have very distinct peaks and the variance between multiple separate fits was

less than 10% of the Q-factor value.

5.2.1.1 Lateral and transverse profile of the CTP

To study the profile of the fundamental and higher order modes 2D monitors are positioned to record the electric fields in the vertical (x-z) plane through the center of the disc, and in the transverse (x-y) plane through the center of the spacer layer. The CTP is excited by a circularly polarized (CP) Gaussian broadband source (1100 nm to 1400 nm) positioned above the disc. The vertical profile showing the distribution of the absolute electric field for a 17.5x GaAs/AlAs DBR, 75 nm GaAs spacer layer and d = 2.6 μm, 25 nm gold disc is shown for the CTP's fundamental mode in figure (3.7(b)). Lateral confinement of the field can be seen under the region covered by the disc (marked in the figure by white lines), with the intensity strongest under the center of the disc and decreasing with depth into the DBR.

Figure (5.12) shows for the same structure the transverse profile of the CTP under the disc at different wavelengths. As mentioned in (3.2.4), cylindrically symmetrical structures should produce CTPs with transverse fields that result from this symmetry, such as those exhibited by circular waveguides or micropillars [95]. These modes consist of an underlying Gaussian beam multiplied with a Laguerre polynomial. The order of a mode LP_{ij} is given by two integers i and j, which describe its radial and angular distribution respectively. At the CTP fundamental mode (λ = 1296 nm), shown by the black dashed line in figure (5.12(a)), the transverse mode corresponds closely to the fundamental LP_{00} mode i.e. a Gaussian consisting of a single central peak. Resonances at the next higher energies in the series, marked by the blue and green dashed lines, show field distributions similar to the higher-order Laguerre-Gaussian polynomials such as LP_{10} and LP_{20}. Normalized profiles and field distributions for these three modes are shown in figure (5.12(b)) and (c) respectively.

5.2.1.2 'Intermediate' disc diameters

For disc diameters between 3 μm and 8 μm the fundamental mode is much harder to identify from the energy spectrum alone. As the discs become larger the spectral separation between different resonances in the multi-mode regime become smaller. This results in greater mode overlap occurring between 1290 nm and 1310 nm. To help identify the different modes it is necessary to compare this with the Purcell factor and transmission. The spectrum for a d = 5.0 μm disc is shown in figure (5.13(a)) with Gaussian fits to the several modes (red dashed lines). These generally align very well with the Purcell enhancement (blue line) except at the longest wavelength peak (at λ = 1309 nm). This peak does not have a corresponding peak in the Purcell enhancement, or any increase in the coupling efficiency ζ (shown in 5.13(b)), or the fraction of the emitted power absorbed. I have therefore identified the next lowest peak as the true fundamental mode of the CTP. In other cases (figure B.7) the Purcell enhancement has the lowest-energy distinct mode, and which does not appear on the spectrum, but does align with the peaks in the ζ

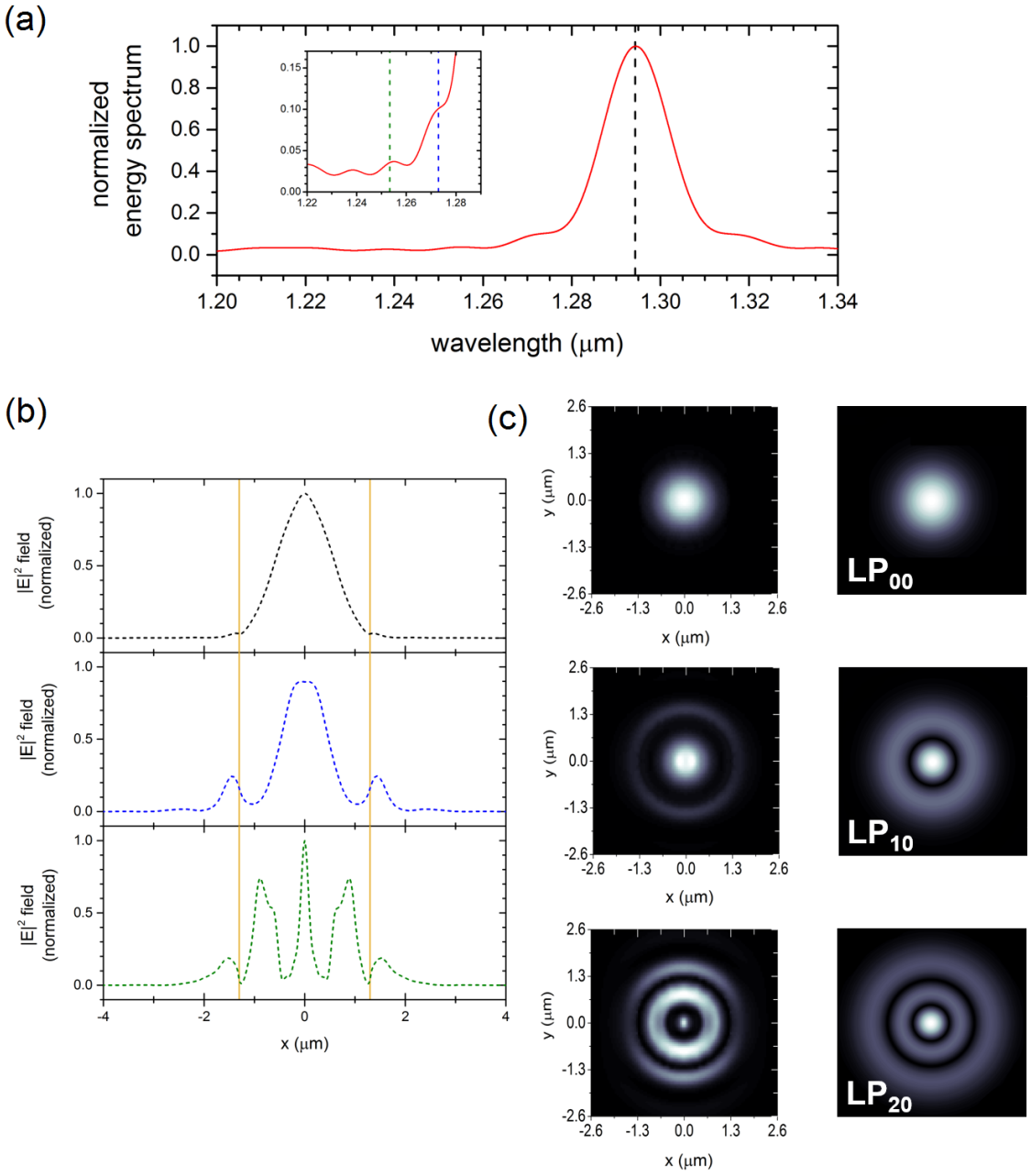

Figure 5.12: (a) Normalized energy spectrum for a $d = 2.6\ \mu m$ disc. The CTP is excited by a CP Gaussian source above the disc as described in (5.2.1.1). **Inset** is a zoom-in showing the energy spectrum on the higher energy side of the fundamental peak. (b) Profiles of the absolute electric field under the disc at the center of the spacer layer ($y = 0$, $z = \frac{s}{2}$) at the wavelengths corresponding to the black, blue and green dashed lines in (a). Gold lines show the location of the disc edge. (c) Distribution of the absolute electric field of the CTP at the frequencies marked in (a). These are identified as corresponding to the fundamental (black line) and the first and second order (blue and green line) transverse modes for a cylindrically-symmetric system, i.e. 00, 10 and 20, respectively. For comparison, spatial profiles of these modes calculated in MATLAB using the standard formula [151] are shown to the right.

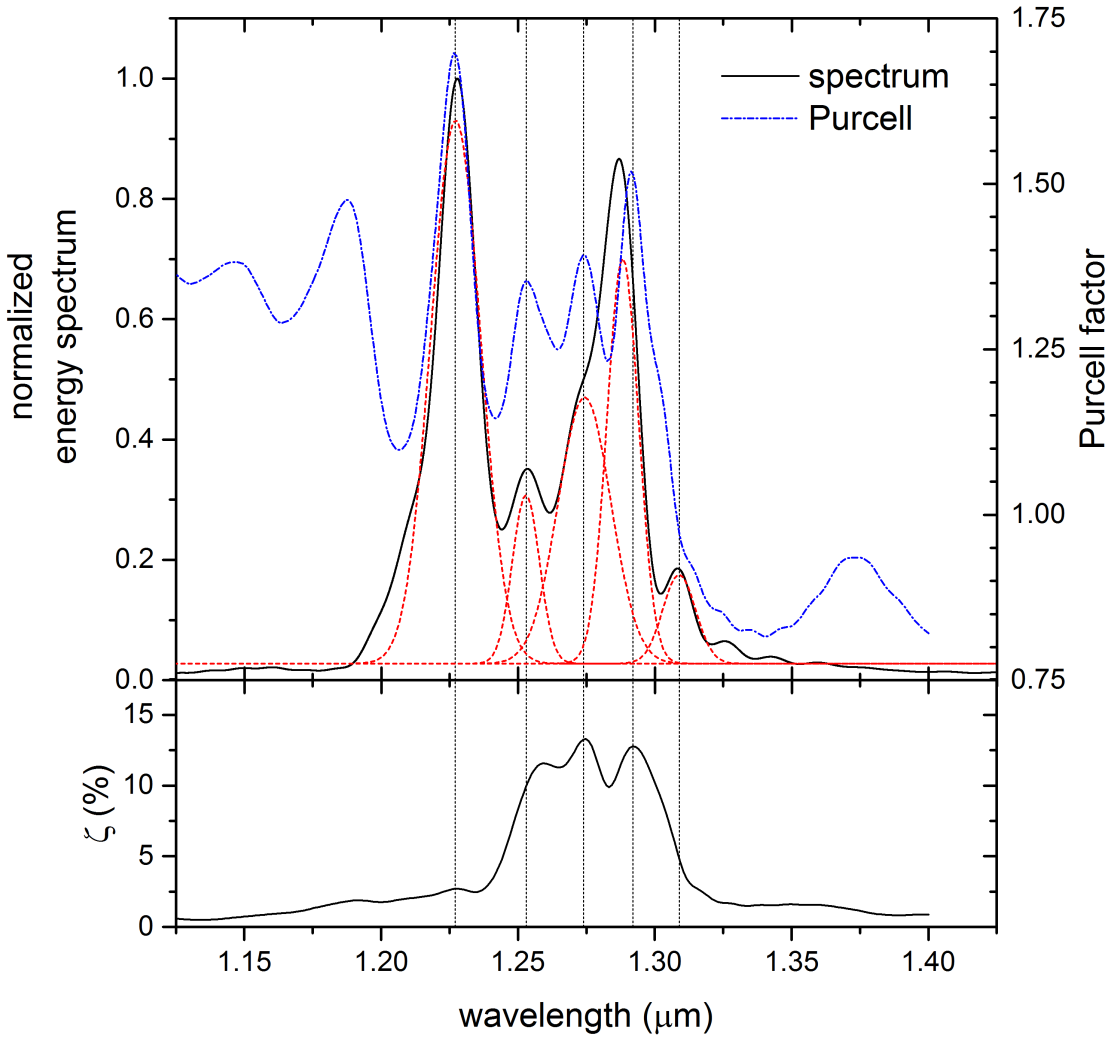

Figure 5.13: (a) Normalized spectrum and Purcell enhancement for a d = 5.0 μm disc. Red dashed lines are Gaussian fits to the peaks and black dotted lines indicate the resonant wavelengths of these fitted modes. (b) Plot of the internal collection efficiency, $\zeta = \beta\eta[1-\alpha]$.

factor. The resonance of the fundamental modes identified this way are shown by the red circles in figure (5.14).

5.2.1.3 Collection efficiency

The total emission into the output mode is calculated using a transmission box around the structure (B.3) and is shown as a function of disc diameter in figure (5.15). The rate into the top channel relative to other emission modes ($\beta\eta$) saturates for the larger discs but begins to decline rapidly below a certain disc size (d ~1.3 μm). This is not due to the reduced Q-factor (5.10) of smaller discs lowering the Purcell enhancement, as this effects the emission rate into all

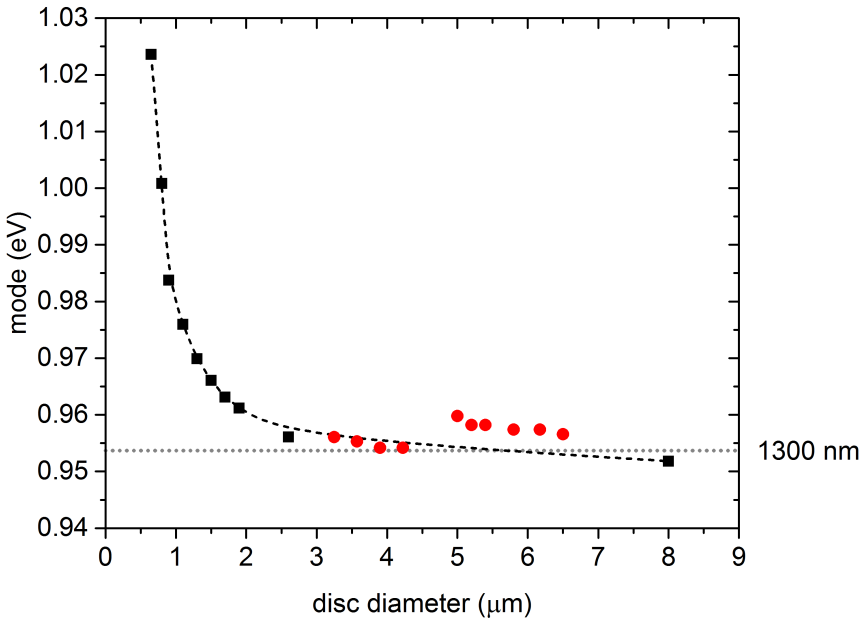

Figure 5.14: Shift of the fundamental modes of the CTP as a function of disc diameter (m = 25 nm, s = 75 nm). Red circles are the resonances identified for intermediate disc diameters between 3 μm and 8 μm, where multimode behaviour makes identifying individual modes difficult, by the energy spectrum, Purcell factor and collection efficiency. The dashed line is a guide to the eye.

channels, but due to scattering at the disc edge increasing the fraction lost into the side channel. However, there is a corresponding increase in the absorptive loss for larger discs; the highest internal collection efficiencies therefore occur for a disc between 1.5 μm and 3.0 μm, shown by the red dashed line. The wavelength dependence is shown in figure (5.11; red line) for a 2.6 μm disc. This peaks at the position of the CTP resonance and decreases as the source frequency is detuned. However, because the Q of a CTPs is low, this bandwidth is still broader than the spectral wander of a typical QD.

The closest similar device is that demonstrated by Gazzano et al. [114] at 910 nm, consisting of a d = 2.5 μm, m = 50 nm gold disc. This predicted a theoretical coupling factor into the CTP mode (β) of close to unity and measured a total collection efficiency of ζ = 28%, twice that of these devices. The same trend of reduced Q-factor with reduced diameter due to scattering is observed, as well as Purcell factors around ~1.5 to 3. The coupling into the mode, which in [114] is calculated analytically using equation (1.3) with $\beta = \frac{F_p}{F_p+\gamma}$, is predicted to be around 50% for a realistic emitter, which is much more comparable to that predicted for my devices (β = 45%). Unity values occur due to the extremely low inhibition factors (γ) predicted, which require very high quantum efficiency emitters. This represents an obvious way of improving β, and hence the collection efficiency. It should also be noted that this efficiency does not distinguish between

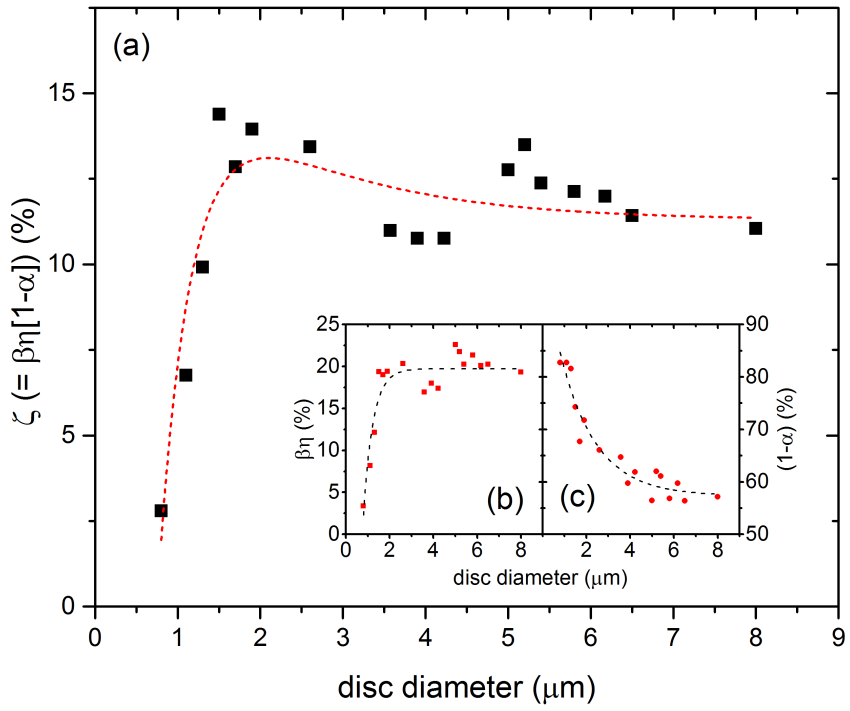

Figure 5.15: Plot of the collection efficiency ($\zeta = \beta\eta[1-\alpha]$) as a function of disc diameter. (b) plot of $\beta\eta$ and (c) (1 - α) as a function of disc diameter. The black dashed lines are an exponential and asymptotic fit respectively to these points, and the red dashed line is their product.

light coupling into the mode that subsequently emits into the top and bottom channel (η). This is usually assumed to be negligible as emission perpendicular to the disc is stopped by the DBR's stopband; but our model predicts that η can be significant, sometimes representing over half of the emission, due to the presence of a large evanescently decaying tail into the DBR and the large refractive index contrast between air and substrate (i.e. GaAs) side of the structure. Changing the substrate layer could reduce this loss channel (see section 5.3.1). More complex mechanisms of improving collection efficiency could be the addition of gratings on the metal layer or solid immersion lenses (SILs) [152], to improve the angular divergence of the emission.

5.2.2 Effect of spatial displacement of the source

The effect on the emission properties when the QD source is displaced in position from the center of the microdisc is also considered. A 2.6 μm disc is chosen because it has a high internal collection efficiency and its fundamental resonance (λ = 1296 nm) is closest to my desired operating wavelength. The source position along the y-axis (origin at y = 0; edge of disk at y = 1.3 μm) is varied as shown in figure (5.16(a)). The angular divergence of the emission is studied by recording the nearfield electric field above the top of the disc and projecting into the farfield. This

decomposes the nearfield results into a superposition of plane waves with different wavevectors and amplitudes (section 4.1.1) and propagates them a set distance (one meter) in a straight line. This produces an intensity plot in terms of the spatial frequency, i.e. the polar and azimuthal angles θ and ϕ (alternatively these farfield results can be multiplied by a complex function that equates to a lens system, which converts this back to the real space domain).

Cross-sections of the angular profile at fixed ϕ angle are shown for different y positions in figure (5.16(b)). When the dipole is positioned under the center of the microdisc (blue line) the angular distribution of the emission closely fits a Gaussian profile with a FWHM of $57.4 \pm 0.9°$. In contrast, the emission from the DBR only (orange line) has a wide emission divergence, with most of the emission concentrated into two lobes at ϕ angle's orthogonal to the dipole orientation. This is shown most clearly in figure (B.8). As the source moves towards the disc edge there is a shift in the emission peak to a wider distribution as it couples less into the fundamental mode, which has its maximum field enhancement at the center (figure 5.12). Instead the emission pattern becomes a mix of the Gaussian and (increasingly) non-Gaussian higher order modes. There is also a drop in field intensity as less light is transmitted through the structure, which I believe is a combination of increased losses into the DBR side channel and scattering from the disc edge.

The external extraction efficiency this distribution corresponds to is demonstrated in figure (5.16(c)), which shows the power transmission in the radial direction through the outer surface as a function of the surface's solid angle (2θ), by integrating the radial Poynting vectors over all ϕ, and between θ and $-\theta$. This is equivalent to eliminating the wavevectors outside the collection of a lens with numerical aperture $NA = nsin(\theta)$. This is then expressed as a percentage of all transmitted power through the top of the structure (i.e. $\theta = \pi/2$).

$$P = \frac{\int_{-\theta}^{\theta}\int_{0}^{2\pi} f(\theta,\phi)\mathrm{d}\phi\mathrm{d}\theta}{\int_{-\frac{\pi}{2}}^{\frac{\pi}{2}}\int_{0}^{2\pi} f(\theta,\phi)\mathrm{d}\phi\mathrm{d}\theta} \tag{5.2}$$

where $f(\theta,\phi)$ is the farfield pattern and $\theta = arcsin(\frac{NA}{n})$. For a dipole at y = 0 (blue line) 90% of light emitted into the top channel would be collected within an NA of 0.7 (compared to under 40% for the bare DBR). The collection decreases as the dipole moves away from the center until the limit where the dipole is outside the disc entirely, which has a 90% collection NA = 0.95, and which is identical to the plot showing a dipole with DBR but no metal layer. The large loss of collection efficiency once the dipole is located more than half a radius from the disc center would have the benefit of spatially filtering the QDs seen in the CTP by limiting the NA of the objective.

In addition to directionality of emission I also expect a change in the Purcell enhancement of a QD in a CTP. Figure (5.16(d)) shows the Purcell factor decreases linearly as a function of source position from the disc center, approaching unity as the source is placed outside the disc entirely, suggesting the CTP does not extend beyond the disc's dimensions. However, this decreasing trend breaks down in the region very close to the disc edge (inset: red squares), where there is a very large enhancement of the Purcell factor. Due to the narrow extent from the disc edge

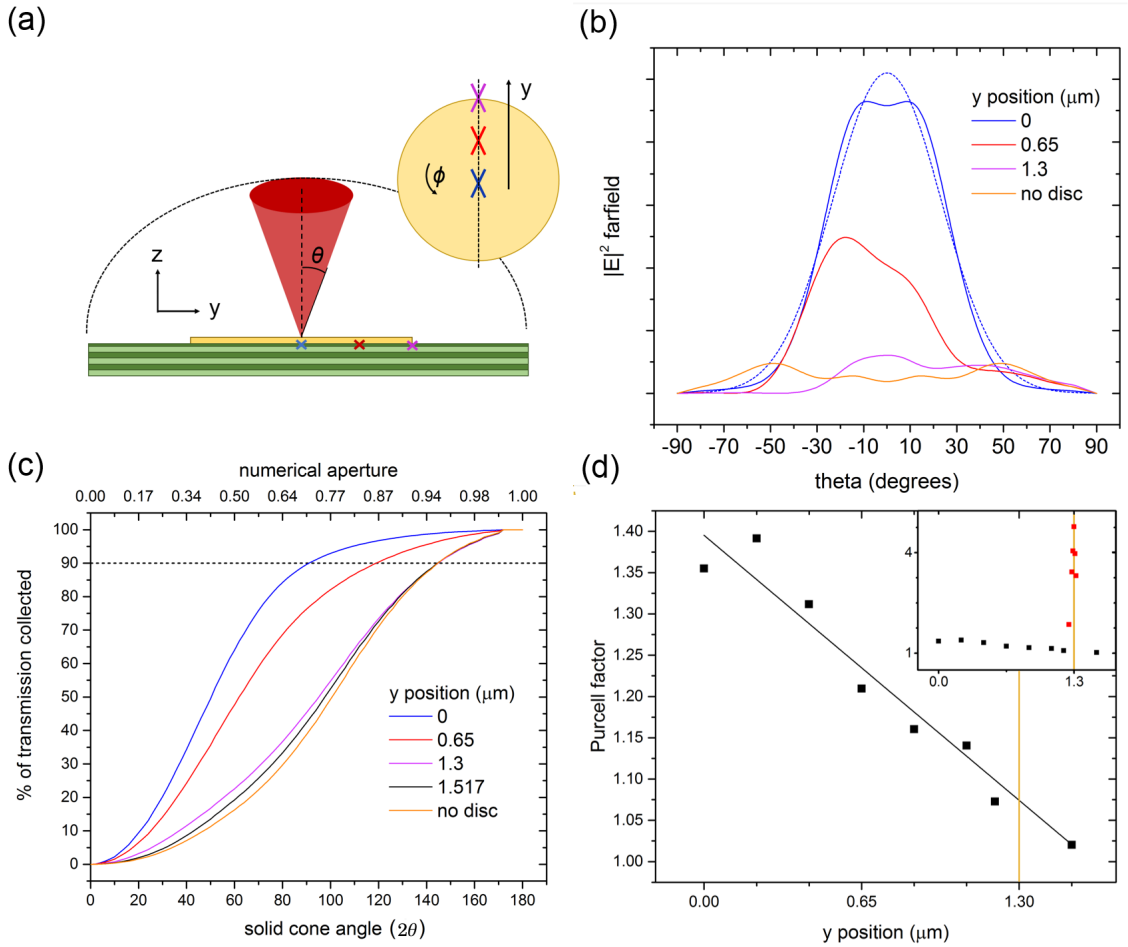

Figure 5.16: (a) Diagram of dipole position under the microdisc. (b) Farfield emission profile through the top of the structure as a function of source y position for a 2.6 μm CTP. The profiles are shown for a fixed ϕ angle orientated along the electric dipole moment and at the mode's fundamental resonance (λ = 1296 nm). The dashed line shows the Gaussian fit for the y = 0 emission. (c) Farfield collection efficiency as a function of numerical aperture. Collection is shown as the percentage of power integrated over all ϕ for a cone with solid angle of 2θ, i.e. the collection by a lens with $NA = sin(\theta)$, over power collected by a lens with NA = 1. (d) Purcell factor as a function of source displacement. Black line shows a linear fit to the data and gold line shows the position of the disc edge. Inset includes additional Purcell factors (red squares) for sources approaching the edge of the disc.

this effect is seen, I propose this is caused by the excitation of surface plasmons occurring at the metal-air interface. This causes an additional (lossy) emission channel only when the source is close enough to couple into an SPP via nearfield excitation and is a cause of the reduced Q-factors that occur for small disc diameters. An apparent discrepancy occurs between the very strong Purcell enhancement observed in the dipole, implying a strong localization of the electric field, and the relatively low electric field intensities seen around the disc edge when the Tamm mode is seen in profile (figure 5.12(b)). However, it should be emphasized that the former shows the CTP excited by a planewave source from the air side. This sort of excitation is possible for Tamm states but not for SPPs (which requires a Kretschmann-type configuration, with the source inside a higher refractive index material relative to, e.g., the air side). In contrast, a dipole source in FDTD will show fluorescence enhancement (relative to being in free space) when located near a metal nanoparticle or edge, as it can excite the SPP via coupling to its nearfield.

5.3 FDTD results of micropillar

In addition to optimizing CTPs as a SPS I also considered how other low Q structures could be improved, specifically low Q semiconductor micropillars (section 1.2.1). As before, the aim is no longer that of simply maximizing the QD-cavity coupling strength but on producing a higher β factor.

5.3.1 Optimizing β factor

Beginning with a previously designed low-Q, high-β micropillar consisting of 5x pair GaAs/AlAs top DBR pair, a (λ/n) GaAs cavity (λ = 900 nm) and 18.5x pair GaAs/AlAs bottom DBR (starting with an AlAs layer), and a 2 μm diameter [31]. This is shown in figure (5.17). The pillar is next excited with a TE dipole source[3] from 850 nm to 950 nm positioned in the center of the cavity layer. Time-domain monitors are positioned in the center of the cavity to record the spectrum and a transmission box is used to measure the emission through the top, bottom and side channels. An example transmission box for a micropillar is shown in the appendix (B.5). Figure (5.18(a)) shows the normalized energy spectrum recorded in the center of the cavity, showing three peaks with a fundamental mode at 910 nm and Q-factor[4] of $\approx$ 220. The nearest higher order mode is blue-shifted by 25 meV from the fundamental mode, so I expect very low rates of loss via coupling into these. Losses through the side channel normalized to the emitted dipole power is shown as the blue line; at the fundamental resonance these are 18%, giving a β factor of 82% (the η factor, the fraction of this going through the top channel, is 65%, giving a total efficiency $\zeta = \beta\eta = 53\%$). The Purcell enhancement as a function of wavelength is shown in figure (5.18(b)).

[3] pulse length = 5.6 fs, pulse offset = 15.9 fs

[4] Because of the higher Q compared to CTPs, the running time of the simulations are increased to allow the fields to fully decay

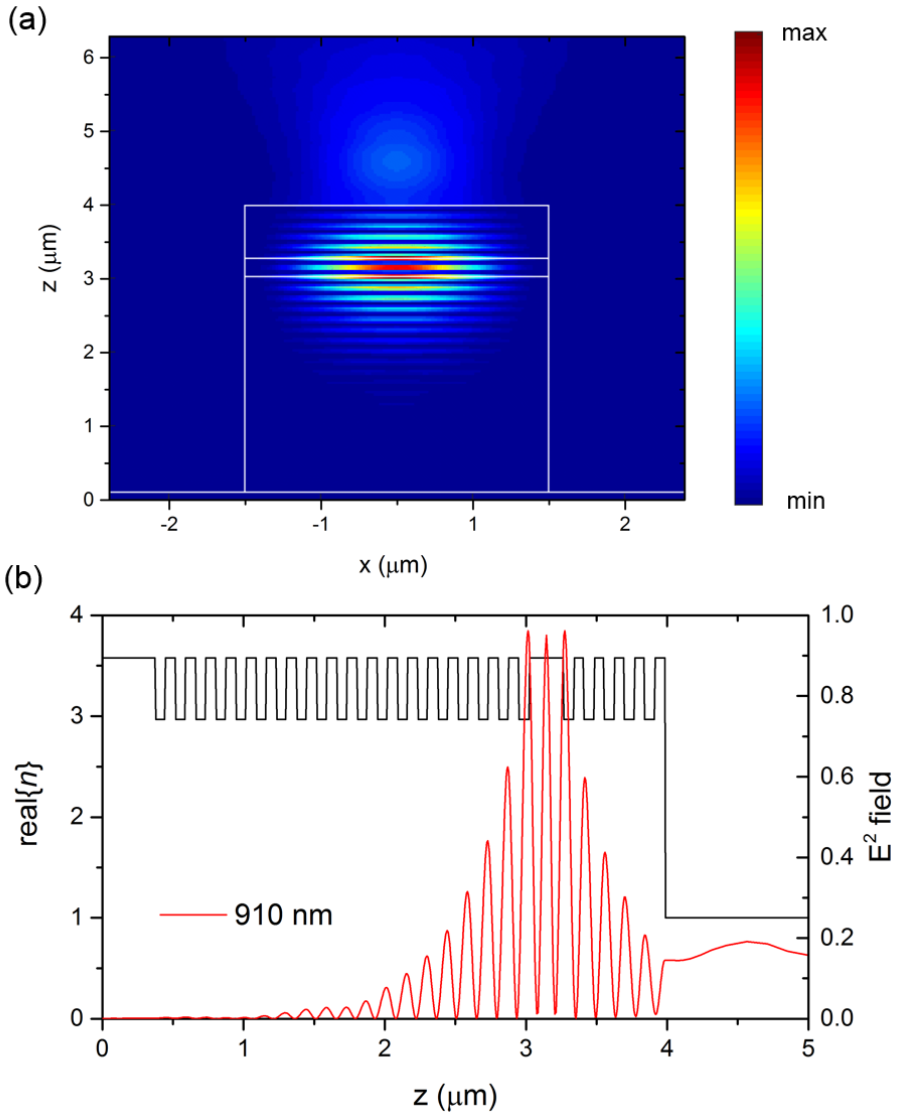

Figure 5.17: (a) FDTD simulation showing the absolute electric field intensity at the fundamental resonance (λ = 910 nm) of a 5x top and 18.5x bottom DBR, (λ/n) cavity micropillar. The source is a CP Gaussian positioned above the pillar. White lines mark the pillar structure. (b) Cross-section of the refractive index and electric field through the center of the structure (x = 0)

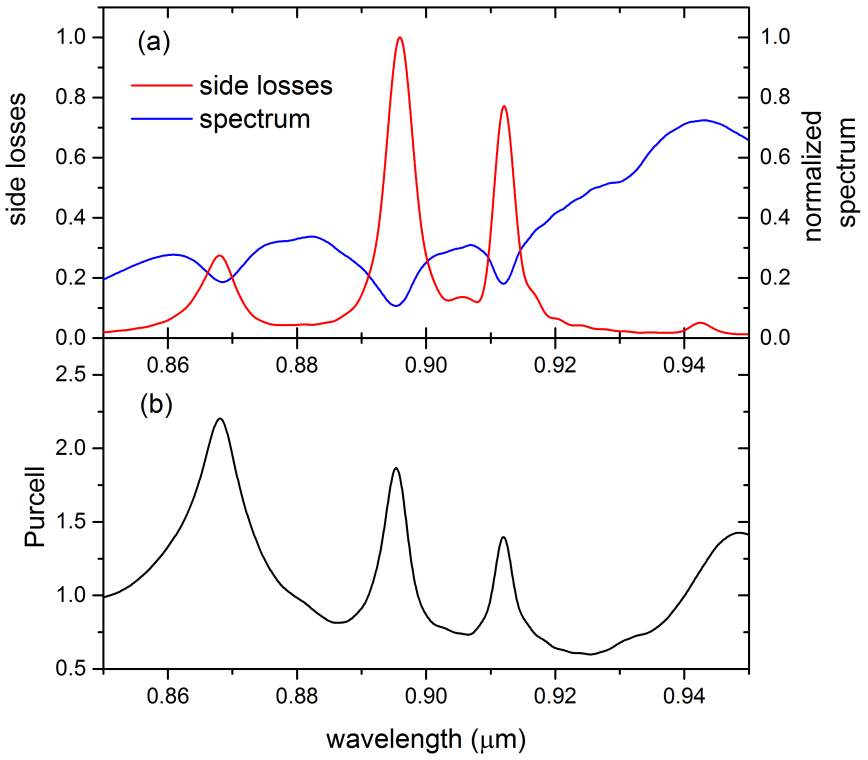

Figure 5.18: (a) Normalized spectrum (red line) for the d = 2.0 μm 5x top and 18.5x bottom GaAs/AlAs pillar. The blue line shows the losses through the side channels of the pillar (γ) normalized by the dipole power. (b) Purcell enhancement of the micropillar.

From this starting point I explored how changing the pillar design could improve the collection efficiency. The pillar diameter has a strong effect, as shown in figure (5.19(a)). There is a slight decrease in β factor as the diameter increases but large oscillations are superimposed over this trend, analogous to the Q-factor oscillations with pillar diameter reported by [27]. These occur with a period of the effective wavelength in GaAs. This is large compared to the fabrication precision that can be attained, so the pillar diameter is likely to be within those regions of higher β where there is less sensitivity to any small variation. The maximum β factor design is d = 1.55 μm which produces a β = 0.90 and an η = 0.75 (compared to 0.82 and 0.65 for the 2 μm diameter pillar respectively). Reducing the diameter also caused a blueshift in the fundamental resonance from λ = 912 nm to 909 nm.

Though this increases the β to almost 90% by the choice of pillar diameter, a quarter of the light in this mode is subsequently lost through the bottom channel despite the asymmetry between the top and bottom DBRs. I believe η remains low due to the simulated micropillar being positioned on a GaAs substrate; transmission through an AlAs-GaAs interface at the bottom of the pillar remains favourable compared to the larger refractive index contrast occurring at a

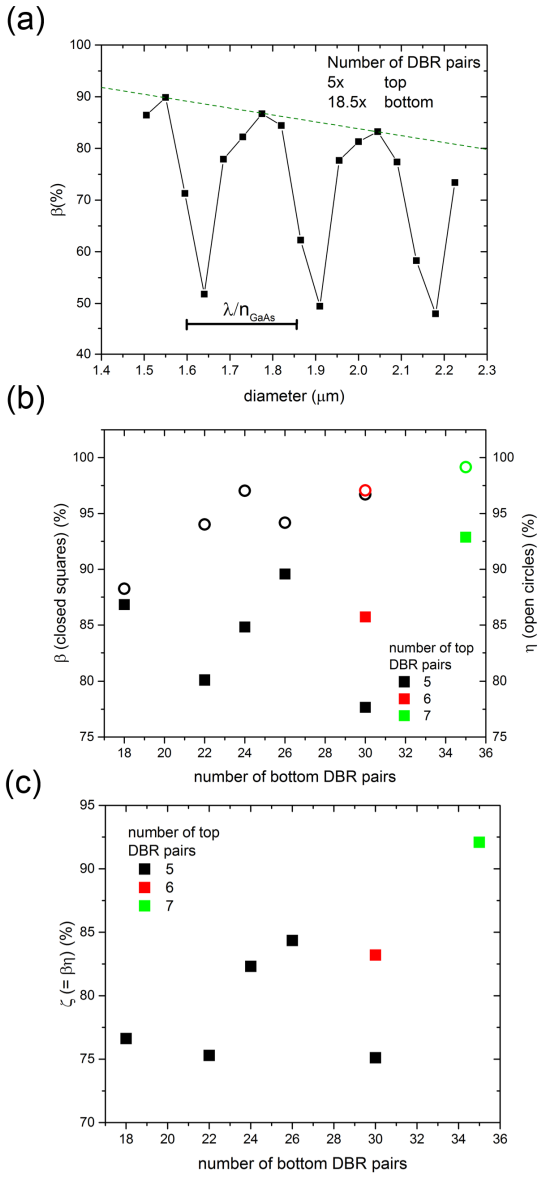

Figure 5.19: (a) Optimization of diameter for a micropillar consisting of a 5x top and 18.5x bottom DBR and (λ/n) GaAs cavity (λ = 900 nm). The oscillations in collection efficiency occur with the period of the effective wavelength in the cavity layer. (b) Optimization of the β (solid squares) and η factors (hollow circles) as a function of different numbers of top and bottom DBR pairs for a d = 1.55 μm pillar. (c) Optimization of the total internal efficiency ($\zeta = \beta\eta$).

GaAs-air interface at the top. Increasing the number of bottom DBR pairs cannot be continued indefinitely as (a) this increases the side losses and (b) there is an upper limit of layers that can be fabricated due to the built-up of strain in the DBRs.

I therefore explored the effect of changing the pillar substrate; as a proof-of-principle I started with an ideal case of a free-standing (i.e. $n_{substrate}$ = 1.0) pillar, equalizing the refractive index contrast between the top and bottom emission channels. Though this might initially seem an unphysical structure, it has been recently demonstrated that epitaxially-grown GaAs structures can be reverse-bonded onto a low refractive index material [153]. The structure is grown starting with the 'top' layer. The 'bottom' is brought into contact with a substrate coated with a UV sensitive glue, the original substrate is removed, and the orientation of the structure becomes flipped. In [153] a photonic wire is attached to an n = 1.46 fiber core with the intent of collecting emission through the bottom (the bonded) face and benefiting from the expanded guided mode of the wire better matching that of the fiber mode. However, my group has proposed this reverse-bonding process be applied to photonic micropillars using a novel citric acid etch that less destructively removes the initial GaAs substrate. The bottom DBR of the resulting flipped pillar can be bonded to a various material, such as a SiO_2 or co-polymer layer, with much lower refractive indices.

For the original structure (d = 2.0 μm, η = 0.65) this change results in an increase of η factor to 0.91. However, there is an associated reduction of β attributed to increased losses by waveguiding into the sides (from β = 0.81 to β = 0.67). This can be restored by the addition of more top DBR pairs to increase the enhancement of the cavity mode but, for the reasons mentioned, this introduces limits of its own. To maximise both β and η a compromise must be reached between the number of top DBR pairs (to increase β) while maintaining the ratio of pairs between the top and bottom DBR, which preserves the η factor. This is shown for a free-standing, d = 1.55 μm pillar in figure (5.19(b)). For a 7x (35.5x) top (bottom) DBR β, η > 90% can be achieved (figure 5.19(c)).

In contrast to reducing the diameter, changing the number of DBR pairs or the refractive index of the substrate material does not produce a shift in the resonance. However, changing the substrate material does result in more complex mode behaviour on the red side of the fundamental wavelength (figure 5.20(a-c)). Because the resonance at 909 nm corresponds to the highest Purcell enhancement, most Gaussian modes etc., and because it aligns with the distinct fundamental mode appearing in the GaAs pillars (orange line), I still identify this to be the fundamental resonance of the free-standing pillars, while the lower energy resonances are neglected.

The fields through the top monitor of the micropillar (z_2) are used to calculate a farfield projection of the pillar emission. From this I calculate the angular distribution of the emission. Figure (5.20(d)) shows the percentage of emission through the top of the pillar that in the farfield occurs within an angle of $nsin(\theta)$ = 0.4, and would be collected by an objective with that NA, normalized against all emission into the farfield (NA = 1.0). Even in the free-standing case,

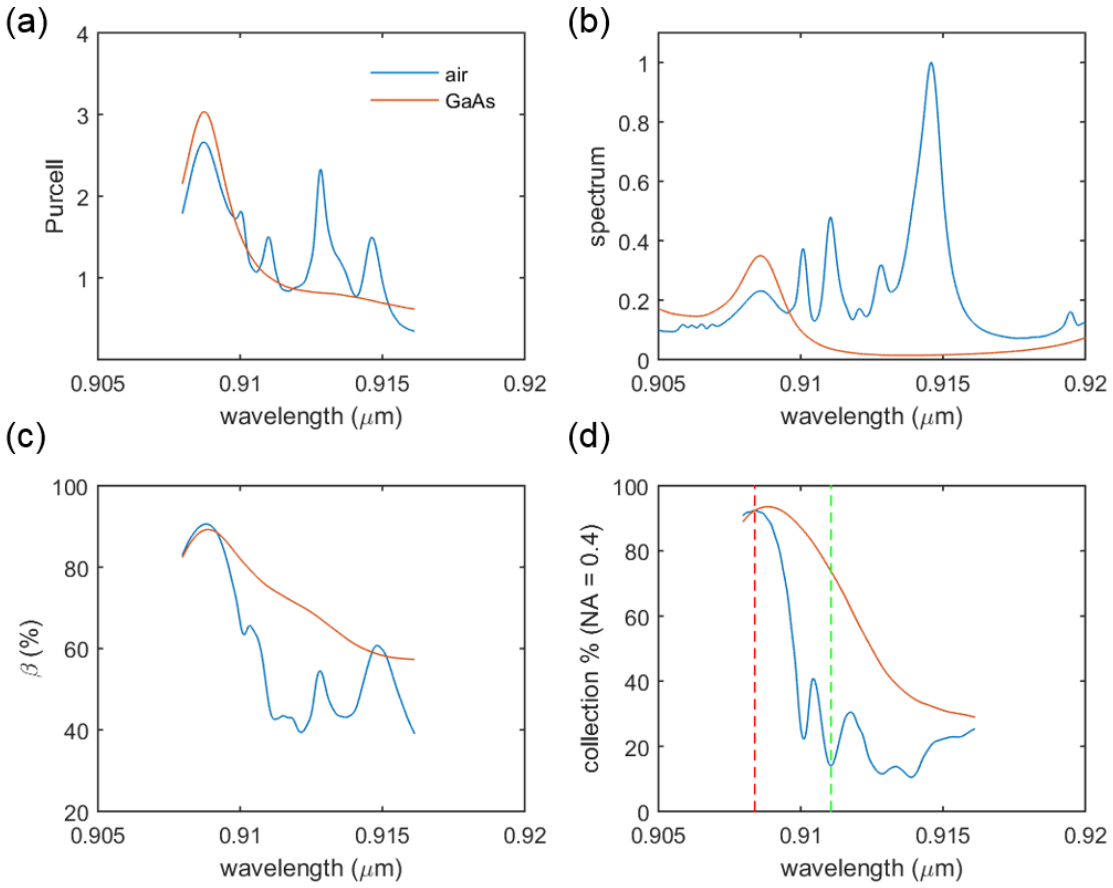

Figure 5.20: Comparison between a 7x (35.5x) d = 1.55 μm free-standing pillar (blue line) and GaAs substrate pillar (orange line); (a) Purcell factor. (b) Normalized spectrum. (c) $\beta = \Gamma/(\Gamma + \gamma)$. (d) The % of photons collected within an NA = 0.4 objective as a function of detuning from the cavity, calculated using the farfield emission through the top of the pillar.

because of the low Q of the pillar, the spectral wander of a QD (~ 10 μeV) is an order of magnitude smaller than the bandwidth with a collection efficiency > 85% for NA = 0.4. The spatial profile of the fundamental mode (marked by the red line in figure 5.20(d)) is shown in figure (5.21(b)) to be Gaussian. When collection at this frequency is plotted as a function of collection angle (figure 5.21(a)) over > 90% is collected within an NA of 0.4 and > 98% within an NA lens of 0.75 typically used for QD spectroscopy. In contrast, the spatial profile of an off-resonance frequency (green line) consists of a central Gaussian and a side band between radial angle, θ = 30° and 50°; this results in the characteristic 'stepped' appearance in figure (5.21(c)).

However, a higher total external collection could be achieved by eliminating a collection objective (that subsequently couples light into an optical fiber through several components, each with an associated loss) but to directly couple into a single-mode fiber instead. If the micropillar cavity is treated as effectively single-mode then the Marcuse approximation can be used to

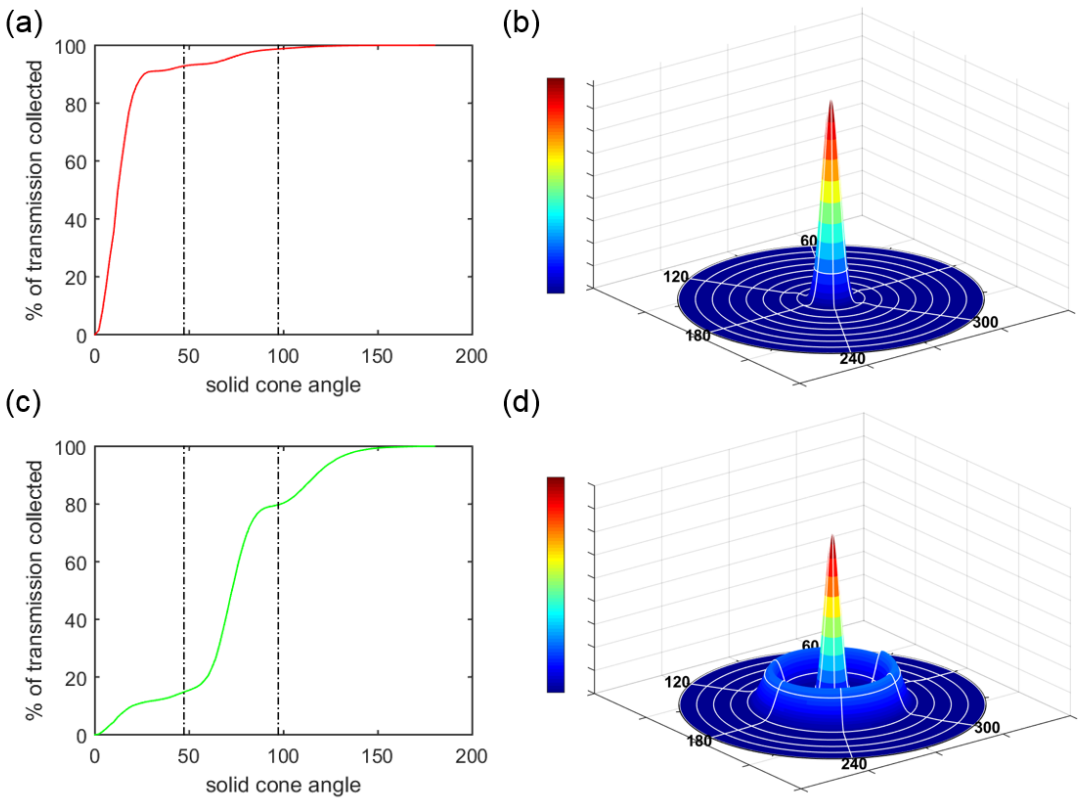

Figure 5.21: The farfield collection through the top of a free-standing 7x (35.5) pillar for different frequencies, shown as a percentage of power collected within a cone with solid angle (= 2θ), i.e. the collection by a lens with NA = $sin(\theta)$, normalized by the power collected by an NA = 1. The red (a) and green (c) lines correspond to the wavelengths marked by dashed lines in figure (5.20(d)). The black lines correspond to an NA of 0.4 and 0.75. (b) and (d) show the farfield projection of these modes through the top surface of the pillar; the fundamental mode at λ = 908 nm (b) shows a Gaussian spatial profile.

calculate the transmission efficiency [154]

$$T = \left(\frac{2w_1 w_2}{w_1^2 + w_2^2} \right)^2 \tag{5.3}$$

where w_1 and w_2 are the mode field diameters (MFDs) of the pillar and fiber modes. For a Gaussian distribution the MFD is where the field intensity ($|E|^2$) reduces to $\frac{1}{e^2}$ of the maximum intensity. Figure (5.22) shows the electric field intensity at the top of our optimized, free-standing pillar (d = 1.55 μm, 7x top and 35.5x bottom DBR pairs) and a normalized Gaussian (blue line) fitted to these points. This has an MFD of 1.28 $\pm$ 0.07 μm. When directly butt-coupled to a HP780 single-moded fiber with an MFD = 5.0 μm (red line), this results in a coupling efficiency of 30.0%, which is represented schematically in (5.22) via the overlap between the pillar and fiber modes.

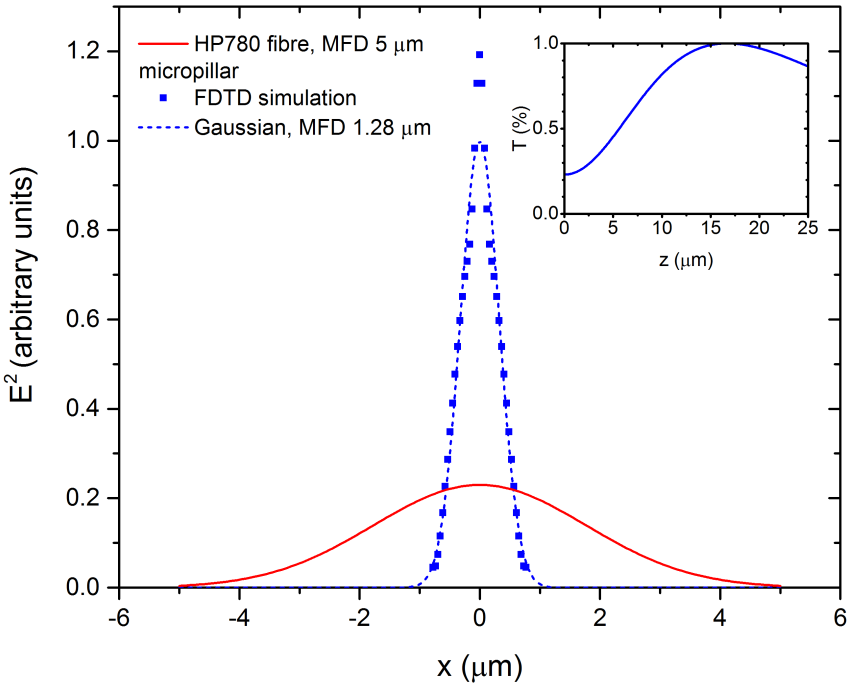

Figure 5.22: Gaussian fitted to the cross-section of the electric field strength through the top of the pillar at the fundamental mode. The Gaussian gives an MFD of 1.28 ± 0.07 μm. The red line shows the cross-section calculated for a fiber mode (HP780 fiber) with an MFD = 5 μm. Its magnitude is scaled so that the overlap between them illustrates the transmission between pillar and fiber when directly butt-coupled (z = 0), calculated using the Marcuse approximation, based on their respective MFDs. **Inset**: Pillar to fiber transmission as a function of thickness of a new optical layer, z, in which the pillar mode can expand.

This can be improved by adding an additional optical layer between the pillar and fiber tip, allowing the pillar MFD to expand as it propagates

$$w(z) = w_{z=0}\sqrt{\left(1+\frac{\lambda^2 z^2}{\pi^2 w_{z=0}^2}\right)} \tag{5.4}$$

This can either be achieved in a monolithic structure by adding a dielectric layer or by actively positioning the fiber above the pillar. At around 16 μm the pillar-to-fiber transmission improves to > 99%. This behaviour is shown by the inset in figure (5.22).

5.3.2 Designing micropillars at 1.3 μm

The optimization technique applied to a previously known low Q pillar is next applied to a pillar designed to produce a fundamental resonance at 1.3 μm for telecoms applications. The pillar

diameter is increased from the previous optimum diameter by the same proportion as the increase in wavelength from 900 nm to 1300 nm (d = 2.25 μm) and consisted of a 7x top and 35.5x bottom GaAs/AlAs DBR with layer thicknesses previously known to produce a stopband centered at 1300 nm. I varied the cavity layer thickness and found a cavity thickness of 403 nm produced a resonance at 1301 nm and a Q-factor of ≈ 370. Variation of the pillar diameter (figure 5.23) results in the same blueshift as the diameter is reduced, and the same oscillations in β factor on the scale of the effective wavelength in GaAs seen previously.

Choosing a diameter of 2.25 μm, which produces a β of 0.93 and η of 0.78 (ζ = 0.73), next is varied the number of top and bottom DBR pairs. This is shown in figure (5.24). All these are calculated with a GaAs substrate. It is noted that between the 5 (30.5), 7 (30.5), 8 (30.5) and 7 (35.5) top (bottom) pillar all produce very similar internal collection efficiencies (5.24(b)). In the absence of any other factor we might be led to simply select the structure with the fewest number of pairs. The 5 (30.5) pillar has a low Q and Purcell compared to the other structures. This results in a relatively low β factor, which is compensated by having a higher η, but which also makes the spectral separation between individual modes less distinct (figure B.9). I therefore decided that the 7 (30.5) pillar would make for a better SPS. This pillar's side emission, Purcell enhancement and farfield collection (> 92% within NA = 0.4) are plotted in figure (5.25).

5.3.2.1 Designing micropillars at 1.3 μm for cold T

To account for the effect of cooling on the resonance a TMM simulation of the micropillar with the same DBR and cavity layer thicknesses is run with the temperature-dependent permittivities described in (5.1.2). Though this accounts for the 30 nm blueshift that occurs between RT and 15 K, the TMM (which is one-dimensional) does not account for the blueshift caused by cavity confinement. Comparing the TMM resonance with resonances produced by FDTD for fixed d = 2.25 μm pillars, from when different cavity thicknesses were explored, showed that this shift occurs with a constant proportion, $\lambda_{TMM} = \alpha\lambda_{FDTD}$, where α = 1.01.

The results of the temperature adjusted pillar design are shown in figure (5.26). This shows the power transmission coefficient (from TMM) of a cold temperature-adjusted design at RT (black line) and cold temperature (red line), both corrected for the pillar blueshift. The RT resonance occurs at λ = 1330 nm and a FDTD simulation of an identical temperature-adjusted pillar (shown via the Purcell enhancement; blue line) closely matches this. When cooled the pillar resonance should then blueshift by 30 nm to the resonance occupied by the cold temperature TMM at λ = 1300 nm.

5.4 Summary

In this chapter I use the TMM and FDTD methods to design and simulate CTPs and low Q micropillars to be resonant at telecoms wavelength and where the β factor can be engineered to a

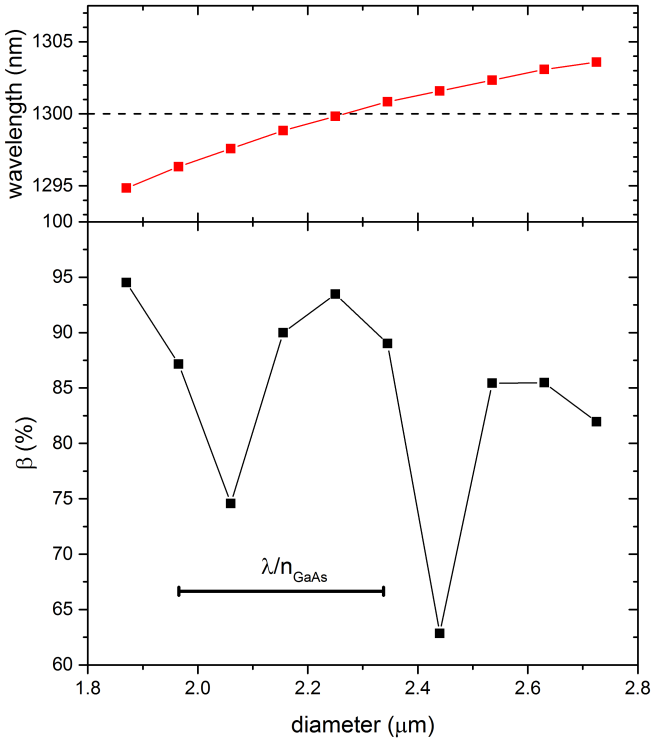

Figure 5.23: Shift in fundamental mode resonance (red line) and β factor (black line) as a function of pillar diameter. As in figure (5.19(a)), the latter oscillate with a period of the effective wavelength. Pillar consists of 7x (35.5x) top (bottom) GaAs/AlAs DBR and 403 nm cavity.

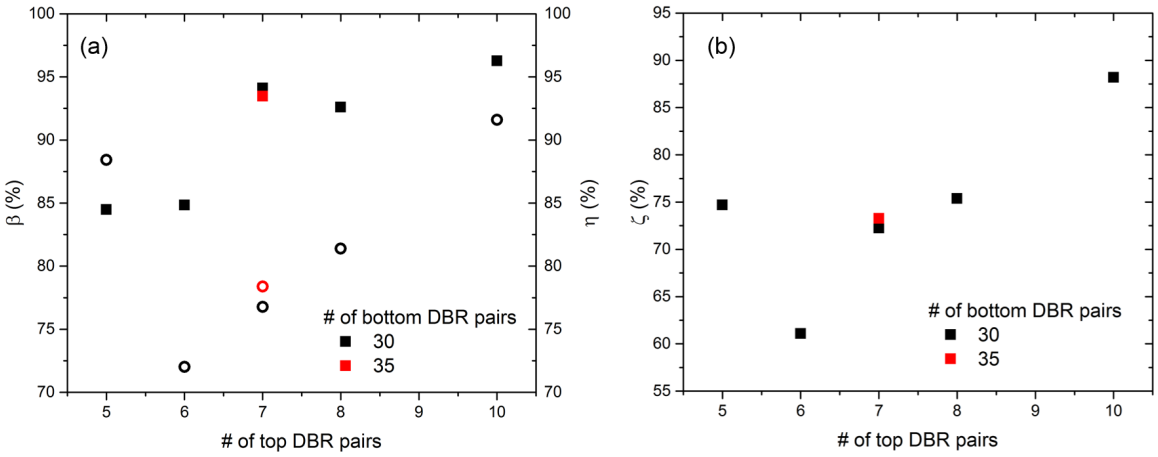

Figure 5.24: Optimization of the β (squares), η (hollow circles; both (a)), and ζ (b) factor as a function of different numbers of top and bottom DBR pairs for a d = 2.25 μm pillar.

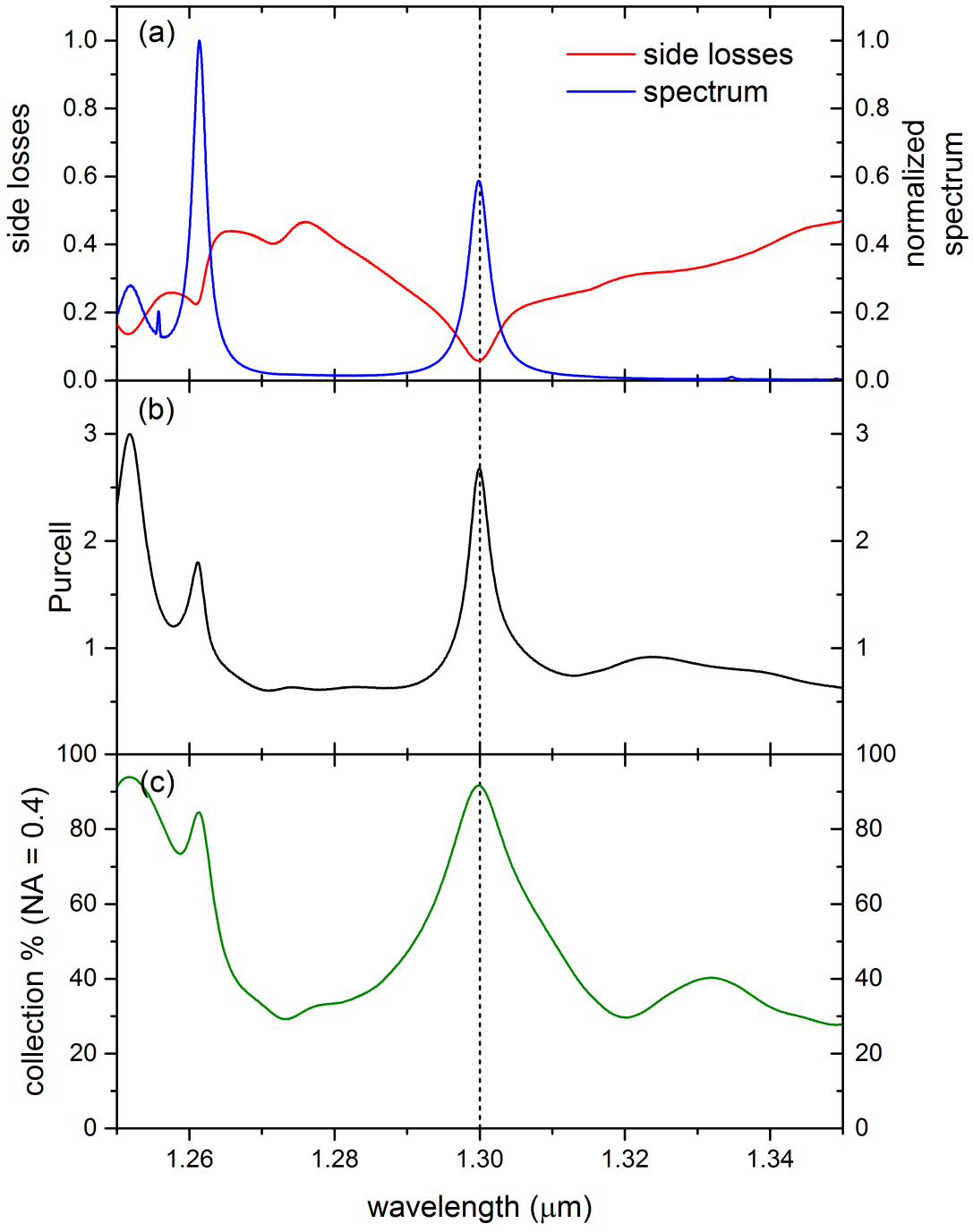

Figure 5.25: (a) Normalized spectrum (red line) and side losses (blue line) for the d = 2.25 μm, 7x (30.5x) DBR pillar. (b) Purcell enhancement. (c). Collection % within an NA = 0.4 objective.

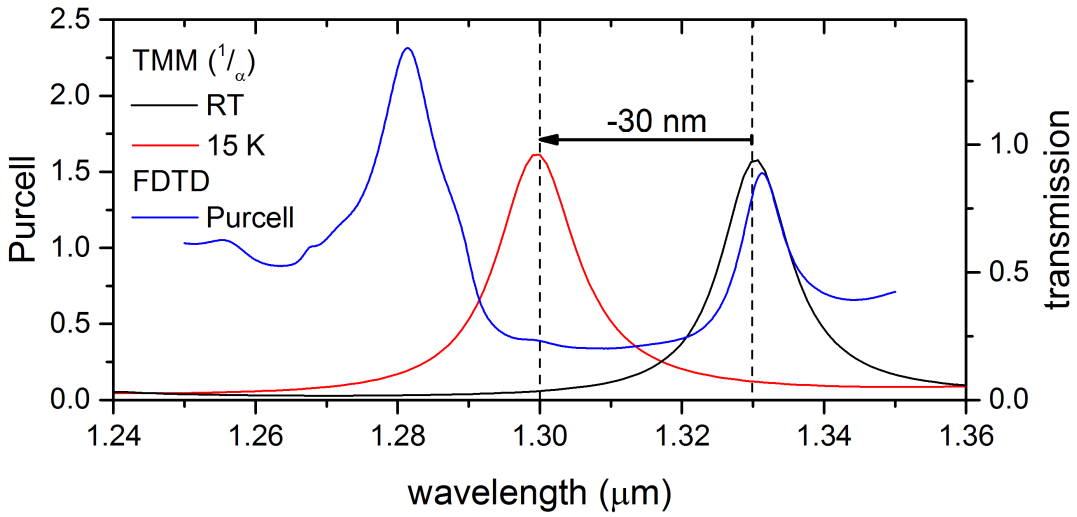

Figure 5.26: TMM calculations showing the transmission for a (97/114) nm GaAs/AlAs DBR and 407 nm cavity micropillar at room temperature (black line) and cold temperature (red line). Both have had their resonances shifted by $\frac{1}{1.01}$ to account for the blueshift of pillar confinement. The blue line shows the resonance (via plotting the Purcell enhancement) of the same specification 7x (30.5x) micropillar in FDTD using the standard material refractive indices; it aligns well with the shift-corrected TMM and would be resonant at 1.3 μm if a similar 30 nm blueshift occurs when cooled.

high value. The optimization method outlined can be extended to any other wavelength that can be made to occur within the stopband of a DBR. The CTP produced by 2.6 μm diameter, m = 25 nm gold disc and s = 75 nm GaAs spacer has its fundamental resonance at λ = 1.3 μm and has emission properties that make it favourable for a high external collection efficiency. Alterations of these designs to lower the operating temperature for SPS use are also described. The tolerances of these structures (e.g., to variation in diameter, QD resonance and position within the cavity) compare favourably to high Q systems in both CTPs and low Q micropillars.

CHAPTER 6

EXPERIMENTAL RESULTS

In this chapter I present an experimental study of confined Tamm plasmon structures. Reflectivity and non-resonant PL measurements are performed on CTPs containing QDs emitting at 1.3 μm, and with varying metal thicknesses and disc diameters. A Fourier image spectrometer is used to measure the angular response of the samples by measuring in the Fourier plane, from which the dispersion relations can be found. These show evidence of confinement as the disc diameter is reduced. Lastly, these designs are successfully integrated into a novel photodetecting device, demonstrating that CTP modes are a realizable tool for scalable optical devices.

6.1 The Sample

The CTP sample measured in this thesis is fabricated by MBE by Ed Clarke at the University of Sheffield National Epitaxy Facility. A DBR containing 17.5x GaAs/AlAs pairs is grown on a GaAs substrate with thicknesses of 95/110 nm, which are expected to produce a photonic stopband at 1.3 μm (as described in 5.1.1). On top of the final (AlAs) layer is grown a 75 nm GaAs spacer layer.

Inclusions of InAs/GaAs quantum-dots-in-a-well (DWELL) are grown within the structure in a layer 5 nm from theAlAs-spacer interface, since this is shown by the TMM to be the position of the maximum field enhancement of the TP (for s = 75 nm and m = 25 nm). The quantum well is a 5 nm layer of $In_{(0.18)}Ga_{(0.82)}As$ in which the InAs seed layer is incorporated; this structure reduces the strain of the QD, which further increases their size and shifts their resonance to 1.3 μm [16, 155]. Before the growth of each DWELL layer the sample is annealed at 580 °C under an As_2 flux to smooth the sample surface before being cooled to 500 °C, and is followed by a 6 nm layer of GaAs before the temperature is returned to 580 °C for the growth of the remaining spacer layer.

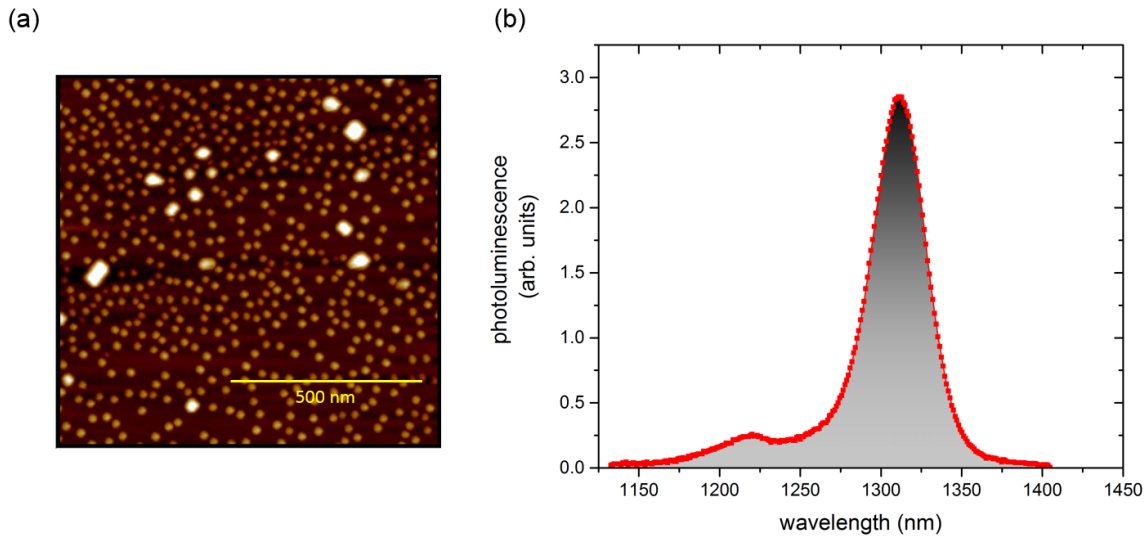

Figure 6.1: Characterization of the QDs. (a) AFM measurement of uncapped QDs grown using the method described. (b) Room temperature PL of the sample before metal deposition (i.e. bare DBR only) with an above-resonance laser source. The emission peak occurs at 1312 nm (FWHM = 40 nm). Measurements were performed by Dr Ed Clarke, University of Sheffield.

The thickness of the spacer is adjusted to compensate for the DWELL, so the effective thickness remains 75 nm GaAs. For room-temperature PL measurements a second sample is used with an additional three InAs/InGaAs DWELL layers included in the topmost GaAs layers of the DBR. These are shown by the red and blue dashed lines respectively in figure (5.3). Characterization of the InAs QDs is shown in figure (6.1). A broad emission from the dots is seen occurring between 1290 nm to 1330 nm, with a peak at 1312 nm and FWHM of 40 nm. A smaller emission peak in the QD sideband, occurring at 1215 nm, is attributed to enhancement from the first Bragg mode of the DBR. The QDs are undoped and have a density of 5.7×10^{10} cm^{-2}.

A layer of PMMA resist is next deposited onto the spacer and photolithography is used to create a pattern for the metal microdiscs of the Tamm structure. The gold layer is added by vapour deposition and a final lift-off of the resist layer produces the finished CTP structure. Samples are fabricated with a range of gold layer thicknesses and these are confirmed by atomic force microscopy (AFM) (performed by Dr Kenneth Kennedy, University of Sheffield). The complete range of thicknesses is found to be 5.4 nm, 11.4 nm, 17.0 nm, 23.1 nm, 28.8 nm, 33.7 nm, 38.0 nm, 43.8 nm and 48.1 nm. The range of disc diameters covers 0.8 μm to 20 μm, with increments of 0.1 μm up to 2.6 μm, and 0.325 μm ($\lambda/4$) from 2.6 μm to 13 μm. A d = 20 μm disc is used to emulate the planar (i.e. non-confined) TPs. An image of the discs is shown in the inset in figure (6.5(b)).

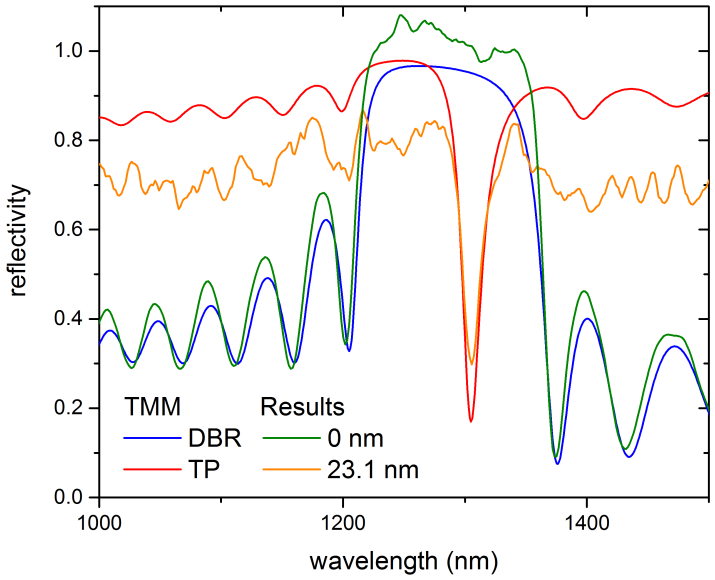

Figure 6.2: Normal incidence reflectivity measurement for the bare DBR (green line) and d = 20 μm CTP (orange line). For comparison blue and red lines show the reflectivity calculated by TMM for the DBR and m = 23.1 nm TP respectively (the metal thickness is characterized by AFM).

6.2 Reflectivity measurements

Reflectivity measurements are taken using the FIS (section 4.1.1) with a 40x (0.75 NA) objective and set in critical illumination using a broad white light source. Both excitation and collection occur through the metal side of the structures. The reflectivity is normalized to the source spectrum which is taken by measuring the reflection of a gold mirror. Figure (6.2) shows the reflectivity at normal incidence for the bare DBR (green line) and d = 20 μm disc (orange line). In the latter a dip in the reflectivity spectrum is observed at the resonance of the TP. Both the stopband of the DBR and reflectivity dip of the TP match very well with those predicted by the TMM for a DBR and planar TP respectively. Angle-resolved reflectivity spectra are taken for the bare DBR and 20 μm disc, shown in figure (6.3(a)), to measure the dispersion relation of the stopband and TP. At higher angles the effective thickness of the DBR period and metal layer at normal incidence is increased, resulting in a shift to higher energies. The 20 μm disc produces a parabolic dispersion expected for planar TPs (figure 3.6).

Figure (6.3(c)) shows that shift in TP resonance shown by the reflectivity dip as a function of the gold layer thickness (all taken for d = 20 μm discs). As the metal layer is reduced the TP has a redshift, from 1305 nm (m = 23.1 nm) to λ = 1356 nm (m = 5.4 nm), that closely follows that predicted by the TMM (blue line) for planar TPs. The magnitude of the reflectivity dip decreases with increasing thickness as the top metal layer (through which the TPs are excited) becomes

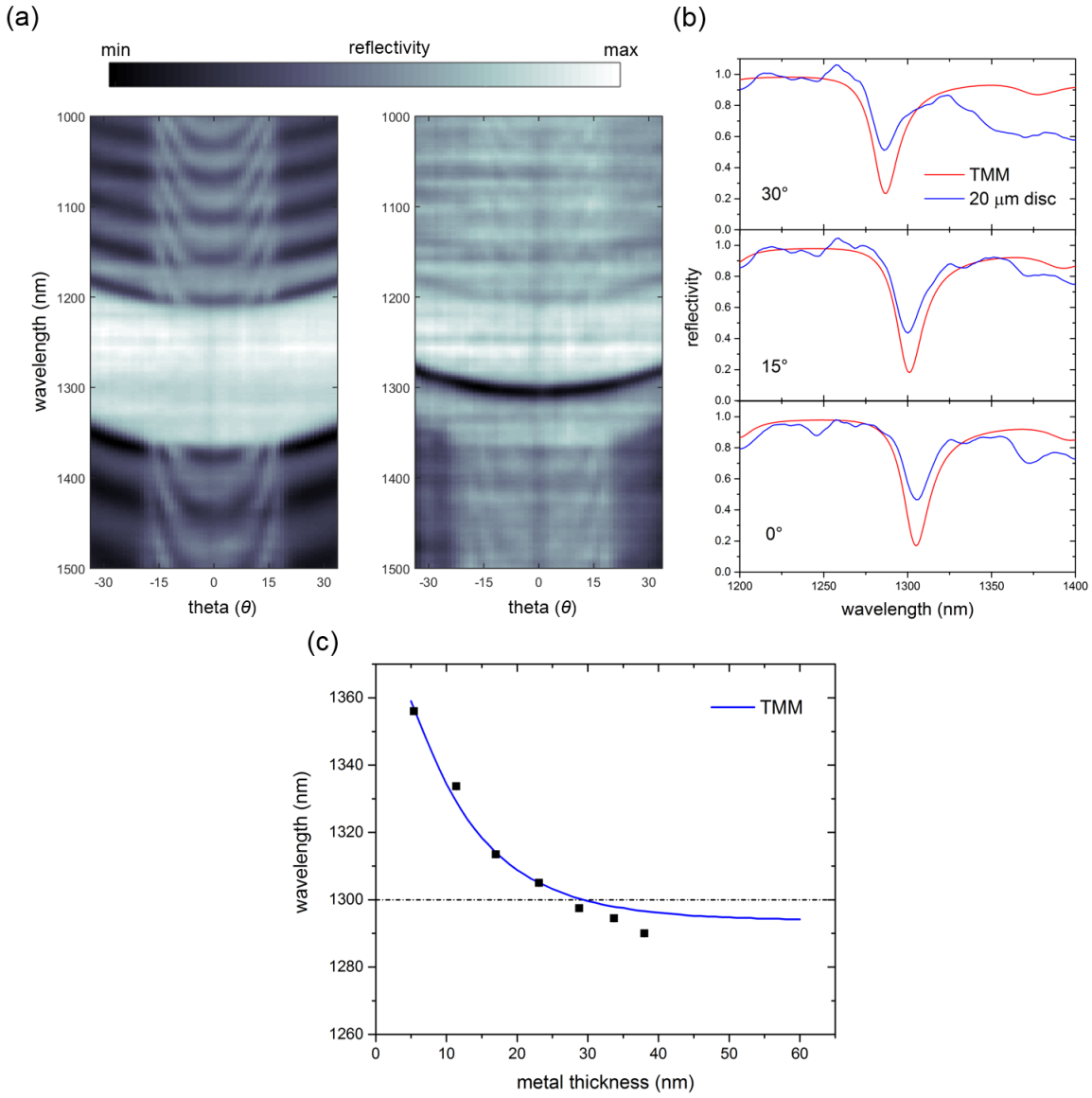

Figure 6.3: (a) Angle-resolved reflectivity measurements showing the dispersion relation for a bare DBR and d = 20 μm CTP. (b) Reflectivity profiles through the latter taken at 0°, 15° and 30° (blue lines) compares the shift in the position of the TP resonance with those predicted by the TMM. (c) Position of reflectivity dip as a function of metal thickness (black squares). The blue line shows the calculated shift in the TP resonance using TMM (figure 5.7(a)).

more reflective and less light penetrates to the DBR interface. This prevents the observation of TP resonances beyond m = 40 nm.

6.3 PL measurements

6.3.1 Varying metal thickness

Room temperature PL is next taken using the FIS by switching the source to a continuous wave 635 nm laser (i.e. above the QD's resonance). These are taken using the 100x (NA = 0.8) objective. I calculate this optical path produces a laser spot size of d = 4.4 μm, though imaging on the FIS camera suggests this is closer to 4.8 μm. The excited QD layers contain emitters with a range of emission wavelengths, so the PL acts as a 1290-1330 nm source that is filtered through the enhancement caused by the TP. An example PL spectrum for a m = 23 nm, 20 μm diameter TP, taken with the spectrometer fiber positioned for collecting emission at normal incidence, is shown in figure (6.4(a)), with the PL from the bare DBR shown for comparison. A distinct enhancement in the PL counts can be seen occurring at 1310 nm, corresponding to the emission peak of the QD layer, as well as a broader phonon sideband at lower wavelengths.

The increase in PL counts shown in figure (6.4) is ~11× that of the same measurement taken with the bare DBR (i.e. without any metal disc). The power reflectivity coefficient, calculated by TMM for an m = 23 nm air-gold-GaAs layer, is R = 0.88, so the count increase occurs in comparison to without the metal layer despite the QDs receiving 12% less pumping power. Emission intensity is shown as a function of pump power in figure (6.4(b)) by adding neutral density (ND) filters of increasing optical density to the laser excitation path, with power normalized to the maximum excitation power of the laser (ND = 0.0). The increase in emission maintains a linear trend, demonstrating that under the current illumination setup the QDs have not yet reached their saturation limit. Angle-resolved PL of the d = 20 μm disc, taken with the 40x objective to allow comparison with the angle-resolved reflectivity, is shown in figure (6.4(c)). The PL enhancement of the QDs follows the position of the TP at higher angles of incidence. This dispersion has the same parabolic dispersion relation shown in the reflectivity measurement, and shares the same gradient, and hence effective mass, of the TP (though PL is shifted to higher wavelengths corresponding to the peak in the QD distribution). This explicitly demonstrates that it is the coupling to the Tamm modes that is the cause of the measured PL increase. Accounting for the different pumping power levels, the emission through the top channel increases by roughly two orders of magnitude in the CTP.

This increase is a combination of the spontaneous emission enhancement (Purcell factor), increasing of the coupling rate ($\beta\eta$) via TPCE into the mode emitted above the disc, and improvements in the extraction with free-space optics due to these modes being less divergent, more Gaussian and more normal to the sample in the farfield. Assuming the modest Purcell enhancements predicted by FDTD ($F_p \approx 1.5$), the change in efficiency resulting from improved

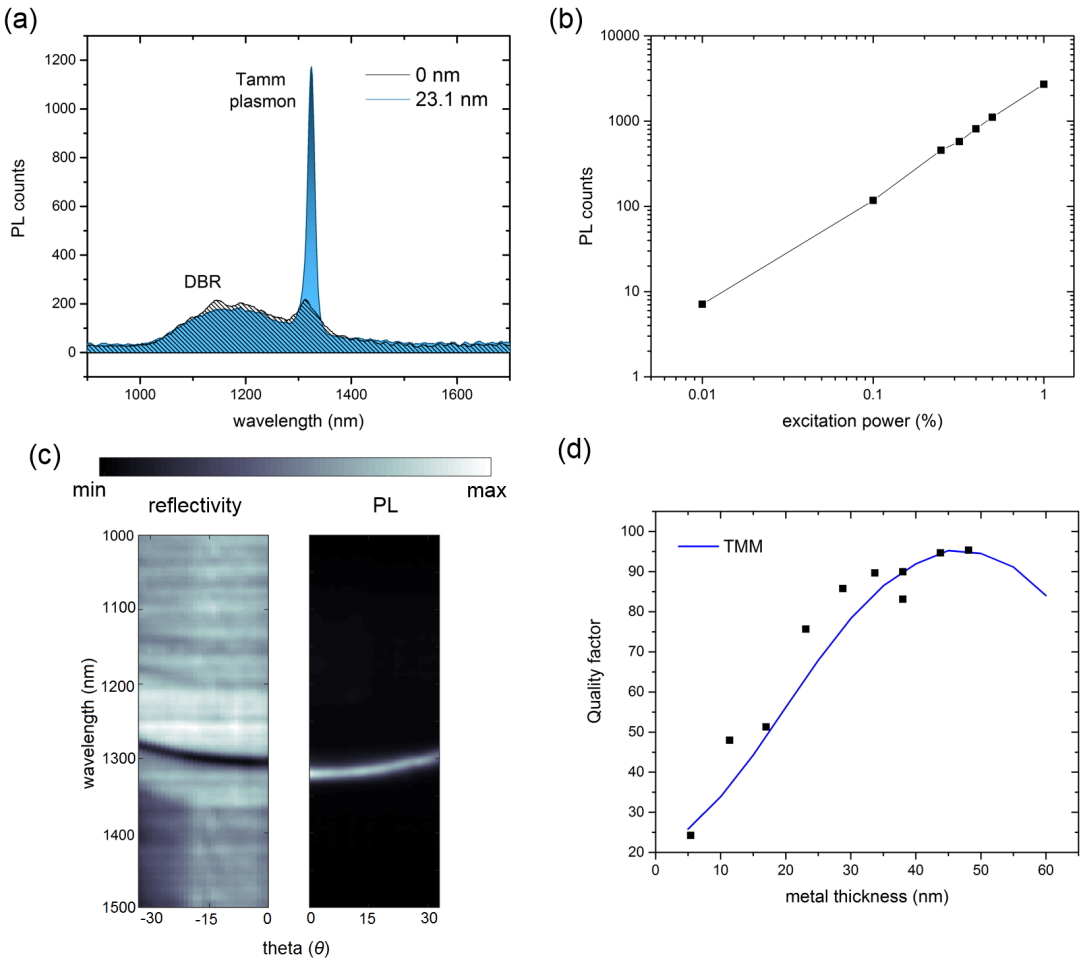

Figure 6.4: (a) Room temperature non-resonant (635 nm) photoluminescence spectra of the QDs without (black line) and with a m = 23 nm (d = 20 μm) metal layer (blue line). Note that in the latter case this increase occurs despite pumping through the metal layer decreasing the excitation power at the QD layer by an estimated 88% (b) PL counts plotted as a function of lasing power to demonstrate that the TP-enhanced dot emission has not been saturated. The highest excitation power from the laser is 0.80 mW, which is reduced by adding ND filters with increasing optical density. (c) Angle-resolved reflectivity and PL measurement (both taken with 40x objective) of the d = 20 μm CTP. The dispersion of PL enhancement has the same relation at higher angles as the relation for the TP mode, demonstrating this is the cause of the increased QD emission. (d) Q-factors of PL peaks as a function of metal thickness. Blue line shows the calculated Q-factor using TMM (figure 5.7(d)).

coupling and channelling of the emission to a Tamm mode is an around 50× increase over the bare DBR.

Given the QD density and laser spot size, a rough estimate of the number of dots under excitation can be given; however, the size of the CTP mode under the 20 μm disc will also be larger than that given simply by the laser spot size without the metal disc, which makes an exact comparison between the two difficult. FDTD simulations of CTPs with the largest disc diameters have coupling rates into the top mode that saturates at around 20%. Given the high density of QDs ($\sim 10^{10}$) the counts per dot indicates that the collection efficiency is much lower than this. One reason for the low brightness may be the relatively broad excitation source being used, together with the high density and high operating temperature, lowering the internal efficiency of the dots or exciting them into non-resonant charged or biexcitonic states. Methods to increase extraction, such as SILs or substrate engineering, are described in section (5.2.1.3) but before more elaborate changes it would be most valuable to measure PL in the low-density, low temperature regime. This would allow time-resolved PL, and hence the coupling rate could be directly calculated using the $\beta = F_p/(F_p + \gamma)$ equation (other measurements are described in further detail in the concluding chapter). Another limit to the brightness in this setup is that the QDs are not pumped to saturation due to the losses exciting through the metal layer. Alternatives to this, such as exciting through the side channel, would add surfaces close to the QDs during fabrication, something TPs specifically benefit from avoiding. The other solution would be to simply use a setup with a higher maximum pumping power.

For the thicker layer, even when the total counts reduce compared to without the metal layer, there is a narrowing of the QD peak in the PL. To better identify the CTP's resonant wavelength and Q-factor the sideband of the QDs is fitted to a skewed distribution and subtracted from the PL spectrum. A Gaussian distribution is then fitted to the remaining peak (an example of this is shown in figure 6.5(a)). The Q-factor of the PL peaks for different gold layer thicknesses are shown in figure (6.4(d)). This shows an increase in the Q-factor with metal layer thickness that closely follows that expected by the TMM (blue line), though the maximum thickness sample I had did not exceed 50 nm (where the predicted turning point occurs). Though the PL peaks are narrower there is a sharp drop in the enhancement observed beyond m = 30 nm, which I attribute to the increased loss from reflectivity and absorption when collecting through the metal layer offsetting any emission increase from the Tamm mode. The enhancement also decreases as the metal layer is reduced, dropping to ~ 8.5× for m = 11.4 nm and ~ 2× for m = 5.4 nm. Some of this is due to the fall in mode quality, but also to the shift in the CTP resonance away from that of the QDs. The highest enhancement occurs for the m = 23 nm CTP already demonstrated.

6.3.2 Varying disc diameter

The PL is next measured for varying disc diameters. The m = 23 nm structures are chosen as these produced the highest intensity emission. Example spectra showing the PL peaks at normal

incidence and with the QD sideband subtracted are shown for a range of diameters in figure (6.5(a)). Gaussian fitting functions (dashed lines) are shown for the 20 μm and 2.6 μm diameter discs. The shift in peak position and Q-factor as a function of diameter are shown in figure (6.5(b)) and (c) respectively. As the diameter is reduced the resonances blueshift as expected when the mode is confined.

There is also a trend of decreasing Q-factor (red line), though there are some oscillations. The initial Q-factor, for the unconfined (d = 20 μm) TP, is ≈80 and retains similar values until the diameter reduces below 8 μm. This is a similar trend observed for the FDTD simulations (blue dashed line; this is the same as the red line in figure 5.10(b)) though the measured Q-factor values for the minimally-confined TPs are 20% lower. The offset in Q-factor between experiment and FDTD decreases with smaller diameters. I believe the qualities of the experimental structures are reduced due to factors not included in the FDTD simulation, such as fabrication imperfections at the spacer-metal interface; as the diameter is decreased other loss mechanisms such as scattering and plasmon-excitation at the disc edges, which are included in FDTD, become dominant.

As the diameter is decreased there are changes in the dispersion seen in the angle-resolved PL (figure 6.6). For the 13 μm disc the emission pattern remains that of the non-confined TPs. However, at smaller diameters the discretization of the modes appears, indicating the onset of confinement. In the 2.6 μm case only a single mode at the fundamental resonance can be observed. The higher-order modes that appear at higher angles and with increasing spectral separation are not experimentally observed in the intermediate discs, though a blueshift in the resonance is, since these modes are much weaker than the fundamental and these structures have an insufficient enhancement off-resonance to be imaged.

6.4 Photodetector CTPs

Though the focus of the thesis has been on the utilization of CTPs to make SPSs, several other devices have been proposed that employ TPs. Photodetectors using planar TPs have been demonstrated to make effective spectrometers due to their higher Q-factors and narrower spectral width compared to SPP-based detectors [156]. These photodetectors enhance the generation of charge carriers in a doped polymer layer that is placed within a metal-metal microcavity positioned adjacent to the DBR. However, since the highest electric field intensities in TPs occurs in the spacer layer of the DBR I have designed CTP photodetectors using QD emitters and which is resonant at 1.3 μm. These were experimentally characterized by Edmund Harbord and Ben Cemlyn. These devices can detect spectral and polarization information from the photocurrent generated by different metal structures, and also have the benefit of being spatially localized.

CTP structures consisting of 17.5x GaAs/AlAs pair DBR, 75 nm GaAs spacer and 25 nm gold layer were fabricated containing a layer of 1.3 μm InAs/GaAs DWELL, using the method previously described except that the upper 50 nm of spacer is n-doped with silicon with a density

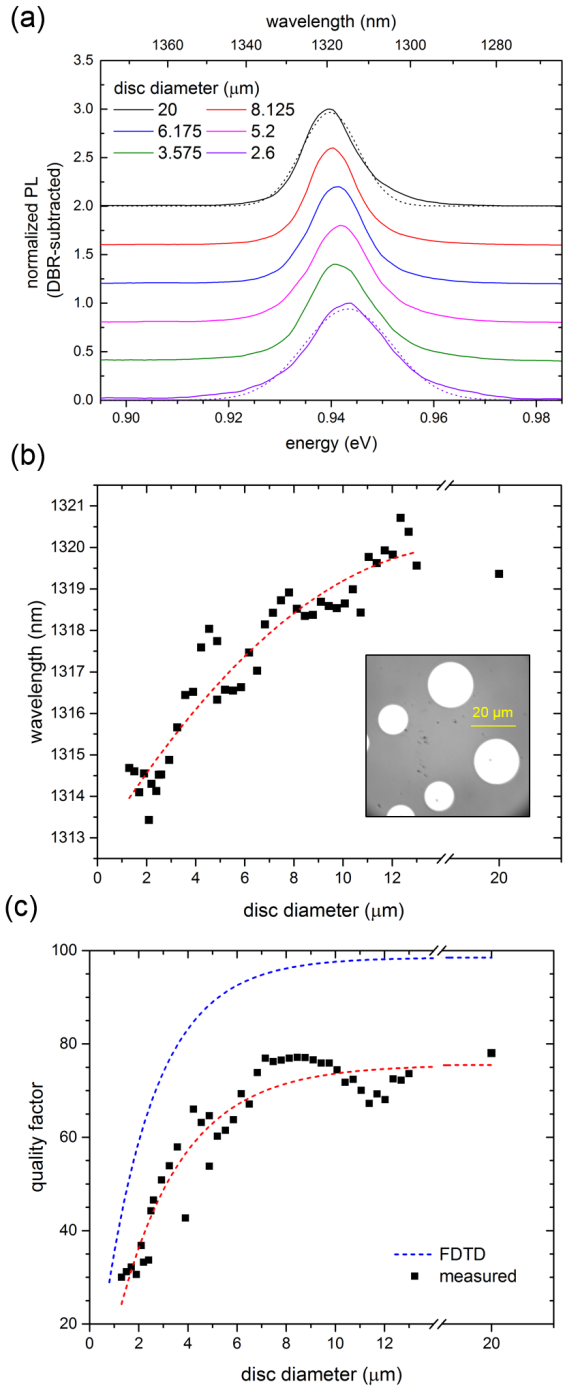

Figure 6.5: (a) Normalized PL spectra of QDs in a CTP for varying disc diameters (m = 23 nm), with the QD sideband (measured from the bare DBR) subtracted and Gaussian fits (dashed lines) added. (b) PL resonance as a function of disc diameter. The red dashed line is a guide to the eye. **Inset**: Real image of the microdiscs taken with the 40x objective (Kohler illumination). (c) PL Q-factors as a function of disc diameter. The red and blue dashed lines are fitted exponentials to the measured and FDTD results respectively.

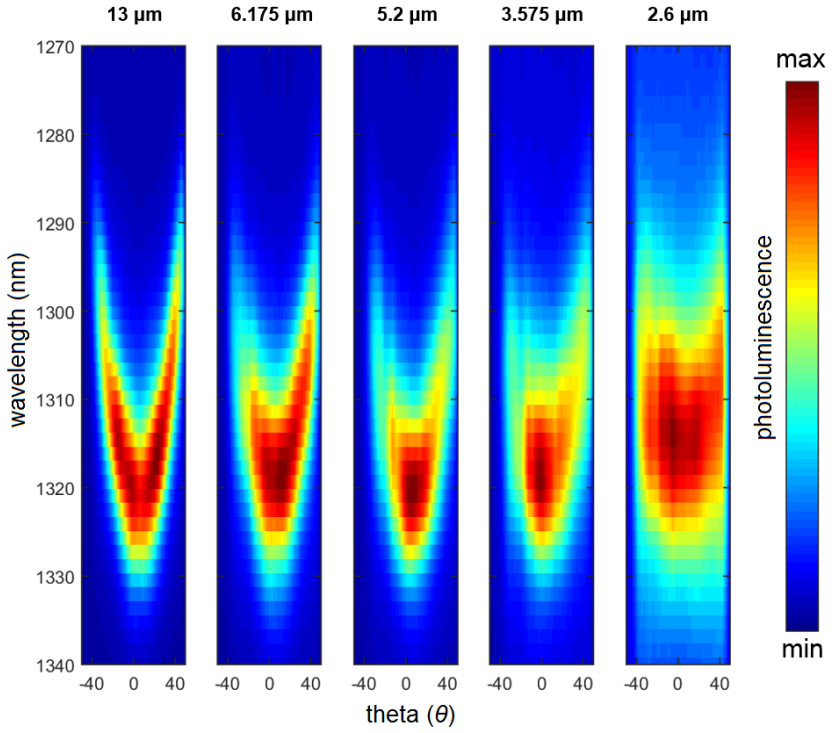

Figure 6.6: Angle-resolved PL (100x objective) for different disc diameters. As confinement is increased by reducing the diameter, there is a transition from a continuous and parabolic dispersion, seen in the planar TPs, to discrete mode at the TP fundamental resonance.

of 2×10^{18} cm^{-3}. Circular metal-to-semiconductor contacts are fabricated around each CTP structure to apply a bias and to measure the photocurrent. These are also gold so can be made in the same fabrication step as the CTP disc (the thickness of the contacts is increased to prevent formation of Tamm plasmons beneath them). A cross-section of the device is shown schematically in figure (6.7(a)) and a scanning electron microscope image in figure (6.8(a)). The optical response of the sample's are measured by the change in photocurrent when the CTP mode is excited. The stronger light-matter coupling of QDs positioned in the mode will produce charge carriers in the spacer layer, reducing the resistance between the contacts. The experimental setup is shown in figure (6.7(b)). The sample is placed beneath the tip of a lens-ended fiber mounted to a mechanical stage through which it is illuminated by a widely tuneable laser. A circulator in the excitation path connects to a optical spectrum analyser, allowing reflectivity to be measured. This arrangement is used to align the fiber relative to the disc to create the maximum coupling with the CTP, which is determined by the minimum reflectivity dip occurring. Because the DC response of these structures are small a lock-in amplifier is used together with a modulation in the excitation source with frequencies ranging between 150 Hz to 30 kHz. This allows us to isolate a photoresponse even from our non-optimized detectors by eliminated any noise contributions that, in the frequency domain, can be distinguished from the known frequency of the modulated

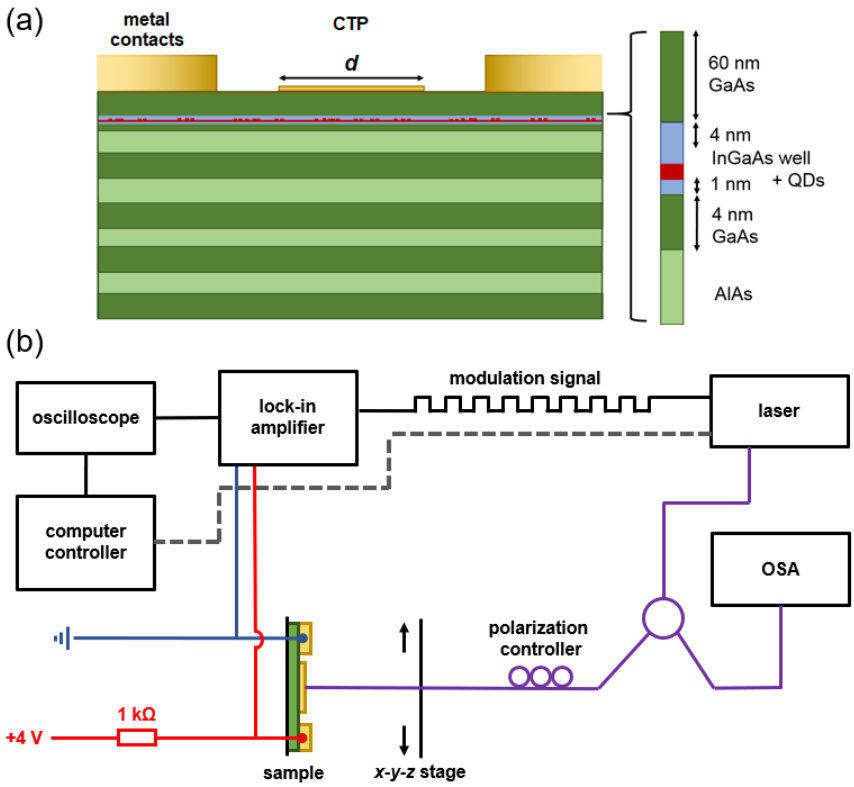

Figure 6.7: (a) Schematic diagram of the CTP photodetector. Light is incidence from above the metal layer. A layer of InAs/GaAs QDs in an InGaAs well act as the absorption medium, reducing the resistance between the two metal contacts.(b) Diagram of the experimental setup; OSA - optical spectrum analyser. The sample is excited by a lens-ended fiber attached to an x-y stage and aligned to the center of the disc (this occurs when the reflected power measured by the OSA is at its minimum).

signal.

The photodetector response for a d = 13 μm disc is shown in figure (6.8(a); black line). A peak in the photocurrent occurs centered at 1300 nm and with a FWHM of 20 nm, much narrower than the QD linewidth measured for the bare DBR. To further show the effect is not purely direct QD absorption the photovoltage decreases almost entirely when the excitation source is focused in the non-metal region between the microdisc and the positive/negative contacts (red and green line). The photovoltage, measured over a narrower spectral range, is taken for d = 7 μm, 8 μm, 10 μm, 12 μm, 16 μm and 20 μm discs and shown in figure 6.8(b). The peak position of the photovoltage blueshifts as diameter is reduced in line with the shift of the CTP response (and hence wavelength of strongest QD coupling), and agrees well with the shift in previous PL measurements with diameter. There is also an increase in the magnitude of the response with smaller disc size. Though these photodetectors do not challenge state of the art devices, for example in terms of sensitivity or switching speed, there are obvious areas to improve their

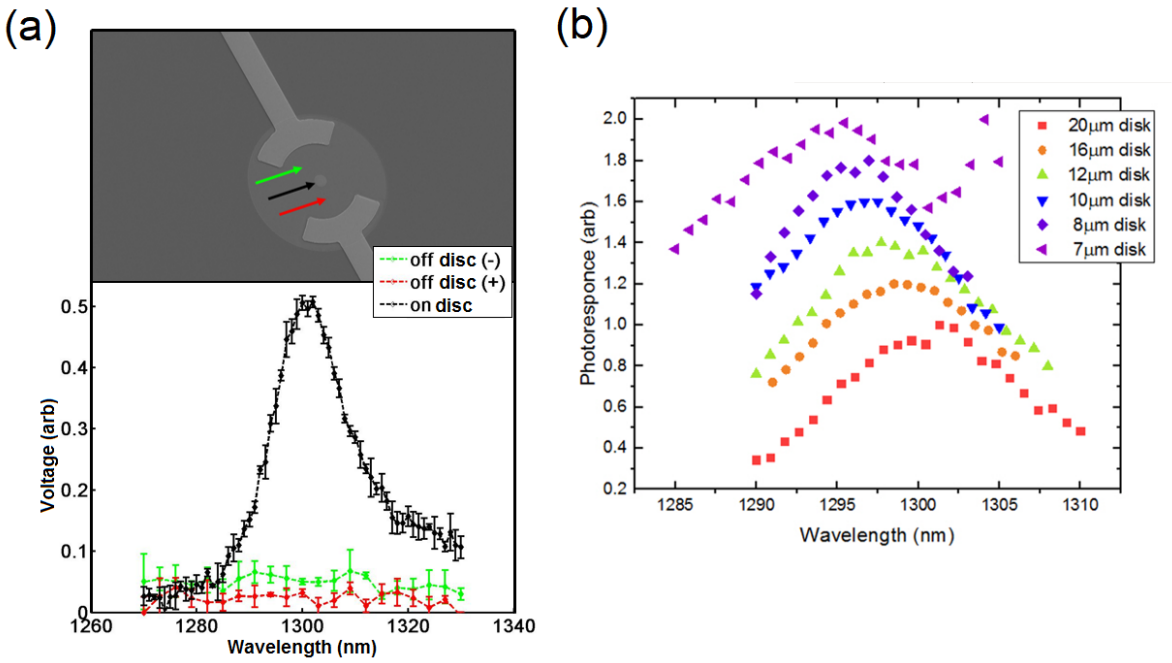

Figure 6.8: (a) SEM image of a d = 13 μm device, and its photodetector response when pumped on (black line) and off (green and red) the disc by a non-resonant (650 nm) laser as a function of wavelength. (b) Photodetector response for different disc diameters.

performance. For example, these uses Schottky contacts, which allows the metal layers for the CTP structure and the contracts to be fabricated simultaneously, but which also produces a large barrier for the charge carriers; in future devices, these could be changed to Ohmic contacts. The overall design is robust, easy to fabricate and highly tuneable. CTPs readily lend themselves to charge-tuneable devices as the metal layer can be used as an n-type contact, e.g. for optical switching.

It has been shown that asymmetrical metal structures produce CTPs with resonances that are non-degenerate for different polarization orientations [112]. By breaking the symmetry of the photodetection devices sensitivity to the polarization of light can be added to the photocurrent. This is shown in figure (6.9). The excitation source polarization is varied using a polarization controller positioned between the circulator and the sample (this is calibrated by measuring the transmission using a free-space polarimeter located behind the sample). Instead of the symmetrical microdiscs, the gold layer is a 3 μm × 8 μm rectangle (figure 6.9(a)). The photocurrent response is measured with the excitation polarization aligned along the long (H) and short (V) axis of the rectangle. As before, the fiber is positioned for each polarization at the minimum reflectivity dip to maximize the coupling with the Tamm mode.

Figure (6.9(b)) shows the photocurrent for the H (black) and V (red) polarization for the 3 μm × 8 μm rectangle. Though small, a blueshift occurs for the short, more confined V-polarized mode

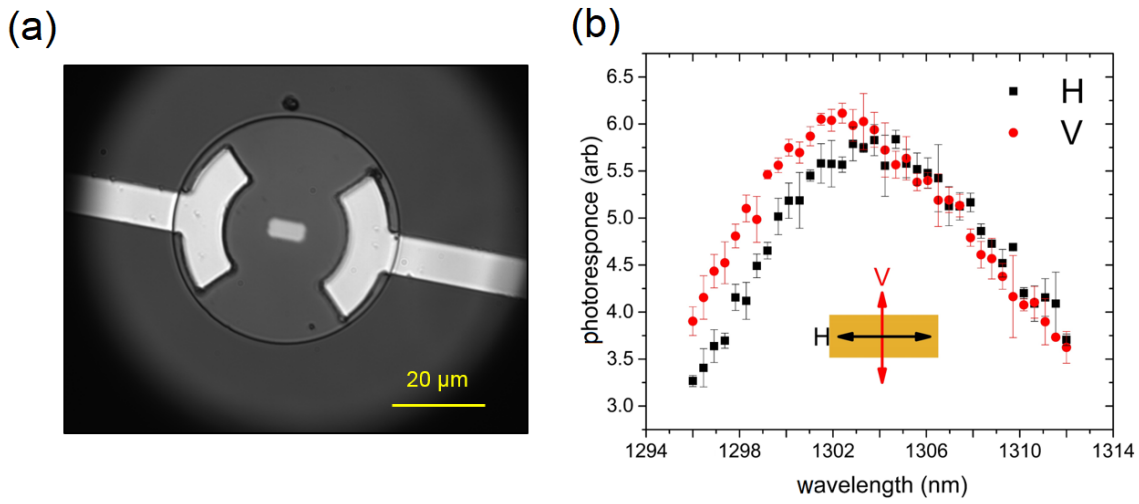

Figure 6.9: (a) Real image (40x objective) of a 3 μm × 8 μm rectangular device. (b) Photodetector responses when the pumping laser is linearly polarized parallel to the long (H) and short (V) axis of the CTP (black and red lines respectively).

relative to H. This shift could be widened by using more asymmetric structures to further lift the degeneracy between the H and V modes. However, there are limitations to how far this could be taken; the effect from lengthening an axis will saturate as beyond a few wavelength's the TP is no longer confined. Conversely, decreasing an axis too much reduces the quality factor for both polarizations (as occurs for the disc CTPs). There is therefore a limit on the possible aspect ratios that can be achieved. The magnitude of splitting between the modes is comparable to that seen by Lheureux et al. [112] (0.2 nm for a 2:1 aspect ratio rectangle, which was found to have the best trade-off between splitting and Q-factor) but this was sufficient to produce a CTP laser with a degree of polarization > 90% due to the high spectral sensitivity of the gain medium. Though this is less in this case (lacking for example a laser's critical threshold) it should be noted that these designs contain a very broad range of QD resonances, whereas future designs be more selective in the dot frequencies, or incorporate the electrical tuning mentioned earlier. Lastly, there is also the interesting possibility of using achiral metal structures to produce CP sensitive modes. Such a Tamm mode would, to my knowledge, be an original result, and the numerical analysis of these kinds of structure an obvious next stage of future research.

6.5 Summary

It has been demonstrated that devices can be fabricated that produce TP modes resonant at telecoms wavelength, and that these modes can be confined using comparatively simple metal deposition techniques. The shifts in CTP resonance and Q-factor as the structure parameters vary agrees remarkably well with those predicted by simulations using TMM and FDTD methods,

the former allowing spectral tuning of the devices. Photoluminescence spectroscopy show the extent CTPs can increase the brightness of QDs positioned in the spacer layer. Our optimum structure produces an enhancement of $\times 11$.

To further show the applicability of these designs, CTP-enhanced photodetectors were designed, and characterized by Edmund Harbord and Ben Cemlyn at the University of Essex. These show an enhanced photocurrent that is responsive to changes in wavelength, spatial position and polarization as functions of the metal layer shape. In addition to sensors, these could be applied as optical switches. Overall, CTPs represent an easily scalable and tuneable alternative to SPPs and micropillars for use in certain optic and quantum optics devices.

CHAPTER 7

Conclusion

In this thesis I have presented theoretical and experimental evidence of QD interaction with CTPs at telecom wavelengths and shown these structures can be incorporated into optical devices. In the simulation study transfer matrix and FDTD methods are used to design CTPs and low Q micropillars that are resonant at 1.3 μm and the effect of different structure parameters on device performance explored. It showed that metal layer thickness, spacer layer thickness, and disc diameter can all be used to tune the resonance position, as expected from other work. In addition, it also considers in greater detail the changes in mode profile and farfield emission as the Tamm plasmon is confined, an area that has previously been neglected, and found that for a well-centered and broadly resonant dipole 90% of its emission into the collection channel is within an NA of 0.7 and 0.4 for an optimized CTP and micropillar respectively. It was found there are several effects that limit the β factor of low Q structures, such as careful choice of diameter and substrate material refractive index, that can in future be used to improve light extraction efficiency.

CTP structures consisting of gold microdiscs were then fabricated and characterized using reflectivity and PL measurements of InGaAs QDs positioned at the predicted maximum field enhancement of the mode. Fourier image spectroscopy is used to measure the change in dispersion relationship of the PL emission as the disc diameter is reduced, demonstrating the onset of confinement effects. An order of magnitude brightness increase of the collected emission when coupled to the CTP is demonstrated, as is the tuneability of the resonance and polarization. These structures are fabricated simultaneously on-chip using a simple, single-stage metal deposition step, without the need for etching. Also, compared to high Q-factor photonic structures a higher yield per device can be achieved. Together, these make CTPs suitable for high scalability.

This work paves the way for future research on CTPs as a SPS. The next step would be to demonstrate a single 1.3 μm QD coupled to a Tamm structure. In addition to being the logical progression in the realization of making SPSs, this would also allow time-resolved PL to measure the Purcell factor and inhibition rates, and hence directly characterize the β factor. Registering individual dots before deposition of the metal layer would also open experimental research of the effect of emitter position. Alterations to the design for low-temperature (i.e. single dot) PL and dependence of dot emission as a function from the center of the CTP are explored in the simulation chapter. The lateral CTP profile could also be directly mapped using scanning near-field microscopy as it has been shown that, though Tamm states are predominantly localized in the DBR, TPCE can extend to fluorophores located above the metal layer [109]. To the best of my knowledge, this would be an entirely novel experiment. Finally, it would be necessary to characterize them in terms of the requirements of a SPS, for example performing photon correlation measurements using a HBT setup, to measure the $g^2(\tau)$ and demonstrate antibunching.

There was very strong agreement between simulated and actual devices in terms of the CTP resonances and Q-factors. However, the collection efficiency was lower than estimated. Improvements in this would be the key area of future interest; this could be by the addition of circular bullseye gratings to the microdisc, SILs, or tailoring the metal layer structure to improve mode-matching between the output and a fiber mode. The thesis also presented work on low Q micropillars and CTP photodetectors. In the former, there is a large potential body of future experimental work using the reverse-bonding method to explore different substrate materials. Any β factor increase here would be general to many semiconductor devices, including CTPs.

The aim of this thesis is to consider the potential of Tamm plasmons for SPSs, a necessary component for the next generation of quantum optical devices. These must (ideally) be scalable, tuneable, bright and deterministic. The first two requirements have favoured the use of solid-state single-emitters, i.e. QDs, while the latter two require high collection efficiencies, something the macroscopic size and noisy environment of QDs seem to oppose. Currently, β factors close to unity can be achieved in high Q micropillars, but at the cost of lower external extraction efficiency [27] and device yield (which limits the scalability). Because of the inhibition of non-resonant modes CTPs can achieve β factors of 50% [114]. The work in this thesis shows there is a great deal of novel optimization remaining that may further improve the collection efficiency of these devices, it shows the range of tuneability of these structures (including to telecoms wavelengths), and demonstrates an order of magnitude increase in the PL emission collected from QDs coupled to these modes. It also successfully demonstrates the integration of these structures into simple, proof-of-principle detector devices that use the confinement of the TP to produce wavelength and polarization sensitivity.

In summary, CTPs are a promising alternative to current efforts to manipulate light at the smallest scales; they are less lossy than SPPs and are easy to fabricate, scale and tune compared

to semiconductor micropillars. The ability to shape the emission profile by tailoring the metal layer structure, such as to that of a fibre mode, is unique to CTPs and can be used to greatly increase the direct-coupling efficiency for a Tamm-based SPS, or to create unique detector effects, such as by using asymmetrical or achiral structures. With improvements in collection efficiency, CTPs are a good candidate for the realization of SPSs for application in several proposed quantum technologies.

APPENDIX A

DISPERSION RELATION OF SPPS

A.1 Separation of variables

Starting with equation (2.5) and substituting $F(x,z) = f(z)g(x)$

$$\left[\frac{d^2}{dz^2} + \frac{d^2}{dx^2} + \kappa_0^2\epsilon(z)\right] F(x,z) = g(x)f''(z) + f(z)g''(x) + \kappa_0^2\epsilon(z)f(z)g(x) = 0 \tag{A.1}$$

and dividing by $F(x,z)$

$$\frac{f''(z)}{f(z)} + \frac{g''(x)}{g(x)} + \kappa_0^2\epsilon(z) = 0 \tag{A.2}$$

$$-\frac{g''(x)}{g(x)} = \frac{f''(z)}{f(z)} + \kappa_0^2\epsilon(z) = \beta^2 \tag{A.3}$$

where β^2 is some constant value, since the left- and right- hand side are dependent solely on variables x and z. Solving the left-hand side first we get a solution for $g(x)$

$$g(x) = e^{j\beta x} \tag{A.4}$$

Hence β, the component of the wavevector in the x direction, must be constant (this is later shown to follow from the interface matching conditions). The equation for $f(z)$ becomes

$$f''(z) + (\kappa_0^2\epsilon - \beta^2)f(z) = 0 \tag{A.5}$$

A.2 Disperion relation of SPP

$$\frac{\kappa_{1z}}{\epsilon_1} = -\frac{\kappa_{2z}}{\epsilon_2} \tag{A.6}$$

$$\kappa_{iz}^2 = \kappa_0^2 \epsilon_i - \beta^2 \tag{A.7}$$

so

$$\frac{\kappa_0^2 \epsilon_1 - \beta^2}{\epsilon_1^2} = \frac{\kappa_0^2 \epsilon_2 - \beta^2}{\epsilon_2^2} \tag{A.8}$$

$$(\kappa_0^2 \epsilon_1 - \beta^2)\epsilon_2^2 = (\kappa_0^2 \epsilon_2 - \beta^2)\epsilon_1^2 \tag{A.9}$$

$$\beta^2 = \kappa_0^2 \left(\frac{\epsilon_1^2 \epsilon_2 - \epsilon_1 \epsilon_2^2}{\epsilon_1^2 - \epsilon_2^2} \right) \tag{A.10}$$

$$\beta^2 = \kappa_0^2 \epsilon_1 \epsilon_2 \frac{(\epsilon_1 - \epsilon_2)}{(\epsilon_1 + \epsilon_2)(\epsilon_1 - \epsilon_2)} = \kappa_0^2 \frac{\epsilon_1 \epsilon_2}{\epsilon_1 + \epsilon_2} \tag{A.11}$$

we are left with the dispersion relationship for the SPP wavevector from equation (2.28)

$$\beta = \kappa_0 \left(\frac{\epsilon_1 \epsilon_2}{\epsilon_1 + \epsilon_2} \right)^{\frac{1}{2}} \tag{A.12}$$

$$\kappa_{iz} = \kappa_0 \left(\frac{\epsilon_i^2}{\epsilon_1 + \epsilon_2} \right)^{\frac{1}{2}} \tag{A.13}$$

To form a mode propagating along the interface it is necessary for β to be real and to form a surface state for κ (the component of the wavevector normal to the interface) to be imaginary (to produce decaying solutions). Hence, it is necessary for the real parts of $\epsilon_1 + \epsilon_2 < 0$ and $\epsilon_1 \epsilon_2 < 0$. In noble metals this is satisfied by having a large negative ϵ_m so that $|\epsilon_m| > \epsilon_d$ is also satisfied.

A.3 Matching condition for a surface state

The result from equation (3.9) for the eigenenergies of a Tamm state can be arrived at intuitively by considering the example described by [84]. If we have a homogenous layer with two arbitrary semi-infinite structures on either side (for example, in the spacer layer of a DBR, as shown in figure (A.1)). Within the layer we introduce two virtual interfaces with amplitude reflection coefficent r_L for a wave propagating right to left onto the left interface (and vice versa for r_R), and distance z apart. Using the TMM method (described in section 2.4.1)

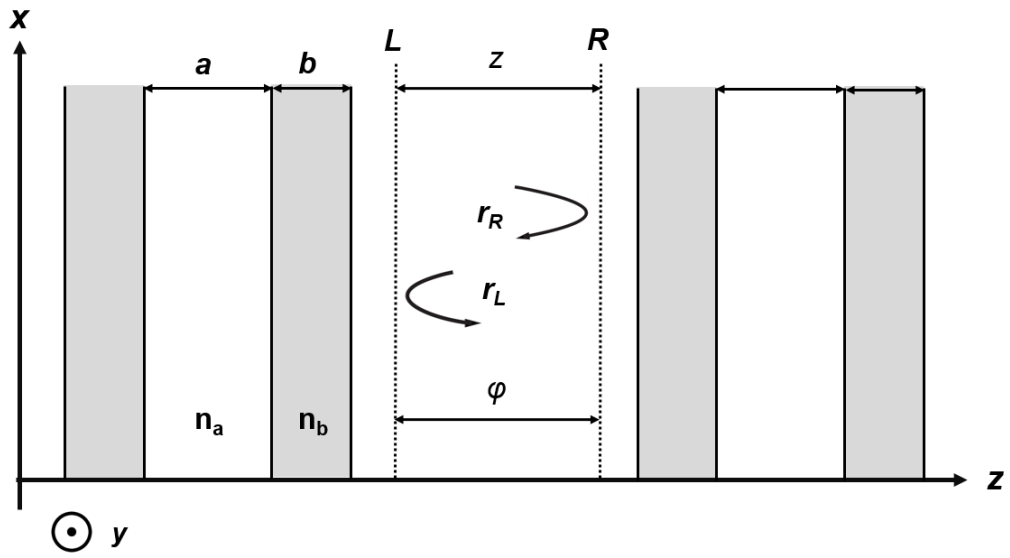

Figure A.1: Diagram showing the virtual interfaces as dotted lines within a uniform layer of a multilayer structure. The wave gains a phase Φ propagating between them.

(A.14) $$\vec{E}_L = L_z \vec{E}_R$$

where L_z is the propagation matrix between the two interfaces.

(A.15) $$E_0 \begin{bmatrix} r_L \\ 1 \end{bmatrix} = \begin{bmatrix} e^{-i\Phi} & 0 \\ 0 & e^{i\Phi} \end{bmatrix} \begin{bmatrix} 1 \\ r_R \end{bmatrix}$$

where E_0 is a constant and $\Phi = n(\omega/c)z$ at normal incidence. From the two equations produced and substituting for E_0 results in

(A.16) $$r_L r_R e^{2i\Phi} = e^{i(\phi_L + \phi_R + 2\Phi)} = 1$$

This is satisfied when $\phi_L + \phi_R + 2\Phi = 2\pi m$. In the cases where $\mathrm{sgn}\{\phi_L\} = \mathrm{sgn}\{\phi_R\}$ (e.g. both DBRs have the same order of layers) this is satisfied for some particular value of Φ, which correspond to the resonance condition for light for a roundtrip in a planar microcavity [25]. For a surface state the virtual boundaries are brought closer together until $z = 0$, which reduces to the surface state condition $r_L r_R = 1$, or $\phi_L = -|\phi_R|$, derived earlier. In other words, it is possible to eliminate the cavity layer entirely when the reflection phase shifts at the interface have equal but opposite magnitude, for example by having two DBRs with different ordering of the high and low refractive index material, or a positive phase shift DBR and a metal layer.

APPENDIX B

SIMULATION METHODS AND FIGURES

B.1 TMM code

The TMM program takes the parameters of the TP structure (metal layer thickness, spacer layer thickness, number of DBR pairs) and source (incident angle, polarization, input side) and calculates its reflection and transmission coefficients using the method described in (2.4.1).

The structure is stored as a structure-array type; its variables are the layer material, its thickness (these are initially set in the 'BuildStructure.m' function) and the (cosine of the) propagation angle (q), from which is calculated the layer matrices (L_mat). If material dispersion is included, these are calculated in the function ('MyMaterialBuilder.m'). This loads .txt files containing refractive index data taken from the cited sources and interpolates them to produce a continuous plot of refractive indices over the wavelength range specified in the main TMM solver (it is important that when this function is called that the filepaths for where the material data is stored are kept up to date).

```
clear ;
clf ;
% Code uses the TMM method to calculate reflection and transmission through
% a structure defined by TMMstructure using the propagation and scattering
% matrix of each period/interface.

StartLambda = 1000 ; EndLambda = 1500 ; L_diff = 0.1 ;
wavelength = StartLambda:L_diff:EndLambda ;

dispersion = 1 ; % material properties fixed or wavelength dependent
MyMaterialBuilder(dispersion,wavelength);

% Design parameters
%%%%%%%%%%%%%%%%%%%%%%%%%%%%%%%%%%%%%%%%%%%%%%%%%%%%%%%%%%%%%%%%%%%%%%%%%%%%%%%
N = 18 ; % NumberOfPeriods in DBR (1/2 more than total i.e. 18 -> 17.5 pairs)
MetalDepth = 25 ;
Spacer1Depth = 0 ;
Spacer2Depth = 75 ;
NoOfLayers = 2*N + 6 ;
%%%%%%%%%%%%%%%%%%%%%%%%%%%%%%%%%%%%%%%%%%%%%%%%%%%%%%%%%%%%%%%%%%%%%%%%%%%%%%%

TE_polarized = 1 ; % TE polarized == 1, TM polarized == 0
phi_0 = asin(0.0) ; % radians
reverse = 0 ; % excitation side (metal first == 0, substrate first == 1)

if dispersion == 0 % no material dispersion; build TMM structure only once
    TMMstructure = BuildStructure(N,MetalDepth,Spacer1Depth,Spacer2Depth,1,reverse) ;
end

for l = 1:length(wavelength)
    if dispersion == 1
        TMMstructure = BuildStructure(N,MetalDepth,Spacer1Depth,Spacer2Depth,l,reverse) ;
    end

    n01 = TMMstructure(1).ncomplex ; TMMstructure(1).q = cos(phi_0) ;
    n02 = TMMstructure(NoOfLayers).ncomplex ; TMMstructure(NoOfLayers).q = sqrt( 1 - (n01*sin(phi_0)/n02)^2) ;

    % For each layer, obtain the layer propagation matrix (L_mat)
    k0 = (2*pi/wavelength(l)) ;
    for layer=2:(NoOfLayers-1)
        TMMstructure(layer).q = sqrt( 1 - (n01*sin(phi_0)/TMMstructure(layer).ncomplex)^2) ; % cos(phi_layer)
        xi = k0 * TMMstructure(layer).ncomplex * TMMstructure(layer).q ; % effective wavevector
        TMMstructure(layer).L_mat = [ exp(-1i*xi*TMMstructure(layer).depth) 0 ; 0 exp(1i*xi*TMMstructure(layer).depth)];
    end

    % For each interface, calculate the interface matrix (I_mat)
    NoOfInterfaces = NoOfLayers-1 ;
    for layer = 1:NoOfInterfaces % interface(j) is the interface between layer j and layer j+1
        n1 = TMMstructure(layer).ncomplex ; n2 = TMMstructure(layer+1).ncomplex ;
        q1 = TMMstructure(layer).q ; q2 = TMMstructure(layer+1).q ;

        if TE_polarized == 1 % see SPIE 7521, 75210G (2009).
            interfaces(layer).r_mat = (n1*q1 - n2*q2)/(n1*q1 + n2*q2);
            interfaces(layer).t_mat = (2*n1*q1)/(n1*q1 + n2*q2) ;
        elseif TE_polarized == 0
            interfaces(layer).r_mat = (n2*q1 - n1*q2)/(n2*q1 + n1*q2) ;
            interfaces(layer).t_mat = (2*n1*q1)/(n2*q1 + n1*q2) ;
        end
        interfaces(layer).I_mat = (1/ interfaces(layer).t_mat )* [1 interfaces(layer).r_mat; interfaces(layer).r_mat 1];
    end

    S_0 = interfaces(NoOfInterfaces).I_mat ;
    for m = NoOfInterfaces:-1:2
        S_0 = interfaces(m-1).I_mat * TMMstructure(m).L_mat * S_0 ;
```

```
    end
    %%%%%%%%%%%%%%%%%%%%%%%%%%%%%%%%%%%%%%%%%%%%%%%%%%%%%%%%%%%%%%%%%%%%%%%%%%%%%%%%
    % From the final S matrix, calculate the reflection and the
    % transmission coefficients (for this wavelength, l)

    % reflection R=|r|^2 = r * conj(r)
    r = S_0(2,1)/S_0(1,1) ;
    reflection(l) = r*conj(r) ;

    % transmission T=|t|^2 * (n_substrate / n_ambient_medium)
    % define transmission_scale is ratio of refractive indicies n_substrate / n_ambient_medium
    % * [cos (phi_substrate) / cos(phi_0) ]
    transmission_ratio = (n02 * TMMstructure(NoOfLayers).q)/(n01 * TMMstructure(1).q) ;
    transmission(l) = abs(1/S_0(1,1))^2 * real(transmission_ratio);

    %absorption(l) = 1 - (reflection(l) + transmission(l)) ;

    % Calculate the reflection phase
    S_1 = interfaces(NoOfInterfaces-1).I_mat ;
    for m = (NoOfInterfaces-1):-1:3
        S_1 = interfaces(m-1).I_mat * TMMstructure(m).L_mat * S_1 ;
    end
    phaseangle(l)= angle(S_1(2,1)/S_1(1,1)) ;

    if mod(l,(100/L_diff)) == 1
        disp(['Lambda = ' num2str(wavelength(l)) ' nm'])
    end
end

function MyMaterialBuilder(dispersion, wavelength)
% makes material files using the data given in the tables in FileDirectory
% taken from references (e.g. Johnson and Christy)

% check file directory information is correct
FileDirectory = 'F:\TMM_(new)\Materials\';
FilePath = 'F:\TMM_(new)\MaterialDispersion\';

% check names of material files match
n_1 = 'GaAs'; n_2 = 'AlAs';
n_metal = 'gold';

f_1 = fopen([FilePath n_1 '.txt'],'wt');
f_2 = fopen([FilePath n_2 '.txt'],'wt');
f_metal = fopen([FilePath n_metal '.txt'],'wt');

if dispersion == 0
    fprintf(f_1,'%f %f %f',1, 3.5,0);
    fprintf(f_2,'%f %f %f',1, 2.9,0);
    fprintf(f_metal,'%f %f %f',1, 0.04, 6.312); % real and imaginery component
else
    f_1 = fopen([FilePath n_1 '.txt'],'wt');
    f_2 = fopen([FilePath n_2 '.txt'],'wt');
    f_metal = fopen([FilePath n_metal '.txt'],'wt');

    %{
        % interpolation -- need to interpolate refractive indices so they are
        % uniformly sampled as the same frequency of the chosen wavelength using
        % interp1(x,v(x),qp)

        % x, the sample points (wavelength)
        % v(x), the values wanting to be interpolated (refractive index)
        % qp, query points - the uniform spacing wanted for x (wavelength)
        %}

    A = load([FileDirectory n_1 '.txt']) ;
```

```
    n_GaAs = interp1(1000*A(:,1),A(:,2),wavelength,'spline') + ...
        1i*interp1(1000*A(:,1),A(:,3),wavelength,'spline');
    %n_GaAs = interp1(1000*A(:,1),A(:,2),wavelength,'spline');
    fprintf(f_1,'%f %f %f\n',[wavelength ; real(n_GaAs) ; imag(n_GaAs)]);

    A = load([FileDirectory n_2 '.txt']) ; % contains real parts only
    n_AlAs = interp1(1000*A(:,1),A(:,2),wavelength,'spline');
    fprintf(f_2,'%f %f\n',[wavelength ; n_AlAs]);

    A = load([FileDirectory n_metal '.txt']);
    n_metal = interp1(1000*A(:,1),A(:,2),wavelength,'spline') + ...
        1i*interp1(1000*A(:,1),A(:,3),wavelength,'spline');
    %n_metal = 0 + 1i*interp1(1000*A(:,1),A(:,3),wavelength,'spline') ;
    fprintf(f_metal,'%f %f %f\n',[wavelength ; real(n_metal) ; imag(n_metal)]);
end
fclose('all');

function TMMstructure = BuildStructure(NoOfPeriods,MetalDepth,Spacer1Depth,Spacer2Depth,lambda,reverse)
%%%
```

```
TMMstructure(5).ncomplex = n_1 ;

% layer 6 -> Q-2 : the Bragg multilayer
for q = 6:(Q-2)
    if mod(q,2) == 1
        TMMstructure(q).depth = H(1) ;
        TMMstructure(q).ncomplex = n_1 ;
    else
        TMMstructure(q).depth = H(2) ;
        TMMstructure(q).ncomplex = n_2 ;
    end
end

TMMstructure(Q-1).ncomplex = n_substrate ;
TMMstructure(Q-1).depth = 1000;

TMMstructure(Q).ncomplex = n_substrate ;
TMMstructure(Q).depth = 0;

if reverse == 1 % reverses order of structure (i.e. excites from substrate side)
    TMMstructure2 = TMMstructure ;

    for j = 1:Q
        TMMstructure(j).ncomplex = TMMstructure2(Q-j+1).ncomplex ;
        TMMstructure(j).depth = TMMstructure2(Q-j+1).depth ;
    end
    clear TMMstructure2
end
```

Loops to sweep over one of these parameters, for example to produce the dispersion plots in figure (3.6), require trivial modification and are not shown. However, a larger modification that calculates the electric field profile is included.

B.1.1 Internal field solver

This program is used to calculate the internal electric field through the structure based on the method described in [133]. Within the commented section (%... %) the complete set of layer and interface matrices are calculated using a copy of the same code in the main TMM solver.

```
% The procedure is adapted from J. Appl. Phys Vol 86, No. 1 (1999) p.487
% and JAP 93 No. 7 p. 3693.

plotLambda = 1300 ;
if isempty(find(plotLambda == wavelength, 1))
    error('plotting␣wavelength␣out␣of␣range')
end
l = find(plotLambda == wavelength) ;

% Build structure
%%%%%%%%%%%%%%%%%%%%%%%%%%%%%%%%%%%%%%%%%%%%%%%%%%%%%%%%%%%%%%%%%%%%%%%%%%%%%%%%
if dispersion == 0 % no dispersion;
    TMMstructure = BuildStructure(N,MetalDepth,SpacerDepth,Spacer2Depth,1,reverse) ;
else
    TMMstructure = BuildStructure(N,MetalDepth,SpacerDepth,Spacer2Depth,l,reverse) ;
end

t = zeros(1,NoOfLayers) ;
for layer = 1:NoOfLayers
    t(layer) = TMMstructure(layer).depth ;
end
t_sum = cumsum(t) ;
```

```
z = 0.5:1:t_sum(NoOfLayers);
z_mat = sum(repmat(z,NoOfLayers,1) > repmat(t_sum',1,length(z)),1)+1;
n = zeros(1,length(z));
for z_i = 1:length(z)
    n(z_i) = TMMstructure(z_mat(z_i)).ncomplex ;
end

%...%

for layer = 2:NoOfLayers

    S_prime = interfaces(layer-1).I_mat ;
    for m = (layer-1):-1:2
        S_prime = interfaces(m-1).I_mat * TMMstructure(m).L_mat * S_prime ;
    end
    S_primeprime = interfaces(NoOfInterfaces).I_mat ;
    for m = NoOfInterfaces:-1:(layer+1)
        S_primeprime = interfaces(m-1).I_mat * TMMstructure(m).L_mat * S_primeprime ;
    end

    z_f = find(z_mat == layer) ;
    % indices of z array that are within that particular layer
    z_pos = z(z_f) - t_sum(layer-1) ;
    % position withn layer (relative to (layer-1) interface

    sj = t(layer) ; sj_prime = sj - z_pos ;
    zeta_j = 2*pi/plotLambda * TMMstructure(layer).ncomplex * TMMstructure(layer).q ;

    E(z_f) = (S_primeprime(1,1)*exp(-1i*zeta_j*sj_prime) + S_primeprime(2,1)*exp(1i*zeta_j*sj_prime))./ ...
             (S_prime(1,1)*S_primeprime(1,1)*exp(-1i*zeta_j*sj) + S_prime(1,2)*S_primeprime(2,1)*exp(1i*zeta_j*sj)) ;
end

E_p = abs(E)' ;
plot(z,n,z,abs(E))
```

B.2 Materials

Data points for the refractive indices used in the TMM are taken from a variety of sources, as described in section (4.2.1.2). These are then interpolated using to produce a continuous range of values over the wavelengths simulated. Below are plots of the dispersion function for the real and imaginary (κ) components for all the materials used in this thesis (at room temperature) between 800 nm and 1800 nm. Experimental values are shown as squares and the interpolated fits as the black line.

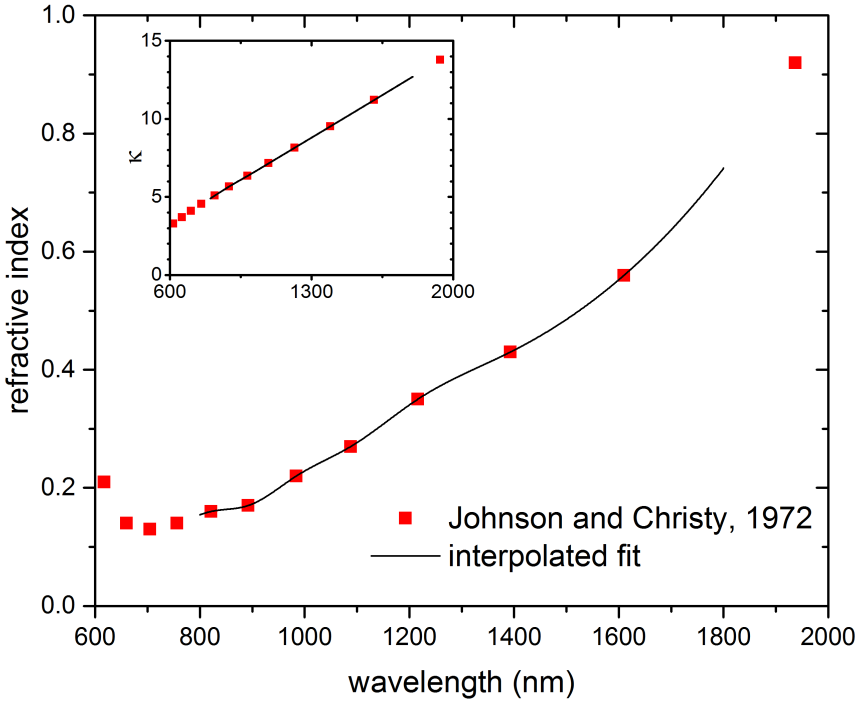

Figure B.1: Real component of refractive index of Gold (Au). The inset shows a plot of the imaginary component.

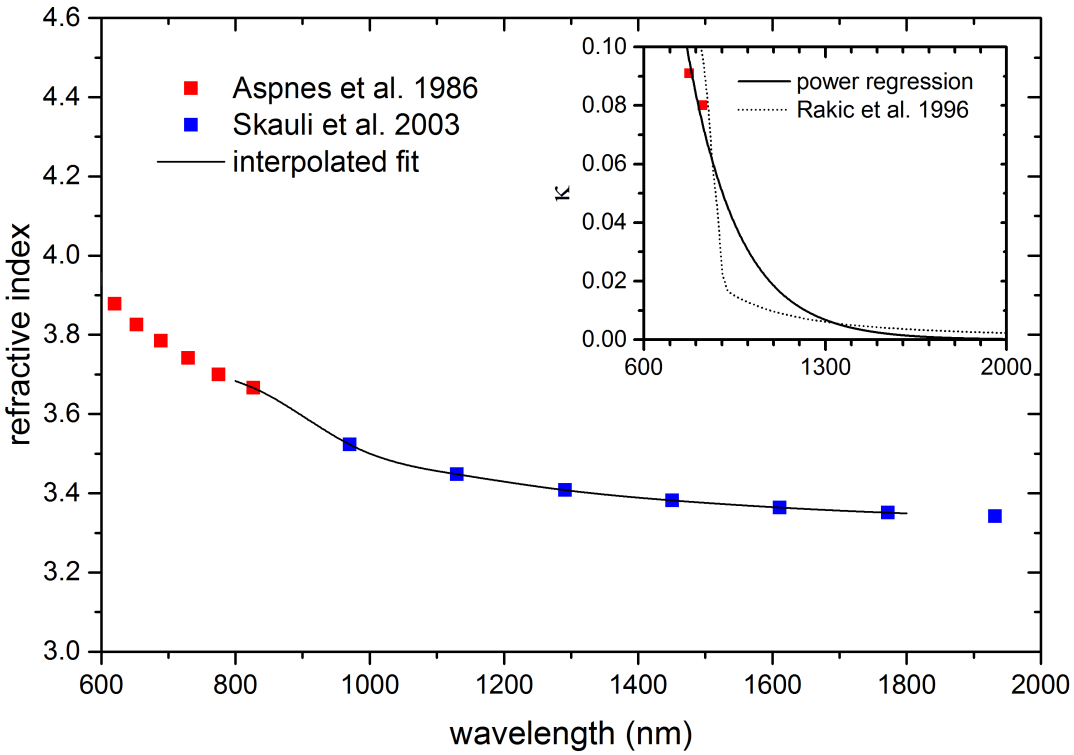

Figure B.2: Real component of refractive index of gallium arsenide (GaAs). The inset shows a plot of the imaginary component. A theoretical model of the dispersion function of GaAs by Rakic et al [138] is the dashed line.

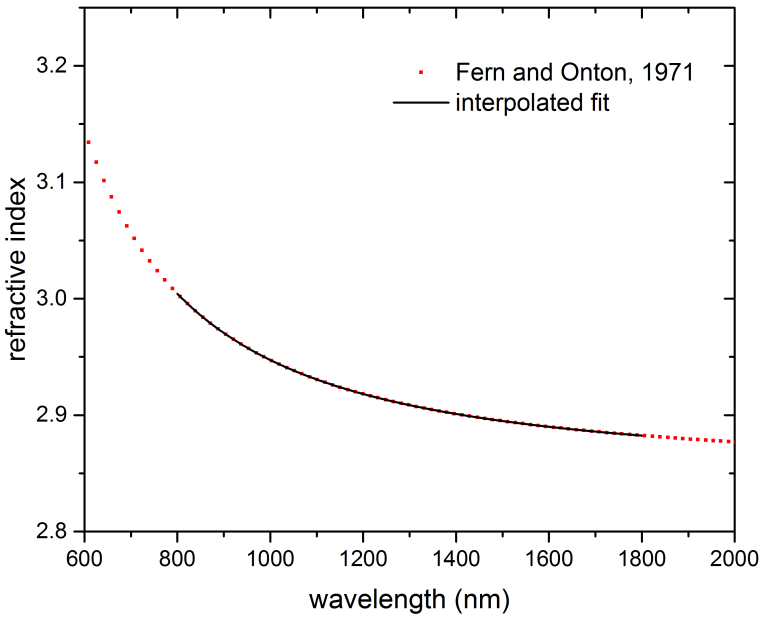

Figure B.3: Real component of refractive index of aluminium arsenide (AlAs).

B.3 Transmission boxes

To find Γ and γ from the FTDT simulation, and hence calculate the efficiency of a design, a set of transmission monitors are positioned around the device to form a complete box. Example transmission boxes are shown for a CTP (figure B.4) and micropillar (figure B.5). These monitors record the amount of power transmitted through the monitor by integrating the Poynting vector through the monitor surface and normalizing to the emitted power. The box measures the transmission through the side channels ($2x$ + $2y$) to estimate γ and through the bottom (z_1) and top (z_2) channels to estimate the coupling rate into the mode Γ. If the simulation contains purely lossless material, then

$$\beta = \frac{\Gamma}{\Gamma+\gamma} = \frac{z_1+z_2}{T} \tag{B.1}$$

where T is the sum through all the monitors. If the simulation contains dispersive material, such as with the CTP, then absorption is an additional loss channel, $\gamma*$, in which case

$$\beta' = \frac{\Gamma}{\Gamma+\gamma+\gamma*} = \frac{\Gamma}{\Gamma+\gamma}(1-\alpha) = \beta(1-\alpha) \tag{B.2}$$

where α (= $\gamma*/(\Gamma+\gamma+\gamma*)$) is the fraction lost through absorption. Lastly, excitation and collection occurs through one side of the structure so only a fraction of the emission into the

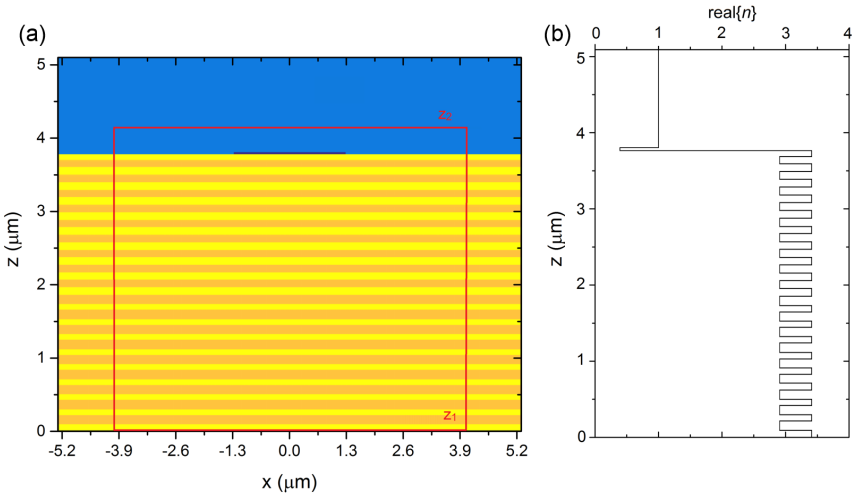

Figure B.4: (a) Transmission box (red lines) and (b) refractive index profile for a d = 2.6 μm 17.5x DBR CTP.

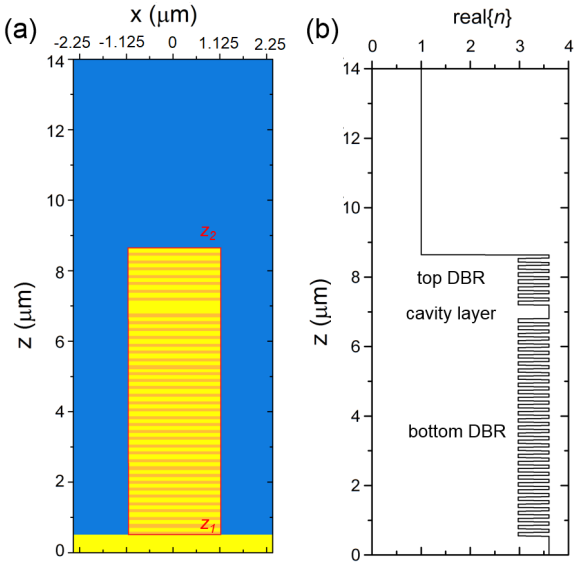

Figure B.5: (a) Transmission box (red lines) and (b) refractive index profile for a d = 2.0 μm, 7x (30.5x) top (bottom) DBR micropillar.

cavity mode goes through this side. An additional factor, called the η factor and separate from the internal efficiency β, shows the ratio of the mode transmitted through the top channel.

$$\eta = \frac{z_2}{z_1 + z_2} \tag{B.3}$$

So, the total internal efficiency, $\zeta = \beta\eta(1-\alpha)$.

B.4 Additional figures for chapter 5

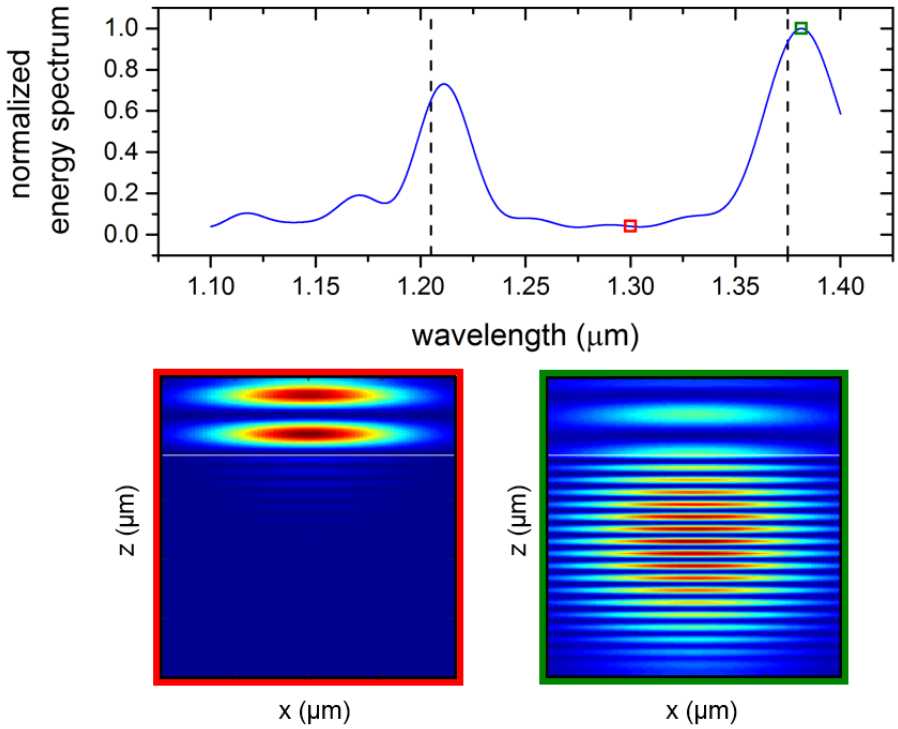

Figure B.6: (a) Normalized spectrum for the DBR only structure (17.5x GaAs/AlAs DBR + spacer layer). (b) Vertical profiles showing the electric field intensity at the wavelength in the center of the DBR's stopband (λ = 1300 nm, red square) and first Bragg mode (λ = 1377 nm, green square). The simulation is excited by a Gaussian source from above the structure, as described in (5.2.1.1).

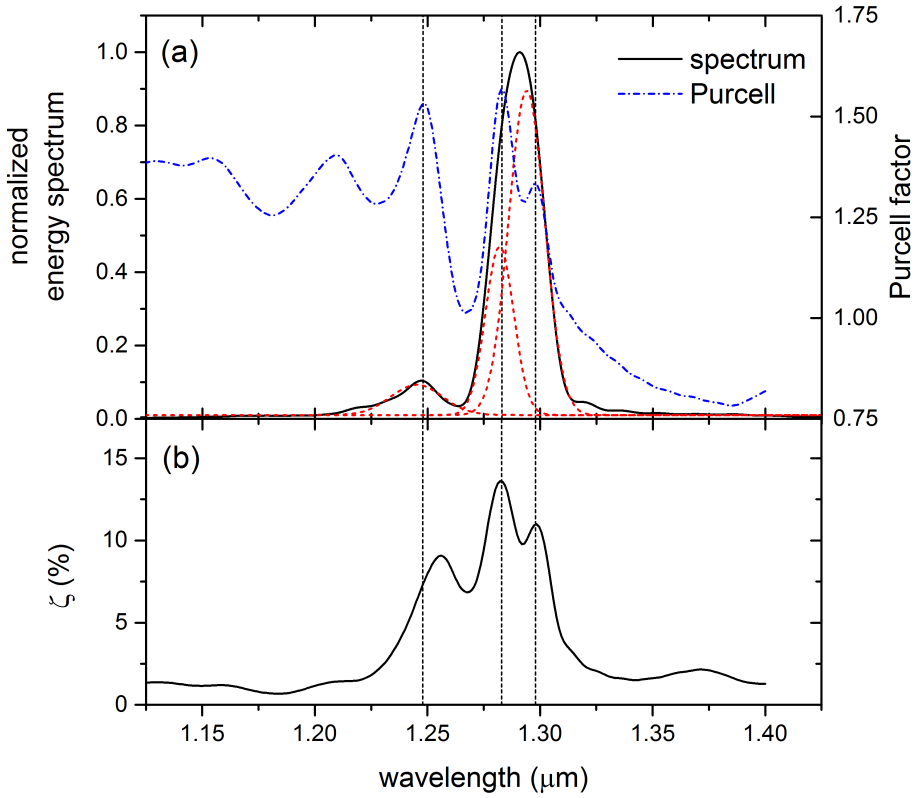

Figure B.7: (a) Normalized spectrum and Purcell enhancement for a d = 3.575 μm disc. The dashed red lines are Gaussians fitted to the spectrum but whose resonances are taken from the resonance in the Purcell enhancement, marked by the dashed lines, though we are unsure of this interpretation. (b) Plot of the internal collection efficiency, ζ.

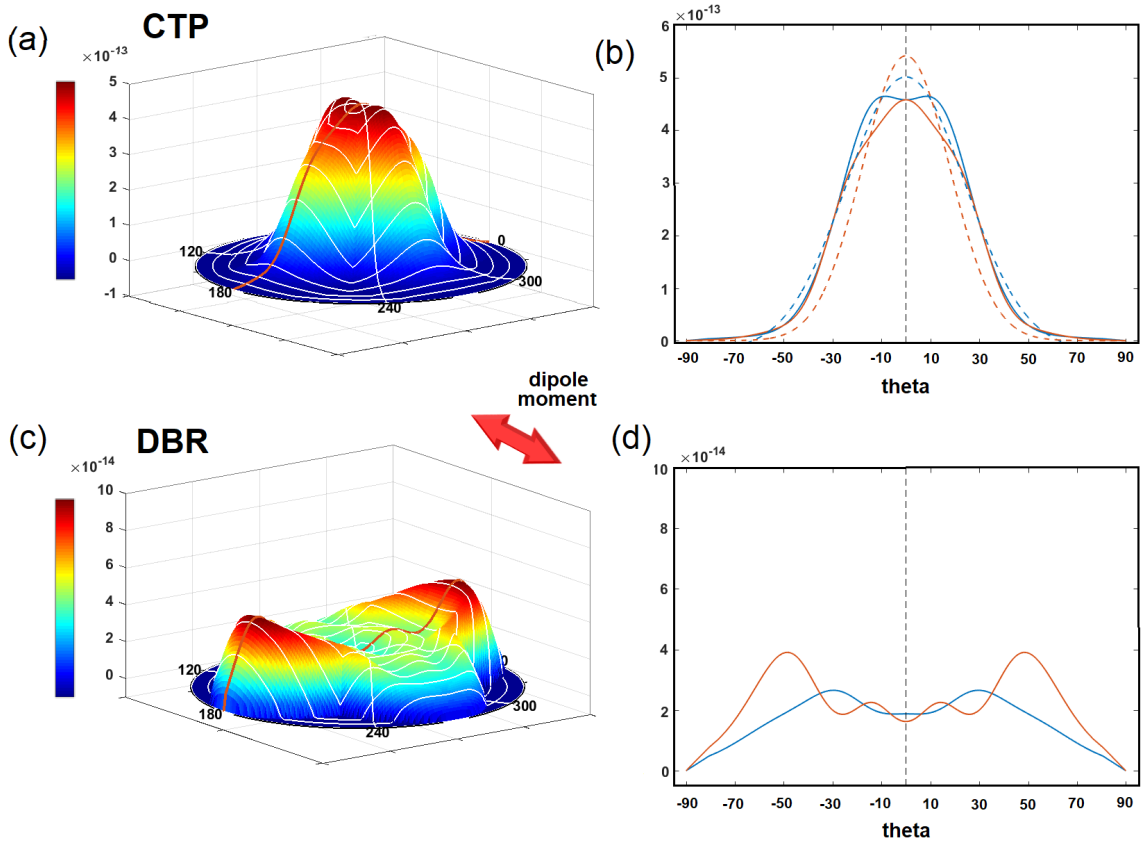

Figure B.8: Projections showing the electric field intensity in the farfield collected (for λ = 1.296 μm) through the top of (a) d = 2.6 μm CTP and (c) DBR. Electric field profiles through these at ϕ angles parallel and perpendicular to the electric dipole moment are shown by the blue and orange lines respectively in (b) and (d). The dashed lines show Gaussian fits to these distributions. Note that the intensity scale of the DBR is one fifth that of the CTP structure.

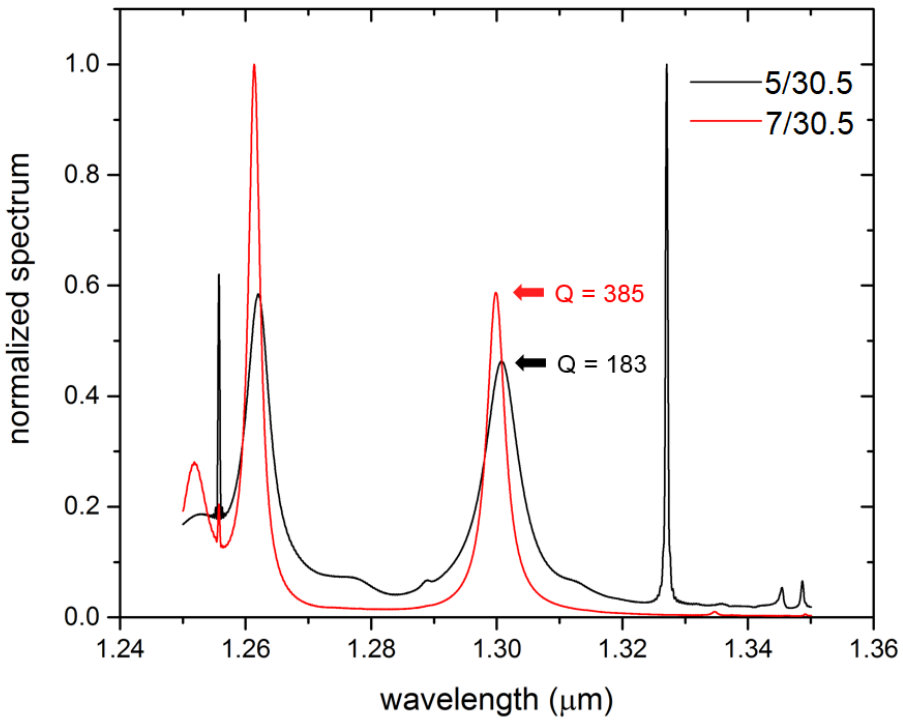

Figure B.9: Normalized spectrum for a d = 2.25 μm pillar with 5 (30.5) and 7 (30.5) top (bottom) DBR pairs. The arrows display their respective Q-factors for the fundamental (1.3 μm) mode.

BIBLIOGRAPHY

[1] A. Einstein, B. Podolsky, and N. Rosen, "Can quantum-mechanical description of physical reality be considered complete?," *Phys. Rev.*, vol. 47, no. 10, p. 777, 1935.

[2] D. Deutsch, "Quantum theory, the Church–Turing principle and the universal quantum computer," *Proc. R. Soc. Lond. A*, vol. 400, no. 1818, pp. 97–117, 1985.

[3] M. Xiao, L.-A. Wu, and H. J. Kimble, "Precision measurement beyond the shot-noise limit," *Phys. Rev. Lett.*, vol. 59, no. 3, p. 278, 1987.

[4] C. H. Bennett, F. Bessette, G. Brassard, L. Salvail, and J. Smolin, "Experimental quantum cryptography," *J. Cryptology*, vol. 5, no. 1, pp. 3–28, 1992.

[5] N. Gisin, G. Ribordy, W. Tittel, and H. Zbinden, "Quantum cryptography," *Rev. Mod. Phys.*, vol. 74, no. 1, p. 145, 2002.

[6] V. Giovannetti, S. Lloyd, and L. Maccone, "Quantum-enhanced measurements: beating the standard quantum limit," *Science*, vol. 306, no. 5700, pp. 1330–1336, 2004.

[7] T. Basché, W. Moerner, M. Orrit, and H. Talon, "Photon antibunching in the fluorescence of a single dye molecule trapped in a solid," *Phys. Rev. Lett.*, vol. 69, no. 10, p. 1516, 1992.

[8] A. Kuhn, M. Hennrich, and G. Rempe, "Deterministic single-photon source for distributed quantum networking," *Phys. Rev. Lett.*, vol. 89, no. 6, p. 067901, 2002.

[9] C. Kurtsiefer, S. Mayer, P. Zarda, and H. Weinfurter, "Stable solid-state source of single photons," *Phys. Rev. Lett.*, vol. 85, no. 2, p. 290, 2000.

[10] S. Buckley, K. Rivoire, and J. Vučković, "Engineered quantum dot single-photon sources.," *Rep. Prog. Phys.*, vol. 75, no. 12, p. 126503, 2012.

[11] E. F. Schubert, *Light-emitting diodes*.
Cambridge University Press, 2003.

[12] C.-K. Hong, Z.-Y. Ou, and L. Mandel, "Measurement of subpicosecond time intervals between two photons by interference," *Phys. Rev. Lett.*, vol. 59, no. 18, p. 2044, 1987.

[13] I. Aharonovich, D. Englund, and M. Toth, "Solid-state single-photon emitters," *Nat. Photonics*, vol. 10, no. 10, p. 631, 2016.

[14] J.-Y. Marzin, J.-M. Gérard, A. Izraël, D. Barrier, and G. Bastard, "Photoluminescence of single InAs quantum dots obtained by self-organized growth on GaAs," *Phys. Rev. Lett.*, vol. 73, no. 5, p. 716, 1994.

[15] V. Ustinov, N. Maleev, A. Zhukov, A. Kovsh, A. Y. Egorov, A. Lunev, B. Volovik, I. Krestnikov, Y. G. Musikhin, N. Bert, *et al.*, "InAs/InGaAs quantum dot structures on GaAs substrates emitting at 1.3 μm," *Appl. Phys. Lett.*, vol. 74, no. 19, pp. 2815–2817, 1999.

[16] K. Nishi, H. Saito, S. Sugou, and J.-S. Lee, "A narrow photoluminescence linewidth of 21 meV at 1.35 μm from strain-reduced InAs quantum dots covered by $In_{0.2}Ga_{0.8}As$ grown on GaAs substrates," *Appl. Phys. Lett.*, vol. 74, no. 8, pp. 1111–1113, 1999.

[17] D. Loss and D. P. DiVincenzo, "Quantum computation with quantum dots," *Phys. Rev. A*, vol. 57, no. 1, p. 120, 1998.

[18] D. Press, T. D. Ladd, B. Zhang, and Y. Yamamoto, "Complete quantum control of a single quantum dot spin using ultrafast optical pulses," *Nature*, vol. 456, no. 7219, p. 218, 2008.

[19] P. Fry, I. Itskevich, D. Mowbray, M. Skolnick, J. Finley, J. Barker, E. O'Reilly, L. Wilson, I. Larkin, P. Maksym, *et al.*, "Inverted electron-hole alignment in InAs-GaAs self-assembled quantum dots," *Phys. Rev. Lett.*, vol. 84, no. 4, p. 733, 2000.

[20] W. L. Barnes, G. Björk, J. M. Gérard, P. Jonsson, J. A. E. Wasey, P. T. Worthing, and V. Zwiller, "Solid-state single photon sources: Light collection strategies," *Eur. Phys. J. D*, vol. 18, no. 2, pp. 197–210, 2002.

[21] D. Armani, T. Kippenberg, S. Spillane, and K. Vahala, "Ultra-high-Q toroid microcavity on a chip," *Nature*, vol. 421, no. 6926, p. 925, 2003.

[22] J. Claudon, J. Bleuse, N. S. Malik, M. Bazin, P. Jaffrennou, N. Gregersen, C. Sauvan, P. Lalanne, and J.-M. Gérard, "A highly efficient single-photon source based on a quantum dot in a photonic nanowire," *Nat. Photonics*, vol. 4, no. 3, p. 174, 2010.

[23] O. J. Trojak, S. I. Park, J. D. Song, and L. Sapienza, "Metallic nanorings for broadband, enhanced extraction of light from solid-state emitters," *App. Phys. Lett.*, vol. 111, no. 2, p. 021109, 2017.

[24] C. Arnold, V. Loo, A. Lemaître, I. Sagnes, O. Krebs, P. Voisin, P. Senellart, and L. Lanco, "Optical bistability in a quantum dots/micropillar device with a quality factor exceeding 200 000," *Appl. Phys. Lett.*, vol. 100, no. 11, p. 111111, 2012.

[25] N. Gregersen, S. Reitzenstein, C. Kistner, M. Strauss, C. Schneider, S. Hofling, L. Worschech, A. Forchel, T. R. Nielsen, J. Mork, *et al.*, "Numerical and experimental study of the Q factor of high-Q micropillar cavities," *IEEE Journal of Quantum Electronics*, vol. 46, no. 10, pp. 1470–1483, 2010.

[26] A. Auffèves, D. Gerace, J.-M. Gérard, M. F. Santos, L. Andreani, and J.-P. Poizat, "Controlling the dynamics of a coupled atom-cavity system by pure dephasing," *Phys. Rev. B*, vol. 81, no. 24, p. 245419, 2010.

[27] S. Reitzenstein and A. Forchel, "Quantum dot micropillars," *J. Phys. D. Appl. Phys.*, vol. 43, no. 3, p. 033001, 2010.

[28] A. Auffèves-Garnier, C. Simon, J.-M. Gérard, and J.-P. Poizat, "Giant optical nonlinearity induced by a single two-level system interacting with a cavity in the purcell regime," *Phys. Rev. A*, vol. 75, no. 5, p. 053823, 2007.

[29] O. Gazzano, S. Michaelis de Vasconcellos, C. Arnold, A. Nowak, E. Galopin, I. Sagnes, L. Lanco, A. Lemaître, and P. Senellart, "Bright solid-state sources of indistinguishable single photons.," *Nat. Commun.*, vol. 4, p. 1425, 2013.

[30] G. Ctistis, A. Hartsuiker, E. van der Pol, J. Claudon, W. L. Vos, and J.-M. Gérard, "Optical characterization and selective addressing of the resonant modes of a micropillar cavity with a white light beam," *Phys. Rev. B*, vol. 82, no. 19, p. 195330, 2010.

[31] P. Androvitsaneas, A. B. Young, C. Schneider, S. Maier, M. Kamp, S. Höfling, S. Knauer, E. Harbord, C.-Y. Hu, J. G. Rarity, *et al.*, "Charged quantum dot micropillar system for deterministic light-matter interactions," *Phys. Rev. B*, vol. 93, no. 24, p. 241409, 2016.

[32] I. Tamm, "A possible binding of the electrons on a crystal surface," *Zh. Eksp. Teor. Fiz*, vol. 3, pp. 34–35, 1933.

[33] A. Sommerfeld, "Ueber die Fortpflanzung elektrodynamischer Wellen langs eines Drahtes," *Ann. Phys. Chem.*, vol. 67, pp. 233–290, 1899.

[34] J. Zenneck, "Uber die Fortpflanzung ebener elektromagnetischerWellen langs einer ebenen Leiterflache und ihre Beziehung zur drahtlosen Telegraphie," *Ann. Phys. Chem.*, vol. 23, pp. 846–866, 1907.

[35] R. Wood, "On a remarkable case of uneven distribution of light in a diffraction grating spectrum," *Proc. Phys. Soc. London.*, vol. 18, pp. 269–275, 1902.

[36] J. D. Jackson, *Classical Electrodynamics*.
Wiley Online Library, 1975.

[37] S. A. Maier, *Plasmonics: fundamentals and applications*.
Springer Science & Business Media, 2007.

[38] A. P. Vinogradov, A. V. Dorofeenko, S. G. Erokhin, M. Inoue, A. A. Lisyansky, A. M. Merzlikin, and A. B. Granovsky, "Surface state peculiarities in one-dimensional photonic crystal interfaces," *Phys. Rev. B*, vol. 74, no. 4, pp. 1–8, 2006.

[39] J. R. Lakowicz, "Radiative decay engineering 5: Metal-enhanced fluorescence and plasmon emission," *Anal. Biochem.*, vol. 337, no. 2, pp. 171–194, 2005.

[40] E. Kretschmann and H. Raether, "Radiative decay of non radiative surface plasmons excited by light," *Zeitschrift für Naturforschung A*, vol. 23, no. 12, pp. 2135–2136, 1968.

[41] R. Ritchie, E. Arakawa, J. Cowan, and R. Hamm, "Surface-plasmon resonance effect in grating diffraction," *Phys. Rev. Lett.*, vol. 21, no. 22, p. 1530, 1968.

[42] S. Shen, E. Forsberg, Z. Han, and S. He, "Strong resonant coupling of surface plasmon polaritons to radiation modes through a thin metal slab with dielectric gratings," *J. Opt. Soc. Am. A*, vol. 24, no. 1, pp. 225–230, 2007.

[43] W. L. Barnes, A. Dereux, and T. W. Ebbesen, "Surface plasmon subwavelength optics," *Nature*, vol. 424, no. 6950, pp. 824–30, 2003.

[44] E. M. Purcell, H. C. Torrey, and R. V. Pound, "Resonance absorption by nuclear magnetic moments in a solid," *Phys. Rev.*, vol. 69, no. 1-2, p. 37, 1946.

[45] J. R. Lakowicz, "Radiative decay engineering 3: Surface plasmon-coupled directional emission," *Anal. Biochem.*, vol. 324, no. 2, pp. 153–169, 2004.

[46] J. A. Schuller, E. S. Barnard, W. Cai, Y. C. Jun, J. S. White, and M. L. Brongersma, "Plasmonics for extreme light concentration and manipulation," *Nature Mater.*, vol. 9, no. 3, p. 193, 2010.

[47] A. Amir and P. Vukusic, "Elucidating the stop bands of structurally colored systems through recursion," *Am. J. Phys.*, vol. 81, no. 4, p. 253, 2013.

[48] P. Yeh, *Optical Waves in Layered Media*.
Wiley-Interscience, 1988.

[49] S. A. Dyakov, V. A. Tolmachev, E. V. Astrova, S. G. Tikhodeev, V. Y. Timoshenko, and T. S. Perova, "Numerical methods for calculation of optical properties of layered structures," in *International Conference on Micro-and Nano-Electronics 2009*, vol. 7521, p. 75210G, International Society for Optics and Photonics, 2010.

[50] E. Yablonovitch, "Inhibited spontaneous emission in solid-state physics and electronics," *Phys. Rev. Lett.*, vol. 58, no. 20, p. 2059, 1987.

[51] L. Rayleigh, "XXVI. On the remarkable phenomenon of crystalline reflexion described by Prof. Stokes," *The London, Edinburgh, and Dublin Philosophical Magazine and Journal of Science*, vol. 26, no. 160, pp. 256–265, 1888.

[52] J. D. Joannopoulos, S. G. Johnson, J. N. Winn, and R. D. Meade, *Photonic crystals: molding the flow of light*.
Princeton University Press, 2011.

[53] S. G. Davison and M. Stęślicka, *Basic theory of surface states*, vol. 46.
Oxford University Press, 1992.

[54] P. Yeh, A. Yariv, and C.-S. Hong, "Electromagnetic propagation in periodic stratified media. I. General theory," *J. Opt. Soc. Am.*, vol. 67, no. 4, pp. 423–438, 1977.

[55] D. Comoretto, *Organic and hybrid photonic crystals*.
Springer, 2015.

[56] D. Kossel, "Analogies between thin-film optics and electron-band theory of solids," in *J. Opt. Soc. Am.*, vol. 56, p. 1434, 1966.

[57] P. Yeh, A. Yariv, and A. Y. Cho, "Optical surface waves in periodic layered media," *Appl. Phys. Lett.*, vol. 32, no. 2, pp. 104–105, 1978.

[58] R. D. Meade, K. D. Brommer, A. M. Rappe, and J. D. Joannopoulos, "Electromagnetic Bloch waves at the surface of a photonic crystal," *Phys. Rev. B*, vol. 44, no. 19, pp. 10961–10964, 1991.

[59] W. M. Robertson and M. S. May, "Surface electromagnetic wave excitation on one-dimensional photonic band-gap arrays," *Appl. Phys. Lett.*, vol. 74, no. 13, pp. 1800–1802, 1999.

[60] A. Angelini, E. Enrico, N. De Leo, P. Munzert, L. Boarino, F. Michelotti, F. Giorgis, and E. Descrovi, "Fluorescence diffraction assisted by Bloch surface waves on a one-dimensional photonic crystal," *New J. Phys.*, vol. 15, no. 7, p. 073002, 2013.

[61] A. P. Vinogradov, A. V. Dorofeenko, A. M. Merzlikin, and A. A. Lisyansky, "Surface states in photonic crystals," *Physics-Uspekhi*, vol. 53, no. 3, pp. 243–256, 2010.

[62] T. Goto, A. V. Dorofeenko, A. M. Merzlikin, A. V. Baryshev, A. P. Vinogradov, M. Inoue, A. A. Lisyansky, and A. B. Granovsky, "Optical Tamm states in one-dimensional magnetophotonic structures," *Phys. Rev. Lett.*, vol. 101, no. 113902, 2008.

[63] W. M. Robertson, "Experimental measurement of the effect of termination on surface electromagnetic waves in one-dimensional photonic bandgap arrays," *J. Lightw. Technol.*, vol. 17, no. 11, p. 2013, 1999.

[64] F. Villa and J. A. Gaspar-Armenta, "Electromagnetic surface waves: Photonic crystal-photonic crystal interface," *Opt. Commun.*, vol. 223, no. 1-3, pp. 109–115, 2003.

[65] S. Brand, R. A. Abram, and M. A. Kaliteevski, "Tailor-made surface plasmon polaritons above the bulk plasma frequency: A design strategy for indium tin oxide," *J. Phys. D. Appl. Phys.*, vol. 43, no. 14, 2010.

[66] W. Gao, M. Xiao, B. Chen, E. Y. B. Pun, C. T. Chan, and W. Y. Tam, "Controlling interface states in 1D photonic crystals by tuning bulk geometric phases," *Opt. Lett.*, vol. 42, no. 8, p. 1500, 2017.

[67] R. Dubey, E. Barakat, M. Häyrinen, M. Roussey, S. K. Honkanen, M. Kuittinen, and H. P. Herzig, "Experimental investigation of the propagation properties of Bloch surface waves on dielectric multilayer platform," *Journal of the European Optical Society-Rapid Publications*, vol. 13, no. 1, p. 5, 2017.

[68] Z. Chen, P. Han, C. W. Leung, Y. Wang, M. Hu, and Y. Chen, "Study of optical Tamm states based on the phase properties of one-dimensional photonic crystals," *Opt. Express*, vol. 20, no. 19, p. 21618, 2012.

[69] M. Shinn and W. Robertson, "Surface plasmon-like sensor based on surface electromagnetic waves in a photonic band-gap material," *Sensors and Actuators B: Chemical*, vol. 105, no. 2, pp. 360–364, 2005.

[70] F. Villa and L. E. Regalado, "Photonic crystal sensor based on surface waves for thin-film characterization," *Opt. Lett.*, vol. 27, no. 8, pp. 646–648, 2002.

[71] A. Sinibaldi, N. Danz, E. Descrovi, P. Munzert, U. Schulz, F. Sonntag, L. Dominici, and F. Michelotti, "Direct comparison of the performance of Bloch surface wave and surface plasmon polariton sensors," *Sensors and Actuators B: Chemical*, vol. 174, pp. 292–298, 2012.

[72] R. Badugu, K. Nowaczyk, E. Descrovi, and J. R. Lakowicz, "Radiative decay engineering 6: Fluorescence on one-dimensional photonic crystals," *Anal. Biochem.*, vol. 442, no. 1, pp. 83–96, 2013.

[73] M. Liscidini, M. Galli, M. Shi, G. Dacarro, M. Patrini, D. Bajoni, and J. Sipe, "Strong modification of light emission from a dye monolayer via Bloch surface waves," *Opt. Lett.*, vol. 34, no. 15, pp. 2318–2320, 2009.

[74] K. Toma, E. Descrovi, M. Toma, M. Ballarini, P. Mandracci, F. Giorgis, A. Mateescu, U. Jonas, W. Knoll, and J. Dostálek, "Bloch surface wave-enhanced fluorescence biosensor," *Biosens. Bioelectron.*, vol. 43, no. 1, pp. 108–114, 2013.

[75] M. Liscidini and J. E. Sipe, "Analysis of Bloch-surface-wave assisted diffraction-based biosensors," *J. Opt. Soc. Am. B*, vol. 26, no. 2, p. 279, 2009.

[76] A. Farmer, A. C. Friedli, S. M. Wright, and W. M. Robertson, "Biosensing using surface electromagnetic waves in photonic band gap multilayers," *Sensors and Actuators B: Chemical*, vol. 173, pp. 79–84, 2012.

[77] R. Rizzo, N. Danz, F. Michelotti, E. Maillart, A. Anopchenko, and C. Wächter, "Optimization of angularly resolved Bloch surface wave biosensors," *Opt. Express*, vol. 22, no. 19, pp. 23202–23214, 2014.

[78] R. Rizzo, M. Alvaro, N. Danz, L. Napione, E. Descrovi, S. Schmieder, A. Sinibaldi, R. Chandrawati, S. Rana, P. Munzert, *et al.*, "Bloch surface wave label-free and fluorescence platform for the detection of vegf biomarker in biological matrices," *Sensors and Actuators B: Chemical*, vol. 255, pp. 2143–2150, 2018.

[79] N. Matsumoto, T. Nakagawa, A. Ando, Y. Sakabe, S. Kirihara, and Y. Miyamoto, "Study of multilayer ceramic photonic crystals in THz region," *Jpn. J. Appl. Phys.*, vol. 44, no. 9S, p. 7111, 2005.

[80] S. Pirotta, X. Xu, A. Delfan, S. Mysore, S. Maiti, G. Dacarro, M. Patrini, M. Galli, G. Guizzetti, D. Bajoni, *et al.*, "Surface-enhanced Raman scattering in purely dielectric structures via Bloch surface waves," *J. Physc. Chem. C*, vol. 117, no. 13, pp. 6821–6825, 2013.

[81] A. V. Kavokin, I. A. Shelykh, and G. Malpuech, "Lossless interface modes at the boundary between two periodic dielectric structures," *Phys. Rev. B*, vol. 72, no. 23, pp. 1–4, 2005.

[82] J. A. Gaspar-Armenta and F. Villa, "Photonic surface-wave excitation: photonic crystal-metal interface," *J. Opt. Soc. Am. B*, vol. 20, no. 11, pp. 2349–2354, 2003.

[83] I. A. Shelykh, M. Kaliteevski, A. V. Kavokin, S. Brand, R. A. Abram, J. M. Chamberlain, and G. Malpuech, "Interface photonic states at the boundary between a metal and a dielectric Bragg mirror," *Phys. Status Solidi A*, vol. 204, no. 2, pp. 522–525, 2007.

[84] M. Kaliteevski, I. Iorsh, S. Brand, R. A. Abram, J. M. Chamberlain, A. V. Kavokin, and I. A. Shelykh, "Tamm plasmon-polaritons: Possible electromagnetic states at the interface of a metal and a dielectric Bragg mirror," *Phys. Rev. B*, vol. 76, no. 16, pp. 1–5, 2007.

[85] B. J. Lee, Y.-B. Chen, and Z. M. Zhang, "Surface waves between metallic films and truncated photonic crystals observed with reflectance spectroscopy," *Opt. Lett.*, vol. 33, no. 3, p. 204, 2008.

[86] M. E. Sasin, R. P. Seisyan, M. A. Kaliteevski, S. Brand, R. A. Abram, J. M. Chamberlain, A. Y. Egorov, A. P. Vasil'Ev, V. S. Mikhrin, and A. V. Kavokin, "Tamm plasmon polaritons: Slow and spatially compact light," *Appl. Phys. Lett.*, vol. 92, no. 25, pp. 1–4, 2008.

[87] S. Brand, M. A. Kaliteevski, and R. A. Abram, "Optical Tamm states above the bulk plasma frequency at a Bragg stack/metal interface," *Phys. Rev. B*, vol. 79, no. 8, pp. 2–5, 2009.

[88] S. H. Tsang, S. F. Yu, X. F. Li, H. Y. Yang, and H. K. Liang, "Observation of Tamm plasmon polaritons in visible regime from ZnO/Al_2O_3 distributed Bragg reflector - Ag interface," *Opt. Commun.*, vol. 284, no. 7, pp. 1890–1892, 2011.

[89] B. Auguié, A. Bruchhausen, and A. Fainstein, "Critical coupling to Tamm plasmons," *J. Opt.*, vol. 17, no. 3, p. 035003, 2015.

[90] M. A. Kaliteevski, A. A. Lazarenko, N. D. Il'inskaya, Y. M. Zadiranov, M. E. Sasin, D. Zaitsev, V. A. Mazlin, P. N. Brunkov, S. I. Pavlov, and A. Y. Egorov, "Experimental Demonstration of Reduced Light Absorption by Intracavity Metallic Layers in Tamm Plasmon-based Microcavity," *Plasmonics*, vol. 10, no. 2, pp. 281–284, 2015.

[91] C. Symonds, A. Lematre, P. Senellart, M. H. Jomaa, S. Aberra Guebrou, E. Homeyer, G. Brucoli, and J. Bellessa, "Lasing in a hybrid GaAs/silver Tamm structure," *Appl. Phys. Lett.*, vol. 100, no. 12, 2012.

[92] C. Symonds, S. Azzini, G. Lheureux, A. Piednoir, J. M. Benoit, A. Lemaitre, P. Senellart, and J. Bellessa, "High quality factor confined Tamm modes," *Sci. Rep.*, vol. 7, no. 1, p. 3859, 2017.

[93] A. Kavokin, I. Shelykh, and G. Malpuech, "Optical Tamm states for the fabrication of polariton lasers," *Appl. Phys. Lett.*, vol. 87, no. 26, pp. 1–3, 2005.

[94] A. V. Kuhlmann, J. Houel, A. Ludwig, L. Greuter, D. Reuter, A. D. Wieck, M. Poggio, and R. J. Warburton, "Charge noise and spin noise in a semiconductor quantum device," *Nat. Phys.*, vol. 9, no. 9, pp. 570–575, 2013.

[95] O. Gazzano, S. M. De Vasconcellos, K. Gauthron, C. Symonds, J. Bloch, P. Voisin, J. Bellessa, A. Lemaître, and P. Senellart, "Evidence for confined Tamm plasmon modes under metallic microdisks and application to the control of spontaneous optical emission," *Phys. Rev. Lett.*, vol. 107, no. 24, pp. 4–8, 2011.

[96] C. Symonds, G. Lheureux, J. P. Hugonin, J. J. Greffet, J. Laverdant, G. Brucoli, A. Lemaître, P. Senellart, and J. Bellessa, "Confined Tamm Plasmon Lasers," *Nano Lett.*, vol. 13, no. 7, pp. 3179–3184, 2013.

[97] K. Lee, J. Wu, and K. Kim, "Enhanced nonlinear optical effects due to the excitation of optical Tamm plasmon polaritons in one-dimensional photonic crystal structures," *Opt. Express*, vol. 21, no. 23, pp. 1890–1892, 2013.

[98] C.-H. Xue, H.-T. Jiang, H. Lu, G.-Q. Du, and H. Chen, "Efficient third-harmonic generation based on Tamm plasmon polaritons.," *Opt. Lett.*, vol. 38, no. 6, pp. 959–61, 2013.

[99] W. L. Zhang, F. Wang, Y. J. Rao, and Y. Jiang, "Novel sensing concept based on optical Tamm plasmon.," *Opt. Express*, vol. 22, no. 12, pp. 14524–9, 2014.

[100] R. Das, T. Srivastava, and R. Jha, "Tamm-plasmon and surface-plasmon hybrid-mode based refractometry in photonic bandgap structures.," *Opt. Lett.*, vol. 39, no. 4, pp. 896–9, 2014.

[101] B. Auguié, M. C. Fuertes, P. C. Angelomé, N. L. Abdala, G. J. A. A. Soler Illia, and A. Fainstein, "Tamm Plasmon Resonance in Mesoporous Multilayers: Toward a Sensing Application," *ACS Photonics*, vol. 1, no. 9, pp. 775–780, 2014.

[102] Y. Gong, X. Liu, H. Lu, L. Wang, and G. Wang, "Perfect absorber supported by optical Tamm states in plasmonic waveguide.," *Opt. Express*, vol. 19, no. 19, pp. 18393–8, 2011.

[103] W. L. Zhang and S. F. Yu, "Bistable switching using an optical Tamm cavity with a Kerr medium," *Opt. Commun.*, vol. 283, no. 12, pp. 2622–2626, 2010.

[104] C. Symonds, A. Lemàtre, E. Homeyer, J. C. Plenet, and J. Bellessa, "Emission of Tamm plasmon/exciton polaritons," *Appl. Phys. Lett.*, vol. 95, no. 15, pp. 2007–2010, 2009.

[105] M. Kaliteevski, S. Brand, R. A. Abram, I. Iorsh, A. V. Kavokin, T. C. H. Liew, and I. A. Shelykh, "Hybrid states of Tamm plasmons and exciton-polaritons," *Superlattices Microstruct.*, vol. 49, no. 3, pp. 229–232, 2009.

[106] T. C. H. Liew, A. V. Kavokin, T. Ostatnický, M. Kaliteevski, I. A. Shelykh, and R. A. Abram, "Exciton-polariton integrated circuits," *Phys. Rev. B*, vol. 82, no. 3, pp. 1–4, 2010.

[107] J. Gessler, V. Baumann, M. Emmerling, M. Amthor, K. Winkler, S. Höfling, C. Schneider, and M. Kamp, "Electro optical tuning of Tamm-plasmon exciton-polaritons," *Appl. Phys. Lett.*, vol. 105, no. 18, 2014.

[108] S. S.-U. Rahman, T. Klein, S. Klembt, J. Gutowski, D. Hommel, and K. Sebald, "Observation of a hybrid state of Tamm plasmons and microcavity exciton polaritons," *Sci. Rep.*, vol. 6, no. April, p. 34392, 2016.

[109] R. Badugu, E. Descrovi, and J. R. Lakowicz, "Radiative decay engineering 7: Tamm state-coupled emission using a hybrid plasmonic-photonic structure," *Anal. Biochem.*, vol. 445, no. 1, pp. 1–13, 2014.

[110] Y. Chen, D. Zhang, D. Qiu, L. Zhu, S. Yu, P. Yao, P. Wang, H. Ming, R. Badugu, and J. R. Lakowicz, "Back focal plane imaging of Tamm plasmons and their coupled emission," *Laser Photon. Rev.*, vol. 8, no. 6, pp. 933–940, 2014.

[111] Y. Chen, D. Zhang, L. Zhu, Q. Fu, R. Wang, P. Wang, H. Ming, R. Badugu, and J. R. Lakowicz, "Effect of metal film thickness on Tamm plasmon-coupled emission.," *Phys. Chem. Chem. Phys.*, vol. 16, no. 46, pp. 25523–30, 2014.

[112] G. Lheureux, S. Azzini, C. Symonds, P. Senellart, A. Lemaître, C. Sauvan, J. P. Hugonin, J. J. Greffet, and J. Bellessa, "Polarization-Controlled Confined Tamm Plasmon Lasers," *ACS Photonics*, vol. 2, no. 7, pp. 842–848, 2015.

[113] C. Symonds, G. Lheureux, J. Laverdant, G. Brucoli, J. Plenet, A. Lemaitre, P. Senellart, and J. Bellessa, "Optical properties of semiconductor in planar plasmonic structures: strong coupling and lasing," *Semicond. Sci. Technol.*, vol. 28, no. 12, p. 124001, 2013.

[114] O. Gazzano, S. Michaelis De Vasconcellos, K. Gauthron, C. Symonds, P. Voisin, J. Bellessa, A. Lemaître, and P. Senellart, "Single photon source using confined Tamm plasmon modes," *Appl. Phys. Lett.*, vol. 100, no. 23, pp. 10–14, 2012.

[115] T. Braun, V. Baumann, O. Iff, S. Höfling, C. Schneider, and M. Kamp, "Enhanced single photon emission from positioned InP/GaInP quantum dots coupled to a confined Tamm-plasmon mode," *Appl. Phys. Lett.*, vol. 106, no. 4, p. 041113, 2015.

[116] F. Feng, K. Ouaret, S. Portalupi, X. Lafosse, M. Nasilovski, W. D. de Marcillac, J. M. Frigerio, C. Schwob, B. Dubertret, A. Maître, P. Senellart, and L. Coolen, "Confined Visible Optical Tamm States," *J. Electron. Mater.*, vol. 45, no. 5, pp. 2307–2310, 2016.

[117] S. Azzini, G. Lheureux, C. Symonds, J.-M. Benoit, P. Senellart, A. Lemaitre, J.-J. Greffet, C. Blanchard, C. Sauvan, and J. Bellessa, "Generation and Spatial Control of Hybrid Tamm Plasmon/Surface Plasmon Modes," *ACS Photonics*, vol. 3, no. 10, pp. 1776–1781, 2016.

[118] R. Dubey, B. V. Lahijani, M. Häyrinen, M. Roussey, M. Kuittinen, and H. P. Herzig, "Ultra-thin Bloch-surface-wave-based reflector at telecommunication wavelength," *Photonics Research*, vol. 5, no. 5, pp. 494–499, 2017.

[119] K. Ishizaki and S. Noda, "Manipulation of photons at the surface of three-dimensional photonic crystals," *Nature*, vol. 460, no. 7253, p. 367, 2009.

[120] I. Iorsh, P. Panicheva, I. Slovinskii, and M. Kaliteevski, "Coupled Tamm plasmons," *Technical Physics Letters*, vol. 38, no. 4, pp. 351–353, 2012.

[121] S. Núñez-Sánchez, M. Lopez-Garcia, M. M. Murshidy, A. G. Abdel-Hady, M. Serry, A. M. Adawi, J. G. Rarity, R. Oulton, and W. L. Barnes, "Excitonic Optical Tamm States: A Step toward a Full Molecular-Dielectric Photonic Integration," *ACS Photonics*, pp. 743–748, 2016.

[122] A. Namdar, I. V. Shadrivov, and Y. S. Kivshar, "Backward Tamm states in left-handed metamaterials," *Appl. Phys. Lett.*, vol. 89, no. 11, p. 114104, 2006.

[123] D. Smirnova, P. Buslaev, I. Iorsh, I. V. Shadrivov, P. A. Belov, and Y. S. Kivshar, "Deeply subwavelength electromagnetic Tamm states in graphene metamaterials," *Phys. Rev. B*, vol. 89, no. 24, pp. 2–5, 2014.

[124] H. Hajian, H. Caglayan, and E. Ozbay, "Long-range Tamm surface plasmons supported by graphene-dielectric metamaterials," *J. Appl. Phys.*, vol. 121, no. 3, 2017.

[125] S. M. Vukovic, "Plasmonic Bragg Reflector and Tamm Plasmon Polaritons in Metal-Dielectric Superlattices," *Acta Phys. Pol. A*, vol. 116, no. 4, pp. 678–680, 2009.

[126] I. Iorsh, A. Orlov, P. Belov, and Y. Kivshar, "Interface modes in nanostructured metal-dielectric metamaterials," *Appl. Phys. Lett.*, vol. 99, no. 15, pp. 2009–2012, 2011.

[127] J. Zhou, N. Zhu, L.-K. Chen, and Y.-T. Fang, "Tamm states of one-dimensional metal-dielectric photonic crystal," *IET Optoelectron.*, vol. 7, no. 1, pp. 9–13, 2013.

[128] G. Isić, S. Vuković, Z. Jašić, and M. Belić, "Tamm plasmon modes on semi-infinite metallodielectric superlattices," *Sci. Rep.*, vol. 7, no. 1, pp. 1–14, 2017.

[129] L. Novotny and B. Hecht, *Principles of Nano-Optics*.
Cambridge University Press, 2012.

[130] L. Chen, M. Lopez-Garcia, M. P. Taverne, X. Zheng, Y.-L. D. Ho, and J. Rarity, "Direct wide-angle measurement of a photonic band structure in a three-dimensional photonic crystal using infrared Fourier imaging spectroscopy," *Opt. Lett.*, vol. 42, no. 8, pp. 1584–1587, 2017.

[131] M. Lopez-Garcia, Y. L. D. Ho, M. P. C. Taverne, L. F. Chen, M. M. Murshidy, A. P. Edwards, M. Y. Serry, A. M. Adawi, J. G. Rarity, and R. Oulton, "Efficient out-coupling and beaming of Tamm optical states via surface plasmon polariton excitation," *Appl. Phys. Lett.*, vol. 104, no. 23, 2014.

[132] M. Richard, J. Kasprzak, R. Romestain, R. André, and L. S. Dang, "Spontaneous coherent phase transition of polaritons in CdTe microcavities," *Phys. Rev. Lett.*, vol. 94, no. 18, p. 187401, 2005.

[133] L. A. Pettersson, L. S. Roman, and O. Inganäs, "Modeling photocurrent action spectra of photovoltaic devices based on organic thin films," *J. Appl. Phys.*, vol. 86, no. 1, pp. 487–496, 1999.

[134] P. B. Johnson and R.-W. Christy, "Optical constants of the noble metals," *Phys. Rev. B*, vol. 6, no. 12, p. 4370, 1972.

[135] R. Fern and A. Onton, "Refractive index of AlAs," *J. Appl. Phys.*, vol. 42, no. 9, pp. 3499–3500, 1971.

[136] T. Skauli, P. Kuo, K. Vodopyanov, T. Pinguet, O. Levi, L. Eyres, J. Harris, M. Fejer, B. Gerard, L. Becouarn, *et al.*, "Improved dispersion relations for GaAs and applications to nonlinear optics," *J. Appl. Phys.*, vol. 94, no. 10, pp. 6447–6455, 2003.

[137] D. Aspnes, S. Kelso, R. Logan, and R. Bhat, "Optical properties of $Al_xGa_{1-x}As$," *J. Appl. Phys.*, vol. 60, no. 2, pp. 754–767, 1986.

[138] A. D. Rakić and M. L. Majewski, "Modeling the optical dielectric function of GaAs and AlAs: extension of Adachi's model," *J. Appl. Phys.*, vol. 80, no. 10, pp. 5909–5914, 1996.

[139] A. Taflove and S. C. Hagness, *Computational electrodynamics: the finite-difference time-domain method*.
Artech house, 2005.

[140] K. Yee, "Numerical solution of initial boundary value problems involving Maxwell's equations in isotropic media," *IEEE Transactions on Antennas and Propagation*, vol. 14, no. 3, pp. 302–307, 1966.

[141] J.-P. Berenger, "A perfectly matched layer for the absorption of electromagnetic waves," *J. Comput. Phys.*, vol. 114, no. 2, pp. 185–200, 1994.

[142] "Lumerical solutions, inc.." `http://www.lumerical.com/tcad-products/fdtd/`.

[143] W. Yu and R. Mittra, "A conformal finite difference time domain technique for modeling curved dielectric surfaces," *IEEE Microwave and Wireless Components Letters*, vol. 11, no. 1, pp. 25–27, 2001.

[144] G. Ortner, M. Schwab, M. Bayer, R. Pässler, S. Fafard, Z. Wasilewski, P. Hawrylak, and A. Forchel, "Temperature dependence of the excitonic band gap in $In_xGa_{1-x}As$/GaAs self-assembled quantum dots," *Phys. Rev. B*, vol. 72, no. 8, p. 085328, 2005.

[145] J. Talghader and J. Smith, "Thermal dependence of the refractive index of GaAs and AlAs measured using semiconductor multilayer optical cavities," *Appl. Phys. Lett.*, vol. 66, no. 3, pp. 335–337, 1995.

[146] J. Talghader and J. S. Smith, "Erratum: "Thermal dependence of the refractive index of GaAs and AlAs measured using semiconductor multilayer optical cavities" [Appl. Phys. Lett. 66, 335 (1995)]," *Appl. Phys. Lett.*, vol. 69, no. 17, pp. 2608–2608, 1996.

[147] G. Knowles, R. Fehse, S. Tomic, S. J. Sweeney, T. Sale, A. R. Adams, E. P. O'Reilly, G. Steinle, and H. Riechert, "Investigation of 1.3 μm GaInNAs vertical-cavity surface-emitting lasers (VCSELs) using temperature, high-pressure, and modeling techniques," *IEEE Journal of Selected Topics in Quantum Electronics*, vol. 9, no. 5, pp. 1202–1208, 2003.

[148] J.-S. G. Bouillard, W. Dickson, D. P. O'Connor, G. A. Wurtz, and A. V. Zayats, "Low-temperature plasmonics of metallic nanostructures," *Nano letters*, vol. 12, no. 3, pp. 1561–1565, 2012.

[149] A. Alabastri, S. Tuccio, A. Giugni, A. Toma, C. Liberale, G. Das, F. D. Angelis, E. D. Fabrizio, and R. P. Zaccaria, "Molding of plasmonic resonances in metallic nanostructures: Dependence of the non-linear electric permittivity on system size and temperature," *Materials*, vol. 6, no. 11, pp. 4879–4910, 2013.

[150] "3D PC cavity analysis using the varFDTD solver, (`https://apps.lumerical.com/diffractive_optics_cavity_3d_pc.html`)." Lumerical Solutions, Inc.
Retrieved Jan 02, 2019.

[151] A. M. Gretarsson, "basic paraxial optics toolkit, (`https://uk.mathworks.com/matlabcentral/fileexchange/15459-basic-paraxial-optics-toolkit?focused=5091293&tab=function`)." MATLAB Central File Exchange.
Retrieved Sep 15, 2018.

[152] O. J. Trojak, C. Woodhead, S.-I. Park, J. D. Song, R. J. Young, and L. Sapienza, "Combined metallic nano-rings and solid-immersion lenses for bright emission from single InAs/GaAs quantum dots," *App. Phys. Lett.*, vol. 112, no. 22, p. 221102, 2018.

[153] D. Cadeddu, J. Teissier, F. R. Braakman, N. Gregersen, P. Stepanov, J.-M. Gérard, J. Claudon, R. J. Warburton, M. Poggio, and M. Munsch, "A fiber-coupled quantum-dot on a photonic tip," *App. Phys. Lett.*, vol. 108, no. 1, p. 011112, 2016.

[154] D. Marcuse, "Loss analysis of single-mode fiber splices," *Bell Syst. Tech. J.*, vol. 56, no. 5, pp. 703–718, 1977.

[155] S. Alharthi, J. Orchard, E. Clarke, I. Henning, and M. Adams, "1300 nm optically pumped quantum dot spin vertical external-cavity surface-emitting laser," *Appl. Phys. Lett.*, vol. 107, no. 15, p. 151109, 2015.

[156] A. Mischok, B. Siegmund, D. S. Ghosh, J. Benduhn, D. Spoltore, M. Böhm, H. Fröb, C. Körner, K. Leo, and K. Vandewal, "Controlling Tamm plasmons for organic narrowband near-infrared photodetectors," *ACS Photonics*, vol. 4, no. 9, pp. 2228–2234, 2017.